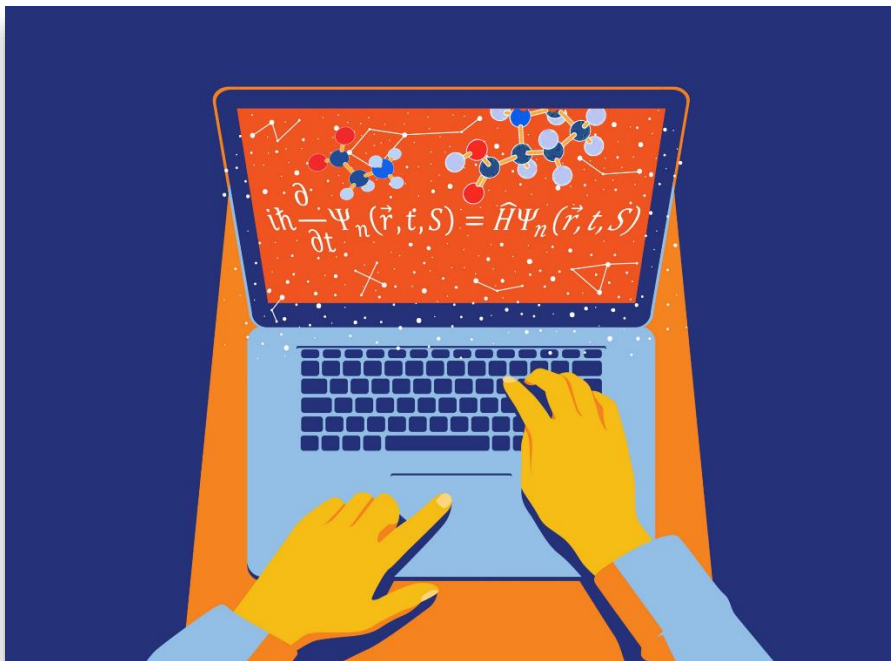




Università degli Studi di Torino

Doctoral School of Sciences and Innovative Technologies
PhD Programme in Chemical and Materials Sciences - XXXII Cycle

***Ab Initio* Computer Simulations of the Cores and
Mantles of Interstellar Dust Grains**



Lorenzo Zamirri

Supervisor:
Prof. Piero Ugliengo

Cover picture: illustration by Federico Gastaldi



Università degli Studi di Torino

Doctoral School of Sciences and Innovative Technologies

PhD Programme in Chemical and Materials Sciences - XXXII Cycle

***Ab Initio* Computer Simulations of the Cores and Mantles of Interstellar Dust Grains**

Candidate: **Lorenzo Zamirri**

Supervisor: Prof. **Piero Ugliengo**

Jury Members: Prof. **Mariona Sodupe**
Universitat Autònoma de Barcelona
Departement de Química

Prof. **Antonino Marco Saitta**
Université Pierre et Marie Curie - Sorbonne
Faculté de Physique - Institut de Minéralogie, de Physique
de Matériaux et de Cosmochimie

Prof. **Nadia Balucani**
Università degli Studi di Perugia
Dipartimento di Chimica, Biologia e Biotecnologie

Head of the Doctoral School: Prof. Alberto Rizzuti

PhD Programme Coordinator: Prof. Mario Chiesa

Torino, Italy, 31/01/2020

Contents

Preface	1
1 Introduction	5
Abstract	5
1.1 The synthesis of the first atoms: the Big Bang theory.....	5
1.2 The synthesis of heavy elements: the star lifecycle.....	9
1.2.1 Star formation: protostars.....	9
1.2.2 Nucleosynthesis processes.....	11
1.2.2.1 The proton-proton cycle.....	12
1.2.2.2 The triple-alpha process.....	12
1.2.2.3 Alpha-capture and CNO cycle.....	12
1.2.3 Stellar evolution.....	14
1.3 The interstellar medium.....	16
1.3.1 Brief historical summary of ISM observations.....	16
1.3.2 ISM regions.....	17
1.3.2.1 Reflection nebulae.....	17
1.3.2.2 Emission nebulae.....	18
1.3.3.3 Dark or (dense) molecular clouds.....	18
1.3.2.4 Diffuse clouds.....	19
1.3.2.5 Other phases of the ISM.....	19
1.3.3 ISM molecules and iCOMs.....	22
1.4 The solid phase of the interstellar medium.....	26
1.4.1 Chronology: extinction and polarization.....	26
1.4.2 Models for the interstellar dust.....	30
1.4.3 Interstellar silicates: forsterite and olivines.....	32
1.4.3.1 Formation of silicates.....	32
1.4.3.2 Amorphous vs crystalline silicates.....	33
1.4.4 Ice mantles: structure and reactivity.....	34
1.4.4.1 Composition and structure.....	35
1.4.4.2 The carbon monoxide/water interface.....	37
1.5 Concluding remarks.....	38
Bibliography	40

2	Computational methods.....	51
	Abstract.....	51
2.1	Quantum chemistry framework.....	51
2.1.1	The Schrödinger equation.....	51
2.1.2	The Born-Oppenheimer approximation.....	52
2.1.3	Variational principle and SCF procedure.....	53
2.1.4	Basis sets.....	55
2.1.4.1	Nomenclatures of localized basis sets.....	56
2.2	Quantum chemistry methods.....	58
2.2.1	The Hartree-Fock method.....	58
2.2.2	<i>Post</i> -Hartree-Fock methods.....	60
2.2.3	The electron density.....	60
2.2.4	The density functional theory.....	61
2.2.4.1	Hohenberg and Kohn theorems.....	61
2.2.4.2	Kohn-Sham formalism.....	63
2.2.4.3	Jacob's ladder: the DFT methods.....	65
2.3	Dispersive interactions.....	68
2.3.1	Grimme's D1 and D2 corrections.....	68
2.3.1.1	D1 and D2 parameters.....	69
2.3.2	Grimme's D3 correction.....	70
2.4	Classical (molecular) mechanics.....	70
2.5	Kinds of calculation.....	73
2.5.1	Optimization procedure.....	73
2.5.2	Frequencies calculation and thermodynamics.....	74
2.5.3	Molecular dynamics.....	76
2.6	Periodic systems.....	77
2.6.1	Reciprocal lattice, basis set and SCF equations.....	78
2.6.2	Dispersion.....	79
2.7	Software.....	80
2.8	Computational details.....	81
2.8.1	The CO/H ₂ O interface (Chapter 3).....	81
2.8.1.1	Static calculations.....	81
2.8.2.1	Dynamic calculations.....	82

2.8.1.3	Interaction energies and frequencies.....	82
2.8.2	Olivine nanoparticles (Chapter 5).....	84
2.8.2.1	QM calculations.....	84
2.8.2.2	CM calculations.....	84
	Bibliography.....	86
3	Ice mantles structure: the CO/H₂O interface.....	95
	Extended abstract.....	95
3.1	Background.....	98
3.2	Ice models and scaled shifts.....	102
3.3	CO/H ₂ O interactions.....	103
3.3.1	Pure CO.....	103
3.3.2	Single CO adsorption on P-ice surfaces.....	106
3.3.3	Multiple CO adsorption on P-ice surface.....	108
3.3.4	CO in H ₂ O cages.....	109
3.3.5	CO entrapped in a water-rich mixture.....	114
3.3.6	Merging the IR signals: global simulated spectrum.....	116
3.4	Concluding remarks.....	120
	Bibliography.....	123
4	Ice mantles reactivity: formation of iCOMs.....	129
	Extended abstract.....	129
4.1	Background.....	132
4.2	PES, kinetics and thermodynamics.....	134
4.3	Water-surfaces modelling.....	138
4.4	Role of water in the iCOMs formation.....	142
4.4.1	Water as a reactant: hydration.....	142
4.4.2	Hydrogenation.....	144
4.4.3	Radical reactions.....	147
4.4.4	The proton-relay mechanism.....	148
4.5	iCOMs and life: the case of glycine.....	153
4.6	Concluding remarks.....	157
	Bibliography.....	162
5	The olivine-like dust grains core.....	177
	Extended abstract.....	177

5.1	Background.....	180
5.2	Generation of olivine nanoparticles.....	183
5.2.1	Bulk cut (BC) crystalline NPs.....	184
5.2.2	Amorphized (A) NPs.....	185
5.2.3	Nucleated (N) NPs.....	187
5.3	Energetic stability.....	192
5.4	Structural descriptors.....	197
5.5	Full IR spectra.....	203
5.6	Concluding remarks.....	208
	Bibliography.....	210
6	Appendix.....	215
6.1	CO on forsterite surfaces.....	215
6.1.1	Fo bulk structural properties.....	215
6.1.2	Computational details.....	216
6.1.3	Slab properties.....	217
6.1.4	CO adsorption.....	220
6.1.4.1	Red-shifts and quadrupolar interactions.....	222
	Bibliography.....	226
7	Published works.....	229
	List of acronyms and abbreviations.....	233
	List of Figures.....	237
	List of Schemes.....	238
	List of Tables.....	238
	Acknowledgements.....	239

Preface

Astrochemistry is a branch of astrophysics dealing with the abundances and reactions of atomic, molecular, ionic and solid species in Space, as well as their interaction with electromagnetic radiations. This discipline is an overlap of astronomy and chemistry. As chemistry links the unanimated and animated world of physics and biology on Earth, respectively, so astrochemistry represents the bridge between astrophysics and astrobiology.

The word “astrochemistry” may be applied to both the Solar System (or, analogously, to other circumstellar environments) and the interstellar medium. The *interstellar medium* is composed by the matter (and radiation) “filling” the Space among stellar systems within a galaxy (like the Milky Way). Therefore, astrochemistry should be considered as the study of the chemical composition, and physical evolution, of the interstellar (and circumstellar) medium. One of the most interesting aspects about astrochemical investigation is its potential relation with the *origin of life on Earth* (and other planets?): indeed, the discovery of organic, and possibly prebiotic, material in the interstellar medium led to the formulation of several theories providing an *exogenous* origin of life. However, we are still really far away from a substantial explanation of how life originated (and, why not, originates), as more investigation is required.

The astrochemical research typically follows a multidisciplinary approach: direct information about the composition of interstellar and circumstellar matter derives from Earth-based or in-orbit *spectroscopic observations* in the whole range of the electromagnetic spectrum (from radio waves to X-rays). Spectroscopic observations can easily provide for atomic/molecular abundances in different environments, but they are not capable to give insights on several chemico-physical processes such as reactions, phase transitions, *etc.* Moreover, the error usually associated with such measurements can be important. *Astrochemical*

differential models and *laboratory experiments* are the two main approaches exploited to “fill the blanks” left from direct observations. Nevertheless, they suffer from some limitations: for example, laboratory experiments can hardly reproduce the typical physical conditions characterizing the interstellar medium (*i.e.*, very low temperatures and number densities, coupled with high-energy photon fluxes coming from nearby stars). On the other hand, astrochemical models are often parameters-dependant, and the values of such (many) parameters are usually derived from direct observations or laboratory experiments (with all the problems associated with these two approaches), or from model systems.

Within this context, the typical *methods of computational chemistry* (both quantum and classical mechanics-based) represent a complementary approach to the astrochemical research. As the other approaches, also computational chemistry methods show pros and cons. Indeed, by computer simulations, we can mimic several different phenomena occurring in Space, such as gas phase reactions, gas-solid interactions, surface diffusion, and so on. However, as always in the case of computational chemistry, results are strongly method- and model-dependant.

In this Thesis, we will deal with different computer simulations of some important astrochemical topics, with a particular reference to the solid fraction of the circumstellar and interstellar media. Specifically, after a short description of some astrochemical aspects (Chapter 1), and a brief introduction to the applied methods (Chapter 2), we will focus the attention on the so-called dust grains, the constituents of the solid phase of galactic matter. In Chapters 3 and 4, we will discuss about some features concerning the ice-coating of such grains, while in Chapter 5 we will move to their cores.

To facilitate the reading, we have organized the three Chapters concerning with the main results (number 3, 4 and 5) of this Thesis in the following way: At the very beginning, we provide an “Extended abstract” where we resume the main

aspects of the topic we will deal with in the given Chapter. For further insights, the interested reader can then refer either to the various Sections of the Chapters or, because all the results we will discuss are already published, directly to the reference works (see Chapter 6).

1 Introduction

Abstract

In this Chapter, we will introduce the reader to some important aspects about how matter forms and organizes itself in our Universe. After a short dissertation about Cosmological theories and some nucleosynthesis processes occurring in stars, we will focus the attention on the composition of the interstellar medium, with particular reference to the structural and chemical properties of dust grains cores (silicates) and mantles (ices).

1.1 The synthesis of the first atoms: the Big Bang theory

As we will discuss in a later Section of this Chapter, the interstellar and circumstellar environments are characterized by a surprisingly rich chemistry. Therefore, one of the most important question in the astrochemical research regards how this rich chemistry can actually occur. There are several theories that try to explain this occurrence (some of which will be shortly presented), therefore a definitive answer does not exist. However, all such theories require the existence of pre-formed matter in form of atoms or atomic ions. In this and the next Sections, we will briefly describe how such atomic matter has/is formed.

The first theoretical evidence of a non-static Universe comes from the Albert Einstein's general relativity work in 1915.¹ In such a work, Einstein (**Figure 1.2**) published the following expression

$$R_{\mu\nu} - \frac{1}{2}Rg_{\mu\nu} + \Lambda g_{\mu\nu} = \frac{8\pi G}{c^4}T_{\mu\nu} \quad 1.1$$

known as *Einstein field equation*. Here, $R_{\mu\nu}$ is the *Ricci curvature tensor*, R is the trace of $R_{\mu\nu}$, $g_{\mu\nu}$ is the metric tensor of space-time, Λ the notorious *Cosmological constant*, G is the Newton's gravitational constant, $T_{\mu\nu}$ is the stress-energy tensor and c is the speed of light. In simple terms, the Einstein field equation can be interpreted in the following way: the metric of the Universe ($g_{\mu\nu}$) is not uniform

(in space and time), but rather strongly depends on the local distribution of energy and momentum ($T_{\mu\nu}$).

In 1927, the Belgian priest and astronomer Georges Edouard Lemaître (**Figure 1.2**), thanks to the work of the U.S. astronomer Edwin P. Hubble (**Figure 1.2**) who first distinguished galaxies from other kind of cosmic clouds, hypothesized that the velocity v at which a given galaxy at distance D from the Milky Way is moving away linearly increases with the distance itself

$$v = H_0 D \tag{1.2}$$

where H_0 is the Hubble constant. Assuming Equation **1.2**, in 1927 Lemaître found a solution to Equation **1.1**. Lemaître's model contains a spatial curvature parameter k which can be positive, negative or null:²

- for $k > 0$, the Universe is open, and the kinetic energy is always greater than the gravitational potential energy, meaning that Universe is destined to an eternal expansion;
- for $k = 0$, the Universe is open but exists in a critical state: the gravitational attraction is not sufficient for the Universe to collapse but is also insufficient for ensure an infinite expansion; as a result, in an infinite period of time, the expansion of the Universe will slow down to zero speed;
- for $k < 0$, the Universe is closed, and the gravitational attraction causes a slowdown of the expansion and a subsequent collapse.

Lemaître's work is nowadays considered as the first seed of the cosmological theories centered around the concept of *Big Bang*. However, it is important to underline that already in 1922, the Russian physicist and mathematician Alexander A. Fridman (**Figure 1.2**) came to similar conclusions, but his work was totally ignored by the Anglo-Saxon-dominated scientific community mainly for political reasons.³ Lemaître's 1927 hypothesis was later experimentally proved

by Hubble in 1929, in his famous work about the redshift of the light coming from distant galaxies.⁴

Another fundamental experimental proof supporting the Big Bang theory is the discovery, in 1964 by the U.S. astronomers Arno Allan Penzias e Robert Woodrow Wilson (**Figure 1.2**), of the so-called *Cosmic microwave background radiation* (CMBR) which would represent the electromagnetic radiation emitted by the first atoms formed after the Big Bang,⁵ and which was predicted to exist in several cosmological models. CMBR shows a black body spectrum with a maximum at ~ 1.9 mm (**Figure 1.1**), which corresponds to an average temperature of 2.728 K.⁶

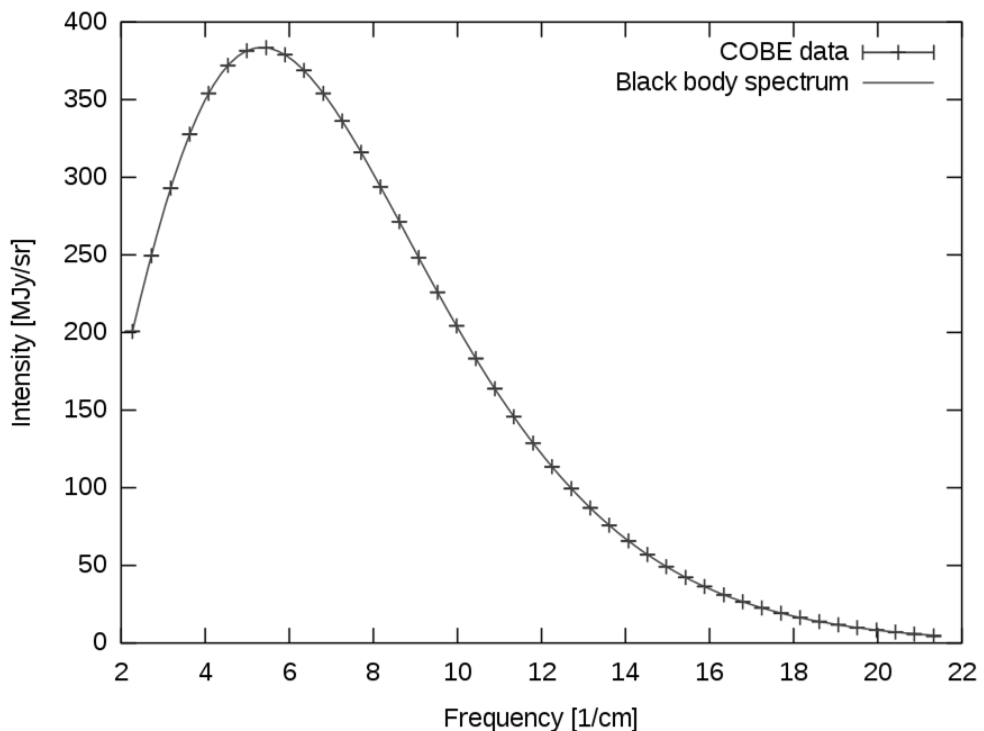


Figure 1.1 Black body predicted spectrum for a radiative source at temperature of 2.728 K (line) compared with experimental measurements (crosses) of CMBR by the COBE satellite.⁶ Reproduced under public domain license.

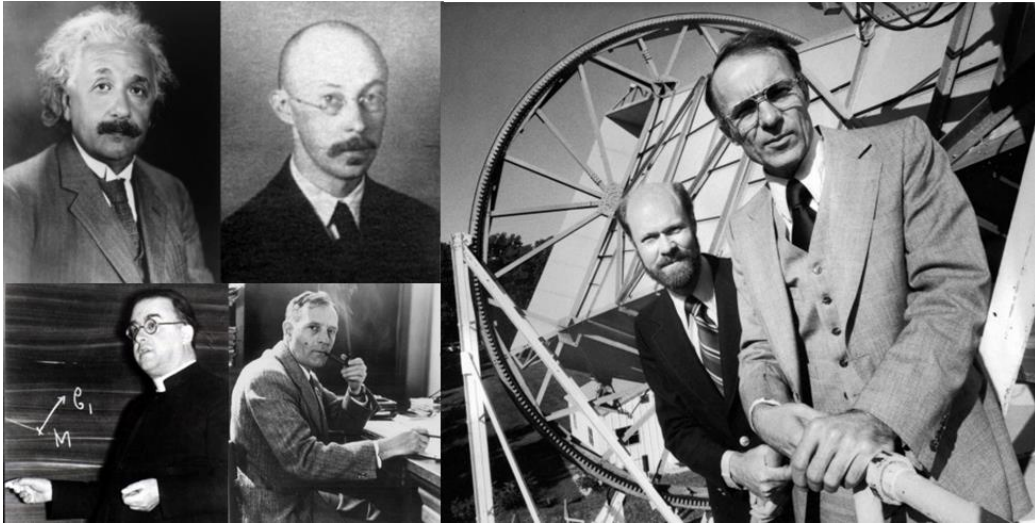


Figure 1.2 Left panel, clockwise: Albert Einstein (1879-1955), Alexander A. Fridman (1888-1925), Edwin P. Hubble (1889-1953) and Georges E. Lemaître (1894-1966). Right panel: Robert W. Wilson (left, 1936) and Arno A. Penzias (1933) pose with the antenna they used to discover the CMBR.

From Lemaître and Fridman times, cosmological theories have dramatically changed, but the original idea of a single event after which the Universe as we know it began to form still persists. For the purposes of this work, it is necessary to stress how after a very short period of time, protons started to form and, therefore, the first nuclear processes – mainly forming deuterium, helium and some lithium nuclei – started. Nevertheless, it required thousands of years for these primeval nuclei to capture electron and thus forming neutral atoms. Some of these events are resumed in **Table 1.1**. At these early stages of the Universe, there was no place for chemistry to occur, since all the matter was in a very simple atomic and ionic form. In order to enrich the Universe in further chemical elements, thus allowing the arising of proper chemical networks, stars need to birth and die. In the next Section, we will discuss about some important aspects of a star lifecycle, with a particular reference to the nuclear processes occurring in its inner shells or during some critical, energetic events.

Table 1.1 The history of the Universe according to the Standard Model. From Ref. 7.

Time since $t = 0$	Average temperature	Comment
10^{-43} s	10^{32} K	End of Planck's era: gravity is distinct from the other forces
10^{-35} s	10^{27} K	Inflation of the Universe – strong force separates
10^{-12} s	10^{15} K	Weak and electromagnetic force separate; protons and neutrons are formed by photon-photon collisions
10^{-2} s	10^{11} K	Electrons and positrons are formed through collisions of photons – nucleosynthesis of H, D, He and some Li begins
180 s	10^9 K	Nucleosynthesis ends
3-7 10^5 s	3000 K	Light atoms are formed: CMBR is emitted
10^9 yr	20 K	Galaxies form
Present	2.728 K	Galaxies and stars

1.2 The synthesis of heavy elements: the star lifecycle

Some instants after the Big Bang, only H, D, He and Li nuclei were present: all other elements appearing in the Periodic Table have been synthesized from stellar-related processes where these light nuclei work as fuel. Since galaxies are dynamic objects, where stars are continuously forming and dying, the Universe is getting richer and richer in heavier elements. Nevertheless, H and He still remain the two most abundant nuclei, together accounting for about 98% of the total baryonic mass of the Universe.⁸

1.2.1 Star formation: protostars

The primeval matter formed after the Big Bang appeared as a diffuse atomic cloud. In order for stars to form, this cloud material had to collapse under gravitational attraction. However, the gravitational collapse is not a simple process since some conditions must be satisfied. First of all, the atomic local density should exceed 10^5 - 10^6 cm^{-3} with temperature values of 10 K or more.⁹

Nevertheless, the collapse will be spontaneous only if the cloud achieves a critical mass called the *Jeans Mass* M_J that, for a spherical cloud, can be predicted to be

$$M_J = \frac{\pi}{6} \frac{c_s^3}{G^{3/2} \rho^{1/2}} \quad 1.3$$

where c_s is the speed of sound in the cloud and ρ is the particle number density.¹⁰ If all these conditions are satisfied, matter begins to collapse under the influence of gravity: little by little, gravitational potential energy is converted into kinetic energy and temperature. The collapse near the center is very rapid and temperature increases until it reaches values of a few hundred kelvins: a core of incandescent material is formed. Together with temperature, also pressure increases, and the gravitational attraction begins to be balanced by the heat of expansion until the contraction stops: a *protostar* has formed. The surface temperature is sufficiently high to cause protostars to emit infrared (IR) radiation, through which they can release some gravitational energy: such a radiation can be seen in big clouds regions where processes of star formation are occurring, regions called *stellar nebulae*.⁷

In the outer regions of a stellar nebula, an envelope of dust and gas material originates: such material continues to fall into the protostar that collapses again. This new contraction continues until the core becomes optically thick, preventing IR photons from escaping, and the temperature reaches 1500-2000 K. The temperature keeps rising and ionization of H atoms starts until, at 10^6 K, the bare protons are colliding with sufficient energy to induce nuclear fusion processes and the protostar develops a solar wind that shakes off the dust material, beginning to shine and entering the so-called *main-sequence* phase.⁷

1.2.2 Nucleosynthesis processes

The average binding energy (BE) *per* hadron (the nuclear BE divided by the number of nucleus constituents) shows a maximum in correspondence of $^{56}_{28}\text{Ni}$ isotope if plotted as a function of the atomic mass number A (**Figure 1.3**). Sometimes, $^{56}_{26}\text{Fe}$ and not $^{56}_{28}\text{Ni}$ is reported to have the greatest average BE: this discordance originates from the actual definition of average BE *per* hadron. However, for our purposes, this disagreement is not fundamental. Therefore, fusion processes would be spontaneous until $^{56}_{28}\text{Ni}$ is reached, and, consequently, nucleosynthesis of heavier isotopes cannot occur within stars, but rather is the result of nuclear processes occurring in the last stages of a star lifecycle. In the following, the four main nucleosynthesis process will be briefly described.

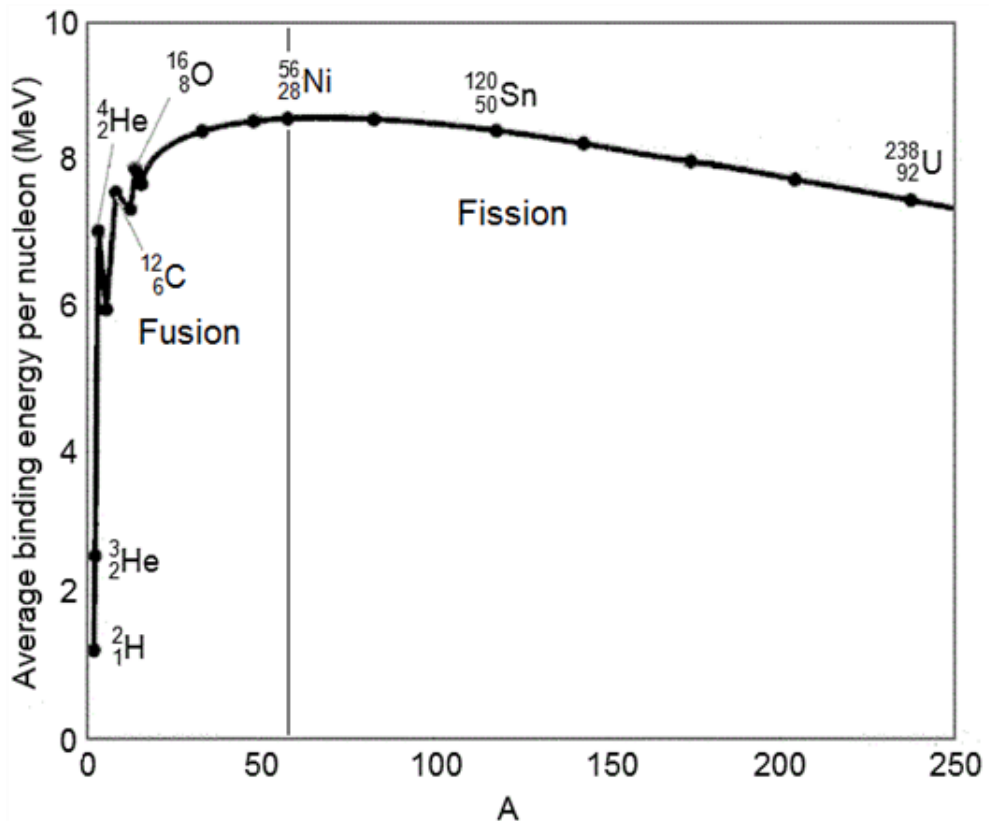
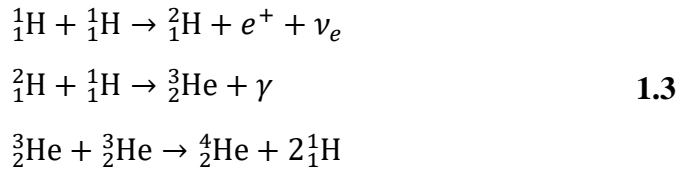


Figure 1.3 Average BE *per* hadron (in MeV) vs atomic mass number A : on the left of the vertical line corresponding to $^{56}_{28}\text{Ni}$ isotope, nuclear fusion is exergonic. From Ref. 7.

1.2.2.1 The proton-proton cycle

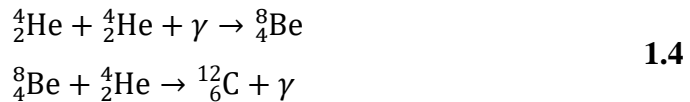
The basic energy source in young stars is the fusion of protons into the ${}^4_2\text{He}$ nucleus in three steps. This process is occurring in our Sun and in other main-sequence stars where it produces about 91% of the total energy. The *proton-proton* cycle proceeds *via* three reaction steps (γ is a gamma-ray, e^+ is a positron and ν_e is the electronic neutrino):



The total energy released in one cycle is 4.30×10^{-12} J. Allowing for the observed mass of the Sun, the total energy produced during one cycle is 6.4×10^{14} J and some 6.0×10^{11} kg of H is converted to He every second.⁷

1.2.2.2 The triple-alpha process

At a temperature of 10^8 K, He starts to “burn” in a two-steps process involving three helium nuclei and forming ${}^{12}_6\text{C}$: the *triple alpha* process.

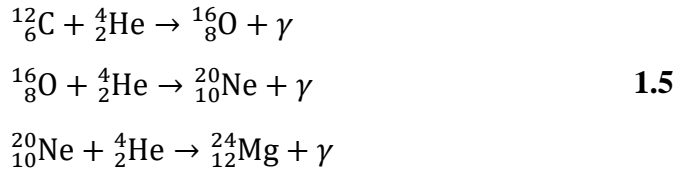


The process is less efficient than the proton-proton cycle, producing about 10% of the energy *per* kg in the Sun. In this kind of stars, there is no sufficient energy to ignite carbon fusion, thus they are destined to become carbon cinders. However, the triple-alpha process produces the most important atomic nucleus for life as we know it, carbon.⁷

1.2.2.3 Alpha-capture and CNO cycle

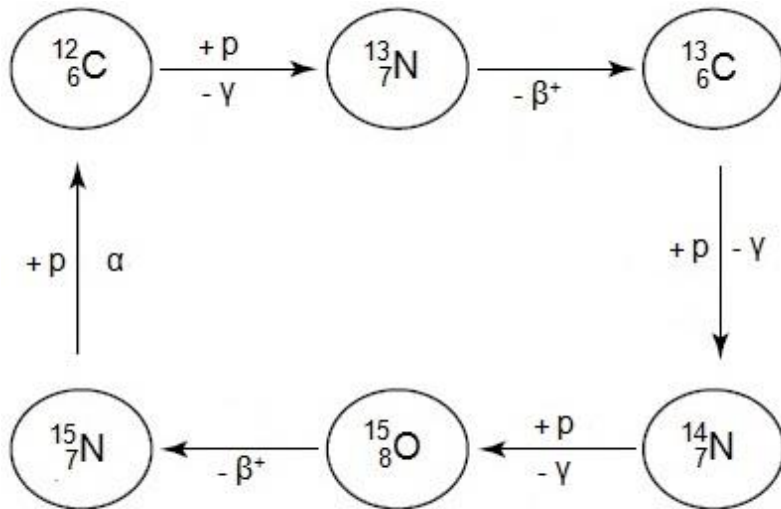
Stars with masses comparable to Sun mass cannot produce heavier nuclei than ${}^{12}_6\text{C}$. With a sufficient initial mass of H, the He core produces ${}^{12}_6\text{C}$, the point at

which the star starts dying. However, in heavier stars, at around 10^8 - 10^9 K, the *alpha-capture* process can occur, producing a large number of different nuclei:



Alpha-capture continues in a similar way producing ${}^{28}_{14}\text{Si}$, ${}^{32}_{16}\text{S}$, ${}^{36}_{18}\text{Ar}$, ${}^{40}_{20}\text{Ca}$, ${}^{44}_{22}\text{Ti}$, ${}^{48}_{24}\text{Cr}$, ${}^{52}_{26}\text{Fe}$ and, finally, ${}^{56}_{28}\text{Ni}$.⁷

${}^{12}_6\text{C}$ can be involved also in the *carbon-nitrogen-oxygen (CNO) cycle* that can produce other nuclei (not all of which are stable) such as ${}^{13}_6\text{C}$, ${}^{13}_7\text{N}$, ${}^{14}_7\text{N}$ and ${}^{15}_8\text{O}$. All of these nuclei can also undergo alpha-capture to produce other elements, as shown in **Scheme 1.1**.⁷



Scheme 1.1 CNO cycle for $T > 1.6 \times 10^7$ K and $M > 1.1$ solar masses. Reproduced from Ref. 7.

Table 1.2 shows the major fusion products as a function of the kind of fuel used by stars of different relative masses with respect to the Sun mass (M_S) and temperature. As it is evident, the role of heavier stars in the cosmic nuclear synthesis of heavy elements is fundamental.

Table 1.2 Stages of thermonuclear generation in stars (M_{\odot} is the Solar mass). Reproduced from Ref. 7.

Process	Fuel	Major products	Approximate core temperature (K)	Minimum mass (M_{\odot})
H burning	H	He	2×10^7	0.1
He burning	He	C, O	2×10^8	1.0
C burning	C	O, Ne, Na, Mg	8×10^7	1.4
Ne burning	Ne	O, Mg	1.5×10^9	5
O burning	O	Mg to S	2×10^9	10
Si burning	Mg to S	Elements near Fe	3×10^9	20

1.2.3 Stellar evolution

The previous Section shows a critical point about stars: the processes occurring within them – and, ultimately, their last stages – depend on the star initial mass. Discussing all possible destinies of stars is far beyond the purposes of this work. Looking at **Figure 1.4**, what is worth mentioning is that, except for very small-massed stars (mass $< 0.08 M_{\odot}$), several stars are somehow destined to end in an energetic explosion. Medium-sized stars will probably generate *planetary nebulae*, while massive stars might end with *supernova remnants*. The formation of this kind of clouds, together with other phenomena such as stellar winds, is fundamental for the re-cycle of matter in the interstellar medium and, therefore, drives the chemistry of interstellar matter.¹¹ The main chemico-physical features of planetary nebulae, supernova remnants and other kind of clouds will be presented more in detail in the Sections 1.3.2.11.3.2.5.

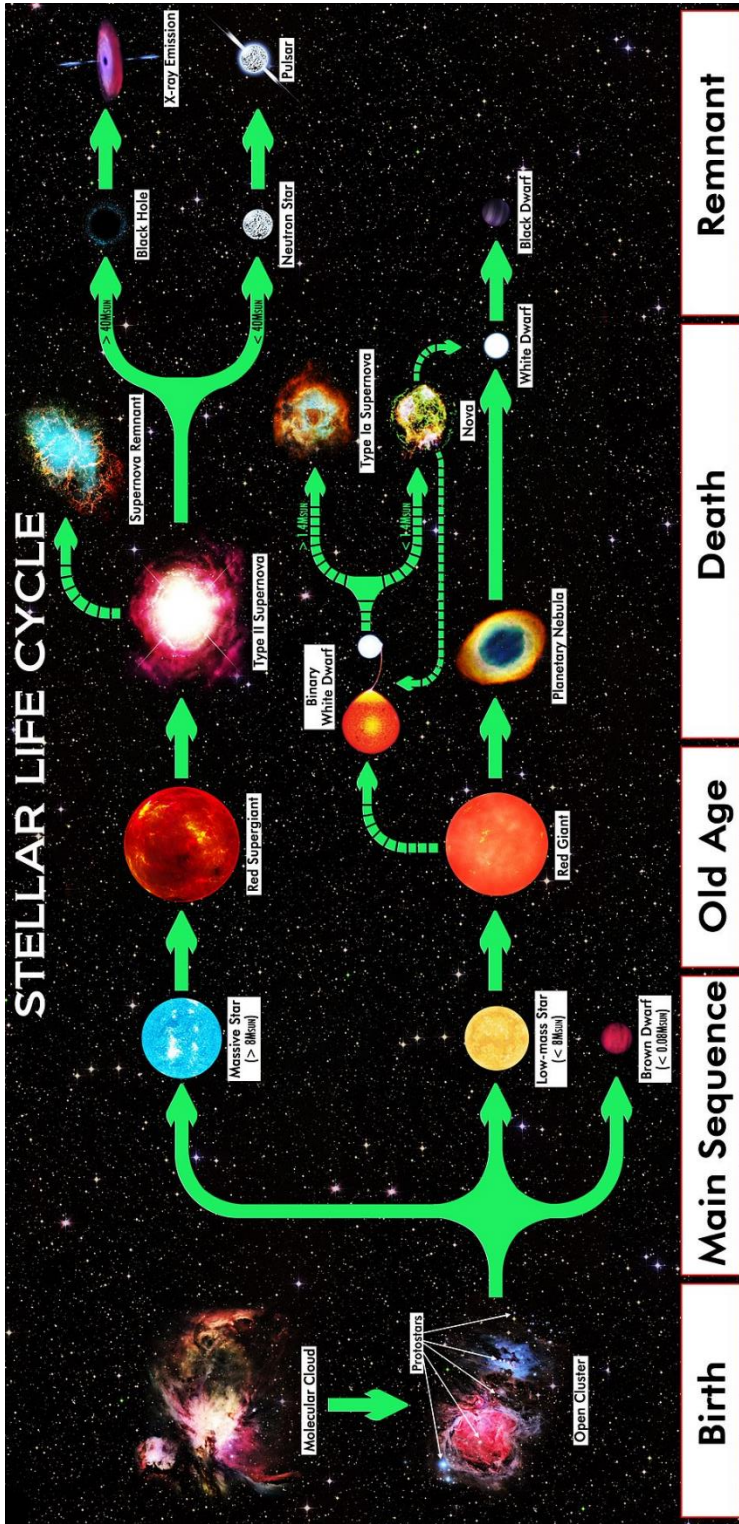


Figure 1.4 Graphical representation of the stellar lifecycle: according to their initial mass, stars are destined to different deaths. From an astrochemical point of view, planetary nebulae and supernova remnants are the most interesting ones. Picture published under creative common license: attribution 4.0 International licence. Available at https://commons.wikimedia.org/wiki/File:star_Life_Cycle_Chart.jpg

1.3 The interstellar medium

So far, we focused the discussion around stars. The Space around stars is usually known as *circumstellar shell* (CSS), and therefore the matter present in CSSs is usually reported as *circumstellar medium*. However, CSS are not isolated objects in Space, with definitive borders: rather, they gradually fall into the *interstellar medium* (ISM), the matter and radiation filling the Space among formed stellar systems.

1.3.1 Brief historical summary of ISM observations

ISM observations date already 1785 when the German astronomer Frederik William Herschel described what are now known as dark molecular clouds (see Section 1.3.2.3) as “holes in the Heavens”, *i.e.*, regions lacking for some unknown reasons of stars.¹² However, we have to wait until 1930, when U.S.-Swiss astronomer Robert J. Trumpler identified the causes for such “holes”: they are due to the presence of interstellar dust solid particles absorbing the light from background stars (Section 1.4.1). More or less in the same period, the first observations in the optical region of the electromagnetic spectrum (EMS) identified the presence of gas phase species in the ISM: in particular, excited atomic and ionic lines originating from hot ($\sim 10^4$ K) sources were identified.¹³ The simplest molecular species were then discovered from electronic transitions observed in absorption against background stars (Section 1.3.3).¹³ The presence of such, and many others, molecules has been definitely confirmed from the development, in the 1950s, of radio astronomy.¹³ Radio astronomy led also to the detection of the $\lambda = 21$ cm hydrogen line (hyperfine transition of the spin of the $1s$ electron),¹⁴ demonstrating the almost ubiquitous presence of the H atom in the ISM.¹³ The presence of solid dust particles was then confirmed after the development of IR observations in the 1960s, that opened the investigation of the solid phase of the ISM material, not only the dust grains cores, but also the ice covering mantles (Section 01.4.4).¹³ The whole EMS was then completely

covered after the development of the Einstein Observatory for X-rays sources by NASA in 1978.¹⁵

Most of the efforts in the astrochemical research are dedicated to the study of the composition and of the chemico-physical evolution of the ISM, as it is characterized by a vivid chemistry and because it represents the reservoir for new stellar formation.^{16,17} In the following, we will discuss some of the most important aspects that are fundamental for this work.

1.3.2 ISM regions

Depending on the chemical composition, the ISM is usually divided into several components.^{13,16–19} The nomenclature for these components is not completely univocal, as often different terms are used to designate the same objects. Within this work, we will adopt the terms presented in Ref. 13.

Figure 1.5 shows a schematic representation of the multiple phases of the ISM, while in **Figure 1.6** we report some example of ISM nebulae discussed below.

1.3.2.1 Reflection nebulae

Reflection nebulae do not shine on their own, at least in the visible, but rather they reflect the starlight coming from near sources.²⁰ Therefore, they show similar spectral features to the nearby stars, even if they usually appear to be bluer in colour. The bluer colour is the result of scattering processes occurring at the surface of dust grains – ubiquitously present in this kind of clouds – as the scattering is more efficient at short than at long wavelengths.¹³ The intensity of incoming starlight is not sufficient to produce ionization of the atomic matter, thus most of the hydrogen persist in atomic form (H I form) and this is what mainly distinguish reflection nebulae from emission nebulae (Section 1.3.2.2). Reflection nebulae often derive from dark clouds (Section 1.3.2.3) and thus are usually found near sites of recent star formation, but can be also found in the surroundings of evolved stars as the results of the ejection of dust material from the CSS.¹³

1.3.2.2 *Emission nebulae*

Contrary to reflection nebulae, *emission nebulae* do emit light by themselves. The responsible of such emission is essentially hydrogen in ionic (H II or H^+) form: the light coming from nearby stars is sufficiently energetic to allow the dissociation of H atoms into a proton-electron pair. After dissociations, free electron can be eventually re-captured by free protons, resulting in an emission.¹³ The most typical and dominant emission is the $\text{H}\alpha$ one from $n = 3$ to $n = 2$ at 656.281 nm, *i.e.*, in the red region of the EMS.²¹ Accordingly, emission nebulae usually appear in the visible as red.¹³ There are three kinds of emission nebulae: *i) planetary nebulae*, *ii) supernova (SN) remnants*, and *iii) H II regions*.¹³ Despite the name, planetary nebulae do not show any connection with planets: the name comes from their spherical shapes that led the first astronomers who observed them to believe they were resembling planets. Rather, they are the results of the explosion of a red giant star (see **Figure 1.4**), one of the last stages of a medium mass-sized star. Similarly, SN remnants are the results of really more energetic SN explosions involving red supergiant stars.¹¹ Both planetary nebulae and SN remnants show very-well defined borders and can be associated with a central remaining star,¹¹ while H II regions do not and cannot.¹³ H II regions are associated with star formation and are usually observed close to molecular clouds (Section 1.3.2.3), as they represent the portion of a molecular cloud that has been photoionized by a new-born star.¹³

1.3.2.3 *Dark or (dense) molecular clouds*

Contrary to emission and reflection nebulae, *dark clouds* manifest themselves by the absence of visible starlight.²⁰ Indeed, they correspond to the “hole in the Heavens” Herschel described in 1785 (Section 1.3.1). This absence is the result of the absorption of starlight by dust grains of the light coming from background stars. The gas temperature in dark clouds is very low (typically 10-20 K), indicating that there are no strong near heating sources.¹³ The very low

temperatures, together with the relatively high number densities (**Table 1.3**) allow the formation of covering ice-mantles around the dust grains cores, responsible for starlight absorption.²² Dark clouds are often referred to as (dense) *molecular clouds* (MCs) because of the observed presence of a large variety of chemical molecular species, mainly H₂ and CO (Section 1.3.3). A particular example of MCs is represented by *giant molecular clouds* (GMCs), usually very bright in the IR and molecular-line emissions. In GMCs, gas and dust temperatures are slightly higher than in normal dark MCs (ranging in between 50 and 100 K), suggesting the presence of internal heating sources (newly formed massive stars). Being particular unstable, GMCs tend to collapse forming the so-called *molecular hot cores*, with temperatures of ~100-300 K and number densities of ~10⁶-10⁷ cm⁻³, noticeably high for the ISM (see **Table 1.3**).^{13,23}

1.3.2.4 Diffuse clouds

As for the H II regions, *diffuse clouds* do not show well defined morphologies. They are mainly composed by atomic hydrogen, and, therefore, they are usually traced by the $\lambda = 21$ cm line (Section 1.3.1).¹³ In the inner regions, where starlight is shielded, simple diatomic species have been observed (H₂, HD, OH, CO, N₂, O₂).¹³ Due to higher temperatures and lower densities (**Table 1.3**), bare dust grains have been observed in diffuse clouds: the absence of ice-covering mantles might explain the relative chemical poorness of such clouds when compared to MCs (Section 1.3.3). Moreover, molecules can be also destroyed in these clouds by incoming UV energetic photons.

1.3.2.5 Other phases of the ISM

So far, we have discussed the most important regions of the ISM, adopting a standard nomenclature. Two other important ones are the *hot coronal gas* regions and the *photodissociation regions* (PDRs).¹³ The former show incredibly high temperatures for the ISM (up to 10⁶ K, see **Table 1.3**), therefore are mainly composed by cationic species (Li I, O V and VI, N V, C IV, *etc.*) and traced by X-

ray emission,¹³ while the latter are intermediate regions at the interface between warm and cold phases of the ISM. From an astrochemical point of view, PDRs are fundamental since they may drive interesting chemical processes: indeed, when the typical molecular species of MCs enter these regions, they undergo photodissociation caused by diffuse galactic starlight, thus forming radical species that might show a various reactivity.¹³

Table 1.3 ISM components and their properties. Adapted from Ref. 13.

ISM component	Common designation	T (K)	Density* (cm^{-3})	State of hydrogen	$\chi^\#$
Hot ionized medium (HIM)	Coronal gas	10^6	$\sim 10^{-3}$	H^+	1
Warm ionized medium (WIM)	Diffuse ionized gas	10^4	>10	H^+	1
Warm neutral medium (WNM)	Intercloud H I or reflection nebulae	10^3 - 10^4	0.1	H	0.1
H II regions	Emission nebulae	10^3 - 10^4	10^2 - 10^4	H^+	1
Atomic cold neutral medium (ACNM)	Diffuse clouds	100	10-100	$\text{H} + \text{H}_2$	$\sim 10^{-3}$
Molecular cold neutral medium (MCNM)	Molecular clouds	10-50	10^3 - 10^5	H_2	$\sim 10^{-7}$
Molecular hot cores	Protostellar cores	100-300	$>10^6$	H_2	$<10^{-8}$

*Density of H_2 in MCs and molecular hot cores, of H in all other phases.

#Ionization fraction.

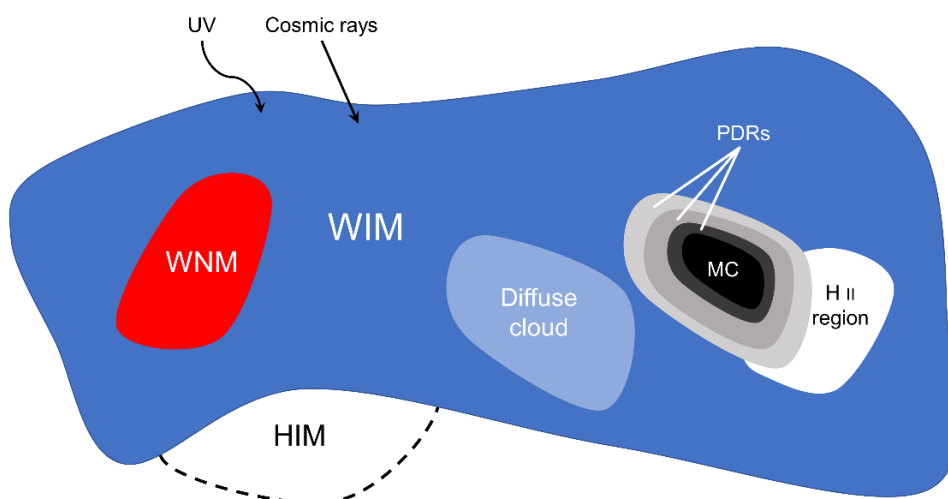


Figure 1.5 Schematic representation of the ISM showing its different phases (see also **Table 1.3**). Adapted from Ref. 13.

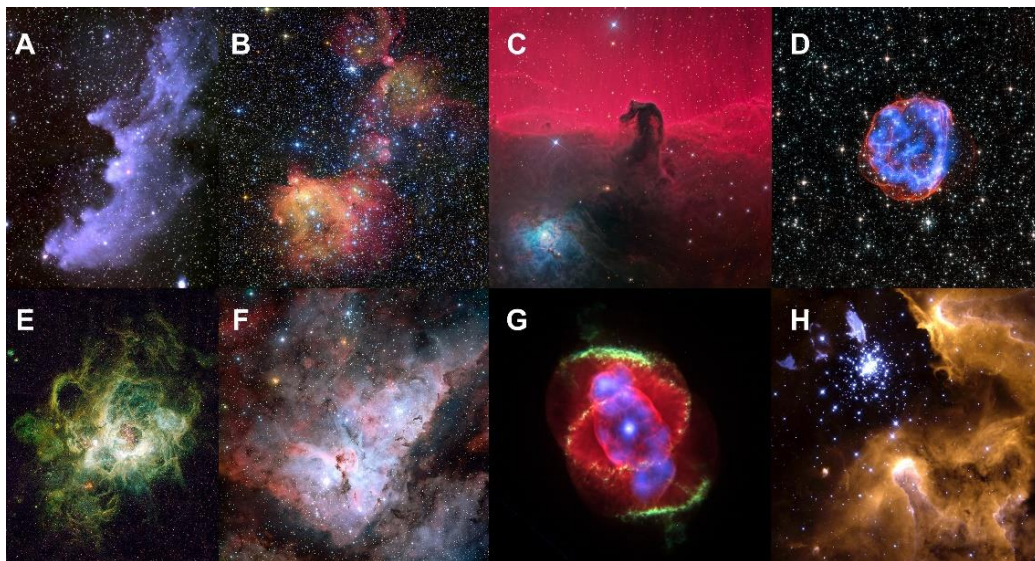


Figure 1.6 Examples of ISM nebulae. A: *Witch Head* reflection nebula associated with the bright star Rigel in the Orion constellation. B: Emission nebula *LHA 120-N 55* in the Large Magellanic Cloud (LMC). C: dark *Horsehead Nebula* (emission nebula IC 434 in the background) in the Orion constellation. D: SN remnant in LMC. E: *NGC 604*, a H II region in the Triangulum Galaxy. F: the *Carina diffuse nebula*. G: Cat’s eye protoplanetary nebula. H: *NGC 3603* nebula in Carina constellation. The interface between dark (H II) and bright matter is a PDR. Pictures published under public domain (A, D, E, G, H) and creative common (B, C, F) licenses.

1.3.3 ISM molecules and iCOMs

In previous Section, we showed how the presence of matter at least in atomic and/or ionic form is ubiquitous in different ISM environments. However, matter in molecular form is only observed in diffuse (mainly simple diatomic molecules such as H_2 , HD, $\text{OH}\cdot$, *etc.*, with few notable exceptions, see **Table 1.4**) and dense molecular clouds, which instead show a prosperous chemistry (**Table 1.5**). ISM molecules have been detected from a combination of techniques: electronic (UV-visible), vibrational (IR) and mostly rotational spectroscopy (micro- and radio-waves).¹³ Before discussing a few important aspects of ISM molecular species, we need to specify that with the terms “ISM molecules/molecular species” we mean not only proper molecules (*i.e.*, isolated neutral compounds) but also radical

Introduction

and charged (*e.g.*, OH \cdot , CH \cdot , HCO $^+$, N $_2$ H $^+$, *etc.*) molecular compounds. This is necessary because of the important presence of such compounds, that would not be stable under terrestrial-like conditions, together with some strange “exotic” species (few examples are C $_5$ N, C $_8$ H and HNC $_3$).

The first molecules to be detected in the ISM, through UV-visible spectroscopy, were CH \cdot , CN \cdot and CH $^+$, in the 1930s-1940s, followed, in the following years, by CO, NH \cdot and O $_2$.^{24,25} Optical observation of more complex species is non-trivial, because of the presence of many molecular lines. Therefore, when it became available in the 1950s, astronomers resorted to the more powerful radio spectroscopy. The first species to be detected from such technique is OH \cdot (1963) followed (end of the 1960s/beginning of the 1970s) by NH $_3$, H $_2$ O, H $_2$ CO, CO, HCN.²⁴ From that, essentially all the molecular species observed so far in the ISM have been detected through radio spectroscopy.^{24,25} **Table 1.4** shows all the species identified up to now from different techniques in diffuse clouds only,²⁵ while **Table 1.5** resume all molecular species observed in all ISM environments (grouped by the number of atoms).^{26,27}

Table 1.4 Species detected in diffuse clouds in the UV-visible (O), infrared (IR) and radio (R) regions. *c*- stands for “cyclic”. Adapted from Ref. 25.

Molecule	Technique	Molecule	Technique	Molecule	Technique
H $_2$	O	HCl	R	H $_3$ O $^+$	R
H $_3^+$	IR	H $_2$ Cl $^+$	R	HF	R
CH \cdot	O, R	C $_2$	O	SH \cdot	R
CH $^+$	O, R	C $_2$ H \cdot	O, R	SH $^+$	R
NH \cdot	O, R	CN \cdot	O, R	H $_2$ S	R
NH $_2$	R	HCN	R	HCl	R
NH $_3$	R	HNC	R	HCO \cdot	R
OH \cdot	O, R	N $_2$	O	<i>c</i> -C $_3$ H $_2$	R
OH $^+$	R	CO	O, R	CS	R
H $_2$ O $^+$	R	HCO $^+$	R	SO $_2$	R
H $_2$ O	R	HOC $^+$	R	CS $^+$	R
C $_3$	O, R	H $_2$ CO	R	<i>c</i> -C $_3$ H	R

Common interstellar molecules are small compounds by terrestrial standards, ranging from 2 to 13-15 atoms. Some of these compounds are usually referred to as *complex organic molecules* (COMs). This term is usually associated with molecules between 6 and 13-15 atoms in which at least one is carbon.²⁸

The presence of organic compounds in the dense ISM led the formulation of some theories providing for an extra-terrestrial or *exogenous origin of life on Earth* (and on other planets?). Briefly, the idea underneath such theories is that the organic matter from which biotic molecules came from might be formed directly in the ISM, and then incorporated by the Solar nebulae and its protoplanetary disk. *Panspermia*, the idea that life might manifest itself throughout the whole Universe, distributed by space dust, meteoroids, asteroids, comets and planetoids, probably represents the most well-known exogenous theory of life.²⁹

The above-mentioned definition of COMs allows us to exclude simple molecules that are sure not *organic*, like H₂O, NH₃ or CO, but also excludes some relevant species as formaldehyde (H₂CO) or methanimine (CH₂=NH). Moreover, other species, although not being categorized as COMs, can play a crucial role in the organic, and eventually pre-biotic, chemistry occurring in the ISM, such as the case of formic acid (HCOOH), hydrogen cyanide/isocyanide (HCN/HNC) or the isocyanic acid (HCNO), just to mention a few.³⁰

There is currently a vivid debate about the formation of COMs in the ISM, and in particular in dense MCs. Two paradigms are usually invoked.³⁰ The first one postulates that COMs are synthesized on the surfaces of dust grains (see Section 1.4.4) following a four-step process that we can call as the “on-surface” paradigm: *i*) gas phase molecules freeze on the surface of the dust grains cores forming a coating layer of ice; *ii*) hydrogenation of the frozen molecules to form saturated species (*e.g.*, CH₃OH from CO) during the cold pre-collapse phase of the MC; *iii*) formation of radicals derived from the frozen hydrogenated species (*e.g.*, CH₃O·, HCO·, NH₂·) due to incidence of UV radiation and cosmic rays on the ice mantles,

Introduction

and *iv*) coupling of radicals to form COMs; at this last step, radicals can diffuse on the ice mantles due to temperature increase (~ 30 K) during the collapse phase.³¹⁻³³

Table 1.5 Identified molecules within the ISM grouped by the number of atoms (*l*- stands for linear while *c*- stands for cyclic). From <https://cdms.astro.uni-koeln.de/cdms/portal/>

	2	3	4	5	6	7	8	9
H ₂	NH	C ₃	c-C ₃ H	C ₅	C ₃ H	C ₆ H	CH ₃ C ₃ N	CH ₃ C ₆ H
AlF	NO	C ₂ H	<i>l</i> -C ₃ H	C ₄ H	<i>l</i> -H ₂ C ₄	CH ₂ CHCN	HCOOCH ₃	CH ₃ CH ₂ CN
C ₂	NS	C ₂ O	C ₃ N	C ₄ Si	C ₂ H ₄	CH ₃ C ₂ H	CH ₃ COOH	(CH ₃) ₂ O
CH	NaCl	C ₃ S	C ₃ O	<i>l</i> -C ₃ H ₂	CH ₃ CN	HC ₃ N	C ₇ H	CH ₃ CH ₂ OH
CH ⁺	OH	CH ₂	C ₃ S	c-C ₃ H ₂	CH ₃ CN	HCOCH ₃	H ₂ C ₆	HC ₇ N
CN	PN	HCN	C ₂ H ₂	CH ₂ CN	CH ₃ OH	NH ₂ CH ₃		C ₈ H ⁻
CO	SO	HCO	C ₂ H ₂ D ⁺	CH ₄	CH ₃ SH	c-C ₂ H ₄ O		CH ₃ CHCH ₂
CO ⁺	SO ⁺	HCO ⁺	HCCN	HC ₃ N	HC ₃ NH ⁺			
CP	SiN	HCS ⁺	HCNH ⁺	HC ₃ NC	HC ₂ CHO			
CSi	SiO	HOC ⁺	HNCO	HCOOH	NH ₂ CHO			
HCl	SiS	H ₂ O	HNCS	H ₂ CHN	C ₃ N			
KCl	CS	H ₂ S	HOCO ⁺	H ₂ C ₂ O				
	HF	HNC	H ₂ CO	H ₃ NCN				
			H ₂ CN	HNC ₃				
			H ₂ CS	SiH ₄				
			H ₃ O ⁺	H ₂ COH ⁺				
			NH ₃					
			SiC ₃					

The second paradigm postulates that COMs are formed directly from gas phase reactions *via* a three-step process sharing the first two steps with the “on-surface” paradigm. However, once formed, the hydrogenated species are directly released into the gas phase by either thermal- (when the grain temperature exceeds ~ 100 K, in the so-called hot cores, see **Table 1.3**) or photo-desorption, where they can then react with other gaseous molecules to form COMs through a series of gas phase processes.^{34–36} In any case, the role of surfaces as catalyst for the formation of molecular species in the ISM is certain. One of the most notorious examples is H_2 formation, that unlikely occurs in gas phase. An extended review about this topic can be found at Ref. 37.

Several computational works have covered the formation of COMs directly on the gas phase (few examples at Refs. 36,38–44), while the formation on the surfaces of dust grains is a more limited field of research. An entire Chapter of this Thesis will be dedicated to the “on-surface” formation of COMs and, accordingly, we will not discuss further about this point in this Introduction.

1.4 The solid phase of the interstellar medium

In the previous Section, we highlighted the fundamental role of dust, solid particles in the formation of simple and complex (organic) molecules in the diffuse and, particularly, in the dense ISM. In the following, we will discuss some important features of these interstellar particles (ISPs).

1.4.1 Chronology: extinction and polarization

Here we present a short summary of some important observations of the solid phase of the ISM, adopting a historical approach. For a detailed dissertation, please refer to Ref. 12.

After Herschel’s 1785 observation of the “holes in the Heavens”, we have to wait until 1847, when German astronomer Wilhelm Struve (1847) noticed that the apparent number of stars *per* unit volume of Space declines in all directions

receding from the Sun.¹² This fact can be explained in two alternative ways: *i*) by assuming an unlikely central position of the Sun in our galaxy, or *ii*) by assuming that starlight coming from distant stars is somehow extinguished. Struve correctly opted for the second explanation. *Interstellar extinction* can be seen as the amount of starlight coming from a given source and not reaching the Earth because of the absorption and scattering by some particles in between the line of sight of such source.^{13,45} Atoms and ions were firstly proposed as extinguishing material, through a Rayleigh scattering mechanism (Rayleigh scattering, which provides for a λ^{-4} dependence of the intensity of the scattered light,⁴⁶ is the elastic scattering of an EM radiation by particles much smaller of the EM radiation wavelength).¹² In 1930, Robert J. Trumpler, working on the inhomogeneous distribution of stellar clusters in the Milky Way, and assuming Struve's explanation, proved with no doubt the presence interstellar dust as source of visual extinction.⁴⁷ In 1936, Jessie Rudnick by the first time measured the $1/\lambda$ linear dependence of extinction in the visual range 400-630 nm (~ 1.59 - $2.5 \mu\text{m}^{-1}$), evidencing the inconsistency of a Rayleigh scattering by atoms and atomic ions.⁴⁸ In the following years, this linear dependence was extended to the 1-3 μm^{-1} range.¹² With the advent of UV and IR observations, the non-linear wavelength dependence of the extinction in a large part of the EMS was well established (from 0.2 to 10 μm^{-1}).¹² The discovery that every line of sight in our galaxy, as well as every galaxy itself, has its specific extinction curve (**Figure 1.7**) evidenced that the ISM is not homogenous in its composition, otherwise all lines of sight would show the same extinction dependence. Nevertheless, some extinction features are common among all the lines of sight: the most notable is the 2175 Å “bump” in the UV region, discovered by Theodor Stecher in 1965, and soon attributed to $\pi \rightarrow \pi^*$ transition in the C-C sp^2 network of *graphite* or of *polycyclic aromatic hydrocarbons* (PAHs) dust grains that might be present in complex mixtures without a specific composition.^{45,49} From that, PAHs and/or graphite dust grains have been always considered as components of the ISPs.

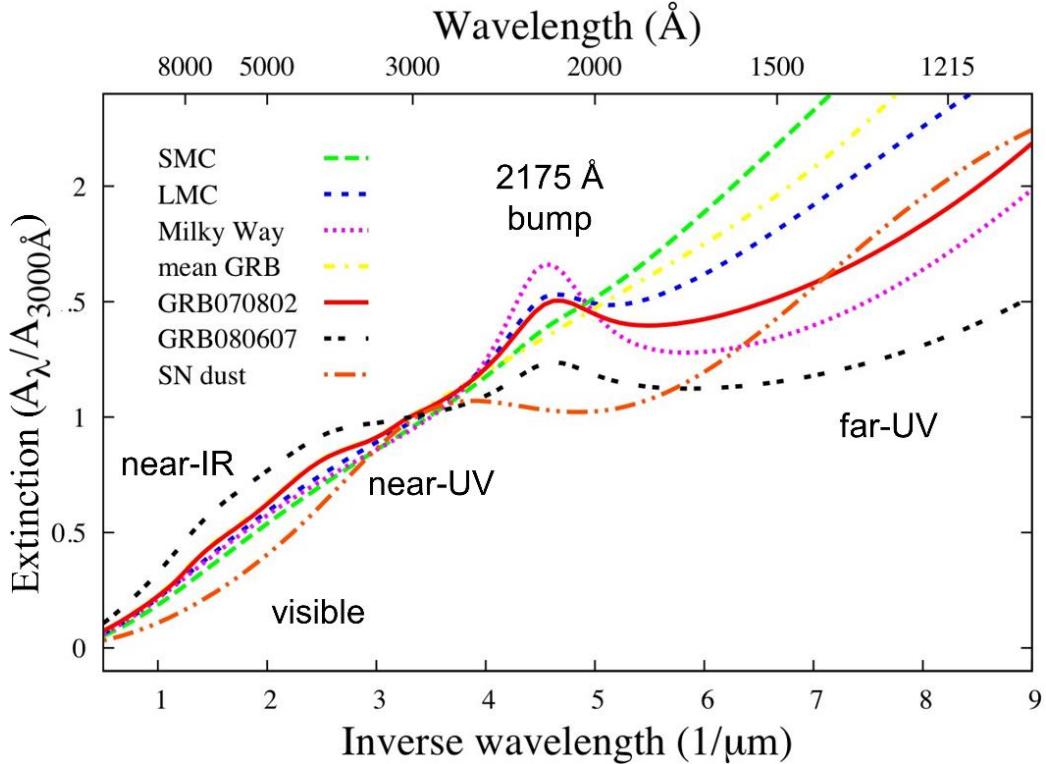


Figure 1.7 Average extinction curve for the Milky Way and for other galaxies (SMC, Small Magellanic cloud, LMC, Large Magellanic cloud, GRB, gamma-ray burst hot galaxies) as a function of the wavelength,

Dirty ices, i.e. water-dominated ices with some inclusions of other important interstellar molecules such as ammonia (NH_3) and methane (CH_4) originating from direct condensation from the gas phase, were among the first (1946) proposals to explain the interstellar extinction curve.¹² A few years later, the general *interstellar linear polarization* was discovered by incident. This polarization was attributed to the differential extinction of starlight by non-spherical grains aligned to a small degree with respect to the galactic plane, probably by the action of the galactic magnetic field.¹² The discovery of such polarization automatically excluded icy grains as candidates of the ISM powder (as they would not be efficient polarizers), and strengthen the graphite hypothesis.¹² Nevertheless, after the first IR observations in the 1960s, dirty ices were reintroduced in the models, with a different role (see below).

By the way it is usually represented, the extinction curve in **Figure 1.7** appears to be featureless in the near- and mid-IR regions. Indeed, this is not true since several *absorption* features have been observed, and most of them shed some light in the knowledge of the chemical composition of ISPs. In the diffuse ISM, a strong feature at 3.3-3.4 μm is usually assigned to the C-H stretching mode of PAHs and/or some forms of hydrogenated amorphous carbon (HAC) particles. This band is usually absent in the dense ISM.⁴⁵ Another very broad feature usually present in the diffuse ISM is the so-called *diffuse interstellar band* (DIB) centred at about 440 nm, which nature is, however, still unclear nowadays.⁴⁵ More important for this Thesis are two features present (in absorption and emission) in both the diffuse and dense ISM and centred at about 9.7 and 18 μm assigned to the Si-O stretching and O-Si-O bending vibrational modes of silicates; being these two bands quite broad and essentially featureless, interstellar silicates are usually reported to be highly amorphous. We will discuss deeper about these silicates in Section 1.4.3. Other important absorption features in the dense ISM have been observed at about 3.1 (O-H stretching of water), 4.27 (CO₂ stretching), 4.62 (C-N stretching in an unidentified “XCN” carrier), 4.67 (C-O stretching in carbon monoxide), 5.83 (C-O stretching in formaldehyde), 7.67 (CH₄ deformation), 8.87 (C-H₃ rocking mode in methanol), 9.01 (umbrella mode in ammonia) μm .²² All these features together contributed to the restoration of water-dominated ices as components of ISPs: instead of being isolated particles, these ices cover the silicate core in dense MCs. We will further discuss about them in Section 1.4.4. Apart from the 9.7 and the 18 μm bands from silicates, other features usually observed in *emission* are the *aromatic interstellar bands* (AIBs) at 3.3, 6.2, 7.7, 8.7, 11.3, 12.0 and 12.7 μm , and the very broad continuum emission in the frequency range 5-100 GHz known as *anomalous microwave emission* (AME), and usually assigned to small (few Ångstroms) spinning particles.⁵⁰⁻⁵²

The study of all extinction (absorption and scattering), polarization and emission features of starlight (together with depletions from the gas to the solid phase) helped astronomers to define some chemico-physical properties of interstellar dust grains (**Table 1.6**), and to build astrochemical models (Section 1.4.2)

Table 1.6 Sources of information about dust grains properties from astronomical observations. Legend: “Ext.” extinction; “Pol.” Polarization; “Abs. (diff.)” absorption line (diffuse); “Abs. (den.)” absorption line (dense); “AIBs” aromatic interstellar bands; “Scatt.” scattered light; “Cont. em.” continuum emission; “Depl.” depletions. Adapted from Ref. 45.

	Ext.	Pol.	Abs. (diff.)	Abs. (den.)	AIBs	Scatt.	Cont. em.	Depl.
Size distribution	✓	✓				✓	✓	
Asymmetry		✓						
PAHs			✓		✓			
Elements								✓
Composition	✓		✓	✓	✓		✓	✓
Inclusions		✓					✓	✓
Ices	✓			✓				

1.4.2 Models for the interstellar dust

All the observations we described in the previous Section helped astronomers to build differential models describing the interstellar dust particles. These models usually depend on several parameters and can furnish some information that cannot be inferred by direct measures. They are usually validated by looking at their prediction about interstellar extinction and polarization.

In 1977, Mathis *et al.* proposed the first example of a dust grains model, now known as Mathis-Rumpl-Nordsieck (MRN) model, that has represented the basis for many further models.⁵³ Briefly, Mathis and co-workers considered the presence of two/three components for the solid phase of the ISM, selected from a list possible candidates: silicates (enstatite, MgSiO_3 , and forsterite, Mg_2SiO_4),

graphite, silicon carbide (SiC), iron and magnetite (Fe_3O_4). Silicates and graphite are essential to the model because they explain the 9.7 and 18 μm and the 2175 \AA features, respectively. All the components were considered to be separate from one another and assumed to consist of spherical grains with radius a following a power-law distribution of the type $n(a)a^{-k}$ (with $n(a)da$ being the number of grains *per* unit volume with radii in the a - $a + da$ range, and k a constant). Using Mie theory for scattering,⁵⁴ they were able to simulate the average extinction curve for the Milky Way by a simple minimization procedure which gave $k = 3.5$.⁵³ The power-law distribution they assumed, which implies small (nanometer-sized) grains to be more present than bigger (submicron-sized) ones, was then incorporated in all the further models. The MRN models have several limitations, the two most important ones being the assumption of separated, non-interacting phases, and then fact that it cannot account for dynamic effects of the ISM, as, for example, aggregation of smaller grains to produce larger ones, destruction due to energetic impacts, and so on. More recently, Bruce Draine and his collaborators developed a new model that, being essentially based on the MRN ones, provides for carbonaceous grains (mixtures of PAHs and other hydrocarbon forms) to be the carrier of the 2175 \AA bump instead of graphite.⁵⁵ Draine and co-workers assumed different size-distributions for the carbonaceous and silicate components, but the fitting for the silicate components gave a value for k very similar to that obtained by Mathis *et al.*⁵⁵ However, as for the MRN one, Draine model cannot account for dynamical effect. A step toward this direction is represented by the *unified* model from Cesare Cecchi-Pastellini and David A. Williams.⁵⁶ One of the main features of this model is that the two main C-based and Si-based components of the solid ISM are not separate, but rather amorphous forms of carbon and hydrocarbons can deposit on silicate cores during the time-evolution of a diffuse cloud. Entering in dense MCs, these biphasic grains can eventually cover in different layer of water-dominated dirty ices.

1.4.3 Interstellar silicates: forsterite and olivines

1.4.3.1 Formation of silicates

In the previous Sections, we underlined the role of silicates as a major component of the solid phase of the ISM. Silicates are believed to form primarily in the stellar envelope of asymptotic giant branch (AGB) stars. AGB stars are quite cold and light (up to 10 solar masses) stars that are near to the end of their lifecycle. Depending on their C/O gas phase ratio, AGB stars can produce both carbonaceous and silicate grains. These latter form when the C/O ratio is lower than one.^{45,57–60} Once formed, silicates are released into the ISM by stellar winds, or by the transformation of AGB stars into (proto) planetary nebulae.^{57,58,61–63} The lifecycle of silicate dust is very complex and involves – besides formation in old, dying stars – destruction, regeneration and processing in the ISM and subsequent incorporation in MCs and protoplanetary disks.^{57,58} Silicate dust is affected to a greater or lesser degree by the astrophysical conditions encountered throughout its journey. Knowledge of the structure and crystallinity of silicate dust can thus provide a diagnostic tool to help understand the physical and chemical conditions in a range of astronomical environments. Silicate formation has been observed not only in (post-)AGB stars envelopes and planetary nebulae (PN), but also in several other environments, such as Novae and SN remnants, the envelopes of red supergiant (RSG) stars and the outflows of luminous blue variable (LBV) stars (**Table 1.7**).

Table 1.7 Sources of different type of interstellar dust particles. Adapted from Ref. 45.

Material	AGB	Post-AGB	PN	Novae	RSG	WR	LBV	SN
Amorphous silicates	✓	✓	✓	✓	✓		✓	✓
Crystalline forsterite	✓	✓	✓		✓		✓	
Crystalline enstatite	✓	✓	✓		✓		✓	
PAHs	✓	✓	✓	✓	✓	✓	✓	
HAC	✓	✓	✓	✓		✓		
Graphite	✓	✓		✓				✓

1.4.3.2 Amorphous vs crystalline silicates

As we deeply discussed, IR observations in both emission and absorption provide the primary source of information regarding the atomistic structure of astronomical silicate dust grains. Comparisons with laboratory IR spectra from carefully prepared samples can help deducing the crystal structures and chemical compositions of the observed dust grain populations. From such studies, it has been confirmed that silicate dust is very magnesium-rich and primarily of either pyroxene (MgSiO_3) and/or olivine (Mg_2SiO_4) composition.^{64,65} Olivines are characterized by isolated SiO_4^{4-} tetrahedral units, while in pyroxenes such units merge together forming single chains. The IR spectra from most lines of sight of the ISM are dominated by the two broad peaks at around 9.7 and 18 μm (Section 1.4.1 and **Figure 1.8**). From laboratory comparisons, such spectra are usually interpreted as originating from *amorphous silicates*.^{57,66–69} Spectral analyses of carefully prepared laboratory samples have revealed that the position and width of these two characteristic IR peaks of dense glassy amorphous silicates vary, to an extent, with respect to the chemical composition (isomorphic substitution of Mg^{2+} with Fe^{2+} , and degree of Si-O polymerization),^{57,66} and the degree of thermal annealing.^{66–68} On the other hand, *crystalline* Mg-pure olivine (known as

forsterite) shows narrow spectral features at 10.0, 11.3, 16.3, 23.5, 27.5, and 33.5 μm , with a weaker, but characteristic band at 69.7 μm , while crystalline Mg-pure pyroxene (enstatite) displays strong bands at 9.4, 9.9, 10.6, 11.1, 11.6, 18.2, 19.3, and 21.5 μm .^{57,64} Interestingly, it has also been shown that experiments irradiating crystalline silicates with high energy ions, thus mirroring the environment of the ISM, can induce atomic disorder and porosity.⁷⁰ Although these irradiated samples spectroscopically appear to be very similar to dense amorphous silicates, they likely retain residual pockets of the original crystal order. By fitting observed IR spectra using various combinations of laboratory spectra, a number of investigations have attempted to gain insights into the properties and structure of amorphous silicate dust from the positions and shapes of the 9.7 and 18 μm silicate features.^{68,71,72} Since the lifecycle of silicate dust involves different types and degrees of energetic processing, insights into the evolutionary history of grain populations and how processed they are can be gained from knowing their crystallinity. By fitting the observed 9.7 μm absorption feature using laboratory IR spectra from both amorphous and crystalline silicate samples, an upper bound on the fraction of crystalline silicate in the ISM of 2.2-2.5% by mass was derived.⁷³⁻⁷⁵

1.4.4 Ice mantles: structure and reactivity

The importance of dust grains is not only linked with their parts as precursor material in the formation of new stars and planetary systems, but also with their potential role as *surface catalysts* for the formation of COMs and other interesting species (Section 1.3.3). The IR observations of the ISM have revealed that in dense MCs, where a surprisingly rich chemistry occurs (**Table 1.5**), the silicate core of dust grains is covered in different layers of water-dominated ices, “dirtied” by the presence of other molecules.²² Hence, the catalytic activity of these grains, if really present, should be associated with the surfaces (and, ultimately, structures and compositions) of the covering ices rather than the surfaces of silicate cores.

This last statement is strengthened by the fact that in diffuse clouds, where the physical conditions do not allow for the formation of the icy mantles, only a few and simple molecular species have been observed (**Table 1.4**).

1.4.4.1 Composition and structure

The presence of solid water (H₂O) in the dense ISM is inferred by means of IR spectroscopy. In particular, the 1-3 μm wavelength region contains combination and overtone modes, in the 3-6 μm region we can find stretching modes, while the 6-30 μm region corresponds to bending and libration modes.²² The composition of the icy mantle is strongly dependent on the composition of the gas in the cloud. After water, that is thought to directly form on the grain surfaces through O and H recombination (rather than by direct adsorption),⁷⁶ carbon monoxide – the main reservoir of carbon – is the second most abundant molecular species,⁷⁷ followed by several other molecules (**Table 1.8**).²² For this reason, these icy mantles are often referred to as *dirty ices*. All the species in such ices have been identified by their IR features; the most prominent ones are (**Figure 1.8**): 4.27 (CO₂ stretching), 4.62 (C-N stretching in an identified “XCN” carrier, likely HCN), 4.67 (C-O stretching in CO), 5.83 (C-O stretching in H₂CO), 6.76 (C-H₃ stretching mode in CH₃OH), 7.67 (CH₄ deformation), and 9.01 (umbrella mode in NH₃, partially hidden by the 9.7 μm feature of silicates) μm .²²

Table 1.8 Relative abundances (with respect to water) of solid phase species in four different sources. From Ref. 78.

Molecule	W33A	NGC 7538/IRS9	Elias29	Elias16
H ₂ O	100	100	100	100
CO	8.1	17	5.0	25
CO ₂	13.2	23	19.7	24
H ₂ CO	3.1	2.2	-	-
CH ₃ OH	17	4.3	<15.6	<2.9
CH ₄	1.5	1.5	<1.6	-
NH ₃	15	15	<7.3	<10

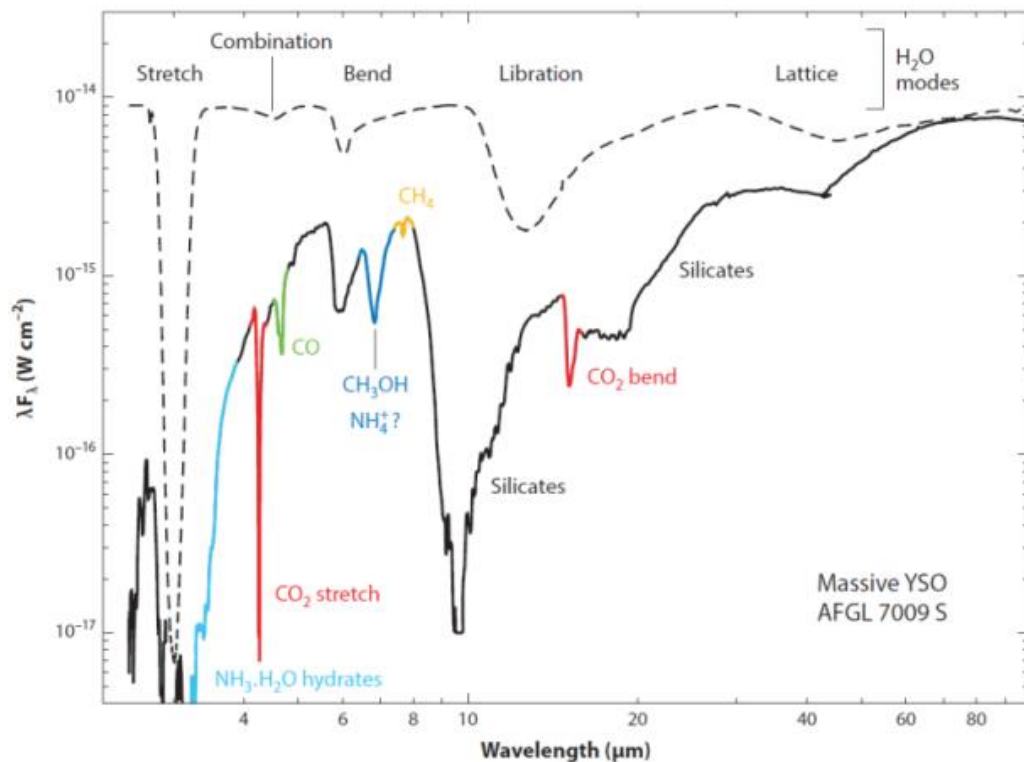


Figure 1.8 IR absorption spectrum around young stellar object (YSO) AFGL 7009 S. The contributions from several solid phase molecules, as well as from amorphous silicates, are indicated close to each peak. From Ref. 22.

Comparisons of astronomical observations^{79,80,81} with experimental works,^{82,83} mainly based on the 3 μm band feature, suggest that interstellar ices might resemble an amorphous ice structure known as *amorphous solid water* (ASW).⁸⁴ Accordingly, they are usually referred to be amorphous and partly porous,⁸⁵ even if the degree of porosity has been recently questioned.⁸⁵ However, IR spectroscopy might be not a definitive technique to derive conclusions about the structural features of these ices.⁸⁶

From astronomical observations, it can be inferred that the components of the dirty ices are not perfectly mixed, but rather forms at least a bi-layered structure:^{87,88} a water-rich phase, called *polar phase*, which contains most of H_2O , CO_2 , NH_3 and is dominated by hydrogenation reactions, and an *apolar phase*,

which comprises most of the CO, the remaining CO₂ and probably most of the CH₃OH.²²

After the formation of these mantles by accretion and grain surface chemistry, these ices can go through thermal processes in which the apolar layers, composed by more volatile species, start desorbing around 20 K. The polar layers instead desorb around higher temperatures ($T > 90$ K). In the evolution of the cloud, these ices are subjected to energetic processes by UV photons or cosmic rays (CRs) which can extract surface species or induce the formation of superficial radical species. These radical might recombine directly on the surface of the grain, or, if released, in the gas phase, eventually leading to the formation of COMs.⁸⁹ Whether their surface catalytic activity is linked with the polar or apolar phase is still not clear. However, all the theoretical works addressing the formation of COMs, that we will extensively discuss in a dedicated Chapter of this Thesis, do not consider explicit CO surfaces, but rather H₂O-only surfaces, and the role of H₂O molecules in promoting hydrogenation.

1.4.4.2 The carbon monoxide/water interface

Carbon monoxide is a key molecular species for astrochemistry, for several reasons. First of all, it is the second most abundant molecule both in the gas (after H₂) and solid (after H₂O) phases of the ISM.^{22,77,90} However, unlike H₂, CO is both vibrational and rotational active, thus it is a molecular probe to trace the evolution of the ISM. In very cold ($T < 25$ K) and very dense (density $> 10^4$ cm⁻³) clouds, CO molecules freeze-out onto the interstellar grain surfaces, disappearing from the gas.^{91,92} The effect can be extreme in particularly dense regions, as prestellar cores and protoplanetary disks, where more than 90% of CO is likely in the solid rather than gas phase.⁹³ Therefore, solid CO may be the major reservoir of elemental carbon (not locked into carbonaceous grains) in a large fraction of the cold ISM.

Understanding the molecular structure of the interstellar solid CO is of great importance. This can only be obtained *via* observations of the 4.647-4.682 μm (2152-2136 cm^{-1}) ^{12}CO and 4.780 μm (2092 cm^{-1}) ^{13}CO absorption features towards astronomical sources and their comparison with “expected” solid CO spectra, based on laboratory and/or theoretical works. Unlike water, CO ice results directly from the sticking of gaseous CO onto the grains. Moreover, water ice is formed before the CO ice.²² Therefore, in principle, CO molecules can be trapped into either a water-rich matrix or in pure-CO layers. UV photons and CRs are believed to affect the iced mantle structure.⁹⁴ The CO/H₂O interplay takes place in several different and peculiar environments, including low pressure and temperature, and is expected to include several competitive aspects such as surface-surface interactions, CO adsorption, migration into ice pores,⁹⁵ and CO trapping into the ice matrices.⁹⁶ Numerous experiments have addressed different aspects of the pure-H₂O and of the CO-containing ices, yielding a great number of data that prompt multiple and sometimes controversial issues. (see Ref. 97 for some examples).

1.5 Concluding remarks

In this non-exhaustive Introduction, we have presented some important topics in astrochemistry. As it is evident, astrochemistry is a wide field of research: its interest is mainly linked with the chemical composition and the physical evolution of the ISM. Unlike for its very first observations at the beginning of XX century, when interstellar matter was considered as a source of noise for stellar investigations, nowadays it is clear how the ISM affects several astrophysical processes, and therefore a comprehensive knowledge of its properties is fundamental. Several efforts, including direct observations, laboratory experiments and theoretical modelling have been done to infer more and more about this important topic.

This Thesis fits within such a context: the aim is to furnish, through computational chemistry simulations, several useful (we hope!) data about some important topics related with the solid phase of the ISM. The two main aspects are the modelling of the silicate core and of the structural (with a particular reference to the CO/H₂O interface) and catalytic properties of the ice mantle. As regards the first point, several studies clearly pointed out a strong lack of crystalline dust grains in the diffuse and dense ISM. However, Chapter 5 of this Thesis is dedicated to explore the possibility that observational IR spectra might not represent a definitive technique to infer the structural features of a population of nanometer-sized grains (with an olivinic-like stoichiometry), that, according to most of dust grains models (Section 1.4.2), are predicted to represent the most important (by number) population of ISM solid particles.⁹⁸ On the other hand, about the second point, the way how CO freezes, namely in what structure (whether trapped in a water-rich matrix or in pure CO layers), affects the temperature at which it returns into the gas phase. In turn, this has important consequences on a variety of situations; for example, on the molecular deuteration of water and trace species,⁹⁹ on the formation of methanol and more complex organic molecules in the protostellar phase,³¹ or on the composition of the gaseous giant planets.¹⁰⁰ Therefore, the CO/H₂O interface will be extensively explored in Chapter 3. Nevertheless, the importance of the ices as surface catalyst in the dense ISM is self-evident: in Chapter 4, we will review several works where this catalytic activity has been explored through the aim of computational chemistry techniques.

Bibliography

- (1) Einstein, A. Die Feldgleichungen Der Gravitation. *Sitzungsberichte der Königlich Preußischen Akad. der Wissenschaften* **1915**, 48, 844–847.
- (2) Lemaître, G. Un Univers Homogène de Masse Constante et de Rayon Croissant, Rendant Compte de La Vitesse Radiale Des Nébuleuses Extra-Galactiques. *Ann. la Soc. Scientifique Bruxelles*. **1927**, 47, 49–59.
- (3) Fridman, A. A. Über Die Krümmung Des Raumes. *Zeitschrift für Phys.* **1922**, 10, 377–386.
- (4) Hubble, E. A Relation Between Distance and Radial Velocity Among Extra-Galactic Nebulae. *Proc. Natl. Acad. Sci. U. S. A.* **1929**, 15, 168–173.
- (5) Penzias, A. A.; Wilson, R. W. A Measurement of Excess Antenna Temperature at 4082 Mc/S. *Astrophys. J.* **1965**, 142, 419–421.
- (6) Boggess, N. W.; Mather, J. C.; Weiss, R.; Bennett, C. L.; Cheng, E. S.; Dwek, E.; Gulkis, S.; Hauser, M. G.; Janssen, M. a.; Kelsall, T.; *et al.* The COBE Mission: Its Design and Performance Two Years after Launch. *Astrophys. J.* **1992**, 397, 420–429.
- (7) Shaw, A. M. *Astrochemistry. From Astronomy to Astrobiology*; John Wiley and Sons: Chichester, England, UK, 2006.
- (8) Holt, S. S. *Cosmic Abundances: Proceedings of the Sixth Annual October Astrophysics Conference in College Park, Maryland, 9-11 October 1995*; Astronomical Society of the Pacific: San Francisco, CA, USA, 1995.
- (9) Ward-Thompson, D.; Scott, P. F.; Hills, R. E.; Andre, P. A Submillimetre Continuum Survey of Pre Protostellar Cores. *Mon. Not. R. Astron. Soc.* **1994**, 268, 276–292.
- (10) Jeans J. H. The Stability of Spherical Nebula. *Philosophical Trans.* **1902**, CXCIX, 1–53.
- (11) McKee, C.; Ostriker, J. P. A Theory of the Interstellar Medium - Three Components Regulated by Supernova Explosions in an Inhomogeneous Substrate. *Astron. J.* **1977**, 218, 148–169.

- (12) Li, A. Interstellar Grains — the 75th Anniversary. *J. Phys. Conf. Ser.* **2005**, 6, 229–248.
- (13) Kwok, S. *Physics and Chemistry of the Interstellar Medium*; University Science Books: Sausalito, CA, USA, 2007.
- (14) Hellwig, H.; Vessot, R. F. C.; Levine, M. W.; Zitzewitz, P. W.; Allan, D. W.; Glaze, D. J. Measurement of the Unperturbed Hydrogen Hyperfine Transition Frequency. *IEEE Trans. Instrum. Meas.* **1970**, 19, 200–209.
- (15) Harvard-Smithsonian Centre for Astrophysics. HEA Heritage Missions: Einstein Observatory. Available at the following link: <https://www.cfa.harvard.edu/hea/hm/heaob.html>.
- (16) Draine, B. T. *Physics of the Interstellar and Intergalactic Medium*; Princeton University Press: Princeton, NJ, USA, 2010.
- (17) Tielens, A. G. G. M. *The Physics and Chemistry of the Interstellar Medium*; Cambridge University Press: Cambridge, England, UK, 2005.
- (18) Williams, D. A. The Interstellar Medium: An Overview. In *Solid State Astrochemistry*; Pirronello, V., Krelowski, J., Manicò, G., Eds.; Proceedings of the NATO Advanced Study Institute on Solid State Astrochemistry, 2000; pp 1–20.
- (19) Cox, D. The Three-Phase Interstellar Medium Revisited. *Annu. Rev. Astron. Astrophys.* **2005**, 43, 337–385.
- (20) Ferriere, D. The Interstellar Environment of Our Galaxy. *Rev. Mod. Phys.* **2001**, 73, 1031–1066.
- (21) Cowley, C.; Wiese, W. L.; Fuhr, J.; Kuznetsova, L. A. Spectra. In *Allen's Astrophysical Quantities*; Cox, A. N., Ed.; Springer: New York City, NY, USA, 2002; pp 53–93.
- (22) Boogert, A. C. A.; Gerakines, P. A.; Whittet, D. C. B. Observations of the Icy Universe. *Annu. Rev. Astron. Astrophys.* **2015**, 53, 541–583.
- (23) Williams, J. P.; Blitz, L.; McKee, C. F. The Structure and Evolution of Molecular Clouds: From Clumps to Cores to the IMF. In *Protostars and*

- Planets IV*; Mannings, V., Boss, A., Russell, S. S., Eds.; University of Arizona Press: Tucson, AZ, USA, 2000; p 30.
- (24) Herzberg, G. Historical Remarks on the Discovery of Interstellar Molecules. *J. R. Astron. Soc. Canada* **1988**, *82*, 115–127.
- (25) Yamamoto, S. *Introduction to Astrochemistry. Chemical Evolution from Interstellar Clouds to Star and Planet Formation*; Springer Japan: Tokyo, Japan, 2017.
- (26) Endres, C. P.; Schlemmer, S.; Schilke, P.; Stutzki, J.; Müller, H. S. P. The Cologne Database for Molecular Spectroscopy, CDMS, in the Virtual Atomic and Molecular Data Centre, VAMDC. *J. Mol. Spectrosc.* **2016**, *327*, 95–104.
- (27) Cologne database <https://cdms.ph1.uni-koeln.de/cdms/portal/home>.
- (28) Herbst, E.; van Dishoeck, E. F. Complex Organic Interstellar Molecules. *Annu. Rev. Astron. Astrophys.* **2009**, *47*, 427–480.
- (29) Hoyle, F.; Wickramasinghe, C. *Lifecloud: The Origin of Life in the Universe*; J.M. Dent and Sons: London, England, UK, 1978.
- (30) Zamirri, L.; Ugliengo, P.; Ceccarelli, C.; Rimola, A. Quantum Mechanical Investigations on the Formation of Complex Organic Molecules on Interstellar Ice Mantles . Review and Perspectives. *ACS Earth Sp. Chem.* **2019**, *3*, 1499–1523.
- (31) Garrod, R. T.; Herbst, E. Formation of Methyl Formate and Other Organic Species in the Warm-up Phase of Hot Molecular Cores. *Astron. Astrophys.* **2006**, *457*, 927–936.
- (32) Öberg, K. I.; Garrod, R. T.; Dishoeck, E. F. van; Linnartz, H. Formation Rates of Complex Organics in UV Irradiated CH₃OH-Rich Ices. I. Experiments. *Astron. Astrophys.* **2009**, *504*, 891–913.
- (33) Ruaud, M.; Loison, J. C.; Hickson, K. M.; Gratier, P.; Hersant, F.; Wakelam, V. Modelling Complex Organic Molecules in Dense Regions: Eley–Rideal and Complex Induced Reaction. *Mon. Not. R. Astron. Soc.*

- 2015**, 447, 4004–4017.
- (34) Charnley, S. B.; Tielens, A. G. G. M.; Millar, T. J. On the Molecular Complexity of the Hot Cores in Orion A-Grain Surface Chemistry as “The Last Refuge of the Scoundrel.” *Astrophys. J.* **1992**, 339, L71–L74.
- (35) Balucani, N.; Ceccarelli, C.; Taquet, V. Formation of Complex Organic Molecules in Cold Objects: The Role of Gas-Phase Reactions. *Mon. Not. R. Astron. Soc.* **2015**, 449, L16–L20.
- (36) Barone, V.; Latouche, C.; Skouteris, D.; Vazart, F.; Balucani, N.; Ceccarelli, C.; Lefloch, B. Gas-Phase Formation of the Prebiotic Molecule Formamide: Insights from New Quantum Computations. *Mon. Not. R. Astron. Soc.* **2015**, 453, L31–L35.
- (37) Vidali, G. H₂ Formation on Interstellar Grains. *Chem. Rev.* **2013**, 113, 8762–8782.
- (38) Vazart, F.; Calderini, D.; Puzzarini, C.; Skouteris, D.; Barone, V. State-of-the-Art Thermochemical and Kinetic Computations for Astrochemical Complex Organic Molecules: Formamide Formation in Cold Interstellar Clouds as a Case Study. *J. Chem. Theory Comput.* **2016**, 12, 5385–5397.
- (39) Skouteris, D.; Vazart, F.; Ceccarelli, C.; Balucani, N.; Puzzarini, C.; Barone, V. New Quantum Chemical Computations of Formamide Deuteration Support Gas-Phase Formation of This Prebiotic Molecule. *Mon. Not. R. Astron. Soc.* **2017**, 468, L1–L5.
- (40) Wakelam, V.; Loison, J.; Mereau, R.; Ruaud, M. Binding Energies: New Values and Impact on the Efficiency of Chemical Desorption. *Mol. Astrophys.* **2017**, 6, 22–35.
- (41) Holtom, P. D.; Bennett, C. J.; Osamura, Y.; Mason, N. J.; Kaiser, R. I. A Combined Experimental and Theoretical Study on the Formation of the Amino Acid Glycine (NH₂CH₂COOH) and Its Isomer (CH₃NHCOOH) in Extraterrestrial Ices. *Astrophys. J.* **2005**, 626, 940–952.
- (42) Walch, S. P.; Bauschlicher Jr, C. B.; Ricca, A.; Bakes, E. L. O. On the

- Reaction $\text{CH}_2\text{O} + \text{NH}_3 \rightarrow \text{CH}_2\text{NH} + \text{H}_2\text{O}$. *Chem. Phys. Lett.* **2001**, 333, 6–11.
- (43) Redondo, P.; Barrientos, C.; Largo, A. Some Insights into Formamide Formation through Gas-Phase Reactions in the Interstellar Medium. *Astrophys. J.* **2013**, 780, 181 (7 pp).
- (44) Huang, L. C. L.; Asvany, O.; Chang, A. H. H.; Balucani, N.; Lin, S. H.; Lee, Y. T.; Kaiser, R. I. Crossed Beam Reaction of Cyano Radicals with Hydrocarbon Molecules. IV. Chemical Dynamics of Cyanoacetylene (HCCCN ; $X^1\Sigma^+$) Formation from Reaction of $\text{CN}(X^2\Sigma^+)$ with Acetylene, $\text{C}_2\text{H}_2(X^1\Sigma_g^+)$. *J. Chem. Phys.* **2000**, 113, 8656–8666.
- (45) Williams, D. A.; Cecchi-Pestellini, C. *The Chemistry of Cosmic Dust*; The Royal Society of Chemistry: Cambridge, England, UK, 2016.
- (46) Young, A. T. Rayleigh Scattering. *Appl. Opt.* **1981**, 20, 533–535.
- (47) Trumpler, R. J. Preliminary Results on the Distances, Dimensions and Space Distribution of Open Star Clusters. *Lick Obs. Bull* **1930**, XIV, 154–188.
- (48) Rudnick, J. On the Reddening in B-Type Stars. *Astrophys. J.* **1936**, 83, 394.
- (49) Stecher, T. P. Interstellar Extinction in the Ultraviolet. *Astrophys. J.* **1965**, 142, 1683.
- (50) Kogut, A.; Banday, a. J.; Bennett, C. L.; Gorski, K.; Hinshaw, G.; Smoot, G. F.; Wright, E. L. Microwave Emission at High Galactic Latitudes. *Astrophys. J.* **1996**, 464, L5–L9.
- (51) Draine, B. T.; Lazarian, A. Diffuse Galactic Emission from Spinning Dust Grains. *Astrophys. J.* **1998**, 494, L19–L22.
- (52) Draine, B. T.; Lazarian, A. Electric Dipole Radiation from Spinning Dust Grains. *Astrophys. J.* **1998**, 508, 157–179.
- (53) Mathis, J. S.; Rumpl, W.; Nordsieck, K. H. The Size Distribution of Interstellar Grains. *Astrophys. J.* **217AD**, 1977, 425–433.
- (54) Mie, G. Beiträge Zur Optik Trüber Medien, Speziell Kolloidaler

- Metallösungen. *Ann. Phys.* **1908**, 330, 377.
- (55) Draine, B. T. Interstellar Dust Grains. *Annu. Rev. Astron. Astrophys.* **2003**, 41, 241–289.
- (56) Cecchi-Pestellini, C.; Cacciola, A.; Iatì, M. A.; Saija, R.; Borghese, F.; Denti, P.; Giusto, A.; Williams, D. A. Stratified Dust Grains in the Interstellar Medium - II. Time-Dependent Interstellar Extinction. *Mon. Not. R. Astron. Soc.* **2010**, 408, 535–541.
- (57) Henning, T. Cosmic Silicates. *Annu. Rev. Astron. Astrophys.* **2010**, 48, 21–46.
- (58) Henning, T. Cosmic Silicates - A Review. In *Solid State Astrochemistry*; Pirronello, V., Krelowski, J., Manicò, G., Eds.; Proceedings of the NATO Advanced Study Institute on Solid State Astrochemistry, 2000; pp 85–103.
- (59) Gail, H.-P.; Sedlmayr, E. Mineral Formation in Stellar Winds. I. Condensation Sequence of Silicate and Iron Grains in Stationary Oxygen Rich Outflows. *Astron. Astrophys.* **1999**, 347, 594–616.
- (60) Gail, H. P.; Sedlmayr, E. Inorganic Dust Formation in Astrophysical Environments. *Faraday Discuss.* **1998**, 109, 303–319.
- (61) Malfait, K.; Waelkens, C.; Waters, L. B. F. M.; Vandebussche, B.; Huygen, E.; de Graauw, M. S. The Spectrum of the Young Star HD 100546 Observed with the Infrared Space Observatory. *Astron. Astrophys.* **1998**, 332, L25–L28.
- (62) Hanner, M. S. The Silicate Material in Comets. *Space Sci. Rev.* **1999**, 90, 99–108.
- (63) Waters, L. B. F. M.; Molster, F. J.; de Jong, T.; Beintema, D. A.; Waelkens, C.; Boogert, A. C. A.; Boxhoorn, D. R.; de Graauw, T.; Drapatz, S.; Feuchtgruber, H.; *et al.* Mineralogy of Oxygen-Rich Dust Shells. *Astron. Astrophys.* **1996**, 315, L361–L364.
- (64) Jäger, C.; Molster, F. J.; Dorschner, J.; Henning, T.; Mutschke, H.; Waters, L. B. F. M. Steps toward Interstellar Silicate Mineralogy. IV. The

- Crystalline Revolution. *Astron. Astrophys.* **1998**, 339, 904–916.
- (65) Molster, F. J.; Waters, L. B. F. M.; Tielens, A. G. G. M. Crystalline Silicate Dust around Evolved Stars II. The Crystalline Silicate Complexes. *Astron. Astrophys.* **2002**, 240, 222–240.
- (66) Jäger, C.; Dorschner, J.; Mutschke, H.; Posch, T.; Henning, T. Steps toward Interstellar Silicate Mineralogy VII. Spectral Properties and Crystallization Behaviour of Magnesium Silicates Produced by the Sol-Gel Method. *Astron. Astrophys.* **2003**, 408, 193–204.
- (67) Speck, A. K.; Whittington, A. G.; Hofmeister, A. M. Disordered Silicates in Space: A Study of Laboratory Spectra of “Amorphous” Silicates. *Astrophys. J.* **2011**, 740, 17 pp.
- (68) Hallenbeck, S. L.; Nuth III, J. A.; Nelson, R. N. Evolving Optical Properties of Annealing Silicate Grains: From Amorphous Condensate to Crystalline Mineral. *Astrophys. J.* **2000**, 535, 247–255.
- (69) Thompson, S. P.; Parker, J. E.; Tang, C. C. The 10 μm Band in Amorphous MgSiO_3 : The Influence of Medium-Range Structure, Defects and Thermal Processing. *Astron. Astrophys. Astrophys.* **2012**, 545, A60.
- (70) Demyk, K.; D’Hendecourt, L.; Leroux, H.; Jones, A. P.; Borg, J. IR Spectroscopic Study of Olivine, Enstatite and Diopside Irradiated with Low Energy H^+ and He^+ Ions. *Astron. Astrophys.* **2004**, 420, 233–243.
- (71) Chiar, J. E.; Tielens, A. G. G. M. Pixie Dust: The Silicate Features in the Diffuse Interstellar Medium. *Astrophys. J.* **2006**, 637, 774–785.
- (72) Fogerty, S.; Forrest, W.; Watson, D. M.; Sargent, B. A.; Koch, I. Silicate Composition of the Interstellar Medium. *Astrophys. J.* **2016**, 830, 71 (11 pp).
- (73) Kemper, F.; Vriend, W. J.; Tielens, A. G. G. M. The Absence of Crystalline Silicates in the Diffuse Interstellar Medium. *Astrophys. J.* **2004**, 609, 826–837.
- (74) Kemper, F.; Vriend, W. J.; Tielens, A. G. G. M. The Absence of Crystalline

- Silicates in the Diffuse Interstellar Medium. *Erratum. Astrophys. J.* **2005**, 663, 534–534.
- (75) Li, M. P.; Zhao, G.; Li, A. On the Crystallinity of Silicate Dust in the Interstellar Medium. *Mon. Not. R. Astron. Soc.* **2007**, 382, L26–L29.
- (76) Dulieu, F.; Amiaud, L.; Congiu, E.; Fillion, J.-H.; Matar, E.; Momeni, A.; Pirronello, V.; Lemaire, J. L. Experimental Evidence for Water Formation on Interstellar Dust Grains by Hydrogen and Oxygen Atoms. *Astron. Astrophys.* **2010**, 512, A30 (5 pp).
- (77) Allamandola, L. J.; Bernstein, M. P.; Sandford, S. A.; Walker, R. L. Evolution of Interstellar Ices. *Space Sci. Rev.* **1999**, 90, 219–232.
- (78) Gibb, E. L.; Whittet, D. C. B.; Boogert, A. C. A.; Tielens, A. G. G. M. Interstellar Ice: The *Infrared Space Observatory* Legacy. *Astrophys. J. Suppl. Ser.* **2004**.
- (79) Dartois, E. The Ice Survey Opportunity of ISO. *ISO Sci. Leg. A Compact Rev. ISO Major Achiev.* **2005**, 293–310.
- (80) Gibb, E. L.; Whittet, D. C. B.; Boogert, A. C. A.; Tielens, a. G. G. M. Interstellar Ice: The Infrared Space Observatory Legacy. *Astrophys. J. Suppl. Ser.* **2004**, 151, 35–73.
- (81) Oberg, K. I.; Boogert, A. C. A.; Pontoppidan, K. M.; van den Broek, S.; van Dishoeck, E. F.; Bottinelli, S.; Blake, G. A.; Evans II, N. J. The Spitzer Ice Legacy: Ice Evolution from Cores to Protostars. *Astrophys. J.* **2011**, 740, 16 pp.
- (82) Oba, Y.; Miyauchi, N.; Hidaka, H.; Chigai, T.; Watanabe, N.; Kouchi, a. Formation of Compact Amorphous H₂O Ice by Codeposition of Hydrogen Atoms with Oxygen Molecules on Grain Surfaces. *Astrophys. J.* **2009**, 701, 464–470.
- (83) Watanabe, N.; Kouchi, A. Ice Surface Reactions: A Key to Chemical Evolution in Space. *Prog. Surf. Sci.* **2008**, 83, 439–489.
- (84) Bowron, D. T.; Finney, J. L.; Hallbrucker, A.; Kohl, I.; Loerting, T.;

- Mayer, E.; Soper, A. K. The Local and Intermediate Range Structures of the Five Amorphous Ices at 80 K and Ambient Pressure: A Faber-Ziman and Bhatia-Thornton Analysis. *J. Chem. Phys.* **2006**, *125*, 194502 (19 pp).
- (85) Fraser, H. J.; Collings, M. P.; Dever, J. W.; McCoustra, M. R. S. Using Laboratory Studies of CO-H₂O Ices to Understand the Non-Detection of a 2152 cm⁻¹ (4.647 μm) Band in the Spectra of Interstellar Ices. *Mon. Not. R. Astron. Soc.* **2004**, *353*, 59–68.
- (86) Zamirri, L.; Casassa, S.; Rimola, A.; Segado-Centellas, M.; Ceccarelli, C.; Ugliengo, P. IR Spectral Fingerprint of Carbon Monoxide in Interstellar Water Ice Models. *Mon. Not. R. Astron. Soc.* **2018**, *480*, 1427–1444.
- (87) Pontoppidan, K. M.; Fraser, H. J.; Dartois, E.; Thi, W.-F.; van Dishoeck, E. F.; Boogert, A. C. A.; D’Hendecourt, L.; Tielens, A. G. G. M.; Bisschop, S. E. A 3-5 mm VLT Spectroscopic Survey of Embedded Young Low Mass Stars I - Structure of the CO Ice. *Astron. Astrophys.* **2003**, *408*, 981–1007.
- (88) Pontoppidan, K. M.; van Dishoeck, E. F.; Dartois, E. Mapping Ices in Protostellar Environments on 1000 AU Scales: Methanol-Rich Ice in the Envelope of Serpens SMM 4. *Astron. Astrophys.* **2004**, *426*, 925–940.
- (89) Öberg, K. I. Photochemistry and Astrochemistry: Photochemical Pathways to Interstellar Complex Organic Molecules. *Chem. Rev.* **2016**, *116*, 9631–9663.
- (90) Klemperer, W. Astronomical Chemistry. *Annu. Rev. Phys. Chem.* **2011**, *62*, 173–184.
- (91) Caselli, P.; Walmsley, C. M.; Tafalla, M.; Dore, L.; Myers, P. C. CO Depletion in the Starless Cloud Core L1544. *Astrophys. J. Lett.* **1999**, *523*, L165–L169.
- (92) Favre, C.; Cleeves, L. I.; Bergin, E. A.; Qi, C.; Blake, G. A. A Significantly Low CO Abundance Toward the TW Hya Protoplanetary Disk: A Path to Active Carbon Chemistry? *Astrophys. J. Lett.* **2013**, *776*, L38 (5 pp).
- (93) Bacmann, A.; Lefloch, B.; Ceccarelli, C.; Castets, A.; Steinacker, J.;

- Loinard, L. The Degree of CO Depletion in Pre-Stellar Cores. *Astron. Astrophys.* **2002**, 389, L6–L10.
- (94) Öberg, K. I.; van Dishoeck, E. F.; Linnartz, H. Photodesorption of Ices I: CO, N₂, and CO₂. *Astron. Astrophys.* **2009**, 496, 281–293.
- (95) Devlin, J. P. Molecular Interactions with Icy Surfaces: Infrared Spectra of Carbon Monoxide Adsorbed in Microporous Amorphous Ice. *J. Phys. Chem.* **1992**, 96, 6185–6188.
- (96) Sandford, S. A.; Allamandola, L. J.; Tielens, A. G. G. M.; Valero, G. J. Laboratory Studies of the Infrared Spectral Properties of CO in Astrophysical Ices. *Astrophys. J.* **1988**, 392, 498–510.
- (97) Al-Halabi, A.; Fraser, H. J.; Kroes, G. J.; van Dishoeck, E. F. Adsorption of CO on Amorphous Water-Ice Surfaces. *Astron. Astrophys.* **2004**, 422, 777–791.
- (98) Li, A.; Draine, B. T. On Ultrasmall Silicate Grains in the Diffuse Interstellar Medium. *Astrophys. J.* **2001**, 550, L213–L217.
- (99) Ceccarelli, C.; Caselli, P.; Bockelée-Morvan, D.; Mousis, O.; Pizzarello, S.; Robert, F.; Semenov, D. Deuterium Fractionation: The Ariadne’s Thread from the Precollapse Phase to Meteorites and Comets Today. In *Protostars and Planets VI*; Beuther, H., Klessen, R. S., Dullemond, C. P., Henning, T., Eds.; Tucson, AZ, USA, 2014; pp 859–882.
- (100) Madhusudhan, N.; Bitsch, B.; Johansen, A.; Eriksson, L. Atmospheric Signatures of Giant Exoplanet Formation by Pebble Accretion. *Mon. Not. R. Astron. Soc.* **2017**, 469, 4102–4115.

2 Computational methods

Abstract

In this Chapter, we will firstly introduce the reader about some typical methodologies employed in the computational chemistry research, from the Hartree-Fock and *post*-Hartree-Fock methods to the density functional theory framework, to end with the classical mechanics (force fields) approach, all within a molecular context. We will then shortly describe the most common kind of calculations and the computational codes we used throughout this Thesis for all calculations. We also underline some of the most important aspects of solid state (periodic) calculations.

2.1 Quantum chemistry framework

2.1.1 The Schrödinger equation

The main purpose in any non-relativistic quantum mechanics (QM) calculation is the solution of the *Schrödinger equation*,¹ a differential equation to partial derivatives that, unlike Newton's equations of motion, is of first order in time derivative of the *wave function* $\Psi_n(\mathbf{R}, t, S)$, a complex function of all spatial degrees of freedom \mathbf{R} , of time t and of any other additional degree of freedom S :

$$i\hbar \frac{\partial}{\partial t} \Psi_n(\mathbf{R}, t, S) = \hat{H} \Psi_n(\mathbf{R}, t, S) \quad 2.1$$

where \hbar is the reduced Planck constant ($\hbar = 1.0546 \times 10^{-34}$ J s) and \hat{H} is the *Hamiltonian operator*, representing the total energy of the system. In coordinates representation, \hat{H} can be written as

$$\hat{H} = -\frac{\hbar^2}{2} \sum_{i=1}^N \frac{\nabla_i^2}{m_i} + V(\mathbf{R}, t) \quad 2.2$$

i.e. as the sum of two terms, the first representing the kinetic energy of N particles with masses m_i and the second representing the total potential energy V .² In case of a time-independent potential, the wave function can be factorized as the

product of two terms, the first purely spatial $\psi(\mathbf{R}, S)$, while the second merely temporal $\Phi(t) = \exp(-iE_n t/\hbar)$. In such cases, Equation 2.1 becomes an eigenvalue equation for the Hamiltonian operator, usually, but not properly, also denoted as Schrödinger equation

$$\hat{H}\psi_n(\mathbf{R}, S) = E_n\psi_n(\mathbf{R}, S) \quad 2.3$$

The n subscripts are used to point out that there are several *eigenfunctions* (*eigenstates* or *stationary states*) ψ_n corresponding to the eigenvalues E_n (which are the allowed values for the total energy of the system) that satisfy Equations 2.1 and 2.3. It is worth underlining that the totality of quantum chemistry codes do solve Equation 2.3, *i.e.* they look for stationary states.³

2.1.2 The Born-Oppenheimer approximation

For a molecular system of N electrons labeled with i and j indices and of M nuclei labeled with a and b indices, in the absence of any external electric and/or magnetic fields, the Hamiltonian operator in atomic units ($\hbar = m_e = |e| = 1 = 1/4\pi\epsilon_0 = 1$), usually denoted as *electrostatic Hamiltonian*, can be written as the sum of five terms²

$$\begin{aligned} \hat{H} &= \hat{T}_e + \hat{T}_n + \hat{V}_{ee} + \hat{V}_{nn} + \hat{V}_{ne} = \\ &= -\frac{1}{2} \sum_{i=1}^N \nabla_i^2 - \frac{1}{2} \sum_{a=1}^M \frac{\nabla_a^2}{m_a} + \frac{1}{2} \sum_{\substack{i,j=1 \\ i \neq j}}^M \frac{1}{|\mathbf{r}_{ij}|} + \frac{1}{2} \sum_{\substack{a,b=1 \\ a \neq b}}^M \frac{Z_a Z_b}{|\mathbf{r}_{ab}|} - \sum_{i=1}^N \sum_{a=1}^M \frac{Z_a}{|\mathbf{r}_{ai}|} \end{aligned} \quad 2.4$$

The eigenvalue equation for the electrostatic Hamiltonian cannot be solved analytically, therefore some approximations need to be introduced. The first, and most important one, is the *Born-Oppenheimer approximation*,⁴ consisting in the assumption of a non-correlation between the electronic and the nuclear motion, based on the fact that even lighter nuclei are much heavier than electrons, so that their motion is usually much slower than the electronic one. Under such

approximation, the spatial wave function $\psi(\mathbf{R}, S)$ further factorizes into a nuclear (ψ_{nuc}) and an electronic (ψ_{el}) term

$$\psi(\mathbf{R}, S) = \psi_{nuc}(\mathbf{r}_{nuc})\psi_{el}(\mathbf{r}_{el}, S; \mathbf{r}_{nuc}) \quad 2.5$$

where we stressed the parametrical dependence of the electronic wave function from the nuclear coordinates. As a consequence of the Born-Oppenheimer approximation, Equation 2.3 for the electrostatic Hamiltonian can be separated into two equations²

$$\hat{H}_{el}(\mathbf{r}_{el}; \mathbf{r}_{nuc})\psi_{el}(\mathbf{r}_{el}, S; \mathbf{r}_{nuc}) = E_{el}(\mathbf{r}_{nuc})\psi_{el}(\mathbf{r}_{el}, S; \mathbf{r}_{nuc}) \quad 2.6$$

$$\left[-\frac{1}{2} \sum_{a=1}^M \frac{\nabla_a^2}{m_a} + E_{el}(\mathbf{r}_{nuc}) \right] \psi_{nuc}(\mathbf{r}_{nuc}) = E\psi_{nuc}(\mathbf{r}_{nuc}) \quad 2.7$$

where $\hat{H}_{el}(\mathbf{r}_{el}; \mathbf{r}_{nuc}) = \hat{T}_e(\mathbf{r}_{el}) + \hat{V}_{ee}(\mathbf{r}_{el}) + \hat{V}_{ne}(\mathbf{r}_{el}; \mathbf{r}_{nuc}) + V_{nn}(\mathbf{r}_{nuc})$ (please note that the electrostatic repulsive operator \hat{V}_{nn} becomes a simple additive term V_{nn}). Solving Equations 2.6 and 2.7 requires a double-step procedure. Firstly, atomic coordinates are inserted into the electronic equation, which, once solved, gives the total electronic energy $E_{el}(\mathbf{r}_{nuc})$, function of the $3M$ nuclear coordinates. Such a function is representable as a hypersurface in a $3M + 1$ -dimensional space and is denoted as *potential energy surface* (PES). The PES is then introduced in the nuclear Equation 2.7, where it represents the potential energy felt by the nuclei, so obtaining the total energy E . The term in brackets in Equation 2.7 is sometimes referred to as *vibrational Hamiltonian*.²

2.1.3 Variational principle and SCF procedure

Once assigned the atomic coordinates, Equation 2.6 must be firstly solved but, unfortunately, it cannot be solved analytically due to the presence of the electronic repulsion term. Therefore, some further approximations must be introduced. Several quantum computational methods are known for introducing different

kinds of approximation. All of them are based on the *variational principle* which states that “the expectation value of the Hamiltonian on a trial function ψ_{trial} is always greater than or equal to the real energy for the fundamental states ψ_0 ”²

$$E_{\text{trial}} = \langle \psi_{\text{trial}} | \hat{H}_{el} | \psi_{\text{trial}} \rangle \geq E_0 = \langle \psi_0 | \hat{H}_{el} | \psi_0 \rangle \quad \mathbf{2.8}$$

where the Dirac’s notation was adopted.⁵ From Equation **2.8**, it is clear that the energy of a system can be represented as a *functional* of the wave function, and thus it is possible to calculate the real fundamental energy by minimizing such a functional

$$\delta E[\psi] = \frac{\partial E[\psi]}{\partial \psi} = 0 \rightarrow E_0 = \min_{\psi \rightarrow N} E[\psi] \quad \mathbf{2.9}$$

where $\psi \rightarrow N$ stands for “every trial wave function which satisfies physical requirements (continuity, normalizability, *etc.*)”^{2,6,7}

Since the electrons are fermions, every wave function that describes a multi-electron system must account for the *Pauli exclusion principle*, a symmetry constraint.⁸ All the methods developed until nowadays utilize for the trial wave function a determinant expression known as *Slater determinant* (ψ_S).⁹ For a system of N electrons, such a determinant is a combination of N *molecular spin-orbitals* $\varphi_\lambda(\mathbf{r}, s) = f_\lambda(\mathbf{r})\sigma(s)$, product of the $f_\lambda(\mathbf{r})$ *molecular orbital* (MO) times the spin function $\sigma(s)$

$$\psi_S = \frac{1}{\sqrt{N!}} \begin{vmatrix} \varphi_1(1) & \varphi_2(1) & \dots & \varphi_N(1) \\ \varphi_1(2) & \varphi_2(2) & \dots & \varphi_N(2) \\ \vdots & \vdots & \ddots & \vdots \\ \varphi_1(N) & \varphi_2(N) & \dots & \varphi_N(N) \end{vmatrix} \quad \mathbf{2.10}$$

where, for brevity, $(\mathbf{r}_i, s_i) \rightarrow (i)$, and $1/\sqrt{N!}$ is a normalization factor.^{6,7} It should be noted that spin orbitals are orthonormal ($\langle \varphi_\mu | \varphi_\nu \rangle = \delta_{\mu\nu}$) due to the presence of the spin factor. MOs are expanded as a *linear combination of atomic orbitals* (LCAO), q atomic function $\chi_l(\mathbf{r} - \mathbf{r}_a)$, centered on nuclei (\mathbf{r}_a) , which are in

general non-orthonormal ($\langle \chi_m | \chi_n \rangle \neq \delta_{mn}$) and that are usually referred to as *basis set* (BS) functions:^{6,7}

$$f_\lambda(\mathbf{r}) = \sum_{l=1}^q c_{l\lambda} \chi_l(\mathbf{r} - \mathbf{r}_a) \quad \mathbf{2.11}$$

Thanks to LCAO, the procedure in Equation **2.9** results in a constrained minimization over the MOs, and, consequently, in an iterative procedure which allows the calculation of the electronic energy, the so called *self-consistent field* (SFC) *procedure*:^{6,7}

1. Definition of the basis set and of the initial coefficients $c_{l\lambda}$ and so of the wave function in form of a Slater determinant.
2. Calculation of the electronic energy associated with such a wave function.
3. Minimization of the energy functional: this leads to several pseudo-eigenvalue equations (Hartree-Fock equations, Kohn-Sham equations) for an operator whose definition depends on the methods. From the resolution of such equations, new coefficients $c_{l\lambda}$ are obtained: they are used to re-evaluate the electronic energy and to re-solve the pseudo-eigenvalue equations. The procedure is iteratively repeated until a given threshold for the difference in energy between two subsequent steps is satisfied.

2.1.4 Basis sets

Essentially, two kind of localized (*i.e.*, centered on nuclear positions \mathbf{r}_a) basis sets have been developed through years (**Figure 2.1**), Slater-type orbitals (STOs), now almost abandoned, and Gaussian-type orbitals (GTOs). The general form of an STO is (n normalization constant)

$$S_{nlm}(r, \theta, \varphi) = nr^{n-1} e^{-\zeta r} Y_l^m(\theta, \varphi) \quad \mathbf{2.12}$$

with Y_l^m being a spherical harmonic and ζ an exponent.^{6,7} The general form of a GTO is

$$G_{ijk}(x, y, z) = nx^i y^j z^k e^{-\zeta(x^2+y^2+z^2)} \quad 2.13$$

where n again is a normalization constant and ζ is the exponent. They are usually classified as s -, p -, d -, f - orbitals depending on the value of the sum $i + j + k$ (s - if such sum is 0, p - if is 1, and so on).^{6,7} STOs better represent the behavior of electrons in atoms, especially for $r \rightarrow 0$, while GTOs are computationally cheaper. To merge together the computational saving typical of GTOs with the good representativeness of STOs, nowadays most of the codes based on localized BSs make use of *contracted Gaussians*, *i.e.* linear combination of simple GTOs called *primitive Gaussians*. Choosing a particular BS introduces some errors due to the incompleteness of such a BS: only an ideal *complete-BS* (CBS) would prevent the presence of these errors.^{6,7}

In solid-state calculations, where periodic boundary conditions (PBC) are applied in all three spatial dimensions, the use of *plane-wave functions* in order to describe valence-shell electrons only is very common; this kind of basis sets must be used in combination with *pseudopotentials* to describe core electrons.¹⁰ One of the main advantages of using plane-waves BS instead of localized ones is that they do not introduce a form of spurious computational error known as basis set superposition error (BSSE),^{6,11} which arises in the calculation of the interaction energy of molecular adducts.¹²

2.1.4.1 Nomenclature of localized basis sets

Most common localized BSs are:¹³

1. Minimal basis sets, now underused: each full, semi-full or empty atomic orbital is represented by a single function. The most common are STO- n G which combine n primitive Gaussians with a single STO.
2. “Double Z” (DZ) and “triple Z” (TZ) basis sets; each inner- and valence-shell orbital is described by two/three Gaussian functions.

3. “Split-valence” basis sets: inner shells orbitals are represented by only one contracted Gaussian function while valence orbitals are represented by two. The most known are *Pople basis set X-YZG* where X is the number of primitive Gaussian functions which constitute the inner orbitals, while YZ are the number of Primitive Gaussians which constitute the valence orbitals.¹⁴
4. “Correlation-consistent” (cc) basis sets: developed by Dunning and co-workers in order to converge systematically to the CBS limit using empirical extrapolation techniques.¹⁵ These BSs are labeled as cc-pVNZ where $N = D, T, Q, 5, 6, \dots$ (double, triple, *etc.*) and the V indicates they are valence-only basis sets.

In order to account for the deformation of the electron density due to the formation of bonds, *polarization functions* are often added. These functions are GTOs with higher values of angular momentum (for example, for block- p elements, d -polarization functions are added) and are usually indicated by asterisks (in the Pople notation). Finally, *diffuse functions*, indicated with “+” (Pople) or “aug” (Dunning), can also be added in order to account for medium and long radius interactions (they are very little localized Gaussian functions with little exponents ζ).

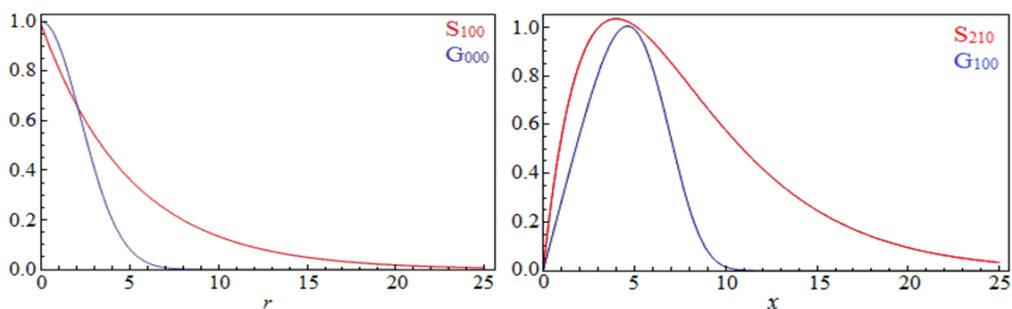


Figure 2.1 Examples of first hydrogen-like orbitals, s (S_{100} and G_{000}) and p (S_{210} and G_{100}).

2.2 Quantum chemistry methods

All the computational methodologies that solve Equation 2.6, *i.e.* based on a QM approach, are known as *ab initio* methods. In the following, a brief description of the most important ones is presented.

2.2.1 The Hartree-Fock method

Historically speaking, the *Hartree-Fock* (HF) *method* represents the first computational method developed independently by Douglas Hartree and Vladimir Fock.^{16–20} Most of the nomenclature that is still adopted nowadays in computational chemistry derives from the HF framework, so it is important to revise its most important aspects.

HF method is based on the strong assumption that electrons are initially non-interacting particles, anyway submitted to symmetry constraints: the repulsive interaction among them is “simulated” by the best set of coefficients obtained by the SCF procedure. The wave function has exactly the form of a Slater determinant and, therefore, it cannot provide for excited states. It is well known that HF method underestimates the total energy of a system of about 2% but it can account exactly for the *exchange energy*, a form of energy with no classical analogue which originates repulsive forces when two electrons are forced to share the same quantum state.^{6,7}

Evaluating the expectation value of the Hamiltonian on a single Slater determinant, added with the repulsive nuclear term, leads to the *Hartree-Fock energy* (E_{HF}):^{6,7}

$$E_{HF} = \sum_{\mu=1}^N \langle \varphi_{\mu}(i) | \hat{h}(i) | \varphi_{\mu}(i) \rangle + \frac{1}{2} \sum_{\mu=1}^N \sum_{\substack{\nu=1 \\ \nu \neq \mu}}^N (\langle \varphi_{\nu}(i) | \hat{J}_{\mu}(i) | \varphi_{\nu}(i) \rangle - \langle \varphi_{\nu}(i) | \hat{K}_{\mu}(i) | \varphi_{\nu}(i) \rangle) + V_{nn} \quad 2.14$$

while minimizing the energy functional (over the MOs) conducts to the *Hartree-Fock equations*, a set of N pseudo-eigenvalue integro-differentials equations for the Fock operator $\hat{F}(i)$, one for each spin-orbital $|\varphi_{\lambda}(i)\rangle$.^{6,7}

$$\hat{F}(i) |\varphi_{\lambda}(i)\rangle = \left\{ \hat{h}(i) + \sum_{\mu=1}^N [\hat{J}_{\mu}(i) - \hat{K}_{\mu}(i)] \right\} |\varphi_{\lambda}(i)\rangle = \varepsilon_{\lambda} |\varphi_{\lambda}(i)\rangle \quad 2.15$$

In Equations 2.14 and 2.15, $\hat{h}(i)$, $\hat{J}_{\mu}(i)$, $\hat{K}_{\mu}(i)$ are the mono-electronic Hamiltonian, the Coulombian and the exchange operators, respectively, defined as

$$\begin{aligned} \hat{h}(i) |\varphi_{\lambda}(i)\rangle &= \left[-\frac{1}{2} \nabla_i^2 - \sum_{a=1}^M \frac{Z_a}{r_{ai}} \right] |\varphi_{\lambda}(i)\rangle \\ \hat{J}_{\mu}(i) |\varphi_{\lambda}(i)\rangle &= \langle \varphi_{\mu}(j) | r_{ij}^{-1} | \varphi_{\lambda}(i) \varphi_{\mu}(j) \rangle \\ \hat{K}_{\mu}(i) |\varphi_{\lambda}(i)\rangle &= \langle \varphi_{\mu}(j) | r_{ij}^{-1} | \varphi_{\mu}(i) \varphi_{\lambda}(j) \rangle \end{aligned} \quad 2.16$$

When the LCAO expression is introduced in the definitions of the Fock operator, the HF equations transform into matrix equations known as *Roothaan-Hall equations*

$$\mathbf{FC} = \mathbf{SCE} \quad 2.17$$

with \mathbf{C} coefficients matrix ($C_{lm} = c_{l\mu}$), \mathbf{S} overlap matrix ($S_{lm} = \langle \chi_l | \chi_m \rangle$), \mathbf{E} diagonal matrix of the energies ($E_{ll} = \varepsilon_{\lambda}$) and \mathbf{F} Fock matrix; please note that the Fock-matrix elements ($F_{lm} = \langle \chi_l | \hat{F} | \chi_m \rangle$) depends on the LCAO coefficients.^{21,22} The Roothaan-Hall procedure is fundamental since it allows to translate the

mathematical complexity of HF equations into a simpler set of linear equations, easy to solve numerically.^{6,7}

2.2.2 *Post-Hartree-Fock methods*

The quantity of energy HF method cannot provide for is usually referred to as *correlation energy* (E_{corr})

$$E_{corr} = E - E_{HF} \quad \mathbf{2.18}$$

where E is the exact energy. This small, but important, energetic quantity accounts for both static (single, double, triple, *etc.* electronic excitations from the ground state to excited energy levels) and dynamic (instantaneous electron-electron punctual interaction) correlation.^{6,7}

To (partially) recover most of E_{corr} term, some *post*-HF methods – namely coupled-cluster (CC), configuration interaction (CI), Møller-Plesset perturbation theory (MPn) – have been developed. Briefly, the idea underneath all these methods is to expand the electronic wave function as a linear combination of different Slater determinants. Because they are based on the explicit expression of the wave function, HF and *post*-HF methods are usually reported to be as *wave function-dependent methods*, and, apart from the HF one, they are usually quite computationally expensive.^{6,7} A completely different QM approach invokes the electron density.

2.2.3 *The electron density*

The main obstacle that can be encountered in solving wave function-based equations such as the HF ones is that the wave function for a system of N electrons depends on $3N$ spatial variables and N spin variables, so the mathematical complexity rapidly increases. A completely different approach is based on the definition of *electron density* which represents the positional probability density

of finding one electron in the volume element $d\mathbf{r}$ given the position of all the other electrons

$$\rho(\mathbf{r}) = N \sum_{s_1} \dots \sum_{s_N} \int \dots \int |\psi(\mathbf{r}_1, s_1, \dots, \mathbf{r}_N, s_N)|^2 d\mathbf{r}_2 \dots d\mathbf{r}_N \quad 2.19$$

i.e., it is a three-variable dependent function.² From its definition, it is clear that $\rho(\mathbf{r})$ is always a positive quantity and that its integral over all-space is equal to N ; moreover, it can be easily shown that for a mono-determinant wave function^{6,7}

$$\rho(\mathbf{r}) = \sum_{\lambda=1}^N \sum_s |\varphi_{\lambda}(\mathbf{r}, s)|^2 \quad 2.20$$

and that it owns cusp properties (**Figure 2.2**).²³

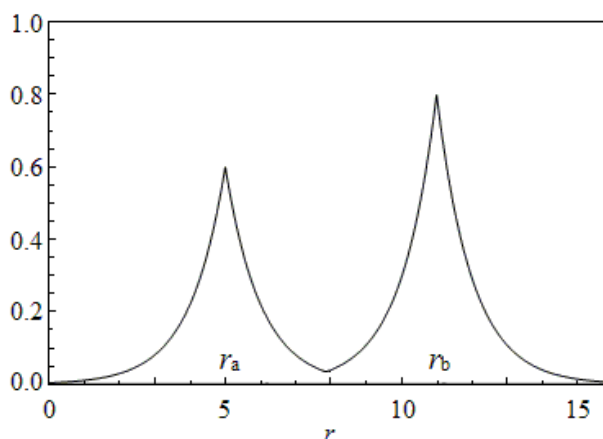


Figure 2.2 Electron density surrounding two bound nuclei at positions r_a and r_b ; note that in the intermediate region (the *bond region*), the electron density is small but still greater than zero

2.2.4 The density functional theory

2.2.4.1 Hohenberg and Kohn theorems

In 1964, Pierre Hohenberg and Walter Kohn published an article where they demonstrated two theorems which would become the theoretical basis for the future (electron) *density functional theory* (DFT).²⁴

Recalling the electron-nucleus attractive term of the electronic Hamiltonian \hat{V}_{ne} as the *external potential* \hat{V}_{ext} (this term is due to the fact that the central object of DFT is the electron density, so any contribute to the potential energy which does not derive directly from the electrons is seen as “external”; in this sense, \hat{V}_{ext} can also contain other terms such as external electric and magnetic fields, *etc.*), Hohenberg and Kohn, with their first theorem, demonstrated that:²⁴

- \hat{V}_{ext} uniquely determines the electronic Hamiltonian \hat{H} that, conversely, uniquely determines the external potential (a similar relation can be found between the Hamiltonian and the ground state wave function);
- the electron density uniquely determines the external potential (and so the Hamiltonian and the wave function) but not *vice-versa*.

This chain of relations can be summarized as

$$\begin{array}{ccc}
 \hat{V}_{ext} & \leftarrow & \rho(\mathbf{r}) \\
 \updownarrow & & \up \\
 \hat{H} & \leftrightarrow & \psi
 \end{array}
 \qquad \mathbf{2.21}$$

From the definitions of electron density, it should be clear that $\psi = \psi[\rho]$ and so it is possible to substitute the functional $E[\psi]$ with the functional $E[\rho]$. With the second theorem, Hohenberg and Kohn demonstrated that, for a given external potential, it is possible to obtain the ground state energy E_0 by minimizing the functional $E[\rho]$ over all the possible electron densities satisfying physical constraints²⁴

$$\delta E[\rho] = \frac{\partial E[\rho]}{\partial \rho} = 0 \rightarrow E_0 = \min_{\rho \rightarrow N, V_{ext}} E[\rho]
 \qquad \mathbf{2.22}$$

and that the electron density which minimizes such functional is exactly the ground state electron density, $\rho_{min}(\mathbf{r}) = \rho_0(\mathbf{r})$. Consequently, each energetic term of the Hamiltonian must be written as a functional of the electron density

$$E[\rho] = T_e[\rho] + V_{ee}[\rho] + V_{ext}[\rho] \quad 2.23$$

However, to exactly solve a DFT equations, we need the explicit expressions of these functionals. For example, it can be easily derived that for $V_{ext}[\rho]$

$$V_{ext}[\rho] = \int \rho(\mathbf{r})V_{ext}(\mathbf{r})d\mathbf{r} \quad 2.24$$

while the other two functionals are in general unknown. $V_{ee}[\rho]$ is usually split as the sum of two terms, the first is the classic (Coulomb) term $J[\rho]$, which describes the interaction of the electron density with itself, and the second is the non-classic contribute $E_{nc}[\rho]$ (unknown). Thus, the total energy functional can be then written as

$$\begin{aligned} E[\rho] &= T_e[\rho] + E_{nc}[\rho] + J[\rho] + V_{ext}[\rho] = \\ &= T_e[\rho] + E_{nc}[\rho] + \frac{1}{2} \iint \frac{\rho(\mathbf{r}_i)\rho(\mathbf{r}_j)}{|\mathbf{r}_{ij}|} d\mathbf{r}_i d\mathbf{r}_j + \int \rho(\mathbf{r})V_{ext}(\mathbf{r})d\mathbf{r} \end{aligned} \quad 2.25$$

2.2.4.2 Kohn-Sham formalism

In 1965, Walter Kohn, together with Lu Jeu Sham, published a second article where they developed a formalism that made the DFT framework actually applicable.²⁵ This *Kohn-Sham formalism* is based on similar assumptions underlying the HF method (initial non-interactive, Pauli principle-constrained electrons), so a single Slater determinant can be written where the elements are not simple MOs, but rather *Kohn-Sham MOs* (KS-MOs) φ_λ^{KS} , also expandable in a LCAO. Such MOs are defined according to the following further assumption: the electron density generated by the KS-MOs (ρ_s) must be equivalent to the ground state electron density ρ_0 , so, according to Equation 2.20²⁵

$$\rho_s(\mathbf{r}) = \rho_0(\mathbf{r}) = \sum_{\lambda=1}^N \sum_s |\varphi_\lambda^{KS}(\mathbf{r}, s)|^2 \quad 2.26$$

This assumption allows to write part of the kinetic functional in terms of the KS-MOs, specifically those contributions $T_S[\rho]$ which derive directly from considering the electron as non-interactive particles²⁵

$$T_e[\rho] = T_S[\rho] + \Delta T_e[\rho] = -\frac{1}{2} \sum_{\lambda=1}^N \sum_s \int |\varphi_{\lambda}^{KS}(\mathbf{r}, s)|^2 d\mathbf{r} + \Delta T_e[\rho] \quad 2.27$$

With these assumptions, only two functionals still remain unknown, $E_{nc}[\rho]$ (non-classical contributions to the potential energy) and $\Delta T_e[\rho]$ (interacting-electrons corrections to the kinetic energy). These contributions are usually merged together in the *exchange-correlation (XC) functional* $E_{XC}[\rho]$. The expression of this XC functional is unknown, therefore, the different DFT methods (see next Section) differentiate themselves by the peculiar mathematical form they assigned to it. Generally speaking, a good XC functional should include: *i)* electron-kinetic correlation, *ii)* exchange contributions, *iii)* Coulomb correlations and *iv)* self-interaction corrections. From the KS formalism, all the energetic functionals in Equation 2.25 become functionals of the KS-MOs, so that a minimization procedure over the KS-MOs can be performed, and, as for the HF method, this leads to pseudo-eigenvalues equations for the *Kohn-Sham operator* \hat{f}^{KS} , known as *Kohn-Sham equations*^{6,7}

$$\hat{f}^{KS}(i)\varphi_{\lambda}^{KS}(i) = \varepsilon_{\lambda}^{KS}\varphi_{\lambda}^{KS}(i) \quad 2.28$$

with

$$\hat{f}^{KS}(i) = -\frac{1}{2}\nabla_i^2 + \hat{V}_{eff}(i) = -\frac{1}{2}\nabla_i^2 - \sum_{a=1}^M \frac{Z_a}{r_{ia}} + \int \frac{\rho(\mathbf{r}_j)}{r_{ij}} d\mathbf{r}_j + \hat{V}_{XC}[\rho] \quad 2.29$$

where $\hat{V}_{XC}[\rho] = \delta E_{XC}[\rho]/\delta\rho$ is the unknown *exchange-correlation potential*. As for the HF equations, also KS equations can be transformed into a matrix form by making use of the LCAO approximation^{6,7}

fC = SCE
2.30

with $f_{lm} = \langle \chi_l | \hat{f}^{KS} | \chi_m \rangle$ Kohn-Sham matrix elements.^{6,7} What we said about the SCF procedure in HF-ambit is still valid in DFT, and, because of the similarity between the two formalisms, the DFT methods require a similar computational cost. However, there is an important difference between HF and DFT, the former being approximate, while the latter being, in principle, exact since it is based on the definition of electron density and so, *de facto*, on the QM principles. Anyway, even DFT introduces, as seen, some approximations which are all synthesized in the unknown exchange-correlation functional $E_{XC}[\rho]$.

 2.2.4.3 *Jacob's ladder: the DFT methods*

Commonly, the XC functional is written as the sum of an exchange and a correlation term

$$\begin{aligned}
 E_{XC}[\rho] &= \int \rho(\mathbf{r}) \varepsilon_{XC}[\rho] \, d\mathbf{r} = E_X[\rho] + E_C[\rho] = \\
 &= \int \rho(\mathbf{r}) \varepsilon_X[\rho] \, d\mathbf{r} + \int \rho(\mathbf{r}) \varepsilon_C[\rho] \, d\mathbf{r}
 \end{aligned}
 \tag{2.31}$$

where ε stands for the *energy density per particle*. Depending on which form is assigned to the ε functionals, several DFT methods have been developed. In 2005, John Perdew resumed all these methods in the *Jacob's ladder* of functional (**Figure 2.3**),²⁶ where the DFT methods are grouped in several classes ordered from minor to major accuracy and computational cost. It should be noted that only the XC functional has a physical meaning, while the two terms in Equation 2.31 have not. First-, second- and third-class functionals are defined as *local* because they evaluate electron density point by point; second- and third-class functionals are also defined as *semi-local* because they depend not only from the electron density but also from its derivatives.

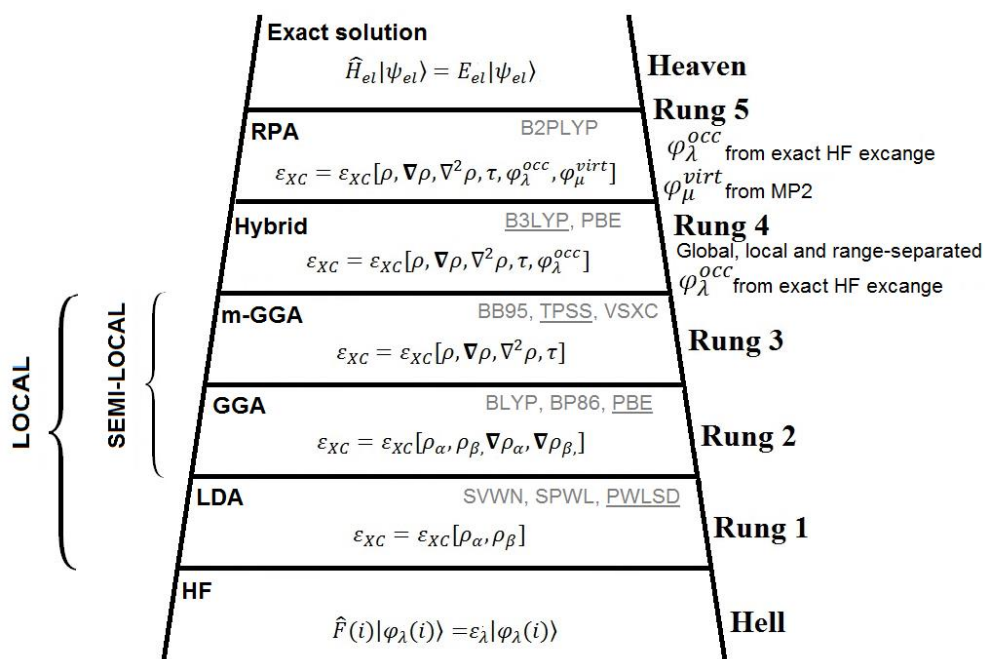


Figure 2.3 Jacob's ladder of functionals: underlined functionals are the most representative of each class according to Perdew.²⁶

First class functionals belong to the *local density approximation* (LDA) based on the assumption that electrons behave like an *uniform electron gas* which was firstly suggested by physicists Llewellyn H. Thomas and Enrico Fermi with their works on the *Thomas-Fermi model*.^{27,28} Such an approximation is not valid for molecules, where the electron density resembles that reported in **Figure 2.2**, but is quite good for solids. The exchange functional can be exactly computed

$$\varepsilon_X[\rho] = -\frac{3}{4}\left(\frac{3}{\pi}\rho(\mathbf{r})\right)^{\frac{1}{3}} \rightarrow E_X^{LDA}[\rho] = -\frac{3}{4}\left(\frac{3}{\pi}\right)^{\frac{1}{3}} \int [\rho(\mathbf{r})]^{\frac{4}{3}} d\mathbf{r} \quad 2.32$$

Generalized gradient approximation (GGA) functionals depend on the reduced gradient of the electron density

$$x(\mathbf{r}) = \frac{|\nabla\rho(\mathbf{r})|}{[\rho(\mathbf{r})]^{4/3}} \quad 2.33$$

The most representative is the Perdew-Burke-Ernzerhof (PBE) functional,^{29,30} for which

$$\varepsilon_X^{PBE} = \varepsilon_X^{LDA} F(x) \quad \varepsilon_C^{PBE}[\rho, \nabla\rho] = \varepsilon_C^{LDA} + H(t) \quad 2.34$$

where $F(x)$ is the 1986-Perdew's functional (P86),³¹ and $H(t)$ is a complex function of the variable $t = kx$ with k constant. Instead, *meta*-GGA functionals depend not only from the reduced gradient but also from its Laplacian $\nabla^2\rho$.

Next-class functionals are called *hybrid* functionals because they incorporate part of the exact HF exchange by including occupied HF MOs (φ_μ^{occ}).^{32,33} The most representative is the B3LYP, where the exchange part derives from the B3 functional (Becke-3 parameters),^{34,35} while the correlation part derives from the Lee-Yang-Parr (LYP) functional³⁶

$$\begin{aligned} E_{XC}^{B3LYP} &= a_0 E_X^{HF} + (1 - a_0) E_X^{LSDA} + \\ &+ a_x (E^{B88} - E_X^{LSDA}) + a_c E^{LYP} + (1 - a_c) E^{VWN} \end{aligned} \quad 2.35$$

where a_0 , a_x and a_c are the three parameters, respectively equal to 0.20, 0.72 and 0.81. B3LYP is an example of *global hybrid* because it adds the HF exchange for every \mathbf{r} ; for *local hybrids*, the percentage of HF exchange depends from \mathbf{r} while for *range-separated hybrids* the exact HF exchange differs region by region.

The last class of functionals belongs to the *random phase approximation*. They also introduce exact HF exchange through occupied molecular orbitals, but they also include *post*-HF correlation through virtual molecular orbitals (φ_μ^{virt}) and, sometimes, they are referred to as *double hybrids*. Resuming, if q is the number of basis set functions, the computational cost increases from the bottom to the top of the Jacob's ladder as

$$\underbrace{\text{LDA} < \text{GGA} < \text{m-GGA}}_{q^3} < \underbrace{\text{hybrids}}_{q^{3.5}} < \underbrace{\text{double hybrids}}_{q^5} \quad 2.36$$

2.3 Dispersive interactions

With *dispersion energy*, it is usually intended a form of energy due to the inter-electronic correlation which manifests itself in medium- and long-radium interactions. Such energy originates from the so-called *dispersive forces* – weak interactions if compared to other kind of interactions – which are important not only in non-polar molecules, but also in periodic systems and in biomolecules such as proteins and DNA. In effect, it is well known that conformations of biomolecules, which are fundamental for their working functions, depend largely on non-covalent interactions such as dispersive interactions.

In the *ab initio* computational context, this kind of interactions is usually explained as double excitations from occupied to virtual MOs and so it is well described by *post*-HF methods accounting for at least these double excitations. However, these methods can be more expansive than DFT ones; therefore, several strategies have been developed in order to account for dispersion energy in DFT-ambit, the simplest one being the addition of a semi-empirical term to the total DFT electron energy

$$E = E_{DFT} + E_{disp} \quad 2.37$$

2.3.1 Grimme's D1 and D2 corrections

In 2004, Stefan Grimme proposed a very simple expression for E_{disp} (in non-periodic systems) known as Grimme correction³⁷

$$E_{disp} = -S_6 \sum_{a=1}^{N_{at}-1} \sum_{b=a+1}^{N_{at}} \frac{C_{6,ab}}{r_{ab}^6} f_{damp}(r_{ab}) \quad 2.38$$

where N_{at} is the total number of atoms, $C_{6,ab}$ is the dispersive coefficient for the pair of atoms ab (separated by a distance r_{ab}), s_6 is a scaling factor whose value depends on the DFT functional and $f_{dmp}(r_{ab})$ is a damping function added to avoid near-singularities for small r_{ab} . In the 2004's work and in a successive 2006's work,³⁸ Grimme proposed the following expression for the damping function

$$f_{dmp}(r_{ab}) = \left[1 + e^{-d\left(\frac{r_{ab}}{r_s} - 1\right)} \right]^{-1} \quad 2.39$$

where $r_s = r_a^* + r_b^*$ is the sum of van der Waals radii for atoms a and b and d is an empirical factor set equal to 20. Other expressions have been proposed for the damping function,³⁹⁻⁴² but it has been demonstrated that they all lead to the same results.⁴³

2.3.1.1 D1 and D2 parameters

Grimme's 2004 and 2006 works are respectively known as D1 and D2 versions. There are few differences between them, the main one being in the way pair-dispersion coefficients are computed:

$$C_{6,ab}^{D1} = 2 \frac{C_{6,a} C_{6,b}}{C_{6,a} + C_{6,b}} \quad 2.40$$

$$C_{6,ab}^{D2} = \sqrt{C_{6,a} C_{6,b}} \quad 2.41$$

where $C_{6,a}$ and $C_{6,b}$ are dispersion coefficients for atoms a and b respectively. For D1 version, single-atom coefficients are evaluated for a few atoms only (taken from a previous work of Wu and Yang⁴⁴) while for D2 version they are evaluated for all elements from H to Xe thanks to the following expression³⁸

$$C_{6,a}^{D2} = 0.05 \mathcal{M}_a \alpha_a \quad 2.42$$

with I_a ionization potential and α_a static polarizability (in atomic units) of atom a and \mathcal{N} number of electrons of the noble gas belonging to the same period of atom a .

2.3.2 Grimme's D3 correction

In 2010, Grimme published a further work where high-order coefficients and three-body interactions are included.⁴⁵ This version, which is much more complex than the two previous ones, is usually referred to as D3 version. In the following, we will briefly show the equations belonging to this approach, but for an extensive and exhaustive explanation of all the energetic terms, we remind to Grimme's 2010 original work.⁴⁵

There are two main differences between D1/D2 and D3: inclusion of a three-body term ($E^{(3)}$) and inclusion of higher-order dispersion coefficients ($n = 6, 8, 10, \dots$) for the two-body term ($E^{(2)}$).

$$\begin{aligned}
 E_{disp} &= E^{(2)} + E^{(3)} \\
 E^{(2)} &= \sum_{a,b} \sum_{n=6,8,10,\dots} s_n \frac{C_{n,ab}}{R_{ab}^n} f_{dmp,n}(r_{ab}) \\
 E^{(3)} &= \sum_{a,b,c} E^{(a,b,c)} f_{dmp,(3)}(\bar{r}_{abc})
 \end{aligned}
 \tag{2.43}$$

where, for brevity, the first sums in $E^{(2)}$ and $E^{(3)}$ expressions run over all the atom pairs and triplets, respectively, $E^{(a,b,c)}$ is a three-body term depending on the internal angles of the triangle formed by r_{ab} , r_{ac} and r_{bc} , and \bar{r}_{abc} is the geometrical average of these three distances.

2.4 Classical (molecular) mechanics

So far, we focused on the description of a molecular system within a QM ambit. However, the computationally cheapest way to describe a multi-atomic system (like molecules, but also solids, see Section 2.6) is through the adoption of a

classical mechanics (CM) methodology. CM-based methods are usually also known as *molecular mechanics* (MM) methods. Briefly, the idea underneath MM methods is to describe the atoms as charge-bearing spheres (with a given radius, typically the van der Waals radius), interacting one another through elastic forces, *i.e.* covalent bonds are assumed to behave as “springs”.^{6,7} More specifically, the total energy of a system is given by the sum of many terms

$$\begin{aligned}
 E &= E_{\text{covalent}} + E_{\text{non-covalent}} = \\
 &= E_b + E_\theta + E_\tau + E_{\text{oop}} + E_{\text{vdW}} + E_{\text{es}} + E_X + (E_H)
 \end{aligned}
 \tag{2.44}$$

where the various energetic terms describe covalent bonds (E_b), angles (E_θ), torsionals (E_τ), out-of-plan contributions (E_{oop}), van der Waals (E_{vdw}) and pure electrostatic (E_{es}) interactions, crossed-terms (E_X) and, eventually, H-bonds (E_H). “Crossed-terms” are energetic contributions mixing two or more coordinates (bond-bond, bond-angle, *etc.*). As for QM methods, also MM ones are subjected to the Born-Oppenheimer approximation. Indeed, even if we cannot properly talk about electrons in MM, the expression in Equation 2.44 can be considered as the analogous of Equation 2.6 for the electron energy, since it does not account for energetic contribution coming from the nuclear distribution. The specific expression of all these terms are listed in Equations 2.45 (b is the bond-length, θ is the angle, τ the torsional, ω the out-of-plane angle, r_{ab}^* the sum of van der Waals radii for a and b atoms separated by the distance $|\mathbf{r}_{ab}|$ and bearing charges q_a and q_b , d is the depth of the potential energy well and ϵ the dielectric constant of a given medium):^{6,7}

$$E_b = \sum_{i=2}^4 k_{b,i}(b-b_0)^i \text{ or } E_b^{Morse} = D(1 - e^{\alpha(b-b_0)})^2$$

$$E_\theta = \sum_{i=2}^4 k_{\theta,i}(\theta - \theta_0)^i \text{ or } E_\theta = k_\theta(1 + \cos\theta)$$

$$E_\tau = k_{\tau,1}(1 + \cos\tau) + k_{\tau,2}(1 - \cos 2\tau) + k_{\tau,3}(1 + \cos 3\tau)$$

$$E_{oop} = k_\omega \omega^2$$

$$E_{vdW}^{L-J} = d \left[\left(\frac{r_{ab}^*}{|r_{ab}|} \right)^{12} - 2 \left(\frac{r_{ab}^*}{|r_{ab}|} \right)^6 \right] \quad \mathbf{2.45}$$

$$E_{vdW}^B = A e^{-B|r_{ab}|} - \frac{C}{|r_{ab}|^6}$$

$$E_{es} = \frac{q_a q_b}{\epsilon |r_{ab}|}$$

$$E_H = d \left[5 \left(\frac{r_{ab}^*}{|r_{ab}|} \right)^{12} - 6 \left(\frac{r_{ab}^*}{|r_{ab}|} \right)^{10} \right]$$

where the various k are proportional constants and A , B and C are dispersion coefficients (E_b^{Morse} , E_{vdW}^{L-J} , E_{vdW}^B are the Morse, Lennard-Jones and Buckingham potentials, respectively). In the framework of MM simulations, the functional form assumed by all the energetic terms in Equations 2.45 together with the specific values of the constants, parameters and net charges is usually known as force field (FF).⁴⁶ The values of such (many) parameters can derive from experimental measures or from high level, *ab initio* calculations. Several FFs have been developed to describe specific class of materials (notable, for the purpose of this work, is the olivine-designed FF by Catlow *et al.*⁴⁷), while only a few can be used to describe the whole periodic table.^{48,49}

2.5 Kinds of calculation

2.5.1 Optimization procedure

Whether the energy is computed from Equation 2.6 or from Equation 2.44, the procedures described so far can only lead to a single point (SP) energy calculations, *i.e.* the evaluation of the energy associated to a certain, fixed structure. However, to correctly represent a chemical system, a minimization procedure on the PES must be followed. The simplest procedure is based on the *harmonic approximation*: the total (electronic added with the nuclear repulsion) energy E around a minimum can be expanded in Taylor series.^{6,7} Zero and first order of such an expansion can be removed (for different reasons). Therefore, neglecting higher order terms, E and its gradient $\mathbf{g}(\mathbf{r})$ can be written as

$$E(\mathbf{r}) = \frac{1}{2} \sum_{a,b=1}^{3M} u_a \frac{\partial^2 E}{\partial u_a \partial u_b} \Big|_{min} u_b = \frac{1}{2} \delta \mathbf{r}^T \mathbf{H} |_{min} \delta \mathbf{r} \quad 2.46$$

$$\mathbf{g}(\mathbf{r}) = \mathbf{H} \delta \mathbf{r} \quad 2.47$$

where E comes from either a QM or MM run, \mathbf{r} represents all atomic coordinates, $\delta \mathbf{r}$ is the vector formed by all atomic displacements $u_a = x_a - x_a^{min}$ around the minimum position and \mathbf{H} is the Hessian matrix of second derivatives, generally non-diagonal. From Equations 2.47, the *Newton* or *quadratic step* $\delta \mathbf{r}$ can be easily obtained; such a step represents the displacement that must be done in order to iteratively approach the closest local minimum. The optimization procedure consists in what follows:

1. Definition of the initial geometry \mathbf{r}_0 .
2. Definition of the initial gradient and Hessian matrix \mathbf{H}_0 .
3. Calculation of the first quadratic step and definition of the new geometry \mathbf{r}_1 .

4. Hessian updating, calculation of the second quadratic step and definition of the second geometry \mathbf{r}_2 , etc.^{6,7}

The procedure ends when some threshold parameters are satisfied. The updated Hessian is written as

$$\mathbf{H}_{n+1} = \mathbf{H}_n + \Delta\mathbf{H}_n \quad 2.48$$

where $\Delta\mathbf{H}_n = \Delta\mathbf{H}_n(\Delta\mathbf{r}, \mathbf{g})$ so that all the diagonal elements are positive,^{6,7} following the Broyden-Fletcher-Goldfarb-Shanno (BFGS) algorithm.⁵⁰⁻⁵³

2.5.2 Frequencies calculation and thermodynamics

The optimization procedure based on the quadratic step cannot ensure the achievement of a minimum, but only of a critical point. However, only minima, that correspond to proper chemical species, and first-order saddle points (transition states, TSs) are of chemical interest. To discern among minima, first-order saddle points and any other kind of stationary point, the Hessian matrix of second derivatives, computed in a given point of the PES, must be diagonalized. This diagonalization procedure can be seen as a unitary transformation of the atomic Cartesian coordinates ($3M$ values, x , y and z for each atom) in a new set of coordinates that are expressed as linear combinations of the Cartesian one, denoted as *normal modes of vibration*, Q_μ .^{6,7} If the diagonal elements (λ_μ) of the Hessian are all positive, we are in correspondence of a minimum, if just one eigenvalue is negative, we are in a first-order saddle point, and so on. After this unitary transformation, the vibrational Hamiltonian in Equation in Equation 2.7 can be written as^{6,7}

$$\hat{H}_{vib} = \sum_{\mu=1}^{3M} \left(-\frac{1}{2} \frac{\partial^2}{\partial Q_\mu^2} + \frac{1}{2} \lambda_\mu \Delta Q_\mu^2 \right) \quad 2.49$$

i.e. as the sum of $3M$ independent oscillators, and the associated energy is known as *zero-point energy* (ZPE, E_{ZP})

$$E_{ZP} = \sum_{v=0}^{+\infty} \sum_{\mu=1}^{3M-5/6} \left(v + \frac{1}{2} \right) \hbar \omega_{\mu} \quad \mathbf{2.50}$$

with $\omega_{\mu} = 2\pi\nu_{\mu} = \sqrt{\lambda_{\mu}}$.^{6,7} The second sum in Equation **2.50** runs only on $3M - 5/6$ values since, for a polyatomic molecule, six Hessian eigenvalues are null because they correspond to linear combinations of atomic coordinates which lead to translations and rotations; for the same reason, for a diatomic molecule ($M = 2$) there is only $3M - 5 = 1$ normal mode of vibration.^{6,7}

Calculating the vibrational frequencies is useful not only to classify PES stationary points, but also because it allows us to relate the computed energies to the more experimentally-meaningful thermodynamics quantity like enthalpy, free energy *etc.* The link between the computed energies and thermodynamic quantities is provided by statistical mechanics relations. In particular, the most important thermodynamic quantities (U , H , S and G are the internal energy, the enthalpy, the entropy and the Gibbs free energy, respectively) in Equations **2.52-2.55** depend on the *partition function* Q (Equation **2.51**) that in turn depends, at least for its vibrational contribution Q_{vib} , on the vibrational frequencies. For all other contributions in Equation **2.51**, simple expressions can be easily derived starting from the definition of Q (centre of Equation **2.51**) and by applying some QM considerations.⁵⁴⁻⁵⁶

$$Q(T) = \sum_{i=0}^{\infty} e^{-E_i/k_B T} = Q_{el} + Q_{vib} + Q_{rot} + Q_{trasl} \quad \mathbf{2.51}$$

$$U(T) = k_B T^2 \left(\frac{\partial}{\partial T} \ln Q(T) \right)_{N,V} \quad \mathbf{2.52}$$

$$H(T) = U(T) + PV(T) \quad \mathbf{2.53}$$

$$S(T) = k_B \ln Q(T) + k_B T \left(\frac{\partial}{\partial T} \ln Q(T) \right)_{N,\Omega} \quad \mathbf{2.54}$$

$$G(T) = H(T) - TS(T) \quad 2.55$$

where E_i is the energy of the i -th quantum level, N the number of particles, Ω the volume, T the absolute temperature, P the pressure and k_B the Boltzmann constant.

Standard static QM or MM calculation are performed a 0 K (more correctly, with no temperature contributions). Under this condition, the internal energy $U(0)$ is the sum of two terms, *i.e.* the total HF/post-HF/DFT/MM energy E (electronic + nuclear) plus the ZPE (rotations and translations are forbidden), and it coincides with the enthalpy $H(0)$ and, in turn, with the Gibbs free energy $G(0)$ (because $PV(0) = 0$).⁵⁴⁻⁵⁶

$$U(0) \equiv H(0) \equiv G(0) = E + E_{ZP} \quad 2.56$$

2.5.3 Molecular dynamics

To account for dynamics effect, *i.e.* to introduce a temperature dependence in QM or MM calculations, we must go over what we showed so far, and introduce the so-called molecular dynamics (MD) simulations. Under the Born-Oppenheimer approximation, nuclei are heavy objects and can be considered as classical particles; therefore, we can describe their motion by classical Newton's motion equations:⁵⁷

$$-\frac{\partial V}{\partial \mathbf{r}_a} = m_a \frac{d^2}{dt^2} \mathbf{r}_a \quad 2.57$$

where V is the potential energy experienced by the nucleus a (mass m_a) at position \mathbf{r}_a , and t is time. Being a 2nd order differential equation with respect to time, Equation 2.57 needs two parameters for each nucleus a to be integrated, the initial position $\mathbf{r}_a^{(0)}$ and velocity $\mathbf{v}_a^{(0)}$. While $\mathbf{r}_a^{(0)}$ values are directly provided by input, initial velocities $\mathbf{v}_a^{(0)}$ are usually randomly assigned by assuming a

Maxwell-Boltzmann distribution at a given temperature. Equation **2.57** is solved iteratively by adopting a small time-step ($t \rightarrow \Delta t \sim 10^{-15}$ s) and by computing at each step i the position of the nucleus a from a Taylor expansion^{57,58}

$$r_a^{(i+1)} = r_a^{(i)} + \frac{\partial r_a^{(i)}}{\partial t} \Delta t + \frac{1}{2} \frac{\partial^2 r_a^{(i)}}{\partial t^2} \Delta t^2 + \dots \quad \mathbf{2.58}$$

This procedure is re-iterated for many steps, usually for a whole time of the order of picoseconds (10^{-12} s). Necessarily, the potential energy V must be computed at each step i : if V is computed from a QM calculation, we talk about *ab initio* MD (AIMD), otherwise about classical MD.^{57,58}

MDs, both classical or *ab initio*, are divided into *ensembles*, depending on which quantities are preserved during the whole time of the MD:

- NVE (or micro-canonical) ensemble, where the number of particles N , the volume V and the total energy of the system E are kept constant;
- NVT (or canonical), as before but temperature T is now kept constant instead of E ;
- NPT (or isobaric) ensemble, where the pressure P is kept constant together with N and T ;
- μ VT (or grand canonical) ensemble, where the chemical potential μ is constant, as V and T .

NVT, NPT and μ VT are the most used for chemical simulations, as usually temperature is constant during chemical processes. Nevertheless, NVE ensemble can be useful to simulate such processes where the exchange of energy is unlikely to occur, as in the interstellar medium.

2.6 Periodic systems

The formalisms that we adopted so far for molecular system can be easily extended, with a few further considerations, to *periodic systems*. A periodic system is characterized by the application of translational symmetry along all the

three (3D), just two (2D) or one (1D) dimensions. When this is the case, we say that PBC have been introduced in the Hamiltonian.

2.6.1 Reciprocal lattice, basis set and SCF equations

For a periodic 3D-system, three basis vectors \mathbf{a}_1 , \mathbf{a}_2 and \mathbf{a}_3 identify the *primitive cell* of the *direct lattice* (or *direct space*). Such a lattice is in relation with the *reciprocal lattice* where the three basis vectors \mathbf{b}_1 , \mathbf{b}_2 and \mathbf{b}_3 define *the (first) Brillouin Zone* (BZ). The reciprocal relation is such that

$$\mathbf{b}_i = 2\pi \frac{\mathbf{a}_j \times \mathbf{a}_k}{\mathbf{a}_i \cdot (\mathbf{a}_j \times \mathbf{a}_k)} \quad 2.59$$

with $i, j, k = 1, 2, 3$. Due to the existence of the reciprocal relations between direct- and reciprocal-lattice basis vectors, every vector in the crystal corresponds to one point in the first Brillouin Zone.

As previously stated, for a periodic system it is very common to use plane-waves basis sets, but also Gaussian basis sets can be used: such functions are defined only for atoms in the primitive cell (χ_l^0) and then translated exploiting the translational symmetry, thanks to translational operators \hat{t} representing the vector (of integer components) $\mathbf{t} = t_1\mathbf{a}_1 + t_2\mathbf{a}_2 + t_3\mathbf{a}_3$, which operates on the χ_l^0 giving the translated functions χ_l^t . The *Bloch theorem* asserts that the eigenstates of the Hamiltonian with PBCs cannot be simple periodic functions, but they have to be periodic plane waves functions,⁵⁹ usually called *Bloch functions* (BFs) X_l^k , which assume the same role of AOs in molecular modeling

$$X_l^k(\mathbf{r}) = \sum_t e^{ik \cdot \mathbf{t}} \hat{t} \chi_l^0(\mathbf{r}) = \sum_t e^{ik \cdot \mathbf{t}} \chi_l^t(\mathbf{r}) \quad 2.60$$

where $e^{ik \cdot \mathbf{t}}$ are phase factors and $\mathbf{k} = k_1\mathbf{b}_1 + k_2\mathbf{b}_2 + k_3\mathbf{b}_3$ is a generic vector of the first Brillouin Zone. The general solutions of the electronic Schrödinger equation in the periodic case are *Crystalline Orbitals* (COs) Φ_λ^k , linear combinations of BFs

$$\Phi_{\lambda}^k(\mathbf{r}) = \sum_{l=1}^q c_{l\lambda}^k X_l^k(\mathbf{r}) = \sum_{l=1}^q \sum_t c_{l\lambda}^k e^{i\mathbf{k}\cdot\mathbf{t}} \chi_l^t(\mathbf{r}) \quad 2.61$$

Following the same procedure used to derive Roothan-Hall equations (or their DFT-analogous), we can obtain

$$\mathbf{f}^k \mathbf{C}^k = \mathbf{S}^k \mathbf{C}^k \mathbf{E}^k \quad 2.62$$

i.e., the elements of every matrix depend from the \mathbf{k} point where they are evaluated. A small unit cell in direct space has a corresponding large unit cell in the \mathbf{k} -space; therefore, many \mathbf{k} points are required to properly sample the electronic bands. Instead, when a unit cell in the direct space is large enough, only one point in $\mathbf{k} = \mathbf{0}$ (Γ point) is already enough to sample the electronic structure.⁶⁰ Every matrix in Equation 2.62 is the Fourier transform of the analogous matrix defined in terms of AOs. For example

$$(f^k)_{lm} = \langle X_l^k | \mathbf{f}^k | X_m^k \rangle = \sum_t e^{i\mathbf{k}\cdot\mathbf{t}} \langle \chi_l^0 | \mathbf{f} | \chi_l^t \rangle = \sum_t e^{i\mathbf{k}\cdot\mathbf{t}} (f^t)_{lm} \quad 2.63$$

2.6.2 Dispersion

The same considerations we did about Grimme's corrections in the molecular case can be easily extended in the periodic case.⁶¹ For example, in the D2 case

$$E_{disp} = -s_6 \sum_{a=1}^{N_{at}-1} \sum_{b=a+1}^{N_{at}} \sum_t \frac{C_{6,ab}}{r_{ab,t}^6} f_{dmp}(r_{ab,t}) \quad 2.64$$

where the third summation runs on all the lattice vectors \mathbf{t} excluding the $a = b$ case for $\mathbf{t} = \mathbf{0}$ (self-interaction) and $r_{ab,t}$ is the distance between atom a in the reference cell and the atom b in all near cells at distance $|\mathbf{t}|$. Such a summation must be truncated: usually, a cut-off distance of 25.0 Å is chosen. The form of the damping function also must be modified

$$f_{dmp}(r_{ab,t}) = \left[1 + e^{-d\left(\frac{r_{ij,t}}{r_s} - 1\right)} \right]^{-1} \quad 2.65$$

2.7 Software

As within the context of this Thesis, we made use essentially of five computational codes, namely CRYSTAL17,⁶¹ CP2K,⁶² Gaussian09,⁶³ VASP (Vienna *ab initio* simulation package),^{64–66} GULP (general utility lattice program),⁶⁷ and LAMMPS (large-scale atomic/molecular massively parallel simulator).⁶⁸ In what follows, we provide a very short description of each code.

The CRYSTAL17 package can perform *ab initio* DFT and HF calculations of periodic (*e.g.*, crystals, surfaces, polymers) as well as non-periodic (*e.g.*, molecules, nanoparticles) systems. The wavefunction is expressed as a linear superposition of crystalline/molecular orbitals which in turn are expanded as linear superpositions of Gaussian-type basis set functions. Three most important features about CRYSTAL17 are: *i*) it is able to compute several electronic properties, like the electrostatic potential maps (very useful for the purposes of this work); *ii*) it fully exploits, if present, the crystalline/molecular symmetry; *iii*) it can be easily compiled on high-performance computing (HPC) architectures, thus medium- and large-sized system can be studied.

Gaussian09 is probably the most known and used QM code. As CRYSTAL17, it makes use of Gaussian-type basis sets, it fully exploits the molecular symmetry and it is able to compute several electronic properties, but unlike CRYSTAL17 it cannot perform periodic calculations and cannot be implemented on HPC architectures.

Unlike the two previous ones, the VASP code make use of plane-waves basis set coupled with pseudopotential. As CRYSTAL17, it can be easily compiled onto HPC architectures.

CP2K is a “hybrid” code which make use of a mixed Gaussian and plane wave BS to evaluate the wavefunction and the electron density, respectively. It can

perform standard *ab initio* (static and dynamic), semi-empirical but also classical calculations.

GULP is an FF-based code that is able to perform geometry optimizations frequency calculations and MDs of both periodic (3D) and molecular system. Being based on the MM framework, GULP calculations are quite fast even for sized systems

Finally, LAMMPS is an open-source program that makes use of message passing interface (MPI) and is dedicated to MD simulations.

As regards the structural modelling and the generation of the initial models, we resorted to different codes: the three most important ones are Moldraw,⁶⁹ VESTA,⁷⁰ and VMD (visual molecular dynamics).⁷¹

2.8 Computational details

In this Section, we shortly report all the computational details concerning the work we will discuss about in next Chapters. More details can be found in the published articles they refer to, *i.e.* Ref. 72, Ref. 73 and Ref. 74, respectively.

2.8.1 The CO/H₂O interface (Chapter 3)

2.8.1.1 Static calculations

All static calculations have been performed with the CRYSTAL17 code,⁶¹ adopting the PBE functional^{29,30} with the Grimme's D2 version for dispersive interactions,³⁸ along with the Ahlrichs VTZ basis set added with polarization functions (hereafter referred to as VTZ*⁷⁵).

Because of we are interested in fine results (*i.e.*, evidencing small differences of few cm^{-1} in the different CO/H₂O configurations), we resorted to a very accurate description of the electron density (through an extra-extra-large integration grid consisting in 99 radial and 1454 angular points) at which the Coulomb integrals are computed (10^{-8} hartree as a thresholds).⁶¹ As regards the reciprocal-space sampling, we adopted a shrink factor of 8, resulting in 14 to 260 k -points

depending on the symmetry of the system.⁶¹ SCF accuracy and geometry optimizations were carried out keeping CRYSTAL default parameters.

Hessian matrix elements have been evaluated through a 6-points formula accounting for two displacements for each atoms along $\pm x$, $\pm y$ and $\pm z$ directions from its equilibrium position,⁶¹ and IR intensities have been computed through the Barry-phase method.^{76,77} IR spectra have been simulated as linear superposition of Gaussian functions centred at the computed frequencies and with heights adjusted to the corresponding absolute IR intensities. The full width at half maximum (FWHM) is set equal to either 3 or 15 cm^{-1} , depending on the case.

2.8.1.2 *Dynamic calculations*

We performed AIMD simulations using the CP2K code.⁶² We run AIMD simulations in order to sample the complex conformational space with the aim to amorphize CO/H₂O ice mixtures. All AIMD simulations are performed at the PBE level,^{29,30} enriched by the D3 a posteriori Grimme correction for dispersive interactions.⁴⁵ A molecular optimized double- ζ BS was applied to all atoms together with the corresponding Goedecker-Teter-Hutter pseudopotential.⁷⁸ The parameters used for the AIMD simulations are: 0.5 fs for the time-step, 15 ps for the production time, Nose-Hoover thermostat at 300 K and 1 bar for the pressure.

2.8.1.3 *Interaction energies and frequencies*

The two main goals of this work about the CO/H₂O interface are: *i*) simulating the energetic of the interaction of the CO molecule(s) with different water ice matrices, namely the interaction energy and enthalpies at 0 K, and, *ii*) the vibrational wavenumbers of the adsorbed CO molecule.

The interaction energy of n molecules μ with a solid (bulk, surface, ...) S is defined by

$$\Delta E = E_{\text{P}}(S \cdots n\mu // S \cdots n\mu) - E_{\text{P}}(S // S) - nE_{\text{M}}(\mu // \mu) \quad \mathbf{2.66}$$

where $E_P(xy//xy)$ is the DFT (plus, eventually, dispersion) total energy for the xy species in the xy geometry computed using its basis set. The subscripts P and M stand for periodic and molecular calculations, respectively.

Equation **2.1** does not account for the deformation of both the solid model and the μ molecules. Such quantities can be evaluated by computing

$$\delta E_S = E_P(S//S \cdot n\mu) - E_P(S//S) \quad \mathbf{2.67}$$

$$\delta E_\mu = E_M(\mu//S \cdot n\mu) - nE_M(\mu//\mu) \quad \mathbf{2.68}$$

The *deformation-free* interaction energy ΔE^* is then defined as

$$\Delta E^* = E_P(S \cdot n\mu//S \cdot n\mu) - E_P(S//S \cdot n\mu) - E_P(\mu//S \cdot n\mu) \quad \mathbf{2.69}$$

As already stated in the *Computational details* Section, when Gaussian functions are used as BS, the BSSE arises.^{6,11} We corrected for BSSE by making use of the Counterpoise (CP) method by Boys & Bernardi,⁷⁹ which consists in using “ghost functions” in the following way

$$\text{BSSE}(S) = E_P(S \cdot [n\mu]//S \cdot n\mu) - E_P(S//S \cdot n\mu) \quad \mathbf{2.70}$$

$$\text{BSSE}(\mu) = E_P([S] \cdot n\mu//S \cdot n\mu) - E_P(\mu//S \cdot n\mu) \quad \mathbf{2.71}$$

$E_Z(x[y]//yx)$ is the energy of the x species, in presence of the ghost functions of the y one, computed in the fully optimized geometry of the complex xy .

The *deformation- & BSSE-free* interaction energy $\Delta E^\#$ is defined as

$$\Delta E^\# = E_P(S \cdot n\mu//S \cdot n\mu) - E_P(S \cdot [n\mu]//S \cdot n\mu) - E_P([S] \cdot n\mu//S \cdot n\mu) \quad \mathbf{2.72}$$

Finally, the correct expression for the interaction energy should also contain the *lateral interaction* E_L among the μ molecules in different replicas of the unit cell

$$E_L = E_P(\mu//S \cdot n\mu) - E_M(\mu//S \cdot n\mu) \quad \mathbf{2.73}$$

The *CP- & deformation-corrected* interaction energy *per* μ molecule is then

$$\Delta E^{\text{CP}} = \frac{\Delta E^* + \delta E + E_L - \text{BSSE}}{n} \quad 2.74$$

where $\delta E = \delta E_S + \delta E_\mu$, and $\text{BSSE} = \text{BSSE}(S) + \text{BSSE}(\mu)$ are the *total deformation* and the *total BSSE* contributions, respectively.

According to Equation 2.49, we computed the enthalpy variations at 0 K for the CO/H₂O ice interactions from

$$\Delta H(0) = \Delta H = \Delta E^{\text{CP}} + \Delta E_{\text{ZP}} \quad 2.75$$

where ΔE_{ZP} is also normalized to the number of molecules n .

2.8.2 Olivine nanoparticles (Chapter 5)

2.8.2.1 QM calculations

For the QM modelling, we used the CRYSTAL17. All calculations were performed within the DFT framework, using the Perdew-Burke-Ernzerhof (PBE) functional,⁸⁰ and a specific basis set consisting of the following contraction: (8s)-(61sp), (6s)-(6211sp)-(1d) and (6s)-(31sp)-(1d) for the Mg, Si and O atoms, respectively. In the following, we will refer at this basis set as ‘‘OIBS’’.

Default thresholds parameters were adopted for all energy calculations, geometry optimizations and IR frequency and intensity calculations. To evaluate the electron density, we used a pruned (75, 974) grid, consisting of 75 radial points and a maximum number of 974 angular points. At these points, Coulomb and exchange integrals were computed. All other technical details regarding these DFT calculations are reported in the SI file.

2.8.2.2 CM calculations

We used the CM-based GULP code to perform the preliminary optimizations of bulk cut NPs, to amorphize the PBE-optimized nanoparticles through MD simulations, and to simulate IR spectra for all NPs. Specifically, for some preliminary optimizations, we used the general Reax FF,^{48,81} while for all other

GULP calculations we used the FF used by Walker *et al.*,⁸² which is based on previously reported FFs developed by Price *et al.*⁸³ and Catlow *et al.*⁴⁷ All the parameters controlling the numerical accuracy of the GULP calculations were kept constant to default values. For geometric optimizations, we used either the standard Broyden-Fletcher-Goldfarb-Shanno (BFGS) algorithm or, when necessary, the Rational Function Optimization (RFO) algorithm.^{84,85} IR intensities were computed from the Born effective charge tensor.⁸⁶ All MD simulations used in the amorphization of bulk cut NPs were performed at either 1800 or 2400 K within the canonical ensemble (NVT) using a 1 fs timestep and with initial velocities randomly generated at 800 K.

For preparing the nucleated NPs we used MD-based simulations using the CM-based LAMMPS code.⁶⁸ Here we progressively built NPs by addition of monomeric species (SiO, O and Mg) following the heteromolecular homogeneous nucleation route proposed by Goumans & Bromley.⁸⁷ Each monomeric addition step was performed within the microcanonical ensemble (NVE) with a timestep of 0.5 fs and using the Berendsen thermostat to maintain the temperature between 1000-800 K, typical for dust nucleation in circumstellar environments.

Bibliography

- (1) Schrödinger, E. Quantisierung Als Eigenwertproblem. *Ann. Phys.* **1926**, *13*, 437–490.
- (2) Levine, I. N. *Quantum Chemistry*; Pearson: London, England, UK, 1970.
- (3) Cohen-Tannoudji, C.; Diu, B.; Laloe, F. *Quantum Mechanics*; Wiley-VCH: Weinheim, Germany, 1977.
- (4) Born, M.; Oppenheimer, R. Zur Quantentheorie Der Molekeln. *Ann. Phys.* **1927**, *389*, 457–484.
- (5) Dirac, P. A. M. A New Notation for Quantum Mechanics. *Math. Proc. Cambridge Philos. Soc.* **1939**, *35*, 416–418.
- (6) Jensen, F. *Introduction to Computational Chemistry*; Wiley: West Sussex, England, UK, 2007.
- (7) Cramer, C. J. *Essentials of Computational Chemistry*; Wiley: West Sussex, England, UK, 2004.
- (8) Pauli, W. Über Den Zusammenhang Des Abschlusses Der Elektronengruppen Im Atom Mit Der Komplexstruktur Der Spektren. *Zeitschrift für Phys.* **1925**, *31*, 765–783.
- (9) Slater, J. C. The Theory of Complex Spectra. *Phys. Rev.* **1929**, *34*, 1293–1322.
- (10) Hellmann, H. A New Approximation Method in the Problem of Many Electrons. *J. Chem. Phys.* **1935**, *3*, 61.
- (11) Cramer, C. J.; Truhlar, D. G. Density Functional Theory for Transition Metals and Transition Metal Chemistry. *Phys. Chem. Chem. Phys.* **2009**, *11*, 10757–10816.
- (12) Liu, B.; Mclean, A. D. Accurate Calculation of the Attractive Interaction of Two Ground State Helium Atoms. *J. Chem. Phys.* **1973**, *59*, 4557–4558.
- (13) Davidson, E. R.; Feller, D. Basis Set Selection for Molecular Calculations. *Chem. Rev.* **1986**, *86*, 681–696.
- (14) Ditchfield, R.; Hehre, W. J.; Pople, J. A. Self-Consistent Molecular-Orbital

- Methods. IX. An Extended Gaussian-Type Basis for Molecular-Orbital Studies of Organic Molecules. *J. Chem. Phys.* **1971**, *54*, 724–728.
- (15) Dunning, T. H. Gaussian Basis Sets for Use in Correlated Molecular Calculations. I. The Atoms Boron through Neon and Hydrogen. *J. Chem. Phys.* **1989**, *90*, 1007–1923.
- (16) Hartree, D. R. The Wave Mechanics of an Atom with a Non-Coulomb Central Field. Part I. Theory and Methods. *Math. Proc. Cambridge Philos. Soc.* **1927**, *24*, 89–110.
- (17) Hartree, D. R. The Wave Mechanics of an Atom with a Non-Coulomb Central Field. Part II. Some Results and Discussion. *Math. Proc. Cambridge Philos. Soc.* **1927**, *24*, 111–132.
- (18) Hartree, D. R. The Wave Mechanics of an Atom with a Non-Coulomb Central Field. Part III. Term Values and Intensities in Series in Optical Spectra. *Math. Proc. Cambridge Philos. Soc.* **1928**, *24*, 426–437.
- (19) Hartree, D. R. The Wave Mechanics of an Atom with a Non-Coulomb Central Field. Part IV. Further Results Relating to Terms of the Optical Spectrum. *Math. Proc. Cambridge Philos. Soc.* **1930**, *24*, 310–314.
- (20) Fock, V. Näherungsmethode Zur Lösung Des Quantenmechanischen Mehrkörper-Problems. *Zeitschrift für Phys.* **1930**, *61*, 126–148.
- (21) Roothaan, C. C. J. New Developments in Molecular Orbital Theory. *Rev. Mod. Phys.* **1951**, *23*, 69–89.
- (22) Hall, G. G. The Molecular Orbital Theory of Chemical Valency. VIII. A Method of Calculating Ionization Potentials. *Proc. R. Soc. Lond.* **1951**, *205*, 541–552.
- (23) Kato, T. On the Eigenfunctions of Many-Particle Systems in Quantum Mechanics. *Commun. Pure Appl. Math.* **1957**, *10*, 151–177.
- (24) Hohenberg, P.; Kohn, W. Inhomogeneous Electron Gas. *Phys. Rev.* **1964**, *136*, B864–B871.
- (25) Kohn, W.; Sham, L. J. Self-Consistent Equations Including Exchange and

- Correlation Effects. *Phys. Rev.* **1965**, *140*, A1133–A1138.
- (26) Perdew, J. P.; Ruzsinszky, A.; Tao, J.; Staroverov, V. N.; Scuseria, G. E.; Csonka, G. I. Prescription for the Design and Selection of Density Functional Approximations: More Constraint Satisfaction with Fewer Fits. *J. Chem. Phys.* **2005**, *123*, 062201 (9 pp).
- (27) Thomas, L. H. The Calculation of Atomic Fields. *Math. Proc. Cambridge Philos. Soc.* **1927**, *23*, 542–548.
- (28) Fermi, E. Eine Statistische Methode Zur Bestimmung Einiger Eigenschaften Des Atoms Und Ihre Anwendung Auf Die Theorie Des Periodischen Systems Der Elemente. *Zeitschrift für Phys.* **1926**, *36*, 73–79.
- (29) Perdew, J. P.; Burke, K.; Ernzerhof, M. Local and Gradient-Corrected Density Functionals Density Functionals in Quantum Chemistry Decompositions of E. *Symp. A Q. J. Mod. Foreign Lit.* **1996**, 453–462.
- (30) Perdew, J. P.; Burke, K.; Wang, Y. Generalized Gradient Approximation for the Exchange-Correlation Hole of a Many-Electron System. *Phys. Rev. B* **1996**, *54*, 16533–16539.
- (31) Perdew, J. P. Density-Functional Approximation for the Correlation Energy of the Inhomogeneous Electron Gas. *Phys. Rev. B* **1986**, *33*, 8822–8824.
- (32) Becke, A. D. Density-Functional Thermochemistry. III. The Role of Exact Exchange. *J. Chem. Phys.* **1993**, *98*, 5648–5652.
- (33) Perdew, J. P.; Ernzerhof, M.; Burke, K. Rationale for Mixing Exact Exchange with Density Functional Approximations. *J. Phys. Chem.* **1996**, *105*, 9982–9985.
- (34) Becke, A. D. A New Mixing of Hartree-Fock and Local-Density-Functional Theories. *J. Chem. Phys.* **1993**, *98*, 1372–1377.
- (35) Becke, A. D. Density-Functional Exchange-Energy Approximation with Correct Asymptotic Behavior. *Phys. Rev. A* **1988**, *38*, 3098–3100.
- (36) Lee, C.; Yang, W.; Parr, R. G. Development of the Colle-Salvetti

- Correlation-Energy Formula into a Functional of the Electron Density. *Phys. Rev. B* **1988**, *37*, 785–789.
- (37) Grimme, S. Accurate Description of van Der Waals Complexes by Density Functional Theory Including Empirical Corrections. *J. Comput. Chem.* **2004**, *25*, 1463–1473.
- (38) Grimme, S. Semiempirical GGA-Type Density Functional Constructed with a Long-Range Dispersion Correction. *J. Comput. Chem.* **2006**, *27*, 1787–1799.
- (39) Johnson, E. R.; Becke, A. D. A Post-Hartree-Fock Model of Intermolecular Interactions. *J. Chem. Phys.* **2005**, *123*, 024101 (7 pp).
- (40) Johnson, E. R.; Becke, A. D. A Post-Hartree-Fock Model of Intermolecular Interactions: Inclusion of Higher-Order Corrections. *J. Chem. Phys.* **2006**, *124*, 174104 (9 pp).
- (41) Becke, A. D.; Johnson, E. R. A Density-Functional Model of the Dispersion Interaction. *J. Chem. Phys.* **2005**, *123*, 154101 (9 pp).
- (42) Becke, A. D.; Johnson, E. R. Exchange-Hole Dipole Moment and the Dispersion Interaction Revisited: High Order Dispersion Coefficients. *J. Chem. Phys.* **2006**, *127*, 014104 (6 pp).
- (43) Grimme, S.; Ehrlich, S.; Goerigk, L. Effect of the Damping Function in Dispersion Corrected Density Functional Theory. *J. Comput. Chem.* **2011**, *32*, 1456–1465.
- (44) Wu, Q.; Yang, W. Empirical Correction to Density Functional Theory for van Der Waals Interactions. *J. Chem. Phys.* **2002**, *116*, 515–524.
- (45) Grimme, S.; Antony, J.; Ehrlich, S.; Krieg, H. A Consistent and Accurate Ab Initio Parametrization of Density Functional Dispersion Correction (DFT-D) for the 94 Elements H-Pu. *J. Chem. Phys.* **2010**, *132*, 154104 (19 pp).
- (46) Allinger, N. L. Force Fields: A Brief Introduction. In *Encyclopedia of Computational Chemistry*; John Wiley and Sons: Hoboken, NJ, USA,

- 2002.
- (47) Catlow, C. R. A.; Price, G. D. Computer Modelling of Solid-State Inorganic Materials. *Nature* **1990**, *347*, 243–247.
- (48) van Duin, A. C. T.; Dasgupta, S.; Lorant, F.; Goddard III, W. A. ReaxFF: A Reactive Force Field for Hydrocarbons. *J. Phys. Chem. A* **2001**, *105*, 9396–9409.
- (49) Rappé, A. K.; Casewit, C. J.; Colwell, K. S.; Goddard III, W. A.; Skid, W. M. UFF, a Full Periodic Table Force Field for Molecular Mechanics and Molecular Dynamics Simulations. *J. Ameical Chem. Soc.* **1992**, *114*, 10024–10035.
- (50) Broyden, C. G. The Convergence of a Class of Double-Rank Minimization Algorithms. *J. Inst. Math. Its Appl.* **1970**, *6*, 76–90.
- (51) Fletcher, R. A New Approach to Variable Metric Algorithms. *Comput. J.* **1970**, *13*, 317–322.
- (52) Goldfarb, D. A Family of Variable Metric Updates Derived by Variational Means. *Math. Comput.* **1970**, *24*, 23–26.
- (53) Shanno, D. F. Conditioning of Quasi-Newton Methods for Function Minimization. *Math. Comput.* **1970**, *24*, 647–656.
- (54) McQuarrie, D. A.; Simon, J. D. *Physical Chemistry. A Molecular Approach*; University Science Books: Sausalito, CA, USA, 1997.
- (55) McQuarrie, D. A. *Statistical Mechanics*; University Science Books: Sausalito, CA, USA, 2000.
- (56) Atkins, P.; de Paula, J. *Physical Chemistry*; Oxford University Press: Oxford, England, UK, 2006.
- (57) Alder, B. J.; Wainwright, T. E. Studies in Molecular Dynamics. I. General Method. *J. Chem. Phys.* **1959**, *31*, 459–466.
- (58) Car, R.; Parrinello, M. Unified Approach for Molecular Dynamics and Density-Functional Theory. *Phys. Rev. Lett.* **1985**, *55*, 2471–2474.
- (59) Bloch, F. Uber Die Quantenmechanik Der Elektronen in Kristallgittern.

- Zeitschrift für Phys.* **1929**, 52, 555–600.
- (60) Pack, J. D.; Monkhorst, H. J. Special Points for Brillouin-Zone Integrations. *Phys. Rev. B* **1977**, 13, 5188–5192.
- (61) Dovesi, R.; Saunders, V. R.; Roetti, C.; Orlando, R.; Pascale, F.; Civalleri, B.; Doll, K.; Harrison, N. M.; Bush, I. J.; D’Arco, P.; *et al.* CRYSTAL17. User’s Manual. 2018.
- (62) Kohlmeyer, A.; Mundy, C. J.; Mohamed, F.; Schiffmann, F.; Tabacchi, G.; Forbert, H.; Kuo, W.; Hutter, J.; Krack, M.; Iannuzzi, M. CP2K. 2013.
- (63) Frisch, M. J.; Trucks, G. W.; Schlegel, H. B.; Scuseria, G. E.; Robb, M. A.; Cheeseman, J. R.; Scalmani, G.; Barone, V.; Petersson, G. A.; Nakatsuji, H.; *et al.* Gaussian09. Gaussian, Inc.: Wallingford, CT, USA 2009.
- (64) Kresse, G.; Furthmüller, J. Efficiency of Ab-Initio Total Energy Calculations for Metals and Semiconductors. *Comput. Mater. Sci.* **1996**, 6, 15–20.
- (65) Kresse, G.; Furthmüller, J. Efficient Iterative Schemes for Ab Initio Total-Energy Calculations Using a Plane-Wave Basis Set. *Phys. Rev. B* **1996**, 54, 11169–11186.
- (66) Kresse, G.; Marsman, M.; Furthmüller, J. VASP On-Line Manual. <https://www.vasp.at/index.php/documentation>.
- (67) Gale, J. D. GULP - A Computer Program for the Symmetry Adapted Simulation of Solids. *J. Chem. Soc. Faraday Trans* **1997**, 93, 629.
- (68) Plimpton, S. Fast Parallel Algorithms for Short-Range Molecular Dynamics. *J. Comput. Phys.* **1995**, 117, 1–19.
- (69) Ugliengo, P.; Viterbo, D.; Chiari, G. MOLDRAW: Molecular Graphics on a Personal Computer. *Zeitschrift für Krist.* **1993**, 207, 9–23.
- (70) Momma, K.; Izumi, F. VESTA 3 for Three-Dimensional Visualization of Crystal, Volumetric and Morphology Data. *J. Appl. Crystallogr.* **2011**, 44, 1272–1276.
- (71) Humphrey, W.; Dalke, A.; Schulten, K. VMD - Visual Molecular

- Dynamics. *J. Mol. Graph.* **1996**, *14*, 33–38.
- (72) Zamirri, L.; Casassa, S.; Rimola, A.; Segado-Centellas, M.; Ceccarelli, C.; Ugliengo, P. IR Spectral Fingerprint of Carbon Monoxide in Interstellar Water Ice Models. *Mon. Not. R. Astron. Soc.* **2018**, *480*, 1427–1444.
- (73) Zamirri, L.; Ugliengo, P.; Ceccarelli, C.; Rimola, A.; Interfaces, N.; Centre, S. N. I. S.; Giuria, P. Quantum Mechanical Investigations on the Formation of Complex Organic Molecules on Interstellar Ice Mantles . Review and Perspectives. *ACS Earth Sp. Chem.* **2019**, *3*, 1499–1523.
- (74) Zamirri, L.; Macià Escatllar, A.; Marinoso Guiu, J.; Ugliengo, P.; Bromley, S. T. What Can Infrared Spectra Tell Us about the Crystallinity of Nanosized Interstellar Silicate Dust Grains? *ACS Earth Sp. Chem.* **2019**, *3*, 2323–2338.
- (75) Schäfer, A.; Horn, H.; Ahlrichs, R. Fully Optimized Contracted Gaussian-Basis Sets for Atoms Li to Kr. *J. Chem. Phys.* **1992**, *97*, 2571–2577.
- (76) Dall’Olio, S.; Dovesi, R.; Resta, R. Spontaneous Polarization as a Berry Phase of the Hartree-Fock Wave Function: The Case of KNbO_3 . *Phys. Rev. B* **1997**, *56*, 10105–10114.
- (77) Noël, Y.; Zicovich-Wilson, C. M.; Civalleri, B.; D’Arco, P.; Dovesi, R. Polarization Properties of ZnO and BeO: An Ab Initio Study through the Berry Phase and Wannier Functions Approaches. *Phys. Rev. B* **2001**, *65*, 0141 (11-20).
- (78) VandeVondele, J.; Krack, M.; Mohamed, F.; Parrinello, M.; Chassaing, T.; Hutter, J. QUICKSTEP: Fast and Accurate Density Functional Calculations Using a Mixed Gaussian and Plane Waves Approach. *Comput. Phys. Commun.* **2005**, *167*, 103–128.
- (79) Boys, S. F.; Bernardi, F. The Calculation of Small Molecular Interactions by the Differences of Separate Total Energies. Some Procedures with Reduced Errors. *Mol. Phys.* **1970**, *19*, 553–566.
- (80) Perdew, J. P.; Burke, K.; Ernzerhof, M. Generalized Gradient

- Approximation Made Simple. *Phys. Rev. Lett.* **1996**, *77*, 3865–3868.
- (81) Gale, J. D.; Raiteri, P.; van Duin, A. . T. C. A Reactive Force Field for Aqueous-Calcium Carbonate Systems. *Phys. Chem. Chem. Phys.* **2011**, *13*, 16666–16679.
- (82) Walker, A. M.; Wright, K.; Slater, B. A Computational Study of Oxygen Diffusion in Olivine. *Phys. Chem. Miner.* **2003**, *30*, 536–545.
- (83) Price, G. D.; Parker, S. C.; Leslie, M. The Lattice Dynamics and Thermodynamics of the Mg₂SiO₄ Polymorphs. *Phys. Chem. Miner.* **1987**, *15*, 181–190.
- (84) Simons, J.; Joergensen, P.; Taylor, H.; Ozment, J. Walking on Potential Energy Surfaces. *J. Phys. Chem.* **1983**, *87*, 2745–2753.
- (85) Banerjee, A.; Adams, N.; Simons, J.; Shepard, R. Search for Stationary Points on Surfaces. *J. Phys. Chem.* **1985**, *89*, 52–57.
- (86) Baroni, S.; de Gironcoli, S.; dal Corso, A.; Giannozzi, P. Phonons and Related Crystal Properties from Density-Functional Perturbation Theory. *Rev. Mod. Phys.* **2001**, *73*, 515–562.
- (87) Goumans, T. P. M.; Bromley, S. T. Efficient Nucleation of Stardust Silicates via Heteromolecular Homogeneous Condensation. *Mon. Not. R. Astron. Soc.* **2012**, *420*, 3344–3349.

3 *Ice mantles structure: the CO/H₂O interface*

Extended abstract

Context

Carbon monoxide (CO) is the second most abundant molecule in the gas phase of the interstellar medium. In dense molecular clouds, it is also present in the solid phase as a constituent of the mixed water (H₂O)-dominated ices covering dust grains. Its presence in the solid phase is inferred from its IR signal. In experimental observations of solid CO/H₂O mixed samples, its IR frequency splits into two components, one blue- and the other a red-shifted with respect to the gas phase signal. However, in astronomical observations, the former has never been observed. Several attempts have been carried out to explain this peculiar behaviour, but the question still remains open (Section 3.1).

Adopted strategy

To shed some light on this unmatching between observations and experiments, we adopted two different periodic crystalline and proton ordered water ice models, namely the so-called P- and C-ice, together with two different clathrates models to simulate the eventual engagement of CO (Section 3.2). Because of water and CO freeze in different moments and ways onto the surface of silicate dust grains, it is likely that aggregates of pure CO might form under dense ISM conditions. Therefore, in Section 3.3.1 we report our results about the modelling of pure CO systems, namely gas phase and solid α -CO. Both structural and vibrational computed values are in good agreement with experimental data, even though some negligible discrepancies were outlined (**Table 3.2**).

CO at the crystalline ice surfaces: low coverage

In Section 3.3.2, we show the fundamental aspects of the CO/H₂O ice interaction for the simplest system involving CO and the water ice, *i.e.* one CO molecule adsorbed on two perfect crystalline surfaces of P-ice. CO was initially adsorbed on dangling hydrogen by either its C and O ends, but only the C-involving interaction (formation of an H-bond), that is the most energetically favoured and produces a quite strong blue-shift of about 15 cm⁻¹, is preserved during the optimization. On the contrary, the O-involving interaction which produces a large red-shift is overcome by non-specific dispersive and quadrupolar

forces (**Figure 3.3**). These results clearly outline how CO is not likely to interact with a water ice through its O atom – at least in absence of any structural constrain – and that the blueshifted peak in experimental spectra can be explained by the HOH··CO interaction.

CO at the crystalline ice surfaces: high coverage

The next step in CO adsorption is the formation of multilayers on top of the water ice. We investigate this situation in Section 3.3.3. As for the previous case, CO molecules involved in H-bonds through their C atoms give blue-shifts of about 15 cm⁻¹ while COs interacting *via* quadrupolar interactions produce quite large red-shifts. However, the CO molecules of the outermost layers only show very little blue- and red-shifts, electing them as possible carriers of the interstellar solid CO features (**Figure 3.4**).

CO entrapped in ice cages

In Section 3.3.4, we report an extensive investigation of CO molecules entrapped in different cages (**Figure 3.5**). Results indicate that their stretching can be either slightly red- and blue-shifted, opening for their presence in interstellar ices. We also excluded the eventuality of substitutional CO, *i.e.* CO substituting one water molecule in the ice matrix, because the water molecules do rather prefer to interact among themselves through a complex network of H-bonds. This fact well highlights one typical feature of CO that we called “hydrophobicity” since, when present in mixtures with CO, the water molecules tend to arrange themselves so that forming cages that closely resemble those from clathrates.

CO within a model of amorphous ice

So far, we only discussed about static calculations and, therefore, to configurations that can be reached without overcoming any energy barrier. However, in Section 3.3.5, we show some results from AIMD simulations on a proper CO/H₂O ice mixture. This is a complex model where different situations are present at the same time, *i.e.* “island” of pure CO, CO involved in H-bonds as well as entrapped in water cages. These AIMD simulations was performed for 15 ps as we show that this is sufficient to achieve a proper mixture, at least from a spectroscopic viewpoint (**Figure 3.7**).

Simulation of the CO vibrational spectrum

The results we discussed about so far concern just one single situation at a time. However, CO in interstellar ices is probably involved in a variety of situations, and the signal we get comprises for all these situations. To compare with observations, in Section 3.3.6 we merge all our spectroscopic results in just one single, overall spectrum (**Figure 3.9**). The comparison with observations is in good agreement, even though our simulated data still show some strongly blue-shifted peaks. We explain the lack of these features in interstellar ices by invoking a statistical explanation: indeed, strong blue-shifts derive only from very specific interactions with certain exposed sites of the water matrix. It is likely that these interactions, if present, might be overshadowed in the final spectrum dominated by signals from CO involved in all other configurations. Moreover, blue-shifted stretching modes are predicted to be less intense than the red-shifted ones.

Some conclusive remarks

From a pure energetic point of view, our results indicate how CO is only physisorbed to the water ice matrix. Indeed, the enthalpy values fall in a $\sim 5\text{--}18$ kJ mol⁻¹ range and, therefore, weak interactions such as dispersive and quadrupolar ones are prominent. Our data can be compared with those usually inferred from classical thermal programmed desorption (TPD) experiments, where different monolayers (MLs) of CO are initially adsorbed onto selected surfaces, such as water ice ones, and then desorbed. Referring to Smith *et al.*,¹ the desorption energies for CO adsorbed on amorphous solid water at very low coverages (< 0.05 ML) are slightly greater than 15 kJ mol⁻¹, in good agreement with our computed ΔH values for DH cases, in particular the DH·CO ones of Section 3.3.2. On the opposite side, the desorption energies for two monolayers can be derived to be approximately equal to 7 kJ mol⁻¹, to be compared with our “interface” models (~ 5 kJ mol⁻¹, **Table 3.3**) in Section 3.3.3. However, please note that a proper comparison cannot be performed because of the lack of a generic definition of monolayer, both from an experimental and computational point of view.

In the following, we extensively treat all the above-mentioned points. For even further details, please refer to Ref. 2.

3.1 Background

In IR observations, gas phase CO is detected at 2143 cm⁻¹ (4.666 μm) due to its C–O stretching mode.³ Therefore, the analysis of the ISM spectra focuses on the splitting and shifts of this signal towards lower (red) or higher (blue) frequencies. Thus, before any investigation, an overview of the detected IR signals for CO/H₂O systems along with their interpretations is done here.

As already mentioned in the “Concluding remarks” of the *Introduction*, the configuration assumed by CO in its solid interface with water may affect different astrophysical processes.^{4–6} At least two rather different ice structures are supposed to be present in the ISM, referred to as the mixed *apolar* and the layered *polar* phase.⁷ In order to reproduce both, as well as their interaction with carbon monoxide, different experimental settings and computational simulations have been performed over the years.

CO experimentally co-deposited in water matrices at low temperatures, as a model of the apolar phase, presents a very peculiar band profile consisting of two main broad features (**Figure 3.1**, left panel): *i*) an intense peak at 2138 cm⁻¹ (4.677 μm), red-shifted with respect to the gas phase and indicating a decreasing of the bond strength (and a corresponding increasing of the C–O bond length), and *ii*) a secondary, less intense, blue-shifted peak at 2152 cm⁻¹ (4.647 μm) corresponding to a shortening/increasing of the bond length/strength. This two-peaks profile has been noted and discussed by many authors.^{8–12}

According to Sandford *et al.*¹² and Jenniskens *et al.*,¹³ the 2138 cm⁻¹ band is due to substitutional CO molecules, *i.e.* CO replacing H₂O lattice molecules, while the 2152 cm⁻¹ band is caused by interstitial CO, *i.e.* CO inside H₂O cages. An alternative interpretation attributes the 2152 cm⁻¹ peak to CO molecules interacting with the –OH dangling groups,^{14,15} hereafter referred to as DH sites, while the 2138 cm⁻¹ is assigned to CO diffused into micropores.⁸

Interstellar H₂O ice is believed to be predominantly amorphous,^{16–19} although its specific morphology remains an open question when referring to its porosity.²⁰ To investigate on the possibility of CO migrating into ice lattice, Al-Halabi and co-workers studied the interaction of CO with amorphous ice by means of classical trajectory calculations and concluded that CO neither penetrate into the ice slab matrix nor diffuse into the surface valley.²¹ The eventuality of CO diffusion appears as a temperature effect:⁸ when ice is warmed up to 30 K, CO mainly desorbs but few molecules are trapped in the H₂O porous structure giving rise to a narrowing of the band at 2138 cm⁻¹ related to CO in water matrix. At temperatures higher than 80 K, the disappearance of the peak at 2152 cm⁻¹ indicates that the DH·CO interaction is lost. Interestingly, the annealing process of CO-rich ices produces a family of new adsorption features, at 2143 cm⁻¹, that have been tentatively associated with the formation of clathrate-like structures.¹²

The CO-layered polar binary system, although prepared following different experimental procedures and theoretical models, presents almost the same spectroscopic pattern (**Figure 3.1**, left panel). At low CO coverage, it can be seen as a gas/surface interaction. When CO concentration increases, a CO/H₂O interface appears, and a layered CO structure starts to grow. To characterize this system, Allouche *et al.*²² performed a combined experimental and computational study of CO adsorption on ice surfaces.²² They measured an adsorption enthalpy of about 10 kJ mol⁻¹, and unambiguously assigned the peak at 2152 cm⁻¹ to CO interacting with DH sites. In the context of this tendency toward a long-range crystalline order, the peak at 2143 cm⁻¹ has been assigned to the adsorption of linearly polarized light in the CO ice phase, which starts to crystallize as the temperature increases.²³ Finally, two combined effects are supposed to give rise to a family of features at 2139–2136 cm⁻¹: CO/CO interactions inside the rising CO multilayer as well as interactions involving dangling O atoms (DO) of the

exposed water molecules occurring at the CO/H₂O interface.²⁴ This band narrows as the temperature increases, due to the progressive CO desorption.²⁵

While nowadays there is a currently general agreement as regards the peak at 2152 cm⁻¹, present both in the apolar mixture and the hydrogenated ice surfaces, and assigned to CO adsorbed on DH sites through its carbon atom, the nature of the 2143 and 2139-2136 cm⁻¹ peaks still remains controversial. Rather surprisingly, the 2152 cm⁻¹ signal has never been observed in any interstellar spectra (**Figure 3.1**, right panel),^{7,9,20,25} while signals around 2143 cm⁻¹ appear as a prominent shoulder of the main red-shifted features at 2138 cm⁻¹.

As it is clear from this brief dissertation, some aspects of this important astrochemical problem still require a comprehensive explanation (in **Table 3.1** we shortly resume some of the proposed assignments), also because most of the works we cited adopted different experimental and computational strategies to derive some conclusions. Therefore, we decided to explore all the possible CO/H₂O interfaces at the same (robust) DFT level of theory, adopting different *periodic* models for the water ice matrix and simulating the absorption of CO in different atomistic environments. We hope that this will help astronomers to clarify some important features about this topic, at least as regards the punctual CO/H₂O ice interaction.

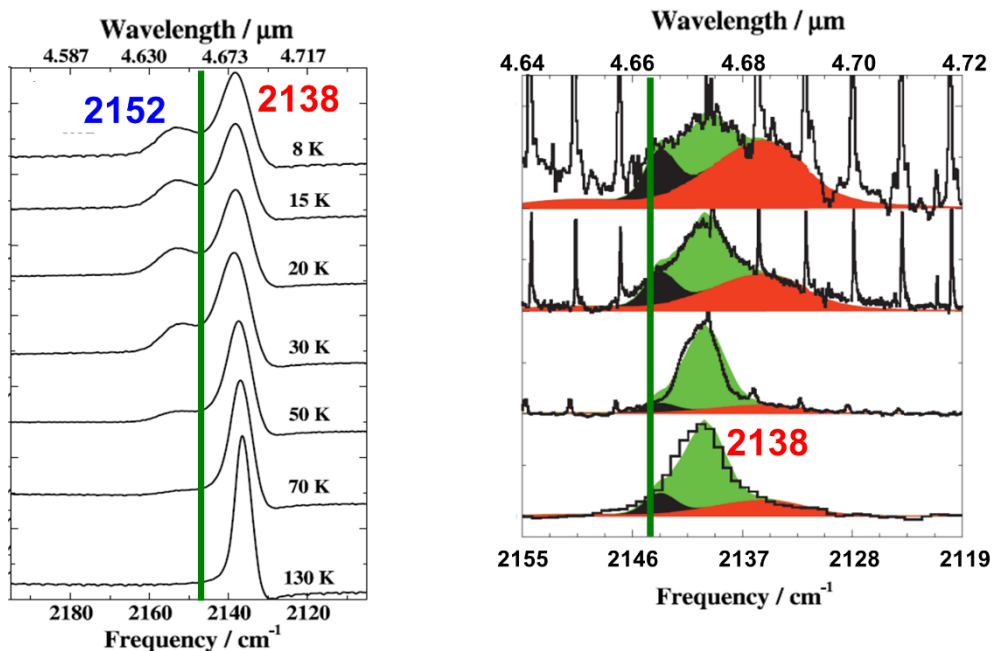


Figure 3.1 IR spectra for the CO/H₂O interface. Left: from experimental co-deposition of CO and water (picture adapted from Ref. 9). Right: from direct observations of the dense ISM (picture adapted from Ref. 7). In both panels, we highlighted the 2143 cm⁻¹ signal of gas phase CO (green line), as well as the presence of the blue- (2152 cm⁻¹) and red- (2138 cm⁻¹) shifted main peaks.

Table 3.1 Resume of some CO/H₂O signals assignments. Adapted from Ref. 21.

Wavenumber (cm ⁻¹)	Assignment	Configuration	Observed?
<i>Apolar phase</i>			
2152	CO in H ₂ O	- Interstitial CO ^a - DH··CO	No
2138-2136	CO in H ₂ O	Substitutional CO ^{a,#}	Only at 2136 cm ⁻¹
<i>Polar phase</i>			
2152	CO/H ₂ O interface	DH··CO ^b	No
2143	CO-CO interactions	LO component of LO-TO splitting ^c	Yes
2139	CO-CO interactions for layer of CO on H ₂ O	CO-OC-CO ^d	Yes
2139	CO/H ₂ O interface	CO interacting with bonded OH ^e	?*
2136	CO in H ₂ O	? [#]	Yes

Molecular configuration of the binding site still not resolved.

* Overwhelmed by pure CO 2139 cm⁻¹ band.

References: a) Sandford *et al.*¹² b) Collings *et al.*¹⁵, Manca *et al.*²⁴, Martin *et al.*²⁶
c) Collings *et al.*⁹ d) Ewing & Pimentel.²⁷ e) Al-Halabi *et al.*²¹

3.2 Ice models and scaled shifts

We are well aware that interstellar ices are likely to be highly amorphous and (partially?) porous. However, simulating amorphous systems is a non-trivial and highly subjective operation from a computational point of view. Keeping this in mind, we adopted two different 3D periodic models of ice to simulate crystalline ice phases, stable at low temperature and pressure (*i.e.* in ISM-like conditions): *i*) the ordinary hexagonal ice *Ih*, and *ii*) the orthorhombic proton-ordered polar ice XI (space group *Cmc2₁*) or *C-ice*. We modelled *Ih* ice with periodic (long-range ordered) structures belonging to the *Pna2₁* space group, usually referred to as *P-ice*, with a unit cell providing a variety of configurations to describe the local proton disorder.²⁸

Specifically, we selected *P-ice* to model ice surfaces, by means of 2D periodic slabs, because it has local disorder, yet forms a simple (001) and (010) surfaces with no dipole component perpendicular to them, and essentially no dipole component parallel to them either.²⁸

Bulk *P-ice* was also used to simulate cages (as a single and 2x2x2 supercell) as well as to simulate a proper mixed ice system (1x1x2 supercell). Cages were also simulated by means of clathrate structures (namely, *sI* and *sIII*) and of a 2x2x2 *C-ice* supercell.

For all these models, we computed the energetics of the interaction/adsorption according to Equations 2.66-2.75. To characterize the nature of the optimized geometries, we computed the CO stretching frequencies only, considered as fragments of the whole systems (this strategy has been already tested and adopted in several previous work,²⁹⁻³¹ and is fully justified by the weak-bound nature of

the CO/H₂O ice complexes). To recover the error associated with the adopted methods, and to partially account for anharmonic effects, we scaled all the computed IR CO-stretching frequencies by a scaling factor s defined as the ratio between the experimental (2143 cm⁻¹) and the computed ($\bar{\nu}_{comp}$) gas phase CO-stretching frequencies:

$$s = \frac{2143 \text{ cm}^{-1}}{\bar{\nu}_{comp,gas}} \quad 2.1$$

Consequently, we defined the *vibrational shifts* ($\Delta\bar{\nu}$) simply as the differences in wavenumber between the computed stretching frequency for the interacting CO molecules ($\bar{\nu}_{comp,solid}$, scaled by the s factor) and 2143 cm⁻¹, *i.e.*:

$$\Delta\bar{\nu} = \bar{\nu} - 2143 = s \cdot \bar{\nu}_{comp,solid} - 2143 \quad 2.2$$

3.3 CO/H₂O interactions

In the following, we will present the results concerning the various CO/H₂O ice interactions we tested in a short way. The energetic and vibrational data for all models are resumed in **Table 3.3**.

3.3.1 Pure CO

In order to have a complete description of CO/H₂O ice interaction, we need to introduce the fundamental energetic and vibrational features of pure CO systems that can be encountered under ISM conditions, *i.e.* gas and solid phase CO.

Gas phase CO possesses a small electric dipole moment μ_E of 0.122 D oriented as C(δ^-)→O(δ^+).³² Within our adopted computational scheme, CO dipole moment has the correct orientation, even if the module is slightly overestimated (0.196 D, **Table 3.2**). Despite its dipole, from an electrostatic point of view, CO must be considered as a quadrupolar molecule (see its ESP map **Figure 3.1**) due to its large electric quadrupole moment.³³ This quadrupole moment exerts a

fundamental role in determining its adsorption properties.^{29,30} The value of the zz (Q_{zz}) component of the quadrupole, computed at PBE/VTZ* level, is -1.49 D \AA , to be compared with the experimental value of -2.63 D \AA .³⁴

In order to highlight the importance of quadrupolar effects, we run very simple molecular calculations on different CO dimers. In **Figure 3.2**, we report the structures corresponding to the only three energy minima the system shows, as represented by their electrostatic potential maps. Further details about these maps can be found in the Appendix. Regardless the initial geometry, in the final optimized ones the two CO molecules assume an (anti)parallel configuration. These results are coherent with the quadrupolar nature of CO.

The other extreme is represented by solid the α -CO cubic crystal structure (space group $P2_13$) with four molecules per unit cell (**Figure 3.2**).³⁵ Our optimized structure has a sublimation enthalpy at 0 K *per* CO (ΔH) of 8.0 kJ mol^{-1} , computed according to Equation **2.75**, in excellent agreement with the experimental one measured at 10 K (8.3 kJ mol^{-1}),³⁶ as reported in **Table 3.2**. As regards the spectral fingerprint, the experimental stretching has been measured at 2138 cm^{-1} .²⁷ Our computed (scaled) stretching frequencies for solid CO are 2139 cm^{-1} (IR inactive, full in-phase stretching) and 2142 cm^{-1} (IR active, out-of-phase stretching) whereas, if the symmetry constraints are released to get closer to a polycrystalline model, both vibrational modes become active and slightly decrease in value (**Table 3.3**). These small differences might be explained by the fact that experimental IR spectra for solid CO show some broadening in the band, centred at 2138 cm^{-1} , as a consequence of the several different contributions in a poly-crystalline-like phase, whereas our computed values refer to a perfect single crystal. However, the absolute differences are almost negligible: moreover, we are able to reproduce the most important experimental aspect, *i.e.* the significant red-shift of solid CO with respect to the gas phase.

Table 3.2 Some pure CO features. Legend: $|\mu_E|$ and Q_{zz} are the module of the electric dipole and of the zz component of quadrupole moments (in D and D Å), d_{C-O} , a_0 MIS are the C–O distance, the lattice cell parameter and the “mean internuclear separation” (in Å), ΔH is the sublimation enthalpy (in kJ mol⁻¹). %Err is the percentage variation of our computed data from experimental values.

Phase	Quantity	Experimental	Computed (our work)	%Err
Gas	$ \mu_E $	0.196 ^a	0.122	37.8
	Q_{zz}	-1.49 ^b	-2.63	76.5
	d_{C-O}	1.128 ^c	1.137	0.8
Solid (α -CO)	a_0	5.64 ^d	5.54	1.8
	ΔH	8.3 ^e	8.0	3.8
	MIS	1.128 ^d	1.136	0.7

References: a) Muentner.³² b) Graham *et al.*³³ c) Mina-Camilde *et al.*³ d) Okray-Hall&James.³⁷ e) Kohin.³⁶

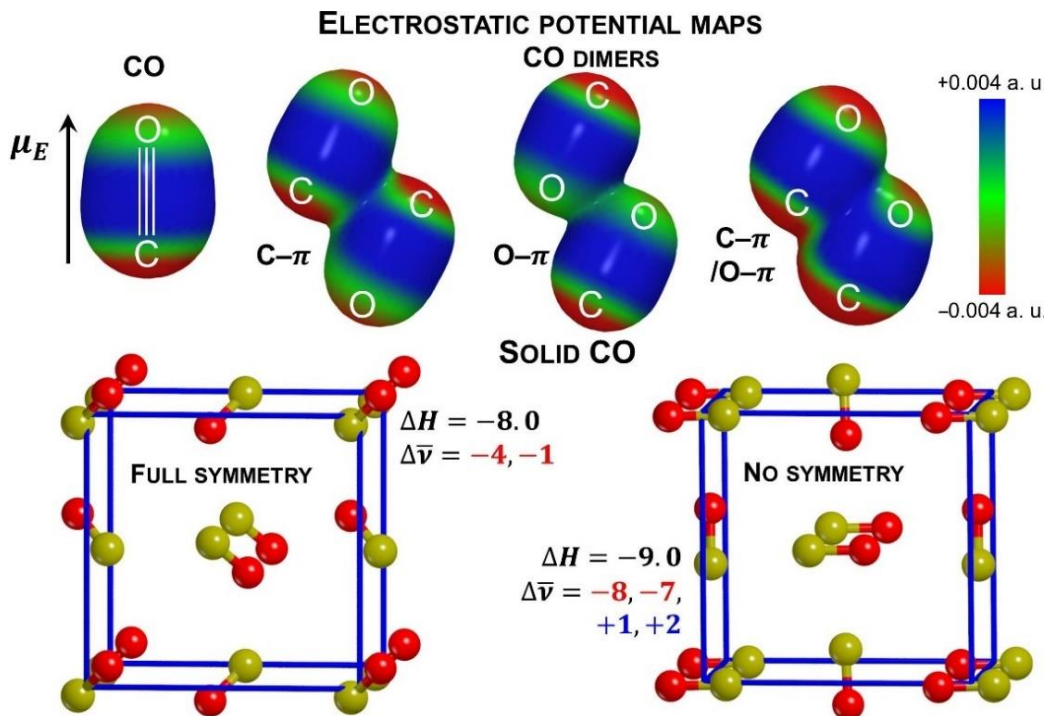


Figure 3.2 Top: molecular ESP maps superimposed to the electron densities for the single CO molecule and CO dimers (electron density iso-value = 10⁻⁵ a.u.). Bottom: optimized structures for solid CO with $P2_13$ (left) and $P1$ (right) symmetry. Sublimation enthalpies per CO (ΔH) in kJ mol⁻¹, vibrational shifts ($\Delta\bar{\nu}$) in cm⁻¹.

3.3.2 Single CO adsorption on P-ice surfaces

Single CO adsorption has been studied on two different ice surfaces cut out from P-ice bulk, corresponding to the (001) and (010) faces. Both surfaces expose in equal proportion dangling DH and DO sites. One CO molecule *per* unit cell was approached to the (010) and (001) DH surface sites *via* its C and O atoms. These configurations, reported in **Figure 3.3**, A) and B) panels for the (010) and (001) cases, will be referred in the following as DH··CO and DH··OC, respectively. On both surfaces, the initial DH··CO interaction is preserved while the DH··OC is lost during the optimization as dispersive and quadrupolar interactions between CO and the surface dominate over H-bonds. In all cases, the CO quadrupolar moment exerts a crucial effect on both energetic and spectroscopic features.

Irrespective of the surface, there are no evidences of a direct interaction involving DO sites, neither via the O atom (positive pole of the dipole) nor via the π system (positive region of the quadrupole). For DH··CO cases, a definitive H-bond is formed between the C atom and the DH on both surfaces, resulting in a blue-shift of $\sim 15\text{ cm}^{-1}$. These results are consistent with previous data.^{22,25,38} For DH··OC cases, specific dispersive interactions cause an increasing of the C–O bond and a consequent red-shift of about -20 cm^{-1} . These data mean that the DH··CO interactions may explain the experimentally observed blue-shifted peak at around 2152 cm^{-1} , but complementary DH··OC cannot explain the 2138 cm^{-1} because it produces too strongly red-shifted values. Moreover, the DH··CO configurations is energetically preferred over the DH··OC one (data also in **Table 3.3**).

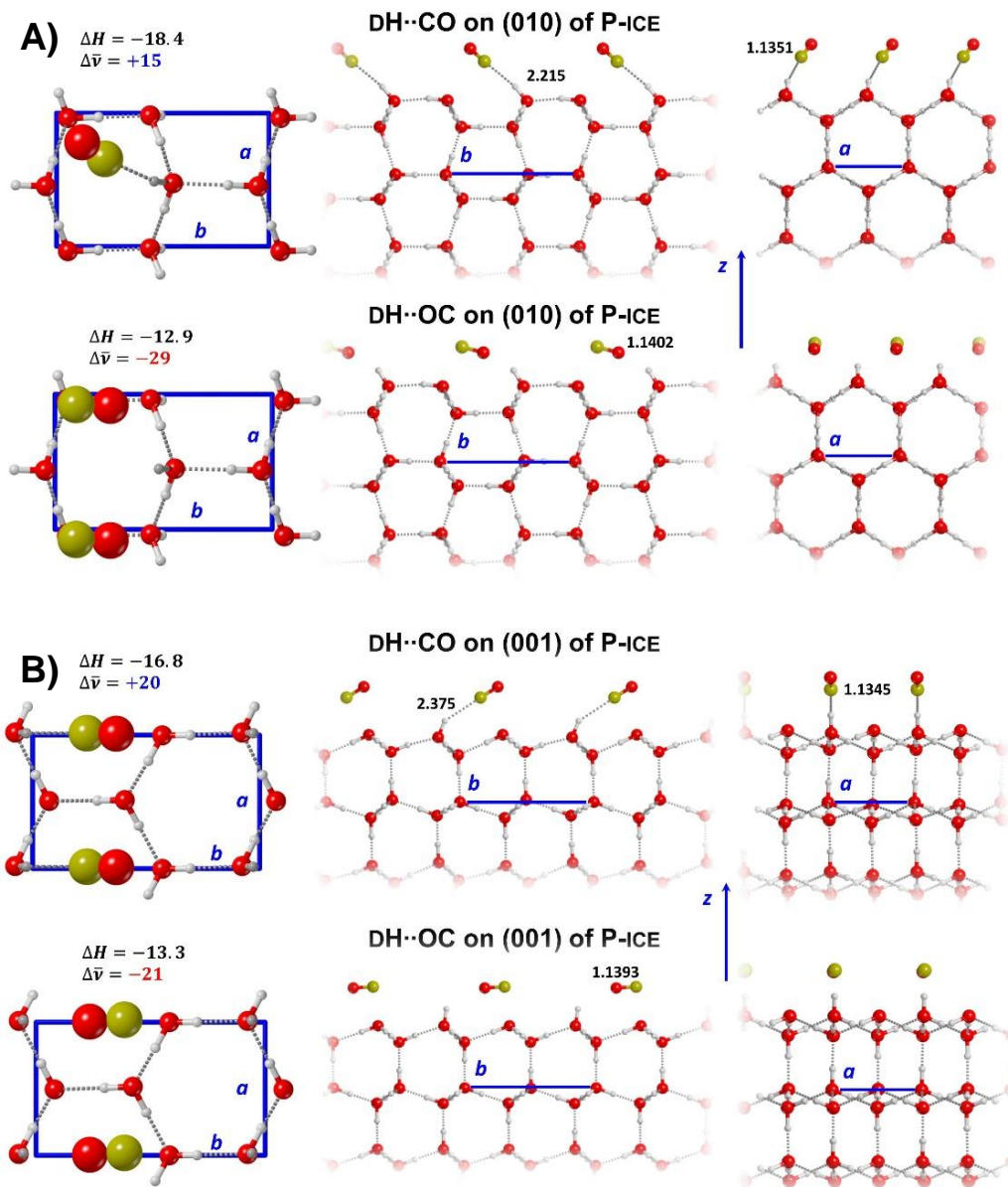


Figure 3.3 Final optimized geometries for CO initially interacting with DH sites of the (010) (panel A) or of the (001) (panel B) P-ice surface *via* either its C (DH·CO) or O (DH·OC) atom. Top (left) and side views along a (centre) and b (right) periodic vectors. z is the direction perpendicular to the cut. In top views, C and O atoms of CO molecules as van der Waals spheres, DHs in dark grey. Adsorption enthalpies *per* CO (ΔH) in kJ mol⁻¹, vibrational shifts ($\Delta\bar{\nu}$) in cm⁻¹, C–O distances and H-bonds in Å.

3.3.3 Multiple CO adsorption on P-ice surface

As the concentration of CO increases up to the monolayer limit, a different kind of model is required to reproduce the CO/H₂O ice interaction. Therefore, we designed two different structures by placing four CO molecules *per* unit cell upon the (001) surface of P-ice only, as in the initial panels of **Figure 3.4**. The optimization procedure yielded to interesting rearrangement in both CO/H₂O ice interfaces: indeed, as in the final panels of **Figure 3.4**, CO molecules reorganize themselves in order to maximize the reciprocal quadrupolar interactions and the H-bonds with the surface. The resulting structures are two CO-layered slabs, slightly resembling the arrangement of CO molecules in the bulk structure. As a consequence of the different surrounding of each CO molecule, the CO stretching band splits in a few components and the overall features of the computed spectra are the same for the two interfaces. Adopting the CO labels of **Figure 3.4**, the high frequency peaks around 2160 cm⁻¹ corresponds to the DH·CO interaction of CO-A. On the contrary, CO-D molecules exposing their O atoms to the H₂O ice surface represent the most red-shifted cases, similarly to the DH·OC interaction in previous Section. The two remaining vibrational modes, which involve the CO molecules of the upper layer, are evidently less affected by the icy water surface and reflect the CO-CO interactions. Therefore, as the availability of DH sites is over, the exceeding CO molecules reorganize and grow up as homogeneous layers on top of the ice surface. As a consequence, a broadening around the 2138 cm⁻¹ IR signal takes place due to the different interactions of the adsorbed CO molecules.

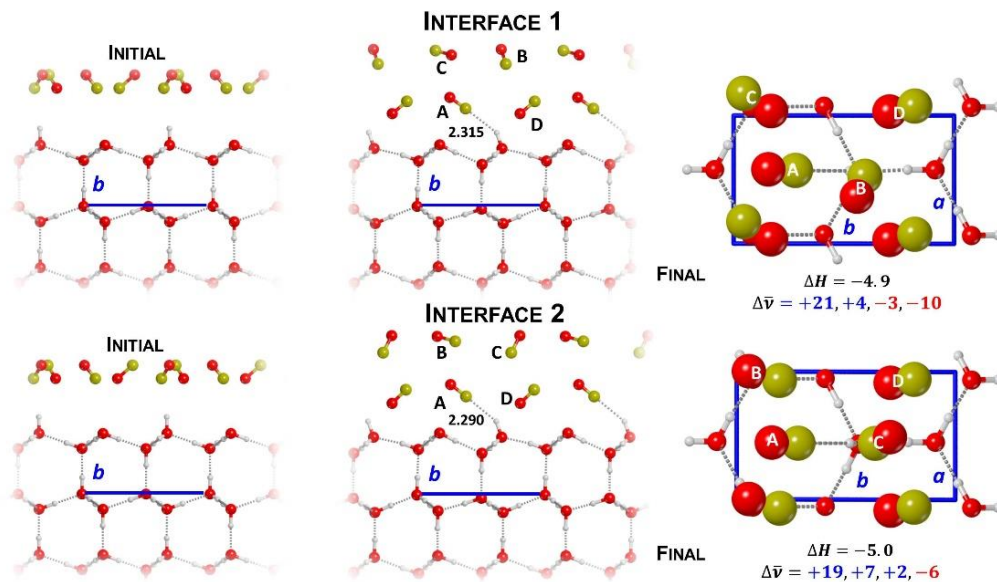


Figure 3.4 CO/H₂O interface models, using the (001) surface of P-ice. Left panels: side views along the a direction of the initial geometries. Centre and right panels: final optimized geometries (side views along a direction, centre, and top views, right). In top views, C and O atoms of CO molecules as van der Waals spheres. Enthalpy variations *per* CO (ΔH) in kJ mol⁻¹, vibrational shifts ($\Delta\bar{\nu}$) in cm⁻¹, H-bonds in Å.

3.3.4 CO in H₂O cages

Sandford *et al.* observed that the thermal annealing of CO/H₂O mixtures facilitates CO diffusion into ice pores, as attested by the narrowing of the signal at 2136 cm⁻¹ and may produce new signals at 2144 cm⁻¹ (4.664 μm) possibly related to the clathrate-like structures formation because the H₂O molecules can rearrange into a more ordered structures.¹² To investigate on these aspects, we simulated the CO engagement into different H₂O-crystalline lattices. In particular, with reference to **Figure 3.5**, we addressed the natural occurring type I CO-clathrate (sI),^{39,40} and the recently discovered structure III methane-clathrate (sIII) that, despite its similarity with hexagonal ice, shows larger cavities,⁴¹ with two CO molecules *per* cage defining eight different initial configurations and exploiting symmetry. According to their spectroscopic features, these eight initial configurations can be grouped into two groups, labelled as sIII_{grp1} and sIII_{grp2}. We

also considered a single CO occupancy, sIII_{x1}, thus breaking the internal symmetry. Finally, the eventuality of CO engagement into crystalline ice was simulated by a 2x2x2 supercell (SC) models of both C- and P-ice.

Data reported in **Table 3.3** show the fundamental role of dispersive interactions in determining the energetics of the engagement process. Indeed, there is no evidence of H-bonds involving the C atom of CO molecules with any water molecule of the surrounding so that without the dispersion contribution CO will be unbound. Nevertheless, in the cases of C- and P-ice SC, steric hindrance predominates also when accounting for dispersive forces, *i.e.* the 12-H₂O molecules cavities are too small to host CO, as indicated by the positive interaction energies and enthalpies.

The analysis of spectroscopic data shows that the formation of different clathrate-like cages around CO molecules can partially explain the observed IR signals for CO in water-dominated environments. The red-shift of the CO stretching frequency is significantly less than in the case of DH·OC. This behaviour can again be explained by invoking quadrupolar interactions between the ice lattice and the CO. A noticeable difference appears in the eight sIII configurations explored. Despite their similarity in terms of CO-CO and CO-lattice distances, see **Figure 3.5**, in the sIII_{grp2} all the four CO stretching modes are blue-shifted, while in the sIII_{grp1}, only one mode is blue-shifted (**Table 3.3**). To enlighten on this aspect, we removed the symmetry and reoptimized the sIII_{grp1} and sIII_{grp2} structures in *PI* space group, ending up with the same frequency pattern (data not shown). We concluded that these blue-shifted modes are not a symmetry artefact but rather the result of the peculiar geometry assumed by the CO molecules inside the cages giving rise to specific intermolecular interactions. As a matter of fact, these signals are completely absent in the single occupied sIII_{x1} system (**Table 3.3**). Our data suggest that both the astronomical features of CO/H₂O mixtures and the controversial red-shifted peaks in the experimental spectra could be due

to trapped CO experiencing the potential field inside a water cage and/or *via* quadrupolar interactions of neighbouring CO molecules.

The very high energetic data for CO entrapped in crystalline C- and P-ice pores suggest that CO could not be able to diffuse into such small pores but does rather prefer to remain adsorbed. In order to test this possibility, from the 3D periodic structure of the P-ice SC in **Figure 3.5**, we cut two different slab models along the [010] direction so that the water cages hosting COs result to be exposed to vacuum (“Expulsion” models, **Figure 3.6**). As the optimizations start, CO molecules tend to be expelled from the surface pores and only weak quadrupole interactions keep them inside newly-formed clathrate-like semi-cages, with a great rearrangement of the water ice matrix. These simulations suggest an “hydrophobic behaviour” of CO and clearly show that CO would hardly diffuse into water-ice pores unless they are at least as large as in clathrates. This behaviour is confirmed by the “substitutional CO” case (Sub_{CO} in **Figure 3.5**), where one CO replaces one water of the P-ice bulk structures forming two H-bonds with two H₂O molecules. Once the structure is relaxed, water lattice rearranges significantly, and a clathrate-like cage forms around CO.

The energy balance, reported in **Table 3.3**, takes into account both the deformation energy and the formation of new H-bonds between H₂O molecules and results in an almost zero value. This result suggests that the formation of a CO/H₂O mixed lattice is rather unlikely, at least at low concentration of carbon monoxide and at the very low temperature characterizing the colder regions of the ISM.

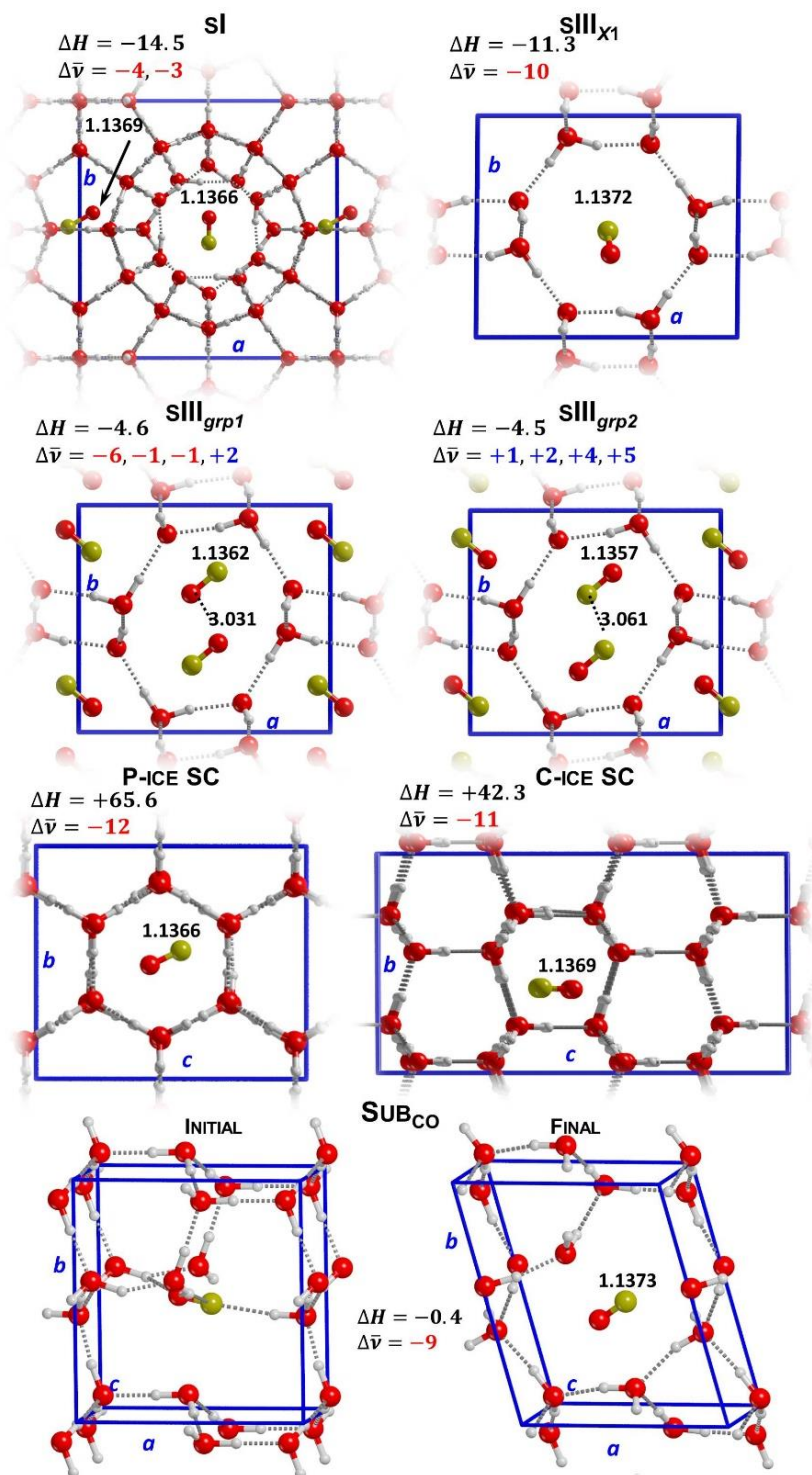


Figure 3.5 CO entrapped in different cage models. Enthalpy variations *per* CO molecule (ΔH) in kJ mol⁻¹, vibrational shifts ($\Delta \bar{\nu}$) in cm⁻¹, distances in Å.

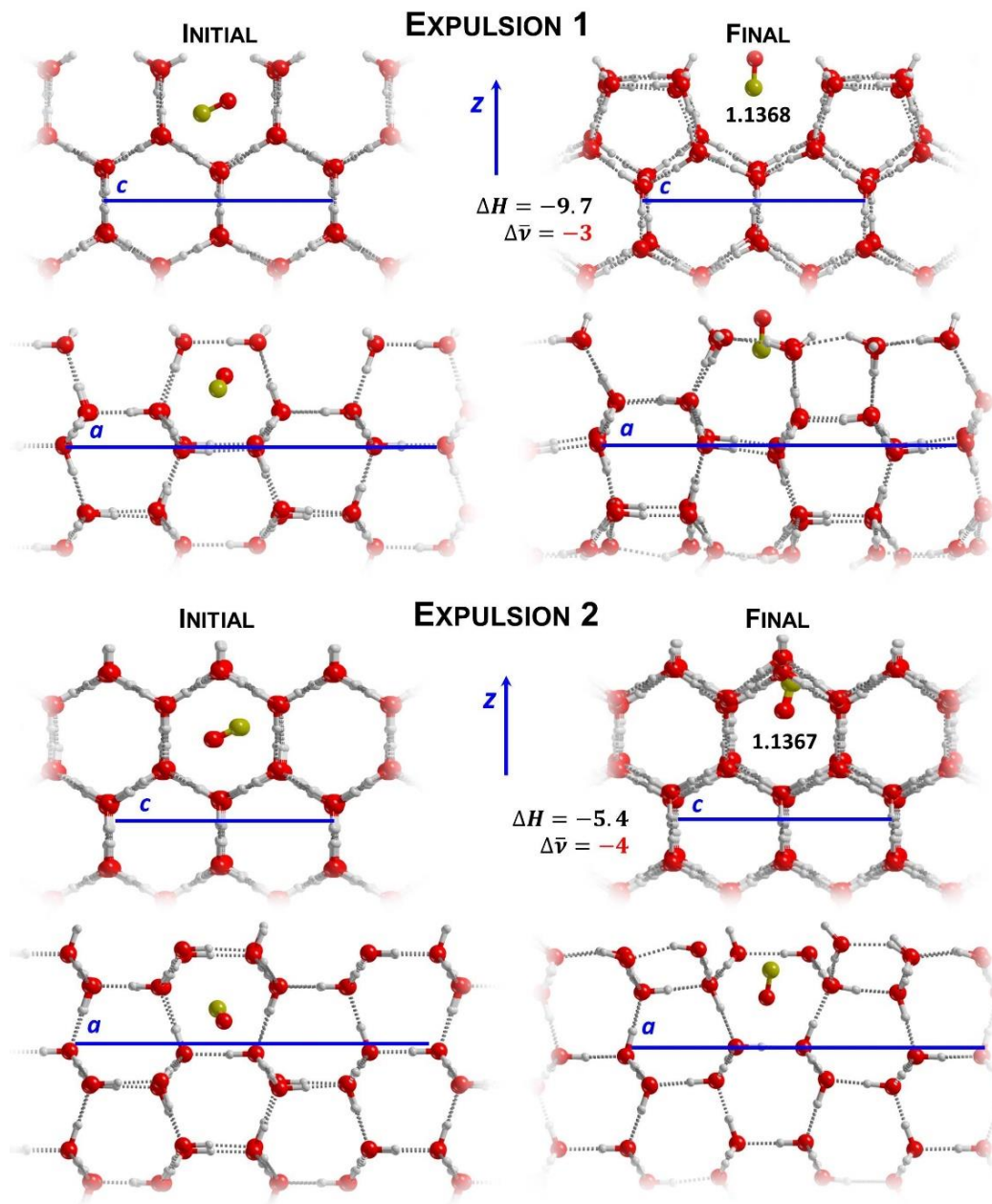


Figure 3.6 Side views for the “expulsion” models, *i.e.* CO expelled from superficial P-ice pores. Initial geometries on the left, final ones on the right. Enthalpy variations *per* CO molecule (ΔH) in kJ mol^{-1} , vibrational shifts ($\Delta\bar{\nu}$) in cm^{-1} , distances in \AA .

3.3.5 CO entrapped in a water-rich mixture

Sub_{CO} can be considered as the simplest model of a CO/H₂O mixed ice. In order to improve the description of these binary systems, we defined a more realistic model by replacing 6 out of 24 water molecules by 6 CO molecules in a 1x1x2 supercell of P-ice to reproduce the CO:H₂O ratio usually reported for the ISM.⁷ The initial geometry was amorphized by running an AIMD simulation with the CP2K code at 300 K for 15.0 ps. After that, 5 snapshots were selected, corresponding to 5.0, 7.5, 10.0, 12.5 and 15.0 ps production time and each structure was optimized at PBE-D2 level with the CRYSTAL17 code. On the final optimized geometries, a complete energy and frequency analysis was performed. Data reported in **Table 3.3**, confirm once again the fundamental role of dispersive interactions to define the energetic configuration of these systems where, as in the case of Sub_{CO}, clathrate-like structures build up around CO molecules.

The 15.0 ps-optimized model turns out to be a reliable representation of a proper mixed CO/H₂O ice structure as its spectrum (blue line in **Figure 3.7**) closely resembles the two-peaks profile of experimental observations (compare with **Figure 3.1**, left panel). Therefore, we performed a detailed energetic analysis to determine the interaction energies and enthalpies of each individual CO molecule within the mixed CO-ice lattice (**Table 3.3**, 15.0 ps MD lines). These quantities were estimated according to Equations **2.74** and **2.75** by setting to zero the deformation energy of the mixed [18 H₂O + 5 CO] system.

As in the Sub_{CO} case, the water lattice tends to form cage structures close resembling the natural cavities in clathrates (**Figure 3.8**). Thus, CO molecules entrapped within these cages and not involved in H-bonds, are characterized by red-shifts. However, during the evolution of the simulation, H-bonds among CO and water could actually form in our model. The CO molecules involved in these H-bonds have, in accordance with our other results on P-ice slabs, quite large blue-shifts. The absolute computed IR intensities for these blue-shifted signals are

smaller than those for red-shifted ones. The lack of the 2152 cm⁻¹ peak – that together with our other previous results was assigned to the DH··CO interaction – might be explained by a low concentration of DH sites in water-dominated ices grown under interstellar conditions. Referring to **Figure 3.8**, it is worth noting that the surroundings of A and B CO molecules that produce blue-shifts are very different from the DH··CO ones as occurring on P-ice surfaces since these molecules are entrapped in water cages. To appreciate the evolution of the spectroscopic signals, the five IR spectra of the corresponding AIMD snapshots are superimposed in **Figure 3.7**.

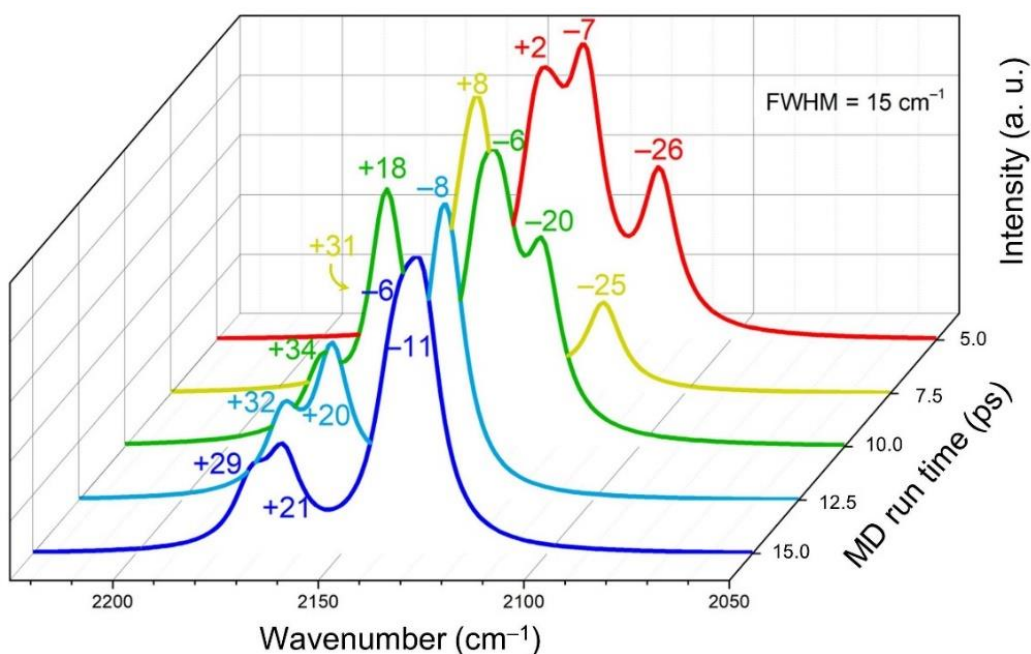


Figure 3.7 Simulated IR spectra for the different AIMD snapshots as a function of the AIMD production time. The values of the vibrational shifts (in cm⁻¹) are reported close to each distinguishable peak. The FWHM for each component of the different spectra is set equal to 15 cm⁻¹.

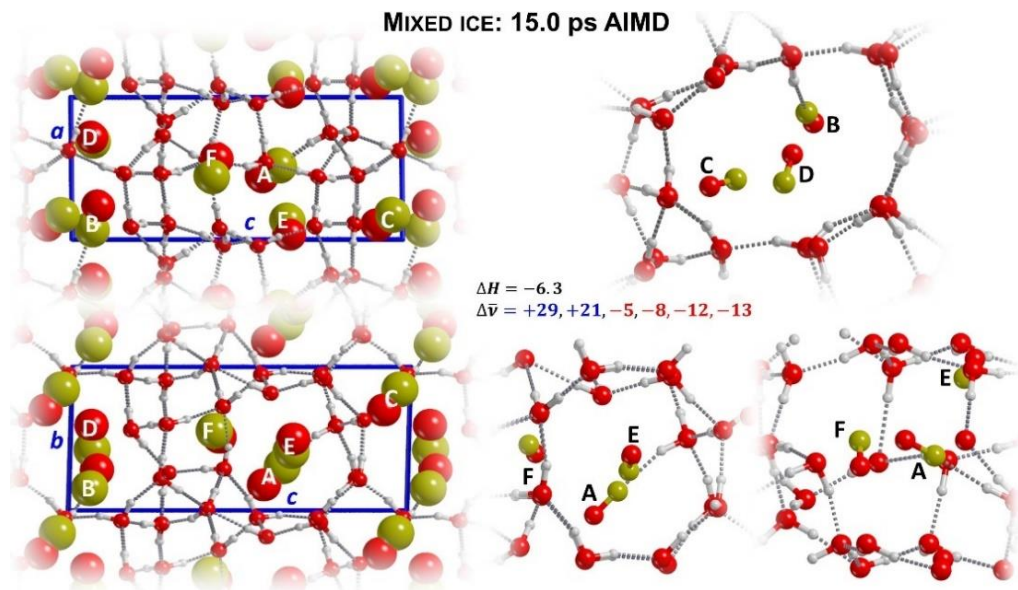


Figure 3.8 Left: view along the *b* (top) and *a* (bottom) lattice vector for the mixed CO/H₂O system. C and O atoms of CO molecules as van der Waals spheres. Right: detailed views of the local water-environments surrounding CO molecules. CO molecules labelled from A to F according to their stretching wavenumbers. Enthalpy variations *per* CO molecule (ΔH) in kJ mol⁻¹, vibrational shifts ($\Delta\bar{\nu}$) in cm⁻¹.

3.3.6 Merging the IR signals: global simulated spectrum

As a general observation, the computed absolute infrared intensities for the CO blue-shifted frequencies are lower than those for red-shifted ones (see **Table 3.3**). This is the result of an “enhancement process” which can be underlined by comparing the absolute intensities of a single CO interacting *via* its C and O atom with the H atom of a water molecule (“Gas phase CO”, “HOC··CO” and “HOC··OC” lines of **Table 3.3**). In the first case (H-bond with the C atom), the CO stretching wavenumber is blue-shifted by 16 cm⁻¹ and has an absolute intensity of 60.86 km mol⁻¹, slightly lower than that for gas phase CO (62.04 km mol⁻¹). On the other hand, when an H-bond forms between water and the O atom of the CO molecule, the CO stretching wavenumber is red-shifted by 7 cm⁻¹ and the absolute intensity is enhanced by more than the 25% (78.28 km mol⁻¹) with respect to the gas phase. This in accordance with previous results where a similar

enhancement has been observed for CO interacting with selected metal ions.⁴² This enhancement on the intensity of red-shifted frequencies could partially explain the lack of the blue-shifted component in astronomical spectra which is very faint and partially hidden. In **Figure 3.9** we report the overall spectrum obtained as a superposition of Gaussian functions centred at the computed scaled frequencies and weighted for the corresponding absolute intensities *per* CO molecule (*i.e.* the absolute intensity of a specific vibrational mode divided by the number of COs involved in that specific mode). The FWHM of each component was arbitrarily set equal to 3 cm⁻¹; this value is comparable with those reported for the three components of the 4.65 μm CO band in interstellar ices.⁷ To build such spectrum, we *a priori* excluded the SC cages because of their unfavoured energetics and also the DHs ones as they envisage slab models that underestimate the typical CO:H₂O ratio in the ISM.⁷ For sake of semi-quantitative comparison, the observed spectrum belonging to the LYSO L 1489 IRS object from Ref. 7 was superimposed. The prediction of the maximum of the peak is in good agreement with the astronomical and experimental observations, even if the band width is slightly overestimated. Blue-shifted peaks are visible in the computed spectrum with intensities definitely lower than the main peak. As we have already addressed, the reason for the missing of these blue-shifted signals in astronomical spectra is probably due to the low concentration of DH sites in interstellar ices, together with what previously asserted for the IR intensities. An interesting and alternative explanation to this problem provides that DH sites could be involved in stronger interactions with other molecular species,²⁰ with particular reference to CO₂.⁴³

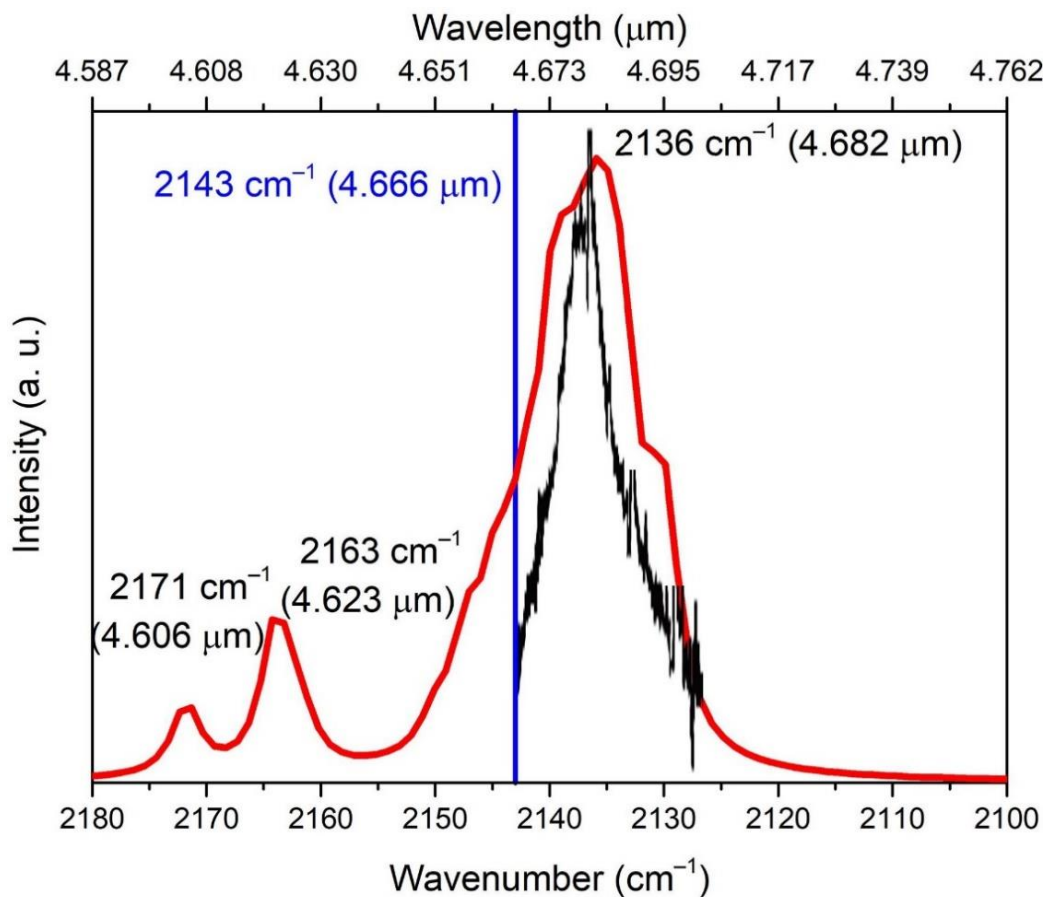


Figure 3.9 Overall simulated spectrum for the CO/H₂O ice interaction. The FWHM of each component is set equal to 3 cm⁻¹. In blue, free gas phase CO stretching reference. The maximum of the signal is at 2136 cm⁻¹ (4.682 μm). The solid black line represents the observed spectrum for LYSO L 1489 IRS object. This last spectrum is taken and adapted from Boogert *et al.*⁷

Table 3.3 Resume of our energetic and spectroscopic computed data. Interaction energies *per* CO (ΔE^{CP}) at PBE-D2 and PBE only levels in kJ mol⁻¹, as well as enthalpy variations *per* CO (ΔH). IR stretching frequencies ($\bar{\nu}$) and shifts ($\Delta\bar{\nu}$) in cm⁻¹, absolute IR intensities *per* CO in km mol⁻¹.

Model	ΔE^{CP}		ΔH	$\bar{\nu}$ ($\Delta\bar{\nu}$)	Intensity	Model	ΔE^{CP}		ΔH	$\bar{\nu}$ ($\Delta\bar{\nu}$)	Intensity
	PBE-D2	(PBE)					PBE-D2	(PBE)			
Gas phase CO	-	-	-	2143 (0)	62.04	Expulsion: model 1	-10.9 (+3.1)	-9.7	2140 (-3)	35.42	
HOH·CO	-	-	-	2159 (+16)	60.86	Expulsion: model 2	-7.7 (+13.5)	-5.4	2139 (-4)	34.71	
HOH·OC	-	-	-	2136 (-7)	78.28	Subco	-3.8 (+18.8)	-0.4	2134 (-9)	101.61	
Solid α -CO	-	-8.0	*	2139 (-4)	0	5.0 ps MD	-2.2 (+13.7)	0.5	2117 (-26)	155.01	
(<i>P2</i> ₁₃ symm.)				2142 (-1)	94				2135 (-8)	147.15	
Solid α -CO	-	-9.0		2135 (-8)	110.83				2136 (-7)	97.65	
(<i>P1</i> symm.)				2136 (-7)	109.4				2143 (0)	97.49	
				2144 (+1)	0.25				2147 (+4)	81.93	
				2145 (+2)	0.03				2147 (+4)	89.93	
(010) DH·CO	-21.0 (-12.9)	-18.4		2158 (+15)	52.49	7.5 ps MD	-10.6 (+3.4)	-7.7	2119 (-24)	114.07	
(010) DH·OC	-14.7 (-3.3)	-12.9		2114 (-29)	92.98				2149 (+6)	176.85	
(001) DH·CO	-19.1 (-9.9)	-16.8		2163 (+20)	49.07				2150 (+7)	52.14	
(001) DH·OC	-15.3 (-5.4)	-13.3		2122 (-21)	90.15				2151 (+8)	77.45	
Interface: model 1	-5.1 (-2.9)	-4.9		2133 (-10)	106.62				2154 (+11)	62.86	
				2140 (-3)	70.54				2174 (31)	67.89	
				2147 (+4)	49.41	10.0 ps MD	-6.5 (+9.9)	-3.4	2123 (-20)	118.5	
				2164 (+21)	48.88				2133 (-10)	125.57	
Interface: model 2	-5.1 (-3.0)	-5.0		2137 (-6)	87.07				2138 (-5)	122.39	
				2145 (+2)	81.81				2160 (+17)	100.2	
				2150 (+7)	33.69				2162 (+19)	82.59	
				2162 (+19)	46.43				2177 (+34)	49.68	
sl	-16.1 (+4.8)	-14.5		2139 (-4)	23.18	12.5 ps MD	-7.3 (+7.2)	-7.1	2135 (-8)	143.96	
				2140 (-3)	181.04				2136 (-7)	138.02	
slII _{sl}	-13.6 (+9.0)	-11.3		2133 (-10)	95.82				2137 (-6)	84.16	
slII _{grp1}	-7.7 (+18.2)			2137 (-6)	78.36				2163 (+20)	86.32	
		-4.6		2142 (-1)	49.88				2163 (+20)	77.67	
				2142 (-1)	0				2175 (+32)	87.23	
				*2145 (+2)	0	15.0 ps MD	-9.5 (+8.6)	-6.3			
slII _{grp2}	-7.6 (+17.8)	-4.5		2144 (+1)	55.94				-5.6 (+23.8)	-1.8	
				2145 (+2)	0				-18.8 (+6.9)	-15.8	
				2147 (+4)	44.62				-15.5 (+6.8)	-12.9	
				*2148 (+5)	0				-12.8 (+11.1)	-10.1	
C-ice SC	+36.6 (+63.9)	+42.3		2132 (-11)	135.72				-23.9 (-2.8)	-20.3	
P-ice SC	+60.5 (+83.1)	+65.5		2131 (-12)	139.15				-25.9 (0.0)	-21.7	
									2172 (+29)	67.92	

*: IR inactive mode

3.4 Concluding remarks

Adsorption of (organic) molecules on or inside ice surfaces of the dust mantle of interstellar grains have received significant attention in astrochemical investigations due to their implication in reactions yielding precursor molecules for life.^{44,45} Specifically, from a chemical point of view, the interest around CO is mainly due to the possible formation of derived species such as carbon dioxide, methanol, formaldehyde and formic acid.^{46,47} In the meanwhile, impressive quantity of spectroscopic measurements has become available and several laboratory and theoretical simulations have crossed their intuition to provide reliable molecular configurations to be associated with each spectroscopic peak. As regards CO, the debate is mainly concentrated on the red- and blue-shifts of its stretching frequency recorded as ISM or laboratory signals with respect to its characteristic gas phase frequency. Then, in order to enlighten on this very small and informative portion of the spectrum, we simulated a wide range of CO/H₂O ice environments adopting different models of water ice (*i.e.* crystalline and amorphous ice bulk, surfaces, clathrates) by means of density functional theory simulations (PBE-D2 level of theory) on periodic and molecular models. Our main goal was to furnish solid theoretical justifications on this topic, with particular reference to the interpretation of both the experimental and astronomical spectra. Because the vibrational shifts involved are very small, we ensured that the calculations were run with an accurate level of theory. The present results, far from being conclusive, provide some general indications on CO/H₂O ice binary system, both as regards its properties and spectroscopic fingerprint:

- dispersive and quadrupolar interactions have a prominent role in determining the structural and spectroscopic features of carbon monoxide interacting with other systems, *e.g.*, other CO and/or water molecules. Within our computational methodology, the electrostatic properties of the

- CO molecule (orientation of the dipole and quadrupole electric moments) are correctly described, even if the value of the CO quadrupole is underestimated with respect the experimental one;
- the most favourable interaction between carbon monoxide and water involves dangling H atoms (DH) of crystalline H₂O ice (P-ice) surface models and the C atom of CO (negative pole of both dipole and quadrupole). It is this specific DH·CO interaction that causes a blue-shift of the CO stretching frequency with respect to the gas phase value. The symmetric DH·OC interactions is weaker and is lost during the geometry optimizations – as the coupled action of dispersive and quadrupolar forces overcomes the DH·OC bond, with a corresponding red-shift of the C–O stretching frequency. The large shift values (in module) for these reference CO/H₂O ice models (in particular the large red-shifts), together with the very low CO/H₂O ratio, suggest that they are probably not representative of a real astronomical ice, at least considering the need of a crystalline ice;
 - the lack of the blue-shifted peak in astronomical spectra could be the result of two factors: firstly, blue-shifted signals are intrinsically less intense than red-shifted ones and, secondly, DH sites are probably scarcely present (but not completely absent) in the interstellar ices covering dust grain cores, probably due to the amorphous nature of ice in which all available DH are engaged in H-bond to maximize the interaction energy within the ice mantle. Please note that alternative explanations to this problem have been also suggested;⁴³
 - the red-shifted peak around 2138 cm⁻¹ present in both astronomical and experimental spectra could be the result of CO involved in different reciprocal configurations with respect to the water-ice matrix such as layered CO/H₂O ices, CO entrapped within water cages of different sizes, pure (crystalline-like) solid CO or proper mixed water ices. For all these models, small red-shifts appear as a result of the establishment of weak,

non-H-bond interactions. However, these interactions could also produce (in all cases but solid CO) small blue-shifted signals;

- CO shows a “hydrophobic behaviour”, which hinders it to penetrate into small ice pores. As a consequence, the presence of CO can induce large rearrangements of the surrounding lattice water molecules, resulting in the formation of clathrate-like cages where a perfect network of H-bonds among H₂O molecules establishes, as happens for the “expulsion” and “Sub_{CO}” models. Consequently, CO could not simply substitute water molecules in the ice lattice;
- as the concentration increases, CO molecules tend to clusterize and/or rearrange forming homogeneous structures bonded together by attractive dispersive and CO-quadrupole dominated interactions, whose morphology is dictated by the ice degree of order. Namely, ordered CO layers form on top of a preformed water-ice surface, whereas CO molecules clusterize inside a proper mixed CO-H₂O matrix. Our results indicate that small blue- and red-shifted peaks could appear in the IR spectrum as a consequence of this “clusterization” process.

We hope the present work could be useful to enlighten some aspects of this important astronomical topic, and to provide atomistic details of the CO/H₂O ice interactions that could be incorporated in further studies more involved in the problem of the actual structure of interstellar ices.

Bibliography

- (1) Smith, R. S.; May, R. A.; Kay, B. D. Desorption Kinetics of Ar, Kr, Xe, N₂, O₂, CO, Methane, Ethane, and Propane from Graphene and Amorphous Solid Water Surfaces. *J. Phys. Chem. B* **2016**, *120*, 1979–1987.
- (2) Zamirri, L.; Casassa, S.; Rimola, A.; Segado-Centellas, M.; Ceccarelli, C.; Ugliengo, P. IR Spectral Fingerprint of Carbon Monoxide in Interstellar Water Ice Models. *Mon. Not. R. Astron. Soc.* **2018**, *480*, 1427–1444.
- (3) Mina-Camilde, N.; Manzanares, C. I.; Caballero, J. F. Molecular Constants of Carbon Monoxide at $v = 0, 1, 2$, and 3. A Vibrational Spectroscopy. *J. Chem. Educ.* **1996**, *73*, 804–807.
- (4) Ceccarelli, C.; Caselli, P.; Bockelée-Morvan, D.; Mousis, O.; Pizzarello, S.; Robert, F.; Semenov, D. Deuterium Fractionation: The Ariadne’s Thread from the Precollapse Phase to Meteorites and Comets Today. In *Protostars and Planets VI*; Beuther, H., Klessen, R. S., Dullemond, C. P., Henning, T., Eds.; Tucson, AZ, USA, 2014; 859–882.
- (5) Garrod, R. T.; Herbst, E. Formation of Methyl Formate and Other Organic Species in the Warm-up Phase of Hot Molecular Cores. *Astron. Astrophys.* **2006**, *457*, 927–936.
- (6) Madhusudhan, N.; Bitsch, B.; Johansen, A.; Eriksson, L. Atmospheric Signatures of Giant Exoplanet Formation by Pebble Accretion. *Mon. Not. R. Astron. Soc.* **2017**, *469*, 4102–4115.
- (7) Boogert, A. C. A.; Gerakines, P. A.; Whittet, D. C. B. Observations of the Icy Universe. *Annu. Rev. Astron. Astrophys.* **2015**, *53*, 541–583.
- (8) Palumbo, M. E. Infrared Spectra and Nature of the Principal CO Trapping Sites in Amorphous and Crystalline H₂O Ice. *J. Phys. Chem. A* **1997**, *101*, 4298–4301.

- (9) Collings, M. P.; Dever, J. W.; Fraser, H. J.; McCoustra, M. R. S. Laboratory Studies of the Interaction of Carbon Monoxide with Water Ice. *Astrophys. Space Sci.* **2003**, *285*, 633–659.
- (10) Collings, M. P.; Dever, J. W.; McCoustra, M. R. S. Sub-Monolayer Coverages of CO on Water Ice. *Chem. Phys. Lett.* **2005**, *415*, 40–45.
- (11) Collings, M. P.; Dever, J. W.; McCoustra, M. R. S. The Interaction of Carbon Monoxide with Model Astrophysical Surfaces. *Phys. Chem. Chem. Phys.* **2014**, *16*, 3479–3492.
- (12) Sandford, S. A.; Allamandola, L. J.; Tielens, A. G. G. M.; Valero, G. J. Laboratory Studies of the Infrared Spectral Properties of CO in Astrophysical Ices. *Astrophys. J.* **1988**, *329*, 498–510.
- (13) Jenniskens, P.; Blake, D.; Wilson, M. A.; Pohorille, A. High-Density Amorphous Ice, the Frost on Interstellar Grains. *Astron. J.* **1995**, *455*, 389–401.
- (14) Devlin, J. P. Molecular Interactions with Icy Surfaces: Infrared Spectra of Carbon Monoxide Adsorbed in Microporous Amorphous Ice. *J. Phys. Chem.* **1992**, *96*, 6185–6188.
- (15) Collings, M. P.; Dever, J. W.; Fraser, H. J.; McCoustra, M. R. S.; Williams, D. A. Carbon Monoxide Entrapment in Interstellar Ice Analogs. *Astrophys. J.* **2003**, *583*, 1058–1062.
- (16) Bowron, D. T.; Finney, J. L.; Hallbrucker, A.; Kohl, I.; Loerting, T.; Mayer, E.; Soper, A. K. The Local and Intermediate Range Structures of the Five Amorphous Ices at 80 K and Ambient Pressure: A Faber-Ziman and Bhatia-Thornton Analysis. *J. Chem. Phys.* **2006**, *125*, 194502 (19 pp).
- (17) Dartois, E. The Ice Survey Opportunity of ISO. *ISO Sci. Leg. A Compact Rev. ISO Major Achiev.* **2005**, 293–310.

- (18) Gibb, E. L.; Whittet, D. C. B.; Boogert, a. C. a.; Tielens, a. G. G. M. Interstellar Ice: The Infrared Space Observatory Legacy. *Astrophys. J. Suppl. Ser.* **2004**, *151*, 35–73.
- (19) Oberg, K. I.; Boogert, A. C. A.; Pontoppidan, K. M.; van den Broek, S.; van Dishoeck, E. F.; Bottinelli, S.; Blake, G. A.; Evans II, N. J. The Spitzer Ice Legacy: Ice Evolution from Cores to Protostars. *Astrophys. J.* **2011**, *740*, 16.
- (20) Fraser, H. J.; Collings, M. P.; Dever, J. W.; McCoustra, M. R. S. Using Laboratory Studies of CO-H₂O Ices to Understand the Non-Detection of a 2152 cm⁻¹ (4.647 μm) Band in the Spectra of Interstellar Ices. *Mon. Not. R. Astron. Soc.* **2004**, *353*, 59–68.
- (21) Al-Halabi, A.; Fraser, H. J.; Kroes, G. J.; van Dishoeck, E. F. Adsorption of CO on Amorphous Water-Ice Surfaces. *Astron. Astrophys.* **2004**, *422*, 777–791.
- (22) Allouche, A.; Verlaque, P.; Pourcin, J. CO Adsorption Isotherms on Ice by Fourier Transform Infrared Spectroscopy and New Insights of the Ice Surface from Quantum Ab Initio Investigations. *J. Phys. Chem. B* **1998**, *102*, 89–98.
- (23) Pontoppidan, K. M.; Fraser, H. J.; Dartois, E.; Thi, W.-F.; van Dishoeck, E. F.; Boogert, A. C. A.; D’Hendecourt, L.; Tielens, A. G. G. M.; Bisschop, S. E. A 3-5 mm VLT Spectroscopic Survey of Embedded Young Low Mass Stars I - Structure of the CO Ice. *Astron. Astrophys.* **2003**, *408*, 981–1007.
- (24) Manca, C.; Roubin, P.; Martin, C. Volumetric and Infrared Co-Measurements of CH₄ and CO Isotherms on Microporous Ice. *Chem. Phys. Lett.* **2000**, *330*, 21–26.
- (25) Al-Halabi, A.; van Dishoeck, E. F.; Kroes, G. J. Sticking of CO to Crystalline and Amorphous Ice Surfaces. *J. Chem. Phys.* **2004**, *120*, 3558–

- 3367.
- (26) Martin, C.; Manca, C.; Roubin, P. Adsorption of Small Molecules on Amorphous Ice : Volumetric and FT-IR Isotherm Co-Measurements Part II . The Case of CO. *Surf. Sci.* **2002**, *503*, 280–284.
- (27) Ewing, G. E.; Pimentel, G. C. Infrared Spectrum of Solid Carbon Monoxide. *J. Chem. Phys.* **1961**, *35*, 925–930.
- (28) Pisani, C.; Casassa, S.; Ugliengo, P. Proton-Ordered Ice Structures at Zero Pressure. A Quantum-Mechanical Investigation. *Chem. Phys. Lett.* **1996**, *253*, 201–208.
- (29) Zamirri, L.; Corno, M.; Rimola, A.; Ugliengo, P. Forsterite Surfaces as Models of Interstellar Core Dust Grains: Computational Study of Carbon Monoxide Adsorption. *ACS Earth Sp. Chem.* **2017**, *1*, 384–398.
- (30) Zamirri, L.; Pantaleone, S.; Ugliengo, P. Carbon Monoxide Adsorption at Forsterite Surfaces as Models of Interstellar Dust Grains: An Unexpected Bathochromic (Red) Shift of the CO Stretching Frequency. *J. Chem. Phys.* **2019**, *150*, 064702 (9 pp).
- (31) Chiatti, F.; Corno, M.; Sakhno, Y.; Martra, G.; Ugliengo, P. Revealing Hydroxyapatite Nanoparticle Surface Structure by CO Adsorption: A Combined B3LYP and Infrared Study. *J. Phys. Chem. C* **2013**, *117*, 25526–25534.
- (32) Muentner, J. Electric Dipole Moment of Carbon Monoxide. *J. Mol. Spectrosc.* **1975**, *55*, 490–491.
- (33) Graham, C.; Imrie, D. A.; Raab, R. E. Measurement of the Electric Quadrupole Moments of CO₂, CO, N₂, Cl₂ and BF₃. *Mol. Phys.* **1998**, *93*, 49–56.
- (34) Chetty, N.; Couling, V. W. Measurement of the Electric Quadrupole

- Moment of CO. *J. Chem. Phys.* **2011**, *134*, 164307(1-5).
- (35) Vegard, I. Struktur Und Leuchtfähigkeit von Festem Kohlenoxyd. *Zeitschrift für Phys.* **1930**, *61*, 3–4.
- (36) Kohin, B. C. Molecular Rotation in Crystals of N₂ and CO. *J. Chem. Phys.* **1960**, *33*, 882–889.
- (37) Okray-Hall, B.; James, H. M. Lattice Dynamics of α Carbon Monoxide. *Phys. Rev. B* **1976**, *13*, 3590–3603.
- (38) Manca, C.; Martin, C.; Allouche, A.; Roubin, P. Experimental and Theoretical Reinvestigation of CO Adsorption on Amorphous Ice. *J. Phys. Chem. B* **2001**, *105*, 12861–12869.
- (39) Dendy Sloan Jr., E.; Koh, C. A. *Clathrate Hydrates of Natural Gases*; CRC Press: Boca Raton, FL, USA, 2007.
- (40) Davidson, D. W.; Desando, M. A.; Cough, S. R.; Handa, Y. P.; Ratcliff, C. I.; Ripmeester, J. A.; Tse, J. S. A Clathrate Hydrate of Carbon Monoxide. *Nature* **1987**, *328*, 418–419.
- (41) Loveday, J. S.; Nelmes, R. J.; Guthrie, M.; Belmonte, S. A.; Allan, D. R.; Klug, D. D.; Tse, J. S.; Handa, Y. P. Stable Methane Hydrate above 2 GPa and the Source of Titan's Atmospheric Methane. *Nature* **2001**, *410*, 661–663.
- (42) Ferrari, A. M.; Ugliengo, P.; Garrone, E. *Ab Initio* Study of the Adducts of Carbon Monoxide with Alkaline Cations. *J. Chem. Phys.* **1996**, *105*, 4129–4139.
- (43) Garrod, R. T.; Pauly, T. On the Formation of CO₂ and Other Interstellar Ices. *Astrophys. J.* **2011**, *735*, 15 (18 pp).
- (44) Wakelam, V.; Loison, J.; Mereau, R.; Ruaud, M. Binding Energies: New Values and Impact on the Efficiency of Chemical Desorption. *Mol.*

- Astrophys.* **2017**, 6, 22–35.
- (45) Penteado, E. M.; Walsh, C.; Cuppen, H. M. Sensitivity Analysis of Grain Surface Chemistry to Binding Energies of Ice Species. *Astrophys. J.* **2017**, 844, 71 (13 pp).
- (46) Karssemeijer, L. J.; Ioppolo, S.; van Hemert, M. C.; van der Avoird, A.; Allodi, M. A.; Blake, G. A.; Cuppen, H. M. Dynamics of CO in Amorphous Water-Ice Environments. *Astron. J.* **2014**, 781, 16.
- (47) Rimola, A.; Taquet, V.; Ugliengo, P.; Balucani, N.; Ceccarelli, C. Combined Quantum Chemical and Modeling Study of CO Hydrogenation on Water Ice. *Astron. Astrophys.* **2014**, 572, A70 (12 pp).

4 Ice mantles reactivity: formation of iCOMs

Extended abstract

In this Chapter, we will show some results about the formation of organic molecules under ISM conditions as catalysed by interstellar ice surfaces. Data are taken and adapted from a review work about this topic we recently published.¹ Please refer to this work for further details.

Context

The ISM is rich in molecules, from simple diatomic to complex organic ones, some of which have a biotic potential. A notable example, in this respect, is represented by the *interstellar complex organic molecules* (iCOMs). Interestingly, the various phases involved in the formation of Solar-type planetary systems lead to an increasing chemical complexity, in which, at each step, more complex molecules form. In dark MCs, the ice-covered grains play a fundamental role in the interstellar chemical complexity as some important reactions are exclusively catalysed by their surfaces. For example, one of the current paradigms on the iCOMs formation assumes that iCOMs are synthesized on the ice mantle surfaces, in which reactants accrete and diffuse to finally react. As the usual approaches employed in astrochemistry (*i.e.*, spectroscopic astronomical observations, astrochemical modelling and laboratory experiments) cannot easily provide details on the iCOMs formation processes occurring on ice mantles at the atomic level, computational chemistry has recently become a complementary tool to fill in this gap. Indeed, it can provide an accurate description (*i.e.*, structures and reactive energy profiles) of these processes. Accordingly, several recent studies simulating the formation of iCOMs on icy surfaces by means of QM and CM methods have appeared in the literature.

Computational aspects

In Section 4.2, we briefly introduce some important computational concepts that are necessary when dealing with simulated chemical reaction. Indeed, reactants, products and intermediates species correspond to minima in the PES of the system, while TSs correspond to 1st order saddle points. The lowest energy path connecting two minima through a TS is usually reported to as the *reaction coordinate*. The difference in free

energy between a TS and the related reactant(s) minimum represents the “Gibbs free activation energy” and can be used to evaluate the kinetics of the reaction adopting simple model equations like the Eyring one (**Figure 4.1**). In effect, from such an equation, we can predict that only reactions showing very low free energy barriers can actually occur in the ISM within the typical evolution time of dense MCs (**Figure 4.2**).

How to model a water surface

In Section 4.3, we briefly expose the methods that can be exploited to define a water surface. Usually, two approaches are adopted, *i.e.* the molecular and the periodic approach, both showing pros and cons (**Figure 4.3**). The former consists in defining a cluster of a given number of water molecules. This cluster can be generated in several ways: by hand, by cutting a bulk structure, from MD simulations or by single additions of water molecules to a preformed core. The main advantage is that most of the computational codes that are available on the market can easily handle cluster models even at high, *post*-HF levels of theory (if sizes are not too large). The disadvantage is that results are strongly model-dependant. On the contrary, periodic models cannot be used for *post*-HF methods, but they better represent a surface (in particular in the crystalline case) and can be used to simulate, at an atomistic level, ice pores through, for example, clathrates models (as we did in the previous Chapter). Another systematic way to simulate pore effects is by explicitly introducing, in the Hamiltonian expression, a term which accounts for the dielectric property of water through its dielectric constant ϵ (polarizable continuum method – PCM). However, specific interactions between the encaged molecule(s) and the water matrix cannot be described if PCM is used. Finally, when the sizes of a cluster model are prohibitive for *post*-HF calculations, the ONIOM methodology can be adopted. It consists in dividing the model into two regions which are described with two different levels of theory: high-level (*post*-HF) methods for the catalytic site and low-level ones (DFT, HF, MM) for the rest of the model.

The role of water in catalysing iCOMs formation

Section 4.4 represents the main part of this Chapter. We present the roles that water can play in catalysing chemical reactions, with obvious reference to iCOMs and related species formation. It is organized in four subsections which correspond to four macro

arguments, *i.e.* hydrogenation (**Scheme 4.1**), hydration (**Figure 4.4**), radicals-involving reactions (**Figure 4.5**) and the proton-relay mechanism (**Figure 4.6**). Hydrogenations are probably the most important reactions occurring in the ISM due to the great abundance of atomic hydrogen in the gas phase. Indeed, the water matrix can act as a concentrator of material from the gas phase, allowing for hydrogenation of “unsaturated” species like carbon monoxide and hydrogen cyanide. However, water can also act as a reactant, hydrating species like formaldehyde which are quite abundant in the solid ISM. Moreover, it can also favour radical-radical and radical-neutral reactions by stabilizing the spin density, thus promoting the radical reactivity. It is also capable of stabilizing ionic pair species which might form as intermediates of iCOMs formation. Finally, the most important role of water is probably the proton-relay mechanism: through this mechanism, where one water molecule contemporarily gives and receives a proton, the water matrix can promote several isomerization reactions, one the most important being the $\text{HCN} \leftrightarrow \text{HNC}$ isomerization.

Glycine

The last section of this Chapter is fully dedicated to glycine, the simplest amino acid. It gained a lot of attention after its discovery in comets and asteroids. The usual way glycine, together with other amino acids, is synthesized in laboratory is through the Strecker synthesis (**Figure 4.9**). However, this synthetic route is not likely to occur in the ISM, even if all its intermediates and reactants are well-known ISM species, because of the presence of too high kinetic barriers. Therefore, other synthetic routes have been explored by many authors, the most promising ones involving radical reactions (**Figure 4.10**).

Some conclusive remarks

Most of the computational works we reviewed outline the effective catalytic role of the water matrix when compared to gas phase reactions. However, the computed thermal kinetic barriers are, in most of the cases, too high to occur within typical evolution times of MCs, at least without considering tunnelling effects. Further work is necessary to improve our description of the water matrix (*i.e.* better atomistic models) and several important reaction channels must be investigated yet.

4.1 Background

Despite the harsh conditions of the ISM, more than 200 interstellar molecules have been discovered so far, with this number steadily increasing with time (Section 1.3.3).² Among them, the class of C-bearing molecules with at least 6 atoms are defined as interstellar complex organic molecules (iCOMs, Refs. 3,4). As we already pointed out in Section 1.3.3, such a definition shows some critical aspects: first of all, it excludes some relevant organic molecules like formaldehyde (H_2CO) and methanimine ($\text{CH}_2=\text{NH}$), with possible pre-biotic implications, but also several other inorganic species like hydrogen cyanide/isocyanide (HCN/HNC) or the isocyanic acid (HCNO) that enters in several pre-biotic syntheses.

Nonetheless, iCOMs have lately received a lot of attention for their potential contribution to the emergence of life and because iCOMs in solar-type hot corinos provide a direct link between interstellar chemistry and the small bodies of the Solar System, *i.e.* comets and asteroids.⁵⁻⁷ Indeed, it is now clear that the formation of a planetary system like the Solar one consists in five major phases in which each step in the evolution from the diffuse to the condensed phases is accompanied by an increase of the complexity in the chemical composition:⁸

1. Condensation of cold ($T \sim 10$ K) and dense (density $> 10^6 \text{ cm}^{-3}$) matter slowly accreting towards the centre. Grain mantles are formed, and simple frozen hydrogenated species are synthesized.
2. As soon as the collapse takes over, a protostar forms. In the innermost hot ($T \geq 100$ K) region (hot corino) the grain mantles sublimate injecting in the gas phase all the frozen molecules and synthesizing others from them.
3. With time, the protostellar envelope is dissipated and a protoplanetary disk is dominant: the small interstellar grains coagulate into the so-called planetesimals.

4. The evolution continues with the formation of planets, comets and asteroids from the planetesimals.
5. Asteroids and comets rains on planets, enriching them with the molecules previously synthesized, possibly representing the seeds for the arise of life.⁸

Although the presence of iCOMs has been known for decades,⁹ the chemical routes that lead to their formation are still matter of intense debate. Two alternative paradigms are invoked in the literature: either iCOMs form in the gas phase,^{10–12} or on the interstellar grain surfaces (Section 1.3.3).^{10,13–15} In both, interstellar grains surfaces play a major role. We extensively treated the structure of these ices in previous Chapter. Here, we briefly remind that they are expected to be composed at least of two phases, that are the water-rich polar phase, mostly containing iced H₂O, CO₂, NH₃ in direct contact with the silicate/carbonaceous core, and the apolar phases, comprising most of the iced CO, the remaining CO₂ and probably most of the iced CH₃OH. Despite this biphasic structure, most of the experimental and theoretical works dealing with iCOMs formation explicitly make use of pure-water ice models.

Investigating iCOMs has been carried out by means of the usual multidisciplinary approach applied in astrochemistry: astronomical spectroscopic observations, astrochemical models, and laboratory experiments. Spectroscopic observations can detect iCOMs in different astronomical sources and provide abundances in the different environments. However, they are not capable to give direct information on how iCOMs are formed, either on the grain-surfaces or in gas phase. Astrochemical models are useful in rationalizing iCOMs observations. However, they require some energetic parameters to be introduced as input data to run. These parameters are derived from laboratory experiments or from model systems and often show large uncertainties. On their hand, laboratory experiments are not able to reproduce realistically the physical conditions of the ISM as well

as the chemical features of the ice grains such as the exact chemical composition.¹⁶ Within this context, computational chemistry techniques is a complementary tool to the other approaches as it can alleviate part of the abovementioned problems. For example, when dealing with a given reaction, they can provide the elementary steps involved in such a reaction. Interestingly, with these profiles, relevant energetic information of the grain surface process (*e.g.*, energy barriers, reaction rates, binding/desorption energies) can be obtained, which in turn can be used as accurate input data in the astrochemical models. However, this approach also holds some disadvantages: the main one is that results depend on both the method chosen to solve the equations describing the systems and the atomistic model adopted to represent the grain surface structure. In gas phase calculations this latter disadvantage is avoided, and hence different works dealing with the formation of iCOMs through gas phase processes are available in the literature, reporting accurate energy profiles and reaction rate coefficients.^{17–24}

4.2 PES, kinetics and thermodynamics

PESs describe the energy of a system (collection of atoms) as a function of its geometry (the position of the atoms). Complete PESs are characterized by calculating the energy of the system as a function of the internal coordinates (bonds, angles and dihedrals). Some stationary points (points with a zero gradient in the PES) have a physical meaning (**Figure 4.2A**): minima correspond to physically stable chemical species (reactants, products and intermediates), while 1st order saddle points correspond to TSs, the highest energy points on the reaction coordinates (the lowest energy paths connecting reactants with products). All other stationary points (*i.e.*, higher order saddle points and maxima) are physically unsounded. When the PESs are described as a function of the reaction coordinate (the coordinate governing the reaction), the surface is called energy profile (see **Figure 4.2B**).

Stationary points are classified by the diagonalization of the Hessian matrix of second derivatives of the potential energy with respect to the atomic displacements from equilibrium positions. Hessian eigenvalues are then related to the frequency vibrational modes of the system: for minima structures, all frequencies are real, while 1st order saddle points have one imaginary frequency.

Reaction kinetics refers to the rate of chemical reactions, which are quantified by the rate constant. Quantitatively, reaction rates can be derived from the classical “transition state theory” originally developed by Henry Eyring, Meredith G. Evans and Michael Polanyi in 1935.²⁵ Starting from the assumption of the existence of a “*quasi-equilibrium*” between reactants and TSs, the kinetic rate constant k of a given reaction can be derived as:^{26,27}

$$k = \kappa \frac{k_B T}{h} e^{-\frac{\Delta G^\ddagger}{RT}} (c^0)^{1-m} \quad 4.1$$

where κ is the transmission coefficient (for reactions without tunnelling assumed to be 1), T the absolute temperature, k_B the Boltzmann constant, h the Planck constant, R the ideal gas constant, c^0 the standard concentration, m the molecularity ($m = 1$ or 2 for uni or bimolecular reactions) and ΔG^\ddagger the Gibbs free energy barrier, *i.e.* the free energy difference between the TS and the reactant(s).

For a unimolecular reaction ($m = 1$), k can be easily related to the half-life time $t_{1/2}$,²⁸ *i.e.*, the time needed to consume half of the initial amount of reactants:

$$t_{1/2} = \frac{\ln 2}{k} = \frac{h}{\kappa k_B T} e^{\frac{\Delta G^\ddagger}{RT}} \ln 2 \quad 4.2$$

At the very low temperatures of the ISM, long half-life times are derived even for very low energy barriers. The dependence of $\log(t_{1/2}/1 \text{ Myr})$ on ΔG^\ddagger for different typical temperatures of the ISM is reported in **Figure 4.2**. Data shown

in the inset clearly indicate that, in the 10-25 K temperature range of MCs,²⁹ only reactions with very low kinetic barriers can occur.

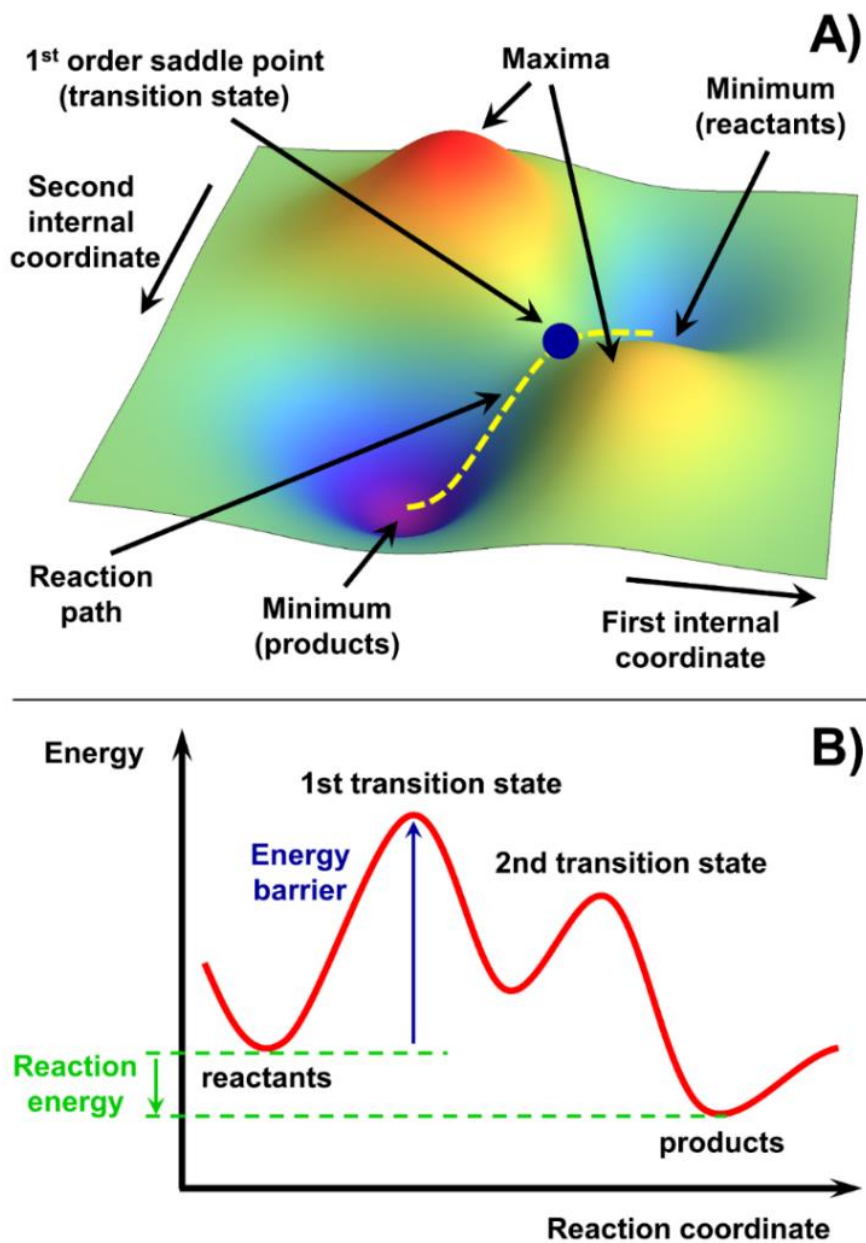


Figure 4.1 A) Example of a potential energy surface (PES) described as a function of two internal coordinates. B) Example of an energy profile. The intrinsic energy barrier (in blue) and the reaction energy (in green) are also shown.

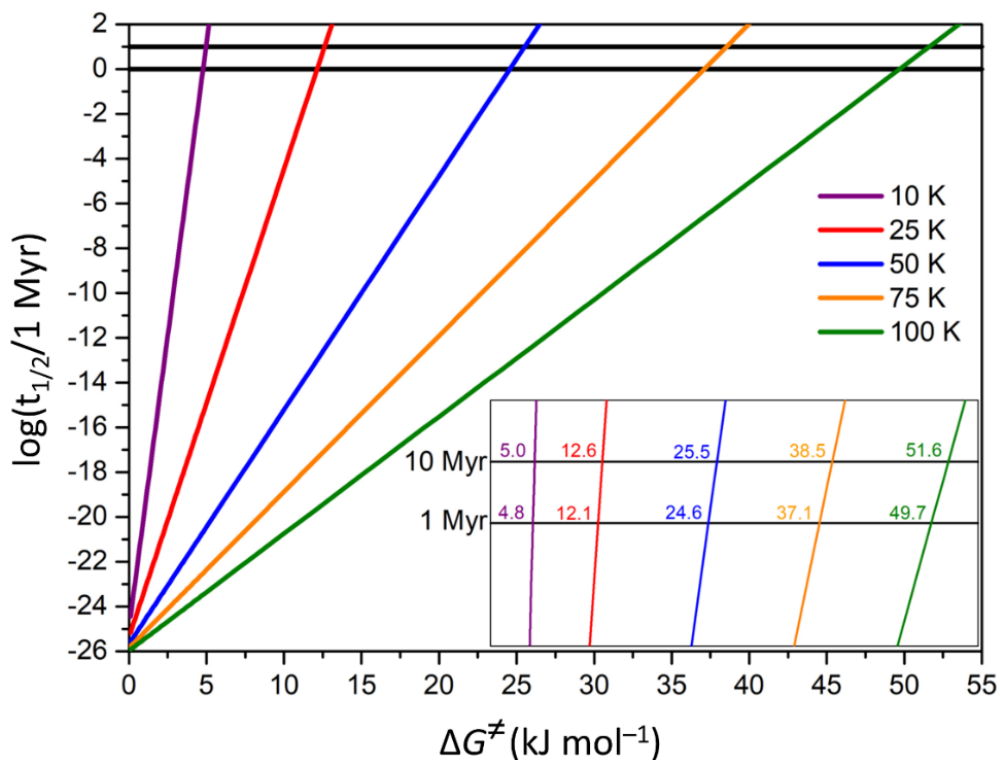


Figure 4.2 Dependence of the half-life time ($t_{1/2}$) with the free energy barrier (ΔG^\ddagger) for a unimolecular reaction at different temperatures (in K). $t_{1/2}$ are normalized to 1 Myr. The two straight horizontal lines represent 1 and 10 Myr, respectively, taken as reference lifetimes of a typical molecular cloud.³⁰ Inset: zoomed view in the $-2 \leq \log(t_{1/2}/1 \text{ Myr}) \leq 2$ range. Numbers at the crossing points are the ΔG^\ddagger values at which $t_{1/2}$ equals 1 and 10 Myr, respectively.

It is worth mentioning that at the particularly low interstellar temperatures, and for not too high and wide barriers, quantum tunnelling may play a prominent role in favouring the reaction rates. There are several ways to account for such tunnelling effects,³¹ such as the semi-classical approaches, in which the transmission coefficient κ is calculated through specific formulae (*e.g.*, the Eckart formula,³² usually used in astrochemical modelling). More evolved is the instanton theory,^{33,34} which is a derivation of the harmonic quantum transition state theory,³⁵ where the tunnelling path is fully optimized in the Feynman-path-

based instanton theory.³⁶ Few examples on the use of the instanton theory in astrochemical reactions can be found elsewhere.^{37,38}

The free energy of a given species can be easily obtained once computed the partition functions (translation, rotational, electronic and vibrational) and applying statistical thermodynamics relations.³⁹ The free energy of a species at temperature T is given by:

$$G(T) = E + E_{ZP} + \epsilon(T) + PV(T) - TS(T) \quad \mathbf{4.3}$$

where E is the total internal energy (electronic plus nuclear) of the species from the electronic structure calculation, E_{ZP} is the ZPE, $\epsilon(T)$ is the thermal contribution to the internal energy, and P , V and S represent the volume, pressure and entropy, respectively. At the low temperatures of the ISM, the last three terms of Equation **4.3** are small and usually neglected. Thus, energy profiles are usually presented in terms of E or $E + E_{ZP}$, with the latter being referred to as “internal energy at 0 K” or, equivalently, “enthalpy at 0 K”.

4.3 Water-surfaces modelling

The accuracy of the theoretical results relies on the specific models adopted to simulate the ice surfaces. Two strategies can be adopted to model the external surfaces of icy grains, *i.e.* the periodic and the cluster approach. The former consists in applying the periodic boundary conditions (PBC) into a unit cell containing the surface catalytic sites, resulting in an infinite 2D slab model (**Figure 4.3A and B**).⁴⁰⁻⁵¹ In contrast, the cluster approach consists of cutting out from the periodic model a finite set of atoms containing the surface sites, so that the surface is essentially modelled by a molecular system (**Figure 4.3C**).

Powerful computer codes have been developed over the years to solve the PBC problem for infinite systems. However, due to their infinite nature, application of highly accurate wave function-based methods is overwhelming, and they can in

practice only be studied using DFT methods. Moreover, localization of transition state structures is less developed compared to molecular codes, thus PES characterization being limited to “simple” reactions. On the contrary, a large variety of quantum molecular programs can properly handle cluster models, characterizing PESs of complex chemical reactions, using even CC methods, depending on the cluster size.

The cluster approach can be limited by: *i*) the need to “heal” dangling bonds resulting from cutting covalent/ionic bonds from the extended system, and *ii*) the size of the cluster, which should be large enough to include the catalytic sites. For this latter, cluster sizes can be prohibitively large, reducing the abovementioned advantages when adopting molecular computer codes. The ONIOM method,^{52–54} where the region of interest (*e.g.*, the region close to the catalytic sites) is treated at high level of theory (*post*-HF), whereas the surrounding region is treated at a lower level (DFT, semi-empirical or even MM, **Figure 4.3E**) may represent an alternative solution.

Interstellar ices are usually reported to be highly amorphous and, partly, porous,^{55–58} although the degree of porosity has recently been questioned.⁵⁹ Amorphous surfaces (**Figure 4.3B**) can be generated by amorphizing (*e.g.*, running MDs at high temperature) the slab model, or by cutting out a previously amorphized bulk system. The presence of pores can influence the reactivity on interstellar ices since: *i*) adsorbates can be entrapped and retained inside the pore (hence favouring reaction with other entrapped species), and *ii*) water molecules may exert a “solvent-like” effect, thus stabilizing intermediates or transition states. A consistent way to simulate pores is through clathrate models (Chapter 3), as clathrate-like IR features have been identified in interstellar ices.⁶⁰ Indeed, as we showed, even for amorphized systems ice water molecules tend to form clathrate-like cages.⁴⁴ A way to account for the “pore stabilizing effects” without making use of an explicit atomistic pore model is by using the “polarizable

continuum model” (PCM).^{61,62} PCM is a computationally cheap technique in which solvation effects are described with a continuous dielectric constant ϵ (the value of liquid water, 78.5, is usually used to simulate solid water^{63–65}). Reactive compounds are immersed within the continuum dielectric medium (**Figure 4.3D**). However, as solvent molecules are not explicitly considered, specific ice-molecule interactions are omitted. Although this can partly be solved by introducing a “first hydration sphere” of explicit water molecules within the PCM cavity,⁶⁶ using a reduced number of water molecules without geometrical constraints can convert the initial pore into a surface due to aggregation phenomena between water molecules.⁴⁴

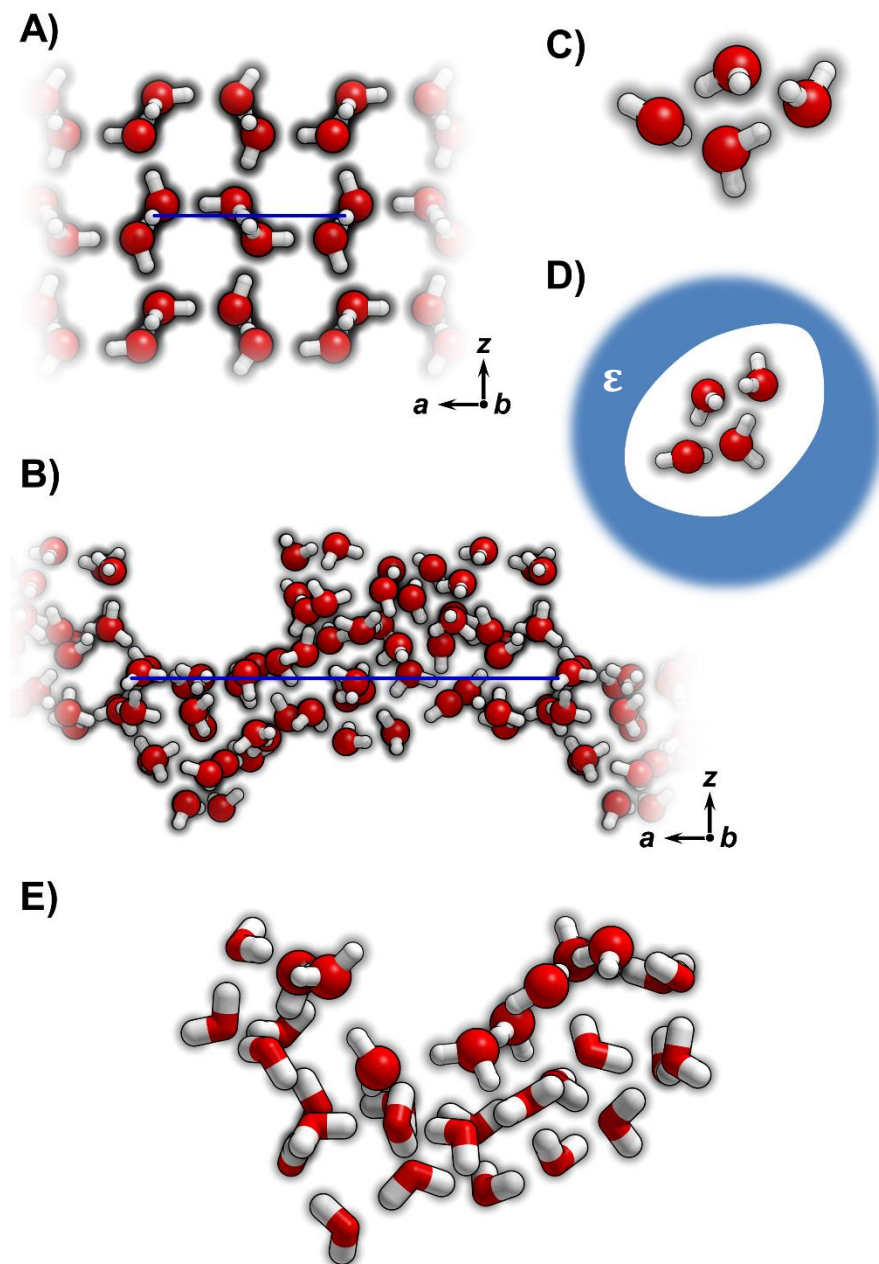


Figure 4.3 Strategies to model water ice surfaces: 2D-periodic slab models (crystalline, A, and amorphous, B). C) minimal cluster of 4 waters. D) PCM approach for a 4 H₂O cluster (blue background represents the continuum dielectric ϵ). E) ONIOM approach for a 33 H₂O cluster: molecules as balls represent the “high level”, those as sticks the “low level”. In A) and B) panels, a and b are the periodic vectors and z is the non-periodic direction (the a vector is represented in blue). H-bonds among water molecules are not represented. Colour legend: oxygen in red, hydrogen in white.

4.4 Role of water in the iCOMs formation

The water ice matrix can catalyse iCOMs formation in several ways: first, it can act as a reactant, allowing for hydration reactions to occur. It can also catalyse reactions by favouring the formation of charged species and/or ionic pairs, which are stabilized by solvation effects. Moreover, acting as a concentrator of atomic and molecular matters from the gas phase, it can favour hydrogenation reactions (atomic hydrogen is the most abundant species of the gas phase ISM). Finally, one of the most important aspects characterizing the water matrix is the proton-relay mechanism, where a proton is transmitted from one end of a given molecule to the other exploiting the complex network of H-bonds among water molecules.

4.4.1 Water as a reactant: hydration

The role of water as a reactant is well-illustrated in **Figure 4.4** for the methanol (CH_3OH) formation starting from the methyl (CH_3^+) cation. This reaction was investigated by David Woon at MP2 and B3LYP levels.⁶⁷ The interaction of CH_3^+ with one H_2O of the ice cluster leads firstly to the formation of CH_3OH_2^+ (*i.e.*, protonated methanol) and then to the release of the extra proton to the ice to finally form CH_3OH . All the processes were found to be barrierless, *i.e.*, they occurred spontaneously during the geometry optimization. Despite the novelty of the path, author highlighted its dependence on the CH_3^+ interstellar abundance, a controversial aspect since its direct observation is difficult due to transition symmetry rules. In the same work, the author illustrated similar hydration mechanisms involving the formyl radical ($\text{HCO}^+ + 2\text{H}_2\text{O} \rightarrow \text{HCOOH} + \text{H}_3\text{O}^+$) and carbon monoxide ($\text{CO} + \text{OH}^+ + \text{H}_2\text{O} \rightarrow \text{CO}_2 + \text{H}_3\text{O}^+$).⁶⁷

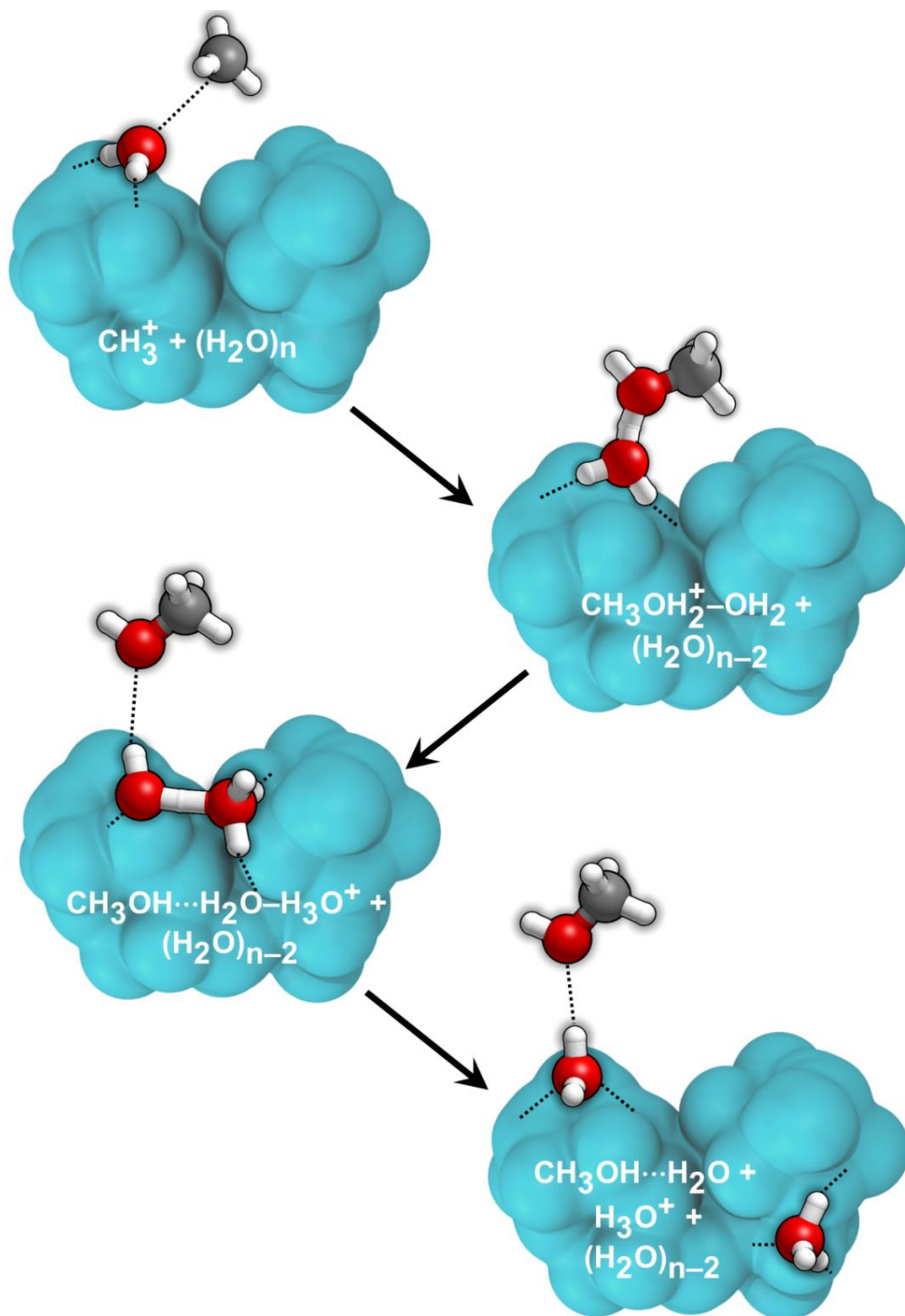


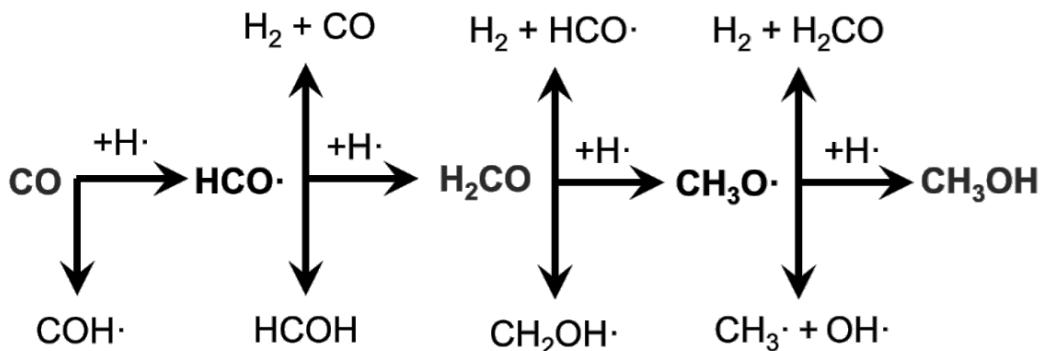
Figure 4.4 Water as a reactant: formation of CH₃OH from CH₃⁺. H₂O molecules directly involved in the reaction are explicitly shown, while the rest are rendered in light blue. Adapted from Ref. 67. Colour legend: oxygen in red, carbon in grey, hydrogen in white.

Two other reactions which have been extensively investigated are the hydration of hydrogen cyanide (HCN) and formaldehyde (H₂CO) to form formamide (NH₂CHO) and methyleneglycol (HOCH₂OH), respectively. The former was studied by Rimola *et al.*⁶⁸, the latter by Duvernay *et al.*⁶⁹ Both reactions were observed to possess too much high barriers to occur under ISM conditions, even if a definite catalytic role of the water matrix was highlighted. Indeed, waters are fundamental to stabilize transient charged species which form as intermediates (H₃O⁺/CN⁻ and H₃O⁺/OH⁻, respectively). Moreover, Duvernay *et al.* also found that the reaction is even more catalysed by the presence of ammonia (NH₃), which analogously form the NH₄⁺/OH⁻ ion pair, because of the increased acidity of the ammonium cation (NH₄⁺) with respect to the hydronium (H₃O⁺) one.⁶⁹ This is important because, as we will discuss in Section 4.4.4, the presence of ammonia with formaldehyde can also lead to the formation of aminomethanol (NH₂CH₂OH) an important intermediate of glycine.

4.4.2 Hydrogenation

Formaldehyde (H₂CO) and methanol (CH₃OH) are among the few molecules that have been widely detected as components of the icy mantles.⁵⁵ From the point of view of iCOMs formation, these two compounds are very important because they are the precursors of more complex species. For instance, their dissociation leads to the formation of HCO·, CH₃O· and CH₂OH· radicals, which can trigger reactions forming iCOMs.

Surface formation of H₂CO and CH₃OH, firstly postulated⁷⁰ and then confirmed experimentally,^{71,72} takes place through successive hydrogenation of CO, which was previously accreted onto dust grains (see **Scheme 4.1**, horizontal path). However, these reactions present competitive processes (represented by the vertical paths), which can make less efficient H₂CO and CH₃OH formation.



Scheme 4.1 Formation of formaldehyde (H₂CO) and methanol (CH₃OH) from successive H·-additions to carbon monoxide (CO, horizontal path). Vertical paths refer to competitive channels. Adapted from Ref. 73.

CO hydrogenation was investigated in a few works by David Woon⁷³ and Albert Rimola and co-workers,⁷⁴ adopting a cluster strategy at *post*-HF (former) and DFT (latter) levels of theory, with and without the inclusion of PCM. The authors concluded that the reaction barriers are slightly too high to occur in the ISM (12–15 kJ mol⁻¹) but a definitive catalytic effect with respect to the gas phase was highlighted. Specifically, as the CO molecule approaches the water ice matrix (DH sites) through its O atom, the DH··OC interaction produces a weakening of the C–O bond, making the C atom more prone to hydrogenation.

Apart from formaldehyde, two other important ISM molecules are formamide and methanimine (H₂C=NH). As regards the former, NH₂CHO attracted great attention after its detection in 1971 in the massive star forming regions Sgr B2 and in Orion KL1.⁹ Since then, dedicated observational campaigns have revealed its presence in a variety of star-forming regions, shock sites and protostellar objects,^{75–80} as well as comets,^{81,82} suggesting a relatively widespread abundance. The astrochemical relevance of formamide arises from manifold aspects: *i*) it is the simplest iCOM containing the four most essential elements for biological systems (*i.e.*, H, C, N and O), *ii*) it is the simplest organic compound containing the amide bond –C(=O)–NH–, the same bond joining amino acids into peptides, and *iii*) there is experimental evidence that it is an effective reactant for the

synthesis, in the presence of naturally-occurring minerals and oxides, of genetic nucleobases and their derivatives.^{83–90}

Song & Kästner studied the HNCO hydrogenation (*i.e.*, $\text{H}\cdot + \text{HNCO} \rightarrow \text{NH}_2\dot{\text{C}}\text{O}$) on an amorphous water ice cluster model at an hybrid QM/MM theory level.³⁷ The second hydrogenation leading to NH_2CHO was considered to be barrierless, involving a radical-radical reaction. This synthetic route was studied in view of the linear correlation between NH_2CHO and HNCO abundances in different sources.⁷⁷ On the ice surfaces, the calculated energy barrier adopting an Eley-Rideal mechanism was found to be 4 kJ mol^{-1} lower than in gas phase (31.8 and 36.2 kJ mol^{-1} respectively, too high to occur in the ISM) due to bond polarizing effects exerted by the ice (similar to hydrogenation of CO and H_2CO). Authors also investigated tunnelling effect thorough instanton theory but they concluded for the tunnelling inefficiency caused by the broad energy barrier width. These results were in agreement with the inefficient hydrogenation of HNCO ices found experimentally.⁹¹

For its part, methanimine can be synthesized from two successive hydrogenations of HCN according to **Scheme 4.2**.



Scheme 4.2 Hydrogenation of HCN leading to the formation of methanimine ($\text{CH}_2=\text{NH}$). $\text{CH}_2\text{N}\cdot$ and $\text{HCNH}\cdot$ are the two possible radical intermediates.

$\text{H}_2\text{C}=\text{NH}$ formation from HCN was investigated by Woon adopting an accurate *post*-HF methodology (with PCM),⁹² concluding that from the first $\text{H}\cdot$ -addition, $\text{CH}_2\text{N}\cdot$ forms was more favourably than $\text{HCNH}\cdot$ (energy barriers of 30.5 and of 53.6 kJ mol^{-1} , respectively), while the second one was considered to be barrierless.

4.4.3 Radical reactions

Radicals are fundamental constituents of the gas phase ISM because they probably form because of the action of cosmic rays and UV photons. Consequently, several authors dedicated attention to iCOMs formation reactions involving just one or two radical species.

One of the most important is probably the formamide formation from amino ($\text{H}_2\text{N}\cdot$) and formyl radical coupling ($\text{H}_2\text{N}\cdot + \text{H}\dot{\text{C}}\text{O} \rightarrow \text{NH}_2\text{CHO}$) that was studied by Rimola *et al.* at DFT level on a water cluster.⁶⁸ Results indicated that the actual biradical system (*i.e.*, the two radicals adsorbed on the ice surface with opposite spin states) was stable, precisely because of the interaction with the surface, and that the coupling had an energy barrier of 3 kJ mol^{-1} . However, it was also found that, when the two radicals are properly oriented, a direct H·-transfer from $\text{HCO}\cdot$ to $\text{NH}_2\cdot$ leading to $\text{CO} + \text{NH}_3$ occurred in a barrierless way. H·-transfers of this kind were also observed in acetaldehyde (CH_3CHO) formation $\text{H}\dot{\text{C}}\text{O} + \dot{\text{C}}\text{H}_3$ by Enrique-Romero *et al.*:⁹³ in this case, CH_3CHO formation competed with $\text{CO} + \text{CH}_4$ formation, pointing out that the reactivity between radicals not always leads to iCOMs formation.

Two examples of reaction involving just one radical are the hydration of the CN· radical ($\text{CN}\cdot + \text{H}_2\text{O} \rightarrow \text{HN}\dot{\text{C}}\text{OH}$, the formamide precursor) and the HO· carbonylation ($\text{HO}\cdot + \text{CO} \rightarrow \dot{\text{C}}\text{OOH}$, **Figure 4.5**). Both the reactions were found to be feasible in the ISM by Rimola and co-workers in two distinct works,^{68,94} making them as possible candidates to formamide and formic acid (HCOOH) formations.

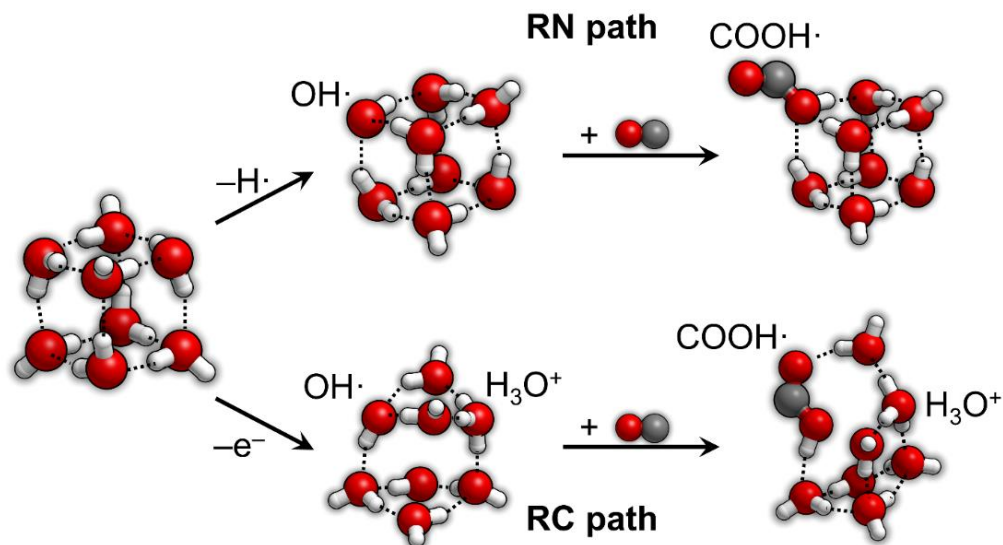


Figure 4.5 Carbonylation of the HO· radical to form $\dot{C}OOH$, a formic acid precursor, as simulated by Rimola *et al.*⁹⁴ through two paths (radical-neutral, RN, and radical-charged, RC). Colour legend: oxygen in red, hydrogen in white, carbon in grey.

4.4.4 The proton-relay mechanism

At the end of previous Section, we briefly discussed about the hydration of the CN· to form HNC $\dot{O}H$. On this latter species, the spin density is localized on the C atom, therefore the second (barrierless) H·-addition would result in the formation of the imine isomer of formamide, *i.e.* HN=CH–OH. However, the HN=CH–OH \rightarrow NH₂CHO reaction was found to have a relatively energy barrier of 40 kJ mol⁻¹.⁶⁸ An alternative, lower energy path involves the isomerization of the HNC $\dot{O}H$ radical to the NH₂ $\dot{C}O$ radical, which, under a further (barrierless) hydrogenation, can form formamide. The isomerization between the two radicals was also investigated in the same work by Rimola *et al.*⁶⁸ Here we take it as an example to illustrate one of the most important aspects of water in catalysing iCOMs formation, *i.e.* its capability to act as a hydrogen-transfer assistant, with hydrogen having a proton (H⁺) character. Upon this role, water molecules belonging to the ice exchange H⁺, *i.e.*, they receive one H⁺ releasing at the same time another one, helping the transfer process. This role of H⁺-transfer assistant

can be shared by different water molecules, thus establishing a H^+ -relay mechanism. Such a behaviour allows both the occurrence of H^+ -transfers through a chain of well-connected water molecules and the reduction of the geometrical strains in TS structures with respect to the gas phase, hence stabilizing them and lowering the energy barriers of the associated H^+ -transfer process. As an example, the TS structures for the $HNC\dot{O}H \rightarrow NH_2\dot{C}O$ isomerization for water ice acting as H^+ -transfer assistant and in gas phase are reported in **Figure 4.6A** and **B**, respectively: the strongly geometrical-strained four-members ring in the gas phase becomes a low strained ten-members ring when three water molecules are present.

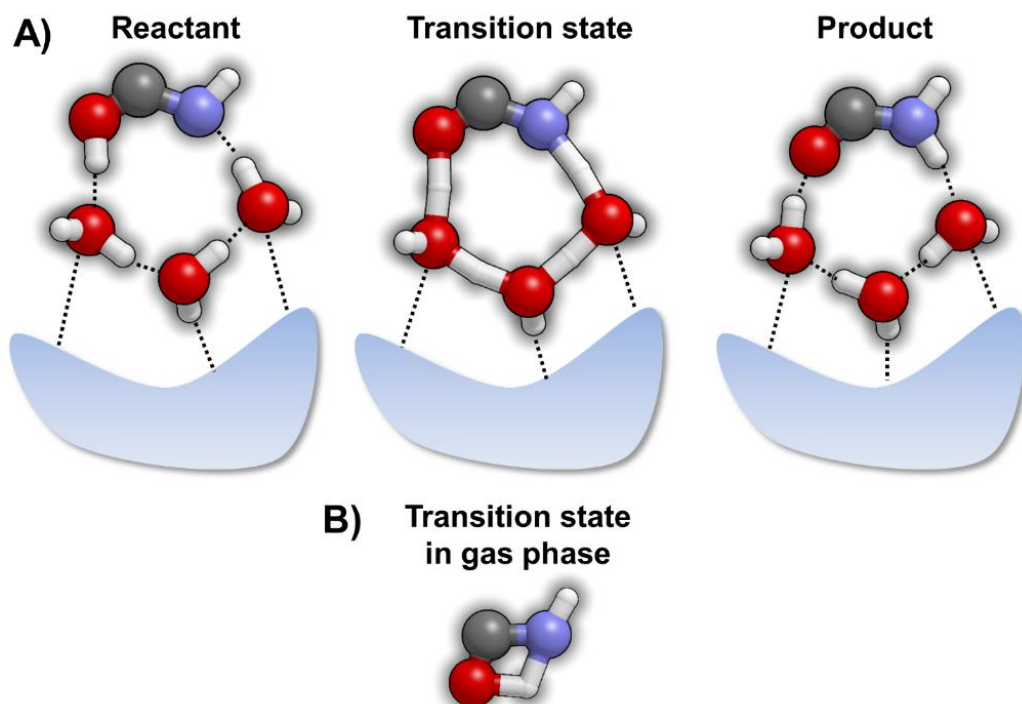


Figure 4.6 The proton-relay mechanism illustrated by the $HNC\dot{O}H \rightarrow NH_2\dot{C}O$ isomerization occurring (as a step of the $CN\cdot + H_2O + H\cdot \rightarrow NH_2CHO$ reaction).⁶⁸ A) a 10-atoms ring is formed in the TS structure when the reaction occurs on an ice surface. B) the strongly constrained gas phase TS structure.

Another reaction which well-illustrates the importance of water as H^+ -transfer is the formation of aminoacetonitrile (NH_2CH_2CN) from $H_2C=NH + HCN$ as studied by Koch *et al.*⁶⁴ (**Figure 4.7**)

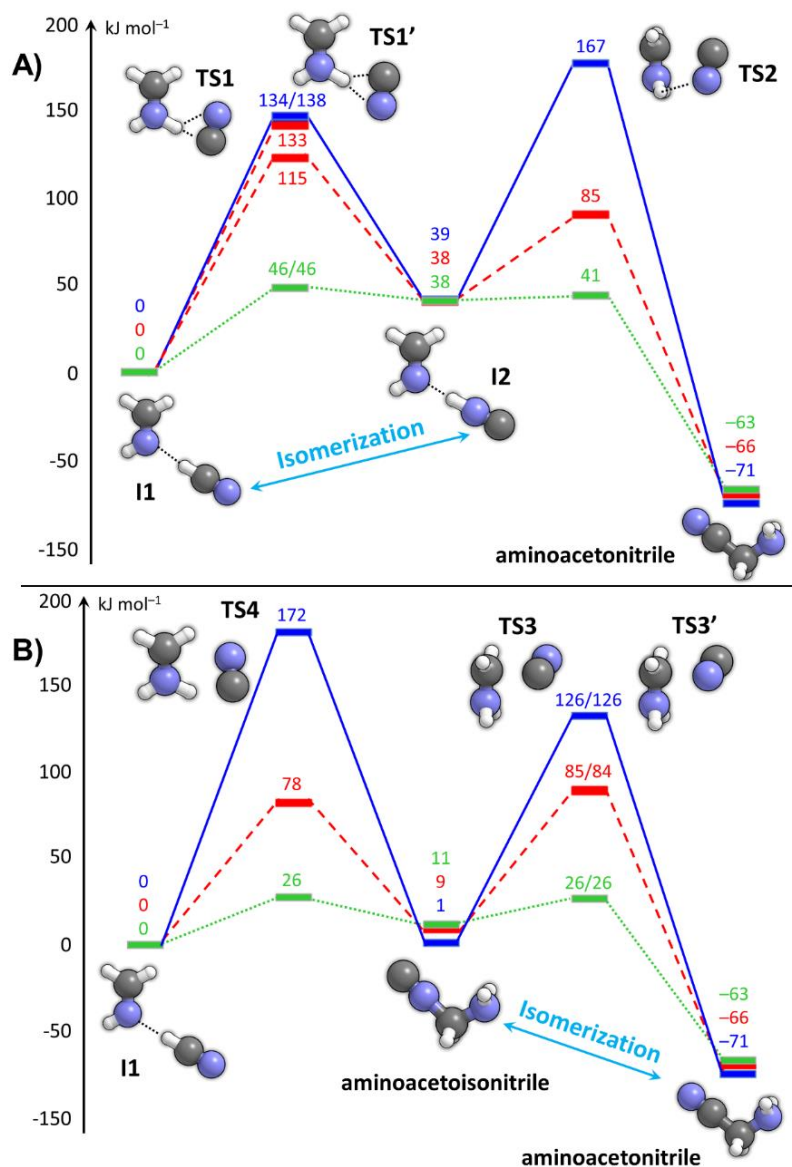
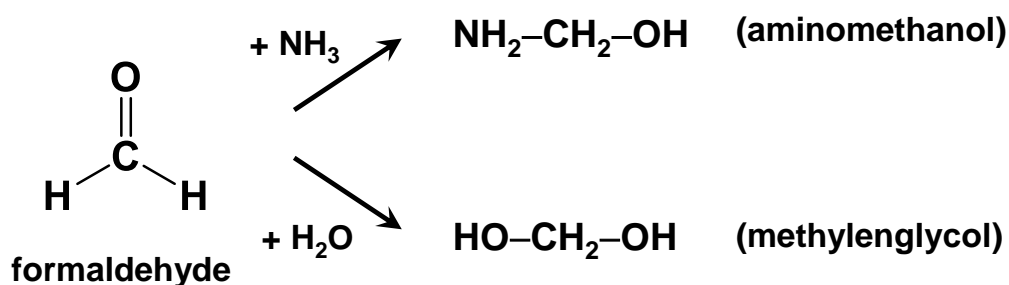


Figure 4.7 Free energy profiles at 50 K for the direct (A) and indirect (B) formation of NH_2CH_2CN from $H_2C=NH$ and HCN in gas phase (solid blue lines), in the presence of a $(H_2O)_2$ (dashed red lines) and $(H_2O)_{14}$ (dotted green lines) clusters. Adapted from Ref. 64. Optimized gas phase geometries are also shown. Colour legends: carbon in grey, nitrogen in blue and hydrogen in white.

This is an important reaction because aminoacetonitrile is another glycine precursors (Section 4.5). However, the direct $\text{H}_2\text{C}=\text{NH} + \text{HCN}$ reaction leads to the isomer aminoacetoisonitrile ($\text{NH}_2\text{CH}_2\text{NC}$, **Figure 4.7B**, from I1 through TS4). Direct formation of $\text{NH}_2\text{CH}_2\text{CN}$ can eventually occur from $\text{H}_2\text{C}=\text{NH} + \text{HNC}$. Therefore, in order to $\text{NH}_2\text{CH}_2\text{CN}$ to form, an isomerization needs to occur: this isomerization can involve either the HCN/HNC pair (**Figure 4.7A**) or the final products $\text{NH}_2\text{CH}_2\text{NC}/\text{NH}_2\text{CH}_2\text{CN}$ (**Figure 4.7B**). In the first case, proton-transfers play a major role, as it is clear from the comparison with gas phase data. The final example we provide where the importance of proton-transfers is usually outlined are the amination of carbonyl compounds according to the upper path of **Scheme 4.3**.



Scheme 4.3 Formation of aminomethanol and methylen glycol by addition of NH_3 and H_2O , respectively, to formaldehyde. An analogous scheme can be drawn in the acetaldehyde (CH_3CHO) and acetone ($\text{CH}_3(\text{CO})\text{CH}_3$) cases.

As **Scheme 4.3** illustrates, these reactions are in competition with the corresponding hydrations. We have already discussed formaldehyde hydration in Section 4.4.1. The amination reaction of formamide has been extensively studied by many authors. Woon,⁹⁵ Courmier *et al.*⁹⁶ and Rimola *et al.*⁹⁷ accounted for a concerted mechanism where the nucleophilic attack of ammonia causes the contemporary weakening of the $\text{C}=\text{O}$ double bond and the formation of a new $\text{O}-\text{H}$ bond through a proton-transfer from the N atom of ammonia to the O atom of formaldehyde. Despite this catalytic activity, all authors concluded for the

unfeasibility of the reaction in the ISM. Similar reactions for the acetaldehyde (CH_3CHO) and acetone ($\text{CH}_3(\text{CO})\text{CH}_3$) cases can be found in the works of Fresneau *et al.*^{98,99}

Chen & Woon,¹⁰⁰ and Riffet *et al.*⁶⁵ investigated an alternative mechanism where the nucleophilic attack spontaneously occurs thanks to the concerted action of the water molecules which stabilize the consequent formed zwitterionic species $\text{NH}_3^+-\text{CH}_2\text{O}^-$. Indeed, in these works, authors explicitly built water clusters to maximize such stabilization (**Figure 4.8**). However, situation like these ones could be unlike in real ice surfaces. The calculated energy barriers are lower than those from the concerted mechanism, making them feasible in the ISM.

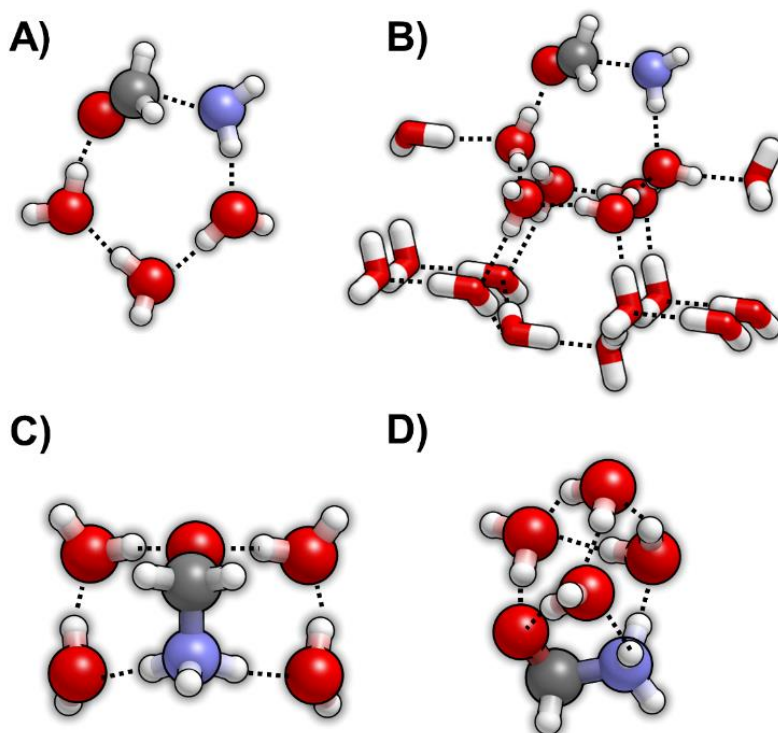


Figure 4.8 Representative initial structures for the formation of $\text{H}_2\text{NCH}_2\text{OH}$ from reaction of H_2CO with NH_3 . A) with a $(\text{H}_2\text{O})_3$ cluster model.⁹⁶ B) with a $(\text{H}_2\text{O})_{18}$ cluster model as water ice surface (atoms involved in the H^+ -transfer assistance were highlighted as balls).⁹⁷ C) with a $(\text{H}_2\text{O})_4$ cluster model;¹⁰⁰ and D) with a $(\text{H}_2\text{O})_4$ cluster model.⁶⁵ In these two later systems, the $\text{NH}_3^+-\text{CH}_2\text{O}^-$ zwitterion was spontaneously formed. Colour legend: oxygen in red, carbon in grey, nitrogen in blue and hydrogen in white.

4.5 iCOMs and life: the case of glycine

So far, we have discussed the formation of some iCOMs and related species under ISM-like conditions. However, the connection with biotic chemistry has not come up yet. In this Section, we will shortly review some results about an important astrochemical topic, that is the formation of the simplest amino acid, glycine ($\text{NH}_2\text{CH}_2\text{COOH}$).

Glycine has been identified in comets^{101–103} and its presence in meteorites (among other amino acids) is usual.¹⁰⁴ The traditional route for the synthesis of amino acids is the Strecker synthesis.¹⁰⁵ It involves different steps, some of them we have already commented above: *i*) reaction of an aldehyde (RCHO , with R being the lateral chain) with ammonia to give the corresponding aminoalcohol, *i.e.*, $\text{RCHO} + \text{NH}_3 \rightarrow \text{NH}_2\text{CH}(\text{R})\text{OH}$; *ii*) dehydration of the aminoalcohol to give the corresponding imine, *i.e.*, $\text{NH}_2\text{CH}(\text{R})\text{OH} \rightarrow \text{CH}(\text{R})=\text{NH} + \text{H}_2\text{O}$; *iii*) reaction of the imine with HCN to give the corresponding aminonitrile, *i.e.*, $\text{CH}(\text{R})=\text{NH} + \text{HCN} \rightarrow \text{NH}_2\text{CH}(\text{R})\text{CN}$, and *iv*) hydrolysis of the nitrile group which is converted firstly into an amide ($-\text{CONH}_2$) and finally to an acid ($-\text{COOH}$) group, *i.e.*, $\text{NH}_2\text{CH}(\text{R})\text{CN} + 2\text{H}_2\text{O} \rightarrow \text{NH}_2\text{H}(\text{R})\text{COOH} + \text{NH}_3$. These steps are schematically represented in **Figure 4.9** for the particular case of glycine formation, in which the starting aldehyde is H_2CO ($\text{R}=\text{H}$).

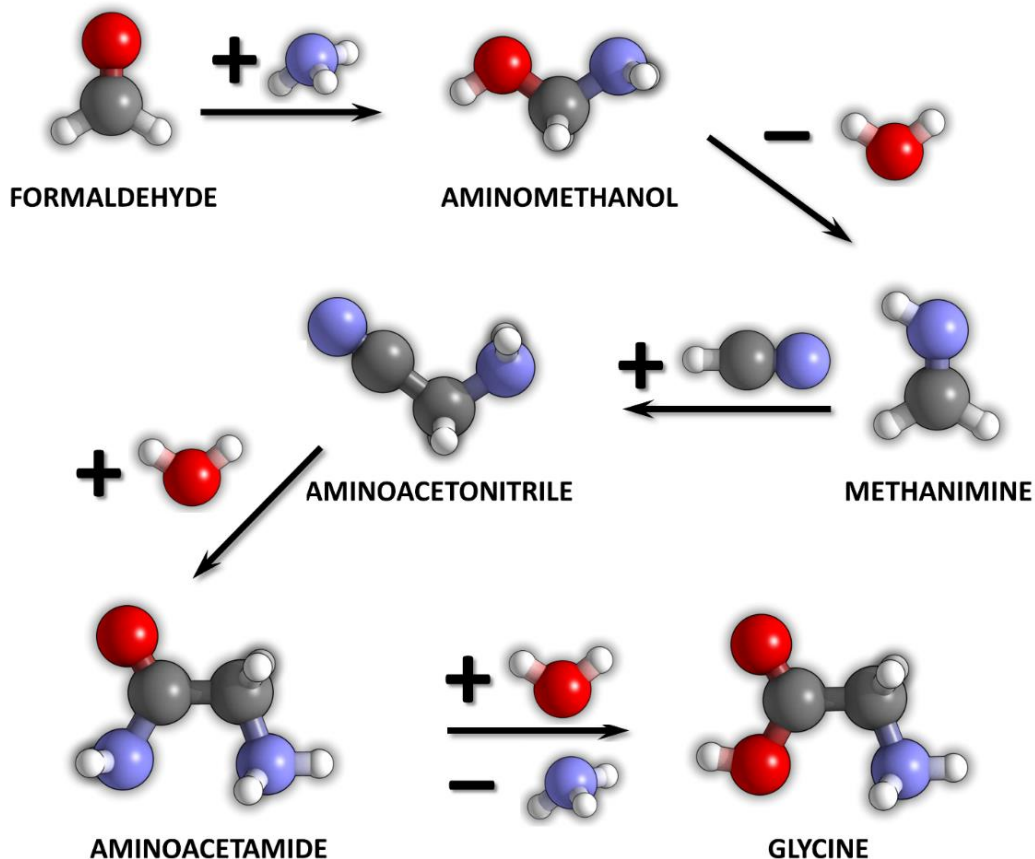


Figure 4.9 Different steps of the Strecker synthesis of glycine from formaldehyde. Colour code: oxygen in red, carbon in black, nitrogen in blue and hydrogen in white.

Interestingly, all the Strecker initial species (H₂CO, NH₃, HCN, H₂O) and some intermediates of glycine formation (NH₂CH₂OH, CH₂=NH and NH₂CH₂CN) have been observed in the ISM; therefore, Rimola *et al.* simulated the whole glycine synthesis on a water ice surface model of 18 H₂O molecules in PCM.⁹⁷ We have already commented some of the steps in **Figure 4.9**; however, for the sake of completeness, we deal here the whole reaction. Briefly, the first step (amination of formaldehyde to form aminomethanol) requires about 40 kJ mol⁻¹ to occur, while the two next steps (dehydration of aminomethanol to methanimine and HCN addition to methanimine to form aminoacetonitrile) require even more energy (about 89 and 73 kJ mol⁻¹). The hydrolysis of the aminoacetonitrile, which

involves the successive nucleophilic attack of two H₂O molecules on the C atom of the nitrile are the most energy requiring, with the highest barriers of the whole process (159 and 163 kJ mol⁻¹). Because of this high energetics, authors concluded that the entire Strecker synthesis is unlikely to occur at the cryogenic temperatures, advocating for external energy inputs such as UV radiation and cosmic rays to overcome the barriers.

These findings stimulated the same authors to investigate an alternative route for glycine formation accounting for these energy inputs.⁹⁴ In Section 4.4.3 we reported the formation of $\dot{\text{C}}\text{OOH}$ on two processed water ice clusters (see **Figure 4.5**). That work was within the context of glycine formation, in which the next step after $\dot{\text{C}}\text{OOH}$ formation was its reactivity with CH₂=NH. On the RN cluster, such a coupling, leading to formation of the $\dot{\text{N}}\text{HCH}_2\text{COOH}$ radical, was computed to have an energy barrier of 50 kJ mol⁻¹. On the RC cluster, authors identified an almost barrierless proton-transfer from the H₃O⁺ species to CH₂=NH, and the formed CH₂=NH₂⁺ cation coupled to $\dot{\text{C}}\text{OOH}$ through a lower energy barrier of 26 kJ mol⁻¹, to form the NH₂CH₂COOH^{·+} radical cation. Due to the enhanced acidity of the CH₂ group of this radical cation, authors simulated that one H atom could be transferred to the ice (energy barrier of ≈ 30 kJ mol⁻¹) so that the NH₂ $\dot{\text{C}}\text{HCOOH}$ radical was ready to react with other radicals, to form different amino acids (*e.g.*, H[·] or H₃C[·] to give glycine or alanine, respectively).

Alternative paths beyond the Strecker synthesis have also been computed. In a couple of works by Nhlabatsi *et al.*, authors investigated the formation of interstellar glycine adopting two different channels based on the CH₂=NH reactivity: *i*) CH₂=NH + CO + H₂O → NH₂CH₂COOH,¹⁰⁶ and *ii*) CH₂=NH + CO₂ + H₂ → NH₂CH₂COOH.¹⁰⁷ For both reactions, authors found a concerted mechanism in which all the components reacted synchronically (**Figure 4.10**). Despite the elegance of these mechanisms, the energy barriers were found to be 172 kJ mol⁻¹ (142 kJ mol⁻¹ if assisted by an additional H₂O molecule) and 303 kJ

mol^{-1} . For these two reactions, authors also investigated a stepwise mechanism initiated by the formation of the $\text{C}(\text{OH})_2$ carbene (via $\text{CO} + \text{H}_2\text{O}$ and $\text{CO}_2 + \text{H}_2$ reactions, respectively), which upon reaction with $\text{CH}_2=\text{NH}$ led to glycine. Although this later step was found to have a relatively low energy barrier (38 kJ mol^{-1}), the processes were hindered by the high energy barriers of the carbene formation (270 and 300 kJ mol^{-1} , respectively).

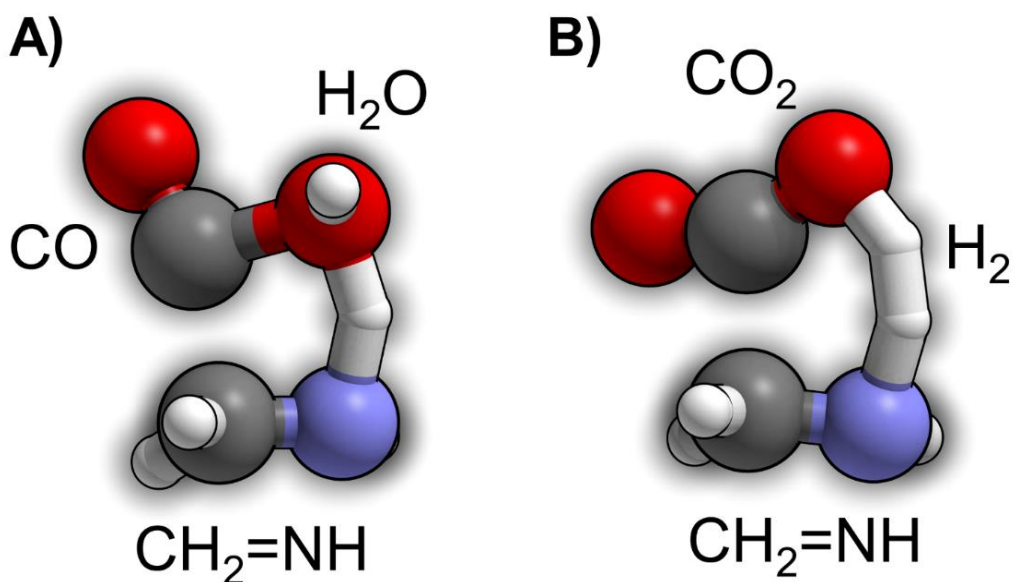
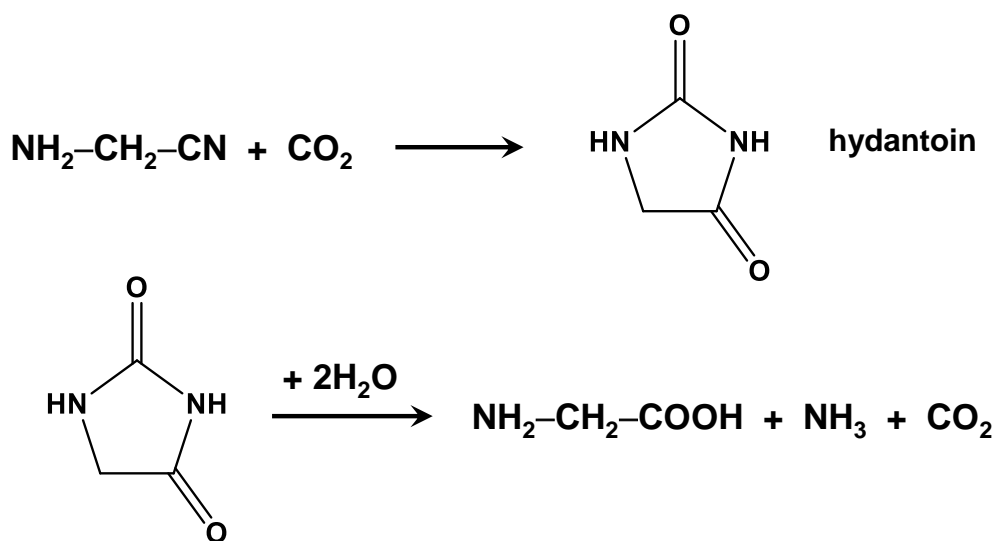


Figure 4.10 Transition states for the concerted formation of glycine from $\text{CH}_2=\text{NH} + \text{CO} + \text{H}_2\text{O}$ (A, Ref. 106) and $\text{CH}_2=\text{NH} + \text{CO}_2 + \text{H}_2$ (B, Ref. 107). Colour code: oxygen in red, carbon in black, nitrogen in blue and hydrogen in white.

Lee and Choe investigated the formation of glycine from HCN oligomers reacting with H_2O .¹⁰⁸ It was found that the HCN trimer, $\text{NH}_2\text{CH}(\text{CN})_2$, reacted with one H_2O molecule to form $\text{NH}_2\text{CH}(\text{CN})\text{CONH}_2$, and that water additions to this compound led to glycine formation through different paths, which were catalysed by one water molecule assisting the H^+ -transfers. It was found the former reaction exhibited an energy barrier of 106 kJ mol^{-1} and that among the different investigated paths, the one involving $\text{NH}_2\text{CH}(\text{CN})\text{CONH}_2 + 2\text{H}_2\text{O} \rightarrow \text{glycine} + \text{HNCO} + \text{NH}_3$ was the most energetically favourable, with an overall energy barrier of 169 kJ mol^{-1} .

Finally, Kayanuma *et al.* investigated the formation of glycine *via* a hydantoin mechanism.¹⁰⁹ Hydantoin (2,4-imidazolidinedione) is an important precursor yielding glycine upon hydrolysis and it can be formed by CO₂ addition to aminoacetonitrile (see **Scheme 4.4**). Hydantoin has been identified in Murchison and Yamato-791198 meteorites.^{110,111} The reaction was simulated by the authors in the presence of two H₂O molecules acting as proton-transfer catalysts. Reactivity of aminoacetonitrile with CO₂ leading to hydantoin involved several steps, the highest energy barrier being 111 kJ mol⁻¹. Hydantoin hydrolysis, performed by two H₂O molecules and accompanied by NH₃ and CO₂ elimination, exhibited intrinsic energy barriers between 176-255 kJ mol⁻¹. Authors pointed out that these energy barriers were too high to be overcome at cryogenic conditions even considering interstellar timescales (10⁶ years).



Scheme 4.4 Formation of hydantoin by reaction of aminoacetonitrile NH₂CH₂CN with CO₂ (above) and its hydrolysis to give glycine (below).

4.6 Concluding remarks

In this Chapter, we briefly reviewed some of the computational works dealing with iCOMs on ice mantles. They are not only focused on standard iCOMs, but also to simpler organic compounds as well as those of increased complexity, *i.e.*,

formation of H_2CO and CH_3OH , NH_2CHO , acidic organic species (*e.g.*, HCOOH), aminoalcohols, $\text{CH}_2=\text{NH}$, acetonitriles and glycine. The different reaction-types yielding their formation have also been revised theoretically: hydrogenation, radical, hydration and amination reactions. For a more detailed analysis, please refer to Ref. 1.

Since water is the main constituent of interstellar ices, ice mantles were simulated by either explicit water molecules or implicitly with PCM solvation models. It was shown that water exerted from moderate to strong catalytic effects in the reactions. They were particularly important when water molecules were explicitly considered due to their role as H^+ -transfer assistants, in which the energy barriers decreased as a consequence of the lower geometrical strains in TS structures than in gas phase. In other cases, water stabilized ion pairs, allowing the occurrence of ion-induced reactions. Despite these catalytic effects, most of the energy barriers were calculated to be significantly high to occur at typical temperatures of MCs (10-25 K) and, accordingly, activation by temperature was in most of the cases claimed.

All the reviewed works have contributed to improve our know-how of the iCOMs formation on ice mantles, by figuring out the processes from a molecular standpoint, providing exclusive structural and energetic features, and helping us to assess their feasibility under interstellar conditions. However, several relevant aspects remain still missing.

One of them deals with the plausibility of the occurrence of water-assisted H^+ -transfer processes adopting a relay mechanism on ice surface mantles. To take place, the implicated waters must be connected by H-bond interactions in a suitable way as they can be capable to donate and receive H^+ properly. However, whether this situation is indeed present or not in actual ice mantles and how the structural state and the presence of other ice components can affect this water catalytic property are still open questions that require further investigations, to be

possible by combining experimental measurements with quantum chemical calculations.

Another interesting aspect is the reliability of the surface models representing the ice mantles. Among the reviewed works, they consisted of either minimal $(\text{H}_2\text{O})_n$ ($n = 1-4$) clusters, in which the mobility of the H_2O molecules was at its maximum, larger clusters ($n > 18-20$), and only in the most recent works they were represented by amorphous clusters of hundreds of H_2O molecules, while adoption of periodic models is very scarce. However, theoretical results can dramatically depend on the ice model and the evaluation of this aspect, *i.e.*, how results are actually affected by the structure and type of the ice model, should represent an important topic of future works dealing with iCOMs formation on atomistic ice models. Accordingly, comprehensive studies, and consistent from a methodological viewpoint, assessing the reliability of the different ice models and analysing how similar/different are the results when using different ice models, are of great importance.

The role of water ice as catalyst has been clearly evidenced here. However, ice mantles are not limited to this role only. For instance, they can also act as reactant suppliers. In the reviewed works, this role was shown when the reactants were also usual ice components, *e.g.*, H_2O itself or CO and NH_3 . However, there are two other roles which have hardly been investigated. One is as reactant concentrator. Indeed, ice surfaces can immobilize and concentrate species, keeping them in close proximity for subsequent reactions. Assessing this role can be carried out by calculating the interaction energies between the reactants and the ice surfaces, which can indicate how strongly reactants are retained on the surfaces. Interaction energies were usually provided in most of the reviewed works but their relationship with the capability of surface ices to act as reactant suppliers is not usual. Another way to assess this role is by simulating the diffusivity of the reactive species. This can be performed with AIMDs, in which

retention times can be provided. Nevertheless, AIMD-based studies devoted to the diffusion properties of the reactants are very scarce. The other role is as third body, *i.e.*, ices quickly absorb the reaction energy excess, thereby stabilizing the product. This role can be investigated theoretically with AIMDs at NVE, where the total energy E is conserved along the whole simulation. These simulations allow elucidating how the nascent reaction energies are partitioned, *i.e.*, what amount transforms into translational and internal energies of the product and what dissipates among the ice. Studies focused on this aspect are also very rare. Remarkably, the lack of this kind of works also evidences that use of AIMDs is very scarce in iCOMs formation investigations, a critical aspect since dynamic effects can be of great relevance especially in those reactions in which thermal heating is essential.

Finally, we address some words claiming for the need to simulate non-investigated reactions. Several important synthetic routes have indeed been simulated successfully but others, which are also important, are still missing. For instance, radical-radical couplings have scarcely been investigated: the $\text{HCO}\cdot + \text{H}_2\text{N}\cdot$ and $\text{H}\dot{\text{C}}\text{O} + \text{H}_3\text{C}\cdot$ reactions have been simulated,^{68,93} while other radical couplings are still to be studied. This is quite surprising since these reactions are assumed to be the main channels to form iCOMs usually detected in diverse astrophysical objects, as mentioned in the Introduction. In the same line, computational simulations have also been useful to identify new formation paths which are not normally accounted for in astrochemical modelling schemes (*e.g.*, $\text{CN}\cdot + \text{H}_2\text{O}$). Moreover, for some identified iCOMs, no reaction mechanisms have been proposed and simulated (*e.g.*, acetone CH_3COCH_3 or vinyl alcohol $\text{CH}_2=\text{CHOH}$). Because of that, extensive quantum mechanical simulations devoted to novel “on-surface” formation paths to check their plausibility will be of great value. In relation to cometary and meteoritic biomolecules, the focus has been done essentially on glycine formation (while no simulations have been done

for the rest of amino acids), on particular paths for nucleobases (see Ref. 1) whereas sugars formation routes have not been addressed. Moreover, understanding the role of the cometary and meteoritic minerals and ices will help us to get a better understanding on the origin of these compounds.

Bibliography

- (1) Zamirri, L.; Ugliengo, P.; Ceccarelli, C.; Rimola, A. Quantum Mechanical Investigations on the Formation of Complex Organic Molecules on Interstellar Ice Mantles. Review and Perspectives. *ACS Earth Sp. Chem.* **2019**, *3*, 1499–1523.
- (2) McGuire, B. A. 2018 Census of Interstellar, Circumstellar, Extragalactic, Protoplanetary Disk, and Exoplanetary Molecules. *Astrophys. J. Suppl. Ser.* **2018**, *239*, 17 (48 pp).
- (3) Herbst, E.; van Dishoeck, E. F. Complex Organic Interstellar Molecules. *Annu. Rev. Astron. Astrophys.* **2009**, *47*, 427–480.
- (4) Ceccarelli, C.; Caselli, P.; Fontani, F.; Neri, R.; López-Sepulcre, A.; Codella, C.; Feng, S.; Jiménez-Serra, I.; Lefloch, B.; Pineda, J. E.; *et al.* Seeds Of Life In Space (SOLIS): The Organic Composition Diversity at 300–1000 Au Scale in Solar-Type Star-Forming Regions. *Astrophys. J.* **2017**, *850*, 176 (15 pp).
- (5) Ceccarelli, C.; Loinard, L.; Castets, A.; Faure, A.; Lefloch, B. Search for Glycine in the Solar Type Protostar IRAS 16293-2422. *Astron. Astrophys.* **2000**, *362*, 1122–1126.
- (6) Cazaux, S.; Tielens, A. G. G. M.; Ceccarelli, C.; Castets, A.; Wakelam, V.; Caux, E.; Parise, B.; Teyssier, D. The Hot Core around the Low-Mass Protostar IRAS 16293-2422: Scoundrels Rule! *Astrophys. J.* **2003**, *593*, L51–L55.
- (7) Ligterink, N. F. W.; Calcutt, H.; Coutens, A.; Kristensen, L. E.; Bourke, T. L.; Drozdovskaya, M. N.; Müller, H. S. P.; Wampfler, S. F.; van der Wiel, M. H. D.; van Dishoeck, E. F.; *et al.* The ALMA-PILS Survey: Stringent Limits on Small Amines and Nitrogen-Oxides towards IRAS 16293–2422B. *Astron. Astrophys.* **2018**, *619*, A28 (11 pp).

- (8) Caselli, P.; Ceccarelli, C. Our Astrochemical Heritage. *Astron. Astrophys. Rev.* **2012**, *20*, 56.
- (9) Rubin, R. H.; Swenson, G. W., J.; Benson, R. C.; Tigelaar, H. L.; Flygare, W. H. Microwave Detection of Interstellar Formamide. *Astrophys. J.* **1971**, *169*, L39–L44.
- (10) Charnley, S. B.; Tielens, A. G. G. M.; Millar, T. J. On the Molecular Complexity of the Hot Cores in Orion A-Grain Surface Chemistry as “The Last Refuge of the Scoundrel.” *Astrophys. J.* **1992**, *339*, L71–L74.
- (11) Balucani, N.; Ceccarelli, C.; Taquet, V. Formation of Complex Organic Molecules in Cold Objects: The Role of Gas-Phase Reactions. *Mon. Not. R. Astron. Soc.* **2015**, *449*, L16–L20.
- (12) Charnley, S. B.; Herbst, E. Reactive Desorption and Radiative Association as Possible Drivers of Complex Molecule Formation in the Cold Interstellar Medium. *Astrophys. J.* **2013**, *769*, 34 (9 pp).
- (13) Garrod, R. T.; Herbst, E. Formation of Methyl Formate and Other Organic Species in the Warm-up Phase of Hot Molecular Cores. *Astron. Astrophys.* **2006**, *457*, 927–936.
- (14) Öberg, K. I.; Garrod, R. T.; Dishoeck, E. F. van; Linnartz, H. Formation Rates of Complex Organics in UV Irradiated CH₃OH-Rich Ices. I. Experiments. *Astron. Astrophys.* **2009**, *504*, 891–913.
- (15) Ruaud, M.; Loison, J. C.; Hickson, K. M.; Gratier, P.; Hersant, F.; Wakelam, V. Modelling Complex Organic Molecules in Dense Regions: Eley–Rideal and Complex Induced Reaction. *Mon. Not. R. Astron. Soc.* **2015**, *447*, 4004–4017.
- (16) Linnartz, H.; Ioppolo, S.; Fedoseev, G. Atom Addition Reactions in Interstellar Ice Analogues. *Int. Rev. Phys. Chem.* **2015**, *34*, 205–237.

- (17) Barone, V.; Latouche, C.; Skouteris, D.; Vazart, F.; Balucani, N.; Ceccarelli, C.; Lefloch, B. Gas-Phase Formation of the Prebiotic Molecule Formamide: Insights from New Quantum Computations. *Mon. Not. R. Astron. Soc.* **2015**, *453*, L31–L35.
- (18) Vazart, F.; Calderini, D.; Puzzarini, C.; Skouteris, D.; Barone, V. State-of-the-Art Thermochemical and Kinetic Computations for Astrochemical Complex Organic Molecules: Formamide Formation in Cold Interstellar Clouds as a Case Study. *J. Chem. Theory Comput.* **2016**, *12*, 5385–5397.
- (19) Skouteris, D.; Vazart, F.; Ceccarelli, C.; Balucani, N.; Puzzarini, C.; Barone, V. New Quantum Chemical Computations of Formamide Deuteration Support Gas-Phase Formation of This Prebiotic Molecule. *Mon. Not. R. Astron. Soc.* **2017**, *468*, L1–L5.
- (20) Wakelam, V.; Loison, J.; Mereau, R.; Ruaud, M. Binding Energies : New Values and Impact on the Efficiency of Chemical Desorption. *Mol. Astrophys.* **2017**, *6*, 22–35.
- (21) Holtom, P. D.; Bennett, C. J.; Osamura, Y.; Mason, N. J.; Kaiser, R. I. A Combined Experimental and Theoretical Study on the Formation of the Amino Acid Glycine ($\text{NH}_2\text{CH}_2\text{COOH}$) and Its Isomer (CH_3NHCOOH) in Extraterrestrial Ices. *Astrophys. J.* **2005**, *626*, 940–952.
- (22) Walch, S. P.; Bauschlicher Jr, C. B.; Ricca, A.; Bakes, E. L. O. On the Reaction $\text{CH}_2\text{O} + \text{NH}_3 \rightarrow \text{CH}_2\text{NH} + \text{H}_2\text{O}$. *Chem. Phys. Lett.* **2001**, *333*, 6–11.
- (23) Redondo, P.; Barrientos, C.; Largo, A. Some Insights into Formamide Formation through Gas-Phase Reactions in the Interstellar Medium. *Astrophys. J.* **2013**, *780*, 181 (7 pp).
- (24) Huang, L. C. L.; Asvany, O.; Chang, A. H. H.; Balucani, N.; Lin, S. H.; Lee, Y. T.; Kaiser, R. I. Crossed Beam Reaction of Cyano Radicals with

- Hydrocarbon Molecules. IV. Chemical Dynamics of Cyanoacetylene (HCCCN; $X^1\Sigma^+$) Formation from Reaction of CN($X^2\Sigma^+$) with Acetylene, $C_2H_2(X^1\Sigma_g^+)$. *J. Chem. Phys.* **2000**, *113*, 8656–8666.
- (25) Laidler, K. J.; King, M. C. Development of Transition-State Theory. *J. Phys. Chem.* **1983**, *87*, 2657–2664.
- (26) Eyring, H. The Activated Complex in Chemical Reactions. *J. Chem. Phys.* **1935**, *3*, 107–115.
- (27) Evans, M. G.; Polanyi, M. Some Applications of the Transition State Method to the Calculation of Reaction Velocities, Especially in Solution. *Trans. Faraday Soc.* **1935**, *31*, 875–894.
- (28) Atkins, P.; de Paula, J. *Physical Chemistry*; Oxford University Press: Oxford, England, UK, 2006.
- (29) Williams, D. A. The Interstellar Medium: An Overview. In *Solid State Astrochemistry*; Pirronello, V., Krelowski, J., Manicò, G., Eds.; Proceedings of the NATO Advanced Study Institute on Solid State Astrochemistry, 2000; pp 1–20.
- (30) Larson, R. B. The Evolution of Molecular Clouds. In *The Structure and Content of Molecular Clouds 25 Years of Molecular Radioastronomy*; Wilson, T. L., Johnston, K. J., Eds.; Springer: New York City, NY, USA, 1993; pp 13–28.
- (31) Meisner, J.; Kästner, J. Atom Tunneling in Chemistry. *Angew. Chemie Int. Ed.* **2016**, *55*, 5400–5413.
- (32) Eckart, C. The Penetration of a Potential Barrier by Electrons. *Phys. Rev.* **1930**, *35*, 1303–1309.
- (33) Miller, W. H. Semiclassical Limit of Quantum Mechanical Transition State Theory for Nonseparable Systems. *J. Chem. Phys.* **1975**, *62*, 1899–1906.

- (34) Richardson, J. O. Derivation of Instanton Rate Theory from First Principles. *J. Chem. Phys.* **2016**, *144*, 114106 (5 pp).
- (35) Andersson, S.; Nyman, G.; Arnaldsson, A.; Manthe, U.; Jónsson, H. Comparison of Quantum Dynamics and Quantum Transition State Theory Estimates of the H + CH₄ Reaction Rate. *J. Phys. Chem. A* **2009**, *113*, 4468–4478.
- (36) Feynman, R. P. Space-Time Approach to Non-Relativistic Quantum Mechanics. *Rev. Mod. Phys.* **1948**, *20*, 367–387.
- (37) Song, L.; Kästner, J. Formation of the Prebiotic Molecule NH₂CHO on Astronomical Amorphous Solid Water Surfaces: Accurate Tunneling Rate Calculations. *Phys. Chem. Chem. Phys.* **2016**, *18*, 29278–29285.
- (38) Rommel, J. B.; Goumans, T. P. M.; Kästner, J. Locating Instantons in Many Degrees of Freedom. *J. Chem. Theory Comput.* **2011**, *7*, 690–698.
- (39) McQuarrie, D. A.; Simon, J. D. *Physical Chemistry. A Molecular Approach*; University Science Books: Sausalito, CA, USA, 1997.
- (40) Demichelis, R.; Bruno, M.; Massaro, F. R.; Prencipe, M.; de la Pierre, M.; Nestola, F. First-Principle Modelling of Forsterite Surface Properties: Accuracy of Methods and Basis Sets. *J. Comput. Chem.* **2015**, *36*, 1439–1445.
- (41) Zamirri, L.; Corno, M.; Rimola, A.; Ugliengo, P. Forsterite Surfaces as Models of Interstellar Core Dust Grains: Computational Study of Carbon Monoxide Adsorption. *ACS Earth Sp. Chem.* **2017**, *1*, 384–398.
- (42) Mukhopadhyay, S.; Bailey, C. L.; Wander, A.; Searle, B. G.; Muryn, C. A. Stability of the AlF₃ (0 0 -1 2) Surface in H₂O and HF Environments: An Investigation Using Hybrid Density Functional Theory and Atomistic Thermodynamics. *Surf. Sci.* **2007**, *601*, 4433–4437.

- (43) Bailey, C. L.; Mukhopadhyay, S.; Wander, A.; Searle, B. G.; Harrison, N. M. Structure and Stability of α -AlF₃ Surfaces. *J. Phys. Chem. C* **2009**, *113*, 4976–4983.
- (44) Zamirri, L.; Casassa, S.; Rimola, A.; Segado-Centellas, M.; Ceccarelli, C.; Ugliengo, P. IR Spectral Fingerprint of Carbon Monoxide in Interstellar Water Ice Models. *Mon. Not. R. Astron. Soc.* **2018**, *480*, 1427–1444.
- (45) Chiatti, F.; Corno, M.; Sakhno, Y.; Martra, G.; Ugliengo, P. Revealing Hydroxyapatite Nanoparticle Surface Structure by CO Adsorption: A Combined B3LYP and Infrared Study. *J. Phys. Chem. C* **2013**, *117*, 25526–25534.
- (46) Boese, A. D.; Sauer, J. Accurate Adsorption Energies for Small Molecules on Oxide Surfaces: CH₄/MgO(001) and C₂H₆/MgO(001). *J. Comput. Chem.* **2016**, *37*, 2374–2385.
- (47) Boese, A. D.; Sauer, J. Accurate Adsorption Energies of Small Molecules on Oxide Surfaces: CO-MgO(001). *Phys. Chem. Chem. Phys.* **2013**, *15*, 16481–16493.
- (48) Escamilla-Roa, E.; Moreno, F. Adsorption of Glycine on Cometary Dust Grains: II — Effect of Amorphous Water Ice. *Planet. Space Sci.* **2013**, *75*, 1–10.
- (49) Escamilla-Roa, E.; Moreno, F. Adsorption of Glycine by Cometary Dust: Astrobiological Implications. *Planet. Space Sci.* **2012**, *70*, 1–9.
- (50) Al-Halabi, A.; Kleyn, A. W.; Van Dishoeck, E. F.; Van Hemert, M. C.; Kroes, G. J. Sticking of Hyperthermal CO to the (0001) Face of Crystalline Ice. *J. Phys. Chem. A* **2003**, *107*, 10615–10624.
- (51) Civalleri, B.; Maschio, L.; Ugliengo, P.; Zicovich-Wilson, C. M. Role of Dispersive Interactions in the CO Adsorption on MgO(001): Periodic

- B3LYP Calculations Augmented with an Empirical Dispersion Term. *Phys. Chem. Chem. Phys.* **2010**, *12*, 6382–6389.
- (52) Chung, L. W.; Sameera, W. M. C.; Ramozzi, R.; Page, A. J.; Hatanaka, M.; Petrova, G. P.; Harris, T. V.; Li, X.; Ke, Z.; Liu, F.; *et al.* The ONIOM Method and Its Applications. *Chem. Rev.* **2015**, *115*, 5678–5796.
- (53) Svensson, M.; Humbel, S.; Froese, R. D. J.; Matsubara, T.; Sieber, S.; Morokuma, K. ONIOM: A Multi-Layered Integrated MO + MM Method for Geometry Optimizations and Single Point Energy Predictions. A Test for Diels-Alder Reactions and Pt(P(*t*-Bu)₃)₂+H₂O Oxidative Addition. *J. Phys. Chem.* **1996**, *100*, 19357–19363.
- (54) Dapprich, S.; Komáromi, I.; Byun, K. S.; Morokuma, K.; Frisch, M. J. A New ONIOM Implementation in Gaussian 98. 1. The Calculation of Energies, Gradients and Vibrational Frequencies and Electric Field Derivatives. *J. Mol. Struct.* **1999**, *462*, 1–21.
- (55) Boogert, A. C. A.; Gerakines, P. A.; Whittet, D. C. B. Observations of the Icy Universe. *Annu. Rev. Astron. Astrophys.* **2015**, *53*, 541–583.
- (56) Collings, M. P.; Frankland, V. L.; Lasne, J.; Marchione, D.; Rosu-Finsen, A.; McCoustra, M. R. S. Probing Model Interstellar Grain Surfaces with Small Molecules. *Mon. Not. R. Astron. Soc.* **2015**, *449*, 1826–1833.
- (57) Collings, M. P.; Anderson, M. A.; Chen, R.; Dever, J. W.; Viti, S.; Williams, D. A.; McCoustra, M. R. S. A Laboratory Survey of the Thermal Desorption of Astrophysically Relevant Molecules. *Mon. Not. R. Astron. Soc.* **2004**, *354*, 1133–1140.
- (58) Garrod, R. T. Three-Dimensional, Off-Lattice Monte Carlo Kinetics Simulations of Interstellar Grain Chemistry and Ice Structure. *Astron. J.* **2013**, *778*, 150 (14 pp).

- (59) Fraser, H. J.; Collings, M. P.; Dever, J. W.; McCoustra, M. R. S. Using Laboratory Studies of CO-H₂O Ices to Understand the Non-Detection of a 2152 cm⁻¹ (4.647 μm) Band in the Spectra of Interstellar Ices. *Mon. Not. R. Astron. Soc.* **2004**, *353*, 59–68.
- (60) Sandford, S. A.; Allamandola, L. J.; Tielens, A. G. G. M.; Valero, G. J. Laboratory Studies of the Infrared Spectral Properties of CO in Astrophysical Ices. *Astrophys. J.* **1988**, *329*, 498–510.
- (61) Cossi, M.; Rega, N.; Scalmani, G.; Barone, V. Energies, Structures, and Electronic Properties of Molecules in Solution with the C-PCM Solvation Model. *J. Comput. Chem.* **2003**, *24*, 669–681.
- (62) Tomasi, J.; Mennucci, B.; Cammi, R. Quantum Mechanical Continuum Solvation Models. *Chem. Rev.* **2005**, *105*, 2999–3094.
- (63) Woon, D. E. Ab Initio Quantum Chemical Studies of Reactions in Astrophysical Ices 4. Reactions in Ices Involving HCOOH, CH₂NH, HCN, HNC, NH₃, and H₂O. *Int. J. Quantum Chem.* **2002**, *88*, 226–235.
- (64) Koch, D. M.; Toubin, C.; Peslherbe, G. H.; Hynes, J. T. A Theoretical Study of the Formation of the Aminoacetonitrile Precursor of Glycine on Icy Grain Mantles in the Interstellar Medium. *J. Phys. Chem. C* **2008**, *112*, 2972–2980.
- (65) Riffet, V.; Frison, G.; Bouchoux, G. Quantum-Chemical Modeling of the First Steps of the Strecker Synthesis: From the Gas-Phase to Water Solvation. *J. Phys. Chem. A* **2018**, *122*, 1643–1657.
- (66) Koch, D. M.; Toubin, C.; Xu, S.; Peslherbe, G. H.; Hynes, J. T. Concerted Proton-Transfer Mechanism and Solvation Effects in the HNC/HCN Isomerization on the Surface of Icy Grain Mantles in the Interstellar Medium. *J. Phys. Chem. C* **2007**, *111*, 15026–15033.

- (67) Woon, D. E. Ion-Ice Astrochemistry: Barrierless Low-Energy Deposition Pathways to HCOOH, CH₃OH, and CO₂ on Icy Grain Mantles from Precursor Cations. *Astrophys. J.* **2011**, *728*, 44–49.
- (68) Rimola, A.; Skouteris, D.; Balucani, N.; Ceccarelli, C.; Enrique-Romero, J.; Taquet, V.; Ugliengo, P. Can Formamide Be Formed on Interstellar Ice? An Atomistic Perspective. *ACS Earth Sp. Chem.* **2018**, *2*, 720–734.
- (69) Duvernay, F.; Rimola, A.; Theule, P.; Danger, G.; Sanchez, T.; Chiavassa, T. Formaldehyde Chemistry in Cometary Ices: The Case of HOCH₂OH Formation. *Phys. Chem. Chem. Phys.* **2014**, *16*, 24200–24208.
- (70) Tielens, A. G. G. M.; Hagen, W. Model Calculations of the Molecular Composition of Interstellar Grain Mantles. *Astron. Astrophys.* **1982**, *114*, 245–260.
- (71) Watanabe, N.; Kouchi, A. Efficient Formation of Formaldehyde and Methanol by the Addition of Hydrogen Atoms to CO in H₂O-CO Ice at 10 K. *Astrophys. J. Lett.* **2002**, *571*, L173–L176.
- (72) Pirim, C.; Krim, L.; Laffon, C.; Parent, P.; Pauzat, F.; Pilmé, J.; Ellinger, Y. Preliminary Study of the Influence of Environment Conditions on the Successive Hydrogenations of CO. *J. Phys. Chem. A* **2010**, *114*, 3320–3328.
- (73) Woon, D. E. Modeling Gas-Grain Chemistry with Quantum Chemical Cluster Calculations. I. Heterogeneous Hydrogenation of CO and H₂CO on Icy Grain Mantles. *Astrophys. J.* **2002**, *569*, 541–548.
- (74) Rimola, A.; Taquet, V.; Ugliengo, P.; Balucani, N.; Ceccarelli, C. Combined Quantum Chemical and Modeling Study of CO Hydrogenation on Water Ice. *Astron. Astrophys.* **2014**, *572*, A70 (12 pp).
- (75) Bisschop, S. E.; Jørgensen, J. K.; van Dishoeck, E. F.; de Wachter, E. B.

- M. Testing Grain-Surface Chemistry in Massive Hot-Core Regions. *Astron. Astrophys.* **2007**, *465*, 913–929.
- (76) Kahane, C.; Ceccarelli, C.; Faure, A.; Caux, E. Detection of Formamide, the Simplest but Crucial Amide, in a Solar-Type Protostar. *Astrophys. J. Lett.* **2013**, *763*, L38 (5 pp).
- (77) López-Sepulcre, A.; Jaber, A. A.; Mendoza, E.; Lefloch, B.; Ceccarelli, C.; Vastel, C.; Bachiller, R.; Cernicharo, J.; Codella, C.; Kahane, C.; *et al.* Shedding Light on the Formation of the Pre-Biotic Molecule Formamide with ASAI. *Mon. Not. R. Astron. Soc.* **2015**, *449*, 2438–2458.
- (78) Takahiro, Y.; Takano, S.; Watanabe, Y.; Sakai, N.; Sakai, T.; Liu, S.-Y.; Su, Y.-N.; Hirano, N.; Takakuwa, S.; Aikawa, Y.; *et al.* The 3 mm Spectral Line Survey toward the Lynds 1157 B1 Shocked Region. I. Data. *Publ. Astron. Soc. Japan* **2012**, *64*, 105 (45 pp).
- (79) Codella, C.; Ceccarelli, C.; Caselli, P.; Balucani, N.; Barone, V.; Fontani, F.; Lefloch, B.; Podio, L.; Viti, S.; Feng, S.; *et al.* Seeds of Life in Space (SOLIS) II. Formamide in Protostellar Shocks: Evidence for Gas-Phase Formation. *Astron. Astrophys.* **2017**, *605*, L3 (7 pp).
- (80) Bianchi, E.; Codella, C.; Ceccarelli, C.; Vazart, F.; Bachiller, R.; Balucani, N.; Bouvier, M.; Simone, M. De; Enrique-Romero, J.; Kahane, C.; *et al.* The Census of Interstellar Complex Organic Molecules in the Class I Hot Corino of SVS13-A. *Mon. Not. R. Astron. Soc.* **2019**, *483*, 1850–1861.
- (81) Bockelée-Morvan, D.; Lis, D. C.; Wink, J. E.; Despois, D.; Crovisier, J.; Bachiller, R.; Benford, D. J.; Biver, N.; Colom, P.; Davies, J. K.; *et al.* New Molecules Found in Comet C/1995 O1 (Hale-Bopp) Investigating the Link between Cometary and Interstellar Material. *Astron. Astrophys.* **2000**, *353*, 1101–1114.
- (82) Biver, N.; Bockelée-Morvan, D.; Moreno, R.; Crovisier, J.; Colom, P.; Lis,

- D. C.; Sandqvist, A.; Boissier, J.; Despois, D.; Milam, S. N. Ethyl Alcohol and Sugar in Comet C/2014 Q2 (Lovejoy). *Sci. Adv.* **2015**, *1*, 1–5.
- (83) Saladino, R.; Crestini, C.; Costanzo, G.; Negri, R.; Di Mauro, E. A Possible Prebiotic Synthesis of Purine, Adenine, Cytosine and 4 (3H)-Pyrimidinone from Formamide: Implications for the Origin of Life. *Bioorg. Med. Chem.* **2001**, *9*, 1249–1253.
- (84) Saladino, R.; Ciambecchini, U.; Crestini, C.; Costanzo, G.; Negri, R.; Di Mauro, E. One-Pot TiO₂-Catalyzed Synthesis of Nucleic Bases and Acylonucleosides from Formamide: Implications for the Origin of Life. *ChemBioChem* **2003**, *4*, 514–521.
- (85) Saladino, R.; Crestini, C.; Costanzo, G.; Di Mauro, E. Advances in the Prebiotic Synthesis of Nucleic Acids Bases: Implications for the Origin of Life. *Curr. Org. Chem* **2004**, *8*, 1425–1443.
- (86) Saladino, R.; Crestini, C.; Ciambecchini, U.; Ciciriello, F.; Costanzo, G.; Di Mauro, E. Synthesis and Degradation of Nucleobases and Nucleic Acids by Formamide in the Presence of Montmorillonites. *ChemBioChem* **2004**, *5*, 1558–1566.
- (87) Saladino, R.; Crestini, C.; Neri, V.; Brucato, J. R.; Colangeli, L.; Ciciriello, F.; Di Mauro, E.; Costanzo, G. Synthesis and Degradation of Nucleobases and Nucleic Acids Components by Formamide and Cosmic Dust Analogues. *ChemBioChem* **2005**, *6*, 1368–1374.
- (88) Saladino, R.; Crestini, C.; Neri, V.; Ciciriello, F.; Costanzo, G.; Di Mauro, E. Origin of Informational Polymers: The Concurrent Roles of Formamide and Phosphates. *ChemBioChem* **2006**, *7*, 1707–1714.
- (89) Saladino, R.; Botta, G.; Bizzarri, B. M.; Di Mauro, E.; Garcia-Ruiz, J. M. A Global Scale Scenario for Prebiotic Chemistry: Silica-Based Self-Assembled Mineral Structures and Formamide. *Biochemistry* **2016**, *55*,

2806–2811.

- (90) Rotelli, L.; Trigo-Rodríguez, J. M.; Moyano-Camero, C. E.; Carota, E.; Botta, L.; Di Mauro, E.; Saladino, R. The Key Role of Meteorites in the Formation of Relevant Prebiotic Molecules in a Formamide/Water Environment. *Sci. Rep.* **2016**, *6*, 38888 (7 pp).
- (91) Noble, J. A.; Theule, P.; Congiu, E.; Dulieu, F.; Bonnin, M.; Bassas, A.; Duvernay, F.; Danger, G.; Chiavassa, T. Hydrogenation at Low Temperatures Does Not Always Lead to Saturation: The Case of HNCO. *Astron. Astrophys.* **2015**, *9*, A91 (9 pp).
- (92) Woon, D. E. Pathways to Glycine and Other Amino Acids in Ultraviolet-Irradiated Astrophysical Ices Determined via Quantum Chemical Modeling. *Astrophys. J.* **2002**, *571*, L177–L180.
- (93) Enrique-Romero, J.; Rimola, A.; Ceccarelli, C.; Balucani, N. The (Impossible ?) Formation of Acetaldehyde on the Grain Surfaces: Insights from Quantum Chemical Calculations. *Mon. Not. R. Astron. Soc.* **2016**, *459*, L6–L10.
- (94) Rimola, A.; Sodupe, M.; Ugliengo, P. Computational Study of Interstellar Glycine Formation Occurring at Radical Surfaces of Water-Ice Dust Particles. *Astrophys. J.* **2012**, *754*, 24–33.
- (95) Woon, D. E. Ab Initio Quantum Chemical Studies of Reactions in Astrophysical Ices 3. Reactions of HOCH₂NH₂ Formed in H₂CO/NH₃/H₂O Ices. *J. Phys. Chem. A* **2001**, *105*, 9478–9481.
- (96) Courmier, D.; Gardebien, F.; Minot, C.; St-Amant, A. A Computational Study of the Water-Catalyzed Formation of NH₂CH₂OH. *Chem. Phys. Lett.* **2005**, *405*, 357–363.
- (97) Rimola, A.; Sodupe, M.; Ugliengo, P. Deep-Space Glycine Formation via

- Strecker- Type Reactions Activated by Ice Water Dust Mantles. A Computational Approach. *Phys. Chem. Chem. Phys.* **2010**, *12*, 5285–5294.
- (98) Fresneau, A.; Danger, G.; Rimola, A.; Duvernay, F.; Theulé, P.; Chiavassa, T. Ice Chemistry of Acetaldehyde Reveals Competitive Reactions in the First Step of the Strecker Synthesis of Alanine Formation of HO–CH(CH₃)–NH₂. *Mon. Not. R. Astron. Soc.* **2015**, *451*, 1649–1660.
- (99) Fresneau, A.; Danger, G.; Rimola, A.; Theulé, P.; Duvernay, F.; Chiavassa, T. Trapping in Water - an Important Prerequisite for Complex Reactivity in Astrophysical Ices: The Case of Acetone (CH₃)₂C=O and Ammonia NH₃. *Mon. Not. R. Astron. Soc.* **2014**, *443*, 2991–3000.
- (100) Chen, L.; Woon, D. E. A Theoretical Investigation of the Plausibility of Reactions between Ammonia and Carbonyl Species (Formaldehyde, Acetaldehyde, and Acetone) in Interstellar Ice Analogs at Ultracold Temperatures. *J. Phys. Chem. A* **2011**, *115*, 5166–5183.
- (101) Elsila, J. E.; Glavin, D. P.; Dworkin, J. P. Cometary Glycine Detected in Samples Returned by Stardust. *Meteorit. Planet. Sci.* **2010**, *44*, 1323–1330.
- (102) Sandford, S. A.; Aléon, J.; Alexander, C. M.; Araki, T.; Bajt, S.; Baratta, G. A.; Borg, J.; Bradley, J. P.; Brownlee, D. E.; Brucato, J. R.; *et al.* Organics Captured from Comet 81P/Wild 2 by the Stardust Spacecraft. *Science*. **2006**, *314*, 1720–1724.
- (103) Altwegg, K.; Balsiger, H.; Bar-Nun, A.; Berthelier, J.-J.; Bieler, A.; Bochsler, P.; Briois, C.; Calmonte, U.; Combi, M. R.; Cottin, H.; *et al.* Prebiotic Chemicals – Amino Acid and Phosphorus – in the Coma of Comet 67P/Churyumov-Gerasimenko. *Sci. Adv.* **2016**, *2*, 5 pp.
- (104) Pizzarello, S. The Chemistry of Life’s Origin: A Carbonaceous Meteorite Perspective. *Acc. Chem. Res.* **2006**, *39*, 231–237.

- (105) Strecker, A. Ueber Die Künstliche Bildung Der Milchsäure Und Einen Neuen, Dem Glycocoll Homologen Körper. *Ann. der Chemie und Pharm.* **1850**, *75*, 27–45.
- (106) Nhlabatsi, Z. P.; Bhasi, P.; Sitha, S. Possible Interstellar Formation of Glycine from the Reaction of $\text{CH}_2=\text{NH}$, CO and H_2O : Catalysis by Extra Water Molecules through the Hydrogen Relay Transport. *Phys. Chem. Chem. Phys.* **2016**, *18*, 375–381.
- (107) Nhlabatsi, Z. P.; Bhasi, P.; Sitha, S. Possible Interstellar Formation of Glycine through a Concerted Mechanism: A Computational Study on the Reaction $\text{CH}_2=\text{NH}$, CO_2 , H_2 . *Phys. Chem. Chem. Phys.* **2016**, *18*, 20109–20117.
- (108) Lee, H. M.; Choe, J. C. Formation of Glycine from HCN and H_2O : A Computational Mechanistic Study. *Chem. Phys. Lett.* **2017**, *675*, 6–10.
- (109) Kayanuma, M.; Kidachi, K.; Shoji, M.; Komatsu, Y.; Sato, A.; Shigeta, Y. A Theoretical Study of the Formation of Glycine via Hydantoin Intermediate in Outer Space Environment. *Chem. Phys. Lett.* **2017**, *687*, 178–183.
- (110) Cooper, G. W.; Cronin, J. R. Linear and Cyclic Aliphatic Carboxamides of the Murchison Meteorite: Hydrolyzable Derivatives of Amino Acids and Other Carboxylic Acids. *Geochim. Cosmochim. Acta* **1995**, *59*, 1003–1015.
- (111) Shimoyama, A.; Ogasawara, R. Dipeptides and Diketopiperazines in the Yamato-791198 and Murchison Carbonaceous Chondrites. *Orig. life Evol. Biosph.* **2002**, *32*, 165–179.

5 The olivine-like dust grains core

Extended abstract

In this Chapter, we will show some results about the modelling of the olivinic core of dust grains present in dense MCs. Data are taken and adapted from a recent published work.¹ Please refer to this work for further details.

Context

IR spectroscopy is the main technique used to identify and characterize silicate dust grains in astronomical environments. Narrow spectral line shapes are assigned to crystalline grains, while broad signals are usually assumed to originate from amorphous material. Using such features, the degree of crystallinity can be estimated and used to help understand the processing of dust occurring in different astronomical environments such as the ISM and CSSs. Herein, we accurately calculate the energetic stabilities and IR spectra of several amorphous and crystalline silicate nanostructures with an astronomically common Mg-rich olivinic (Mg_2SiO_4) stoichiometry and with sizes ranging from hundreds to thousands of atoms, generated through three different strategies. Crystalline pure-Mg olivine (forsterite) shows narrow spectral features at 10.0, 11.3, 16.3, 23.5, 27.5, and 33.5 μm , while silicates from diffuse and dense ISM usually show two broad bands at about 9.7 and 18 μm .

Generation of the nanoparticles

To simulate interstellar silicates, we adopted three distinct sets of olivine nanoparticles (NPs), namely bulk cut (BC), amorphized (A) and nucleated (N). Their names reflect the way they are generated. Indeed, BC particles come from the application of the so called “top-down methodology”, that consists in the following: starting from the forsterite unit cell and the Wulff polyhedron (the shape of a perfect, macroscopic crystal), we defined different electrically neutral NPs of increasing size (14, 30, 50, ..., Mg_2SiO_4 formula-units, *i.e.* they are all stoichiometric, **Figure 5.3**). These NPs have been submitted to a two-steps geometry relaxation, involving an initial pre-optimization at a given MM level, and a subsequent proper optimization at DFT level (**Figure 5.4**). Because of the way they

are generated, BC particles can be considered as the most crystalline phase with an olivine stoichiometry at the nanoscale level.

On their hand, A NPs derive from BC ones. Indeed, DFT-optimized BC NPs have been submitted to classical, high temperature, MDs with the aim of “shaking” the atomic positions, and then annealed again at DFT level (**Figure 5.5**). These A particles retain some forsterite features, such as the presence of isolated tetrahedral units coordinating Mg ions through their O atoms.

Finally, N NPs come from the opposite way, *i.e.* from a nucleation process on a preformed core. This process involved many steps, at which of them we added a fragment (SiO, Mg or O atoms) and then we allowed such a fragment to relax through classical MD runs and a subsequent annealing at DFT level. The resulting stoichiometries are the same as that for the BC and A NPs (so that a proper comparison among the three sets can be easily performed), but the composition of N NPs is quite distinct from the other two sets, as N NPs appear as “solid mixtures” of MgO, olivine and pyroxene (**Figure 5.6**).

Energetic characterization

The energetic comparison (**Figure 5.7**) of the three sets of NPs clearly points out some fundamental aspects. First of all, A NPs result to be more stable than the corresponding BC ones at each size. This is a natural consequence of the geometrical constraints at which BC NPs are subjected, and it is consistent with previous studies on similar topics for different material. Nevertheless, BC NPs converge faster to the bulk limit than A ones, and this is consistent with the fact that, at a certain size, crystalline NPs must be more stable than amorphous ones. From our data, we were able to roughly predict the size of this crossing point to be around 12 nm, far away from the sizes we are able to explore within this work. Finally, N NPs are the less stable particles at all sizes, coherently with their “glassy-like” nature.

Structural description

The energetic analysis suggests the existence of at least three different materials with an olivine-like composition at the nanoscale level in the ISM, namely a crystalline phase retaining most of the forsterite structural features, an amorphous olivine with isolated

tetrahedral units and a further phase with no direct relation with the forsterite structure (**Figure 5.8**). These three phases are well represented by our three sets. The experimental structural characterization of these three phases at such small sizes (nanometers) would be prohibitive, but with direct access to the atomistic geometries, we are able to provide such a structural description.

Briefly, we interpreted the perfect crystalline order of forsterite as the result of the presence of two kinds of order, namely the periodic, long-range order deriving from the perfect repetition of the silicate SiO_4 tetrahedral units (and of the MgO_6 octahedral ones), and the local order deriving from the correct orientation and disposition of such units. To characterize these two kinds of order, we defined three structural descriptors (root-mean-square-displacements of the silicon atoms with respect to their very initial positions – RMSD-Si – as indicator for the periodic order, **Figure 5.9**), and the average Mg coordination number ($\langle \text{Mg CN} \rangle$, **Figure 5.9**) and the distortion of silicate units (**Figure 5.10**) as descriptors for local order. All our three parameters clearly indicate that the three BC, A and N sets are structurally distinct and distinguishable, confirming the conclusion we got from an energetic point of view.

Vibrational spectra

On the whole set of NPs, we recorded the IR vibrational spectra at MM level, after a proper comparison with some spectra obtained at the more accurate DFT level. The comparison of such spectra for the three sets is fundamental since IR spectroscopy represents the principal technique to observe ISM silicates.

The spectra for the smallest NPs are characterized by a “forest” of different signals deriving from their molecular-like nature. However, as sizes increase, the two-peaks profile typical of ISM silicates arises, even for the BC (crystalline-like) NPs (**Figure 5.11**). The direct consequence is that it is impossible to distinguish BC and A NPs from their IR spectra, while some differences can be highlighted for N ones.

Some conclusive remarks

Through all the calculations reported in this work, we show that crystalline forsterite-like grains are metastable with respect to amorphous grains. However, from our careful

analysis, we also show that the IR spectra of such nanosilicate grains cannot be unambiguously used to identify their structural nature. In particular, our work indicates that amorphous and crystalline silicate nanograins cannot be distinguished based on their spectroscopic features, casting doubt on the calculated fraction of crystalline material in the ISM. There are several astronomical implications to our results. For example, the higher energetic stability of amorphous NPs with respect to their crystalline counterparts highlights the necessity to include such considerations in theoretical works of the formation of silicates in different environments. Moreover, the non-distinguishability of crystalline-like material from amorphous ones indicates the necessity to revise our viewpoint on ISM silicates.

5.1 Background

Silicates are fundamental for the life cycle of solid matter in the Universe and are abundantly and ubiquitously detected as dust particles in several environments, *e.g.*, dense MCs, CSSs of young and old stars, comets and the diffuse ISM.^{2–6} As we have already pointed out in the Section 1.4.3.1, the lifecycle of silicate dust involves different steps: generation in the CSSs of old dying stars, destruction, regeneration and processing in the ISM, with the eventual incorporation in MCs (where they show ice mantles) and protoplanetary disks.^{2,3} Therefore, the silicate dust is strongly affected, by a certain degree, by the physical conditions that have characterized its history. Knowing the structure of the silicate dust can thus provide a diagnostic tool to help understand the conditions in a range of astronomical environments.

IR spectra provide the primary source of information regarding the atomistic structure of astronomical silicate dust grains. Observations where well-defined IR peaks can be discerned give strong support for the presence of highly crystalline grains (*e.g.*, in some circumstellar environments).⁷ In such cases, comparisons with laboratory spectra from carefully prepared samples can help determine the crystal structures and chemical compositions of the dust grain populations. From

such studies, it has been confirmed that crystalline silicate dust is very magnesium rich and primarily of either pyroxene (MgSiO_3) or olivine (Ol, Mg_2SiO_4) composition.^{8,9} IR absorption spectra from silicates in the ISM, however, show no sharp features, but rather they are dominated by two broad peaks centred at around 9.7 and 18 μm . Although these peaks can be confidently attributed to vibrational Si-O bond stretching and O-Si-O bond bending modes, respectively, such spectra are usually interpreted as originating from amorphous silicates.² This assignment is supported by noting the similarity of such observed IR spectra with those from experimentally prepared bulk amorphous silicates.¹⁰⁻¹³ Spectral analysis of carefully prepared laboratory samples have revealed that the position and width of the two characteristic IR peaks of dense glassy amorphous silicates vary, to an extent, with respect to the chemical composition,^{2,10} and the degree of thermal annealing.¹⁰⁻¹² Interestingly, it has also been shown that experiments irradiating crystalline silicates with high energy ions, thus mirroring the environment of the ISM, can induce atomic disorder and porosity.¹⁴ Although these irradiated samples spectroscopically appear to be very similar to dense amorphous silicates, they likely retain residual pockets of the original crystal order. By fitting observed IR spectra using various combinations of laboratory spectra, a number of investigations have attempted to gain insights into the properties and structure of amorphous silicate dust from the positions and shapes of the 10 and 18 μm silicate features.^{12,15,16} The lifecycle of silicate dust involves different energetic processes; therefore, the history and the processing degree of ISM grains can be inferred from knowing their crystallinity. Although observations clearly point to the almost total lack of crystalline dust grains in the diffuse ISM, we explore the possibility that observational IR spectra from putative amorphous grain populations could have contributions from a population of *quasi*-crystalline nanosized silicate grains.

In this Chapter, we will deal with atomistic models of nanoparticles (NPs) with

diameters varying between ~ 1.2 and ~ 4.6 nm and with a pure Mg_2SiO_4 olivine composition. It has been estimated that such small NP grains could form up to 10% of the mass of the silicates in the ISM without violating observational constraints and, if so, could form the largest population of ISM silicate dust grains by number.¹⁷ Indirect support for the existence of such a population of nanosilicate grains also comes from their potential role in explaining the anomalous microwave emission (AME) in the ISM.^{18–20} We employ both QM and CM calculations to model our nanograins with varying degrees of crystallinity and provide a detailed analysis of their structure and relative energetic stabilities. Our main focus is on how the crystallinity of such nanograins is reflected in their IR spectra.

All computational details for the calculations we will show in this Chapter are collected in Section 2.8.2. Because we are mainly interested in IR spectra, we checked the reliability of the selected PBE/OIBs and Walker FF methodologies by comparing the spectroscopic features of experimentally-acquired crystalline forsterite with the simulated ones. **Figure 5.1** contains such comparison among IR spectra (the experimental spectrum from a sample of amorphous olivine material is also included for the sake of completeness). Experimental spectra are adapted from a very recent work and reproduced with authors' permission.²¹ The comparison of the simulated spectra with the experimental one from crystalline forsterite is good, even if not in perfect accordance: however, for our purposes, it is sufficient because shows that both PBE/OIBS and Walker FF give acceptable results.

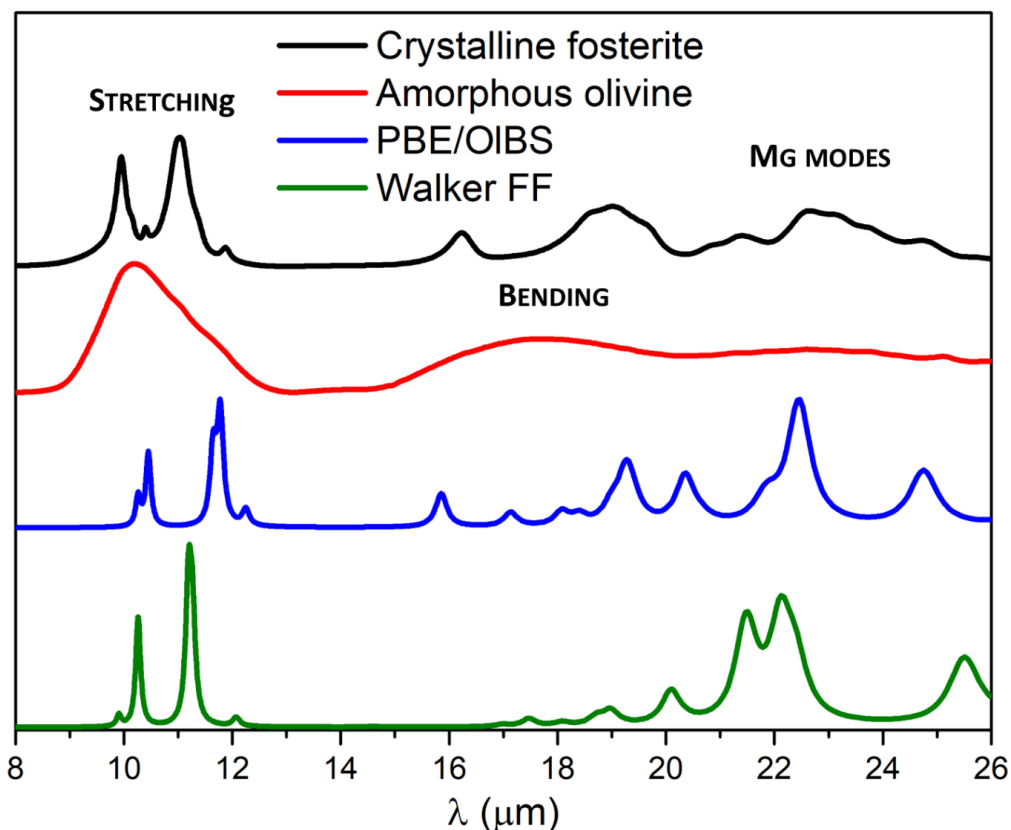


Figure 5.1 Experimental spectra (from Ref. 21) for crystalline forsterite (in black) and amorphous olivine (in red) compared with the simulated ones at PBE/OIBS (in blue) and Walker FF ones (green). Intensity in arbitrary units: spectra are vertically transposed for the sake of clarity.

5.2 Generation of olivine nanoparticles

Here we will explain the procedures we followed to generate our different NP models, then we present and analyse the results from an energetic and structural point of view (Sections 5.3 and 5.4) and, finally, we show and discuss the IR spectra of the NPs (Section 5.5). **Figure 5.2** schematically summarises the methods we followed to produce our atomistic NP models, the calculations performed within this Chapter, and the methods used to define the initial geometries of our Ol NPs. **Figure 5.3**, **Figure 5.4**, **Figure 5.5**, and **Figure 5.6** show the initial and PBE/OIBS-optimized of some NP structures.

To simulate OI NPs, we developed three different sets of models, namely *bulk cut* (BC) or *crystalline, amorphized* (A) and *nucleated* (N) NPs. Hereafter we label our NPs as “ $N_y Z$ ” where N represents the number of formula-units, $Z = \text{BC, A}$ or N (*i.e.*, it indicates the set which the particle belongs to) and y can be any additional information necessary to identify the NP in question.

5.2.1 Bulk cut (BC) crystalline NPs

Bulk cut NPs have been generated following the top-down methodology, starting from the Wulff construction (the shape of a macroscopic, perfect crystal, **Figure 5.2**, panel **A**, top-right corner) of forsterite. We note that this method has already been successfully used to model NPs of binary oxide systems such as titania and zirconia.^{22,23} The main steps we followed in this top-down approach were:

- using CRYSTAL, we firstly optimized the crystallographic structure of the forsterite unit cell at a PBE/OIBS level of theory (top-left corner of panel **A** of **Figure 5.2**);²⁴
- using the VESTA software,²⁵ we replicated the unit cell several times and then cut along the crystallographic directions representing the most energetically stable surfaces in forsterite crystals,²⁶ as derived from previous DFT calculations.²⁷ During this phase, the initial choice of the unit cell origin can play a fundamental role in the final shape and stability of the resulting NP, thus we also studied bulk cuts after translating the forsterite unit cell. NPs generated after this translation have been labelled with “trasl”.

The NPs generated after this top-down method represent our initial set (**Figure 5.3**). After some *a posteriori* structural modification, and pre-optimization using Reax FF, we finally fully optimized the NPs at a PBE/OIBS level of theory (see resulting structures in **Figure 5.4**). All the details concerning the top-down procedure, the *a posteriori* NP modifications and the Reax FF optimisations are

reported in the supporting information (SI) file of the published article.¹ For the largest NP studied in this work (418 formula-units) we followed a slightly different procedure, *i.e.*, we skipped the PBE/OIBS optimization (since it is too computationally-demanding at such sizes), and therefore, all the energetic and structural results of next Sections concerning this NP refer to the Walker FF-optimized structure (right-hand side of **Figure 5.2B**).

5.2.2 Amorphized (A) NPs

Using the GULP code, BC PBE/OIBS-optimized NPs were heated using classical MD simulations at 1800 K with the aim of amorphizing their structures, *i.e.* “shaking” the atomic positions. For one NP only (30a BC), we also tested a higher temperature of 2400 K, to check for temperature effects on the final structure and morphology of the NP (see Sections 5.3, 5.4 and 5.5 for details). For most NPs, after a 10 ps equilibration, we ran MD simulations for 20 ps of production time. For the largest 418 formula-units NP, a significantly longer 200 ps production time was found to be necessary to amorphize the NP. These amorphized particles were then optimised at a PBE/OIBS level of theory using CRYSTAL (see **Figure 5.2**, panel **B**). The final optimized NP structures are shown in **Figure 5.5**.

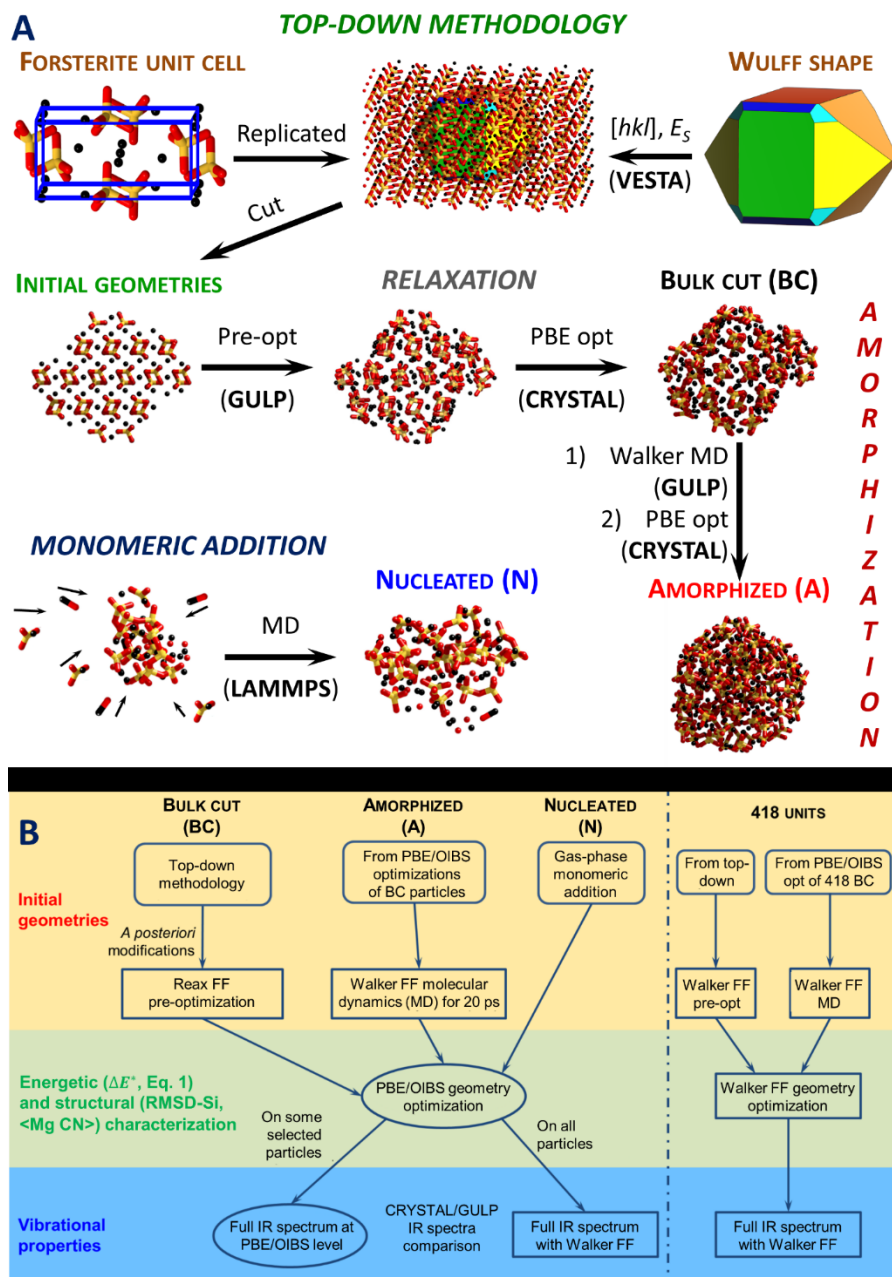


Figure 5.2 A: graphical representation of the procedures we followed to obtain our three sets of Ol NPs. Atom colour code: Si in yellow, O in red, Mg in black. **B:** schematic representation of the methods employed in the work. In rounded rectangles we outline the methodologies we used to define the initial geometries of our NPs. Square rectangles and ellipses represent FF and PBE/OIBS calculations, respectively. The scheme on right of the straight dot-dashed line refers to the 418 formula-units NP, for which slight modifications were necessary.

5.2.3 Nucleated (N) NPs

Since the A NPs were generated by thermal annealing of BC NPs, it is possible that they can still retain geometric similarities with the original structures. As silicates in the ISM may form by condensation from the gas phase under non-equilibrium conditions, amorphous silicate grains, therefore, might be completely unrelated to the forsterite bulk structure. Consequently, we also constructed NPs using a bottom-up procedure through monomeric addition (SiO, O and Mg fragments) ensuring no relationship with the forsterite crystal structure and then ran MD at 1800 K simulations using the LAMMPS code.²⁸ These N NPs were then finally optimised at a PBE/OIBS level of DFT theory using CRYSTAL (see resulting NP structures in **Figure 5.6**).

It is worth noting that, as a consequence of the way they are generated, these N NPs often appear to display as a solid solution of MgO, pyroxenes (-Si-O- chains) and pure olivine, although their stoichiometries are the same as that of pure forsterite. This *differentiation of phases* is particularly evident for the smaller particles (see, for example, the 30 N particle of **Figure 5.6**): indeed, their structures are quite distinct to that of forsterite, *i.e.* isolated tetrahedral SiO₄ units whose O atoms coordinate to Mg ions in an octahedral manner (forsterite unit cell structure is reported in top top-left corner of **Figure 5.2**, panel **A**).

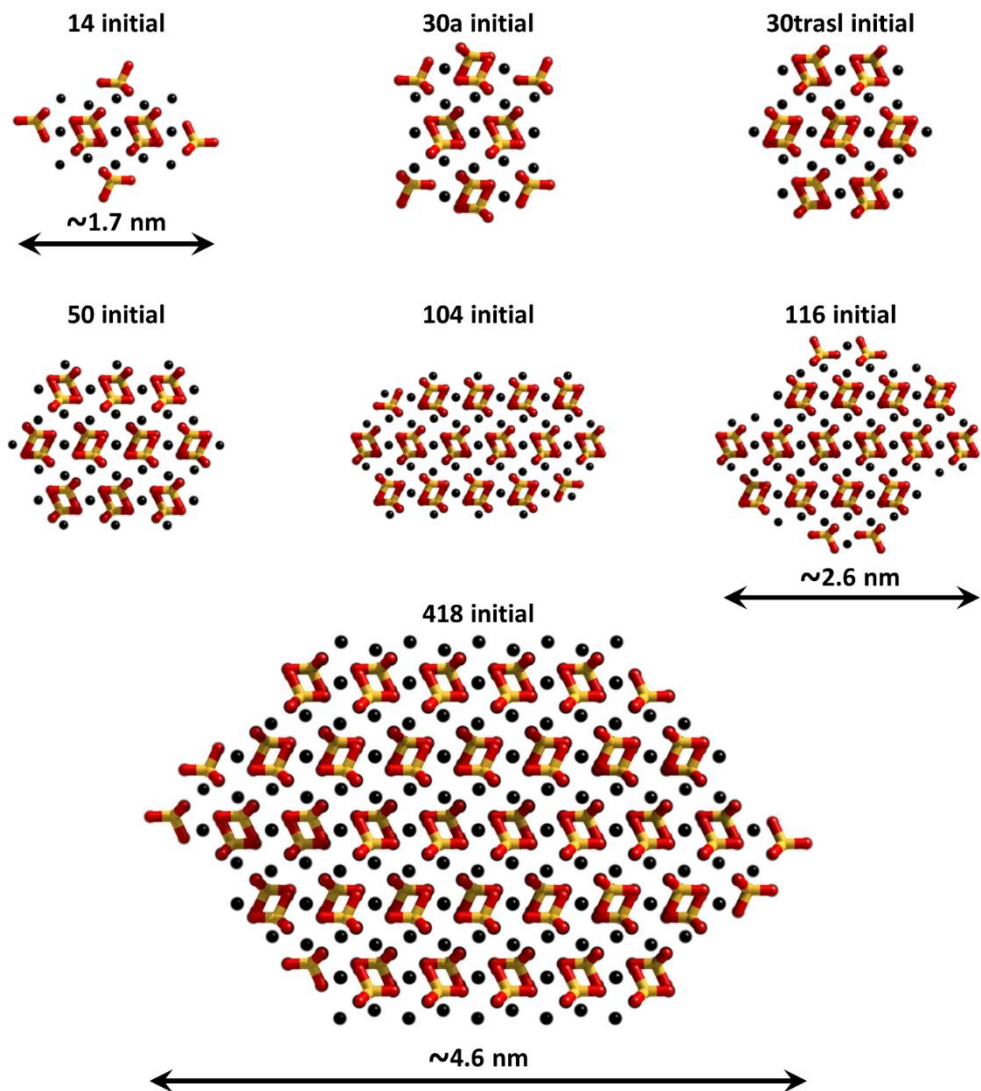


Figure 5.3 Structures of the set of initial Ol NPs (see Section 5.2.1). Only a selection of NPs is shown. Colour code: same as **Figure 5.2**. Note that the relative NP sizes are not to scale. The dimensions of some particles are also reported.

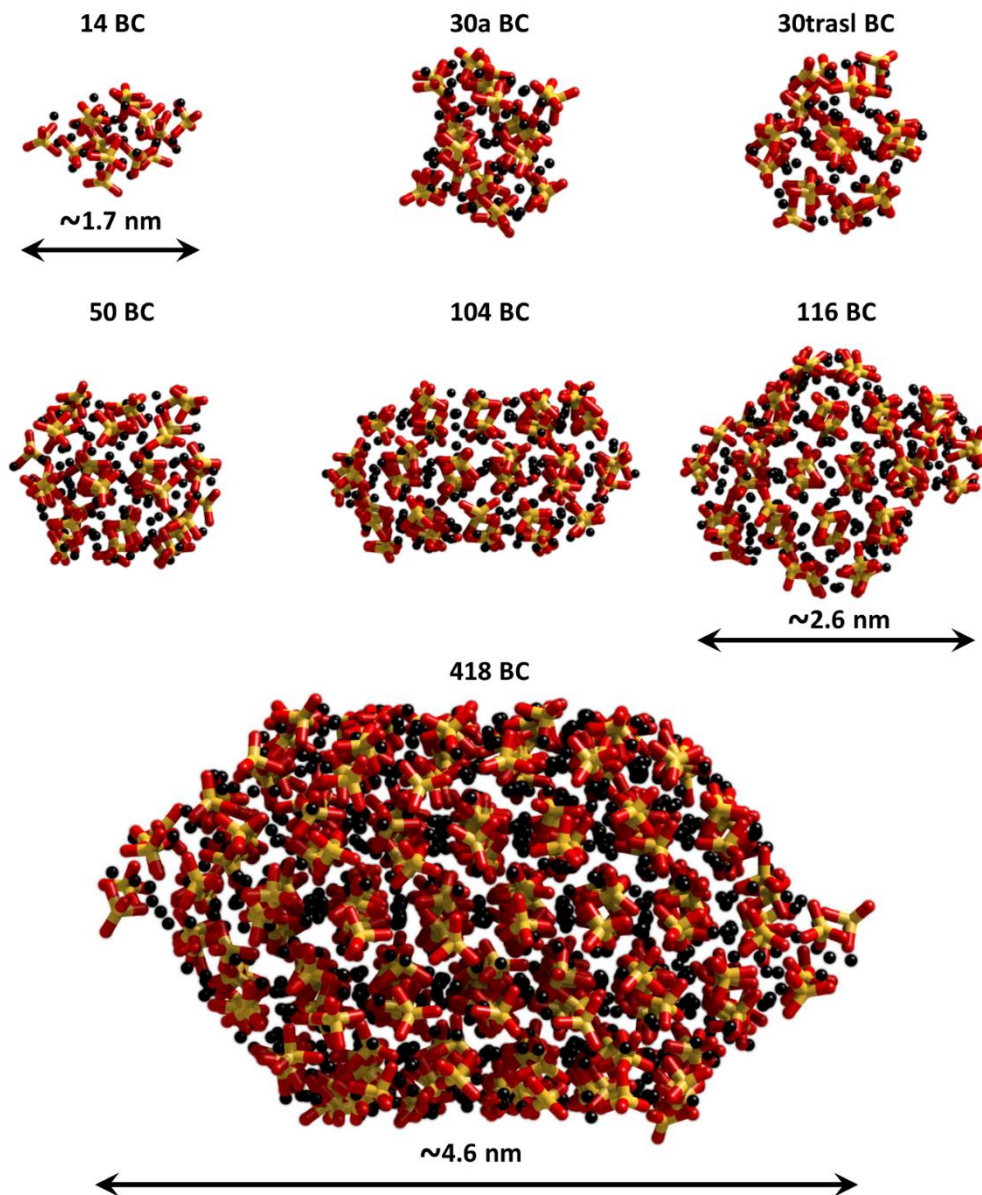


Figure 5.4 Structures of the set of PBE/OIBS-optimised bulk cut (BC) NPs particles (Section 5.2.1). Only a selection of NPs is shown. Colour code: same as **Figure 5.2**. Note that the relative NP sizes are not to scale. The dimensions of some particles are also reported.

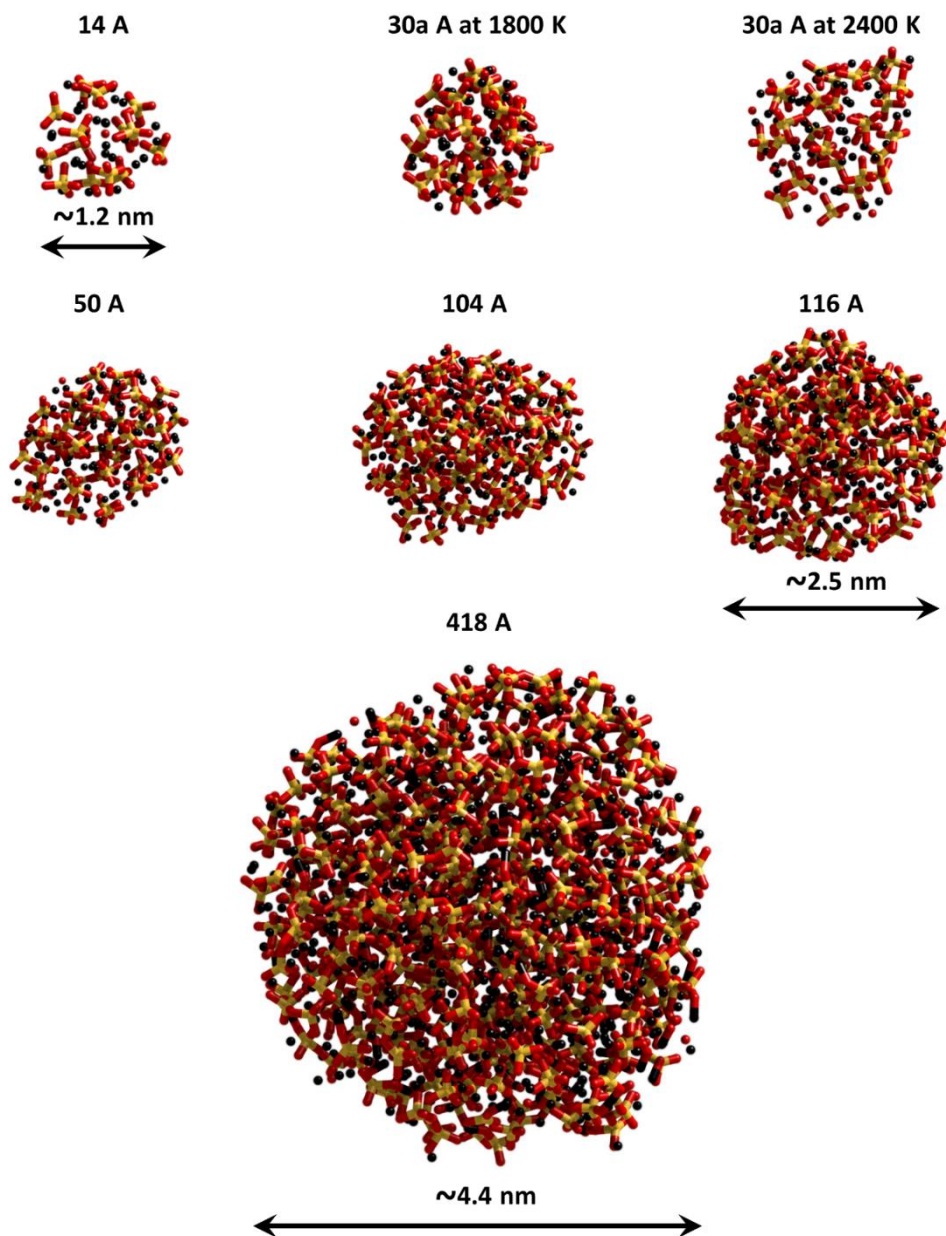


Figure 5.5 Structures of the set of amorphized (A) NPs, after PBE/OIBS optimization (Section 5.2.2). Only a selection of NPs is shown. Colour code: same as **Figure 5.2**. Note that the relative NP sizes are not to scale. The dimensions of some particles are also reported.

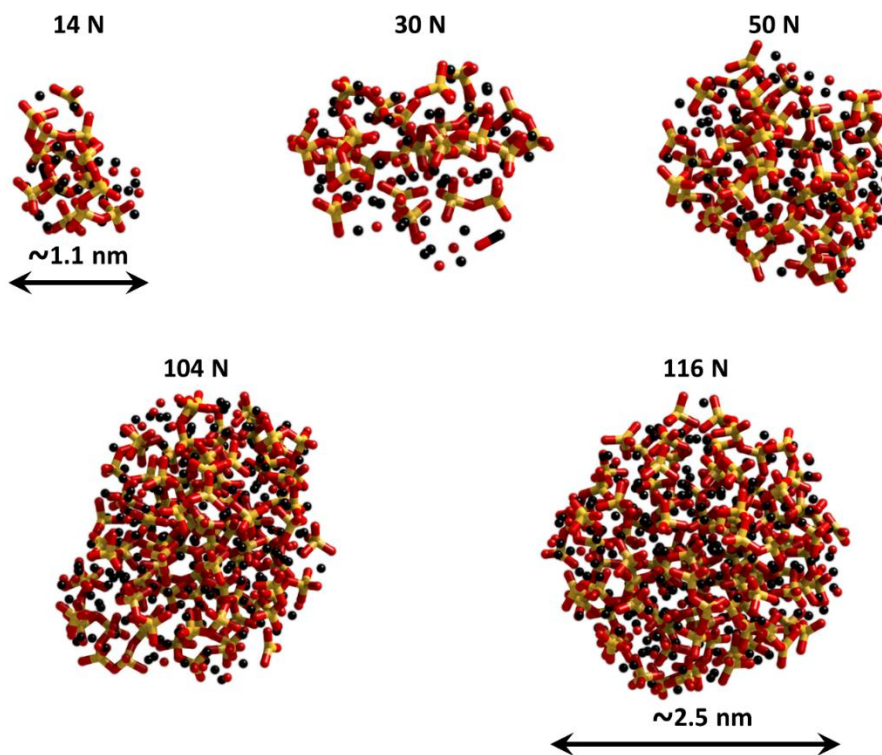


Figure 5.6 Structures of set of nucleated (N) NPs, after PBE/OIBS optimization (Section 5.2.3). Only a selection of NPs is shown. Colour code: same as **Figure 5.2**. Note that the relative NP sizes are not to scale. The sizes of some particles are also reported.

5.3 Energetic stability

The relative energetic stability of our PBE/OIBS-optimized NPs *per* Mg_2SiO_4 formula-unit with respect to the forsterite bulk (ΔE^*) has been computed according to Equation 5.1.

$$\Delta E^* = \frac{1}{N} E_{NP} - \frac{1}{4} E_{bulk} \quad 5.1$$

where E_{NP} is the energy of an Ol NP of N formula-units, and E_{bulk} is the energy corresponding to a unit cell of crystalline forsterite containing 4 Mg_2SiO_4 units.

ΔE^* values (in kJ mol^{-1}) for all NPs are reported in **Table 5.1**, together with other structural properties. We have grouped the data with respect to the number of formula-units N in order to facilitate a comparison between NP models of the same size. The NPs containing 30 formula-units are used as a test case to show the effect of different methods to generate the crystal cuts as well as different annealing temperatures. 30a BC and 30b BC NPs correspond to two different crystalline cuts for the 30 formula-units non-translated NP (**Figure 5.4**). The 30a A at 1800 K and 30a A at 2400 K NPs have been amorphized using two MD runs at 1800 and 2400 K, respectively (**Figure 5.5**).

The overall energetic stability is clearly affected by the different processes involved in the generation of a given NP which highlights the importance of carefully generating such NPs in order to estimate the amorphous *vs* crystalline stability cross-over size regime. For example, the difference in energy *per* formula-unit between the 30a BC and 30trasl BC NPs is 23.6 kJ mol^{-1} (**Table 5.1**). This result highlights the importance of generating top-down BC NPs from unit cells with different translated origins. Generally, this can also be seen from the fact that the lowest lying BC NP structure (highlighted in bold in **Table 5.1**) is neither consistently in the translated (“trasl”) nor in the non-translated series. Conversely, different amorphization temperatures (1800 *vs* 2400 K) do not appear

to significantly affect the final results, at least from an energetic stability (ΔE^*) point of view.

Table 5.1 Summary of energetic and structural data for all PBE/OIBS-optimized olivinic NPs. n is number of atoms, N the number of Mg_2SiO_4 formula-units. Relative energies with respect to forsterite bulk (ΔE^* , Equation 5.1) are in kJ mol^{-1} *per* formula-unit. $\langle \text{Mg CN} \rangle$ values correspond to the overall average coordination numbers of Mg ions. Root-mean-square-displacements of the silicon atoms (RMSD-Si) are given in Å. ΔE^* values for the most stable bulk cut and amorphized NP for each N are highlighted in bold

NP model	n	N	$N^{-1/3}$	ΔE^*	$\langle \text{Mg CN} \rangle$	RMSD-Si
14 BC	98	14	0.415	420.1	4.25	1.12
14 A				382.0	4.14	3.95
14 N				474.2	4.04	-
30a BC	210	30	0.322	357.9	4.35	0.95
30b BC				346.4	4.48	1.05
30trasl BC				334.3	4.55	0.90
30a A at 1800 K				331.1	4.37	3.24
30a A at 2400 K				340.5	4.30	6.44
30trasl A				327.0	4.50	3.40
30 N				417.5	4.18	-
50 BC	350	50	0.271	298.7	4.64	0.78
50trasl BC				311.5	4.61	0.98
50 A				282.0	4.56	2.86
50trasl A				280.2	4.64	2.04
50 N				350.7	4.31	-
60 BC	420	60	0.255	304.3	4.53	1.09
60trasl BC				301.0	4.55	0.85
60 A				281.6	4.56	3.32
60trasl A				273.6	4.54	1.70
60 N				350.1	4.43	-
80 BC	560	80	0.232	287.0	4.71	1.04

The olivine-like dust grains core

80trasl BC				294.2	4.68	0.73
80 A				272.4	4.61	3.72
80trasl A				255.4	4.65	2.26
80 N				323.4	4.38	-
92 BC	644	92	0.222	263.3	4.72	0.67
92trasl BC				281.5	4.71	0.77
92 A				264.9	4.58	3.45
92trasl A				246.8	4.65	2.15
92 N				329.3	4.39	-
104 BC	728	104	0.213	267.4	4.78	0.55
104trasl BC				259.9	4.72	0.64
104 A				262.7	4.53	2.94
104trasl A				249.0	4.67	2.18
104 N				318.5	4.45	-
116 BC	812	116	0.205	255.9	4.84	0.83
116trasl BC				272.2	4.71	0.94
116 A				250.6	4.63	3.04
116trasl A				235.5	4.69	2.15
116 N				308.3	4.49	-
418 BC*	2926	418	0.13	82.9	5.04	0.97
418 A*				86.0	4.74	9.21

*: data from Walker FF-optimizations only (see **Figure 5.2**, panel **B**, right-hand side).

Figure 5.7 provides the ΔE^* values as a function of $N^{-1/3}$, following the spherical cluster approximation (SCA) that relates the energy of a NP with the ratio between its surface and bulk atoms.²⁹ We note that the SCA is only a first order geometric approximation that does not take into account the atom/electronic degrees of freedom (*e.g.*, surface stress) in realistic NPs, which roughly correspond to higher order terms.²² We find that the lowest energy structures of each family of crystalline, amorphous and nucleated NPs follow well a simple fitted $N^{-1/3}$ dependence, with R^2 values of 0.982, 0.986 and 0.979, respectively. Hence, even if some of the NP structures do not correspond to the lowest energy minima for

that family of NPs, these simple fits can provide a tentative estimate of the size dependent energetic trends for each of the NP families.

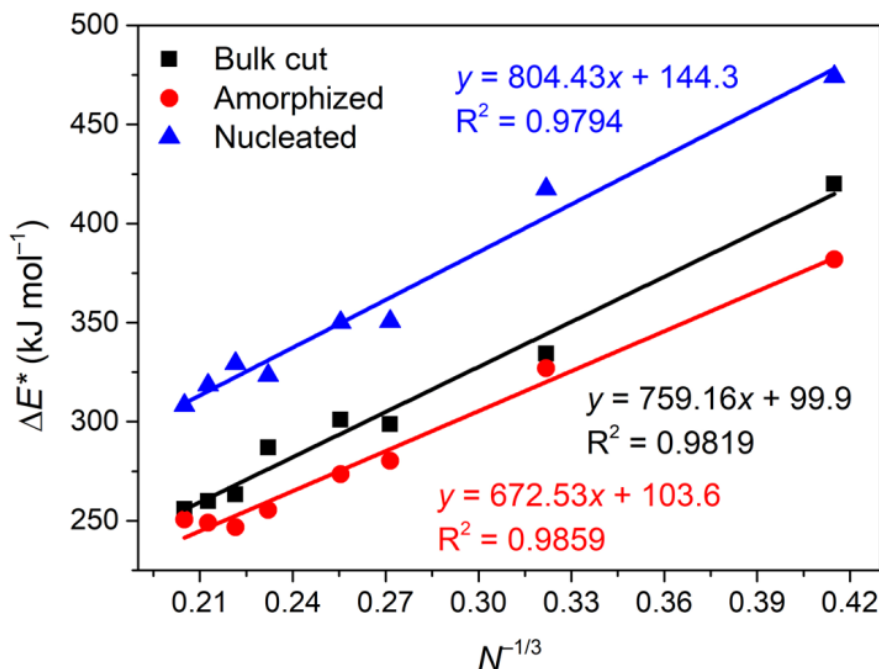


Figure 5.7 Relative energies with respect to forsterite bulk *per* formula-unit (ΔE^*) for the most stable NPs we found for each size, as a function of the number of formula-units (N): the linear correlation fitting parameters and R^2 values are also reported close to each respective line.

We first note that the A NPs are the most energetically stable NPs for all considered sizes. Although A NPs are always more stable than N and BC NPs, we highlight how the largest A NPs of 104 and 116 formula-units are higher in energy *per* unit than the smaller 92 unit A NP. This result clearly indicates that the 104 and 116 A NP models are not the most stable amorphous NPs for their size. As found in other NPs systems,²² the BC NP structures are more energetically unstable relative to the A NPs for the smallest sizes, but converge faster to the bulk limit (*i.e.*, the fitting line for BC NPs has a steeper slope than that for A NPs), as expected by the fact that crystalline forsterite is the most stable bulk phase of the Mg-rich olivine family. This implies that any process which

generates small crystalline NPs will be generating metastable particles which will, upon annealing, evolve towards amorphous structures. Although the exact energy evolution for each family is not precise due to the use of the SCA and the fact that not all NPs are the lowest energy for their type and size, we can extrapolate the fitted lines to roughly estimate the energetic cross-over point between amorphous and crystalline NPs. Following a previous study,³⁰ we convert the number of formula-units to the radius of a NP assuming a spherical shape and a volume *per* Mg_2SiO_4 unit extracted from bulk forsterite. With the current available data, the cross-over between A and BC NPs appears to occur at a diameter of ~ 12 nm, which is quite far away from the NP sizes explored within this work. Finally, the N NPs appear to be the most energetically unfavourable species, typically being $\sim 50 \text{ kJ mol}^{-1}$ less stable than the BC NPs. It is reasonable to suggest that the large metastability of N NPs arises from their “glass-like” silicate disorder and the sub-optimal mixing of MgO units into their structure. There is still an ongoing debate on the formation mechanisms of silicate dust in the envelopes of AGB stars. Observational evidence seems to show the preferential formation of amorphous material with respect to crystalline NPs,³¹ while thermodynamics based on extended systems always assume the formation of the most stable bulk phase, which is crystalline Ol.³² The results in this work highlight the necessity to consider the formation of amorphous Ol NPs as a possible route for the condensation of silicate species in CSS, probably aiding to bridge the discrepancy between purely thermodynamic arguments and observational evidence. It must also be considered that, although on thermodynamics grounds the smallest silicate grains should be amorphous, the actual structure of dust particles of such dimension in CSSs and the ISM will not depend only on the energetics, but also on several processes like accretion from nucleation centres, temperature-related kinetics effects, high- and low-energy collisional events involving cosmic rays and/or other dust particles.^{2,3,7,33,34}

5.4 Structural descriptors

The energetic analysis performed in previous Section suggests the existence of at least three energetically-distinguishable phases of small NPs with an Ol-like stoichiometry: amorphous material with mainly isolated SiO_4 tetrahedra, crystalline forsterite, and glass-like NPs with some segregated pockets of MgO and more polymerised silica units. From an energetic point of view, these three phases are represented by our three sets of A, BC and N NPs, respectively. Experimental characterization of these phases at such a small scale would be extremely challenging. Theoretically, however, with direct access to the detailed atomistic structure, we can begin to quantitatively analyse the structural differences among these three NP families.

Silicates are structurally complex inorganic materials due to the presence of both ionic (Mg-O) and covalent (Si-O) bonds, with the former being weaker than the latter. The difference in bond energy causes Mg cations to be more mobile, while the SiO_4 anionic units are more rigid but can create complex polymerized networks with little energetic cost. In order to structurally characterize our NPs, we first take the crystalline forsterite phase as a crystalline benchmark which we describe in terms of tetrahedral units of SiO_4 that are regularly interspaced by octahedrally coordinated Mg cations. Secondly, we assume that the degree of crystallinity of NPs can be described by two structural measures which we take to be optimal in the Ol bulk crystal: *i*) short-range structural order, which is related to the orientation and distortion of SiO_4 tetrahedra and MgO_6 octahedra, at their fixed lattice sites, and *ii*) long range periodic order, which is related to the repeated presence of the SiO_4 and MgO_6 units along the crystal lattice vectors.^{24,26} In this work, we use the average Mg-coordination number ($\langle \text{Mg CN} \rangle$) and the structural distortion of SiO_4 tetrahedra to describe short range order and the root-mean-square-displacement of silicon atoms (RMSD-Si) with respect to their very initial positions (**Figure 5.3**) to describe long range order. The use of $\langle \text{Mg CN} \rangle$ as a

short-range order descriptor is justified by the fact that reorientation of silicate tetrahedra and displacement of Mg cations from their equilibrium geometries will cause changes in the Mg-O distances and hence to the coordination numbers. It is reasonable to assume that amorphization using mild temperatures will involve small changes in the orientation and/or distortion of the different units, especially for the lower coordinated (*i.e.* least well bound) atoms at the surface. Surface relaxation of an NP can thus be seen as a local amorphization taking place at the outermost layers of the NP which should be reflected in the $\langle \text{Mg CN} \rangle$ values and the spatial distribution of SiO_4 structural distortion. On the other hand, a higher temperature amorphization should cause a strong displacement of the different SiO_4 units, with the possibility of inducing polymerization of the silicate skeleton. The displacement of the SiO_4 units can be analysed through the RMSD-Si. Although the RMSD-Si is a natural way in which to compute the displacement in the MD amorphized NPs with respect to the corresponding parent BC NP, the comparison with the nucleated NPs is not straightforward, as the atomic assignment cannot be unequivocally matched to an original crystalline structure. We therefore only provide RMSD-Si values for the A NPs in order to compare MD amorphized NP structures with the BC NPs.

In **Figure 5.8**, we show illustrative examples of crystalline (left), locally-amorphized (centre) and globally-amorphized (right) Ol structures. In the left panel, the perfect periodic structure of crystalline forsterite can be easily recognized, with the oxygen atoms of the isolated silicate tetrahedra coordinating to the Mg cations. In the centre panel, a mild amorphization has partially altered the original crystalline structure, but some crystalline features are evidently retained, while in the right panel, a higher temperature amorphization results in a structure lacking any clear remnants of crystallinity. Although the structures in the right and centre panels of **Figure 5.8** both represent amorphous Ol, both RMSD-Si and $\langle \text{Mg CN} \rangle$ structural descriptors can help us to analyse whether

they have some intrinsic structural features that allow one to distinguish them in our NPs.

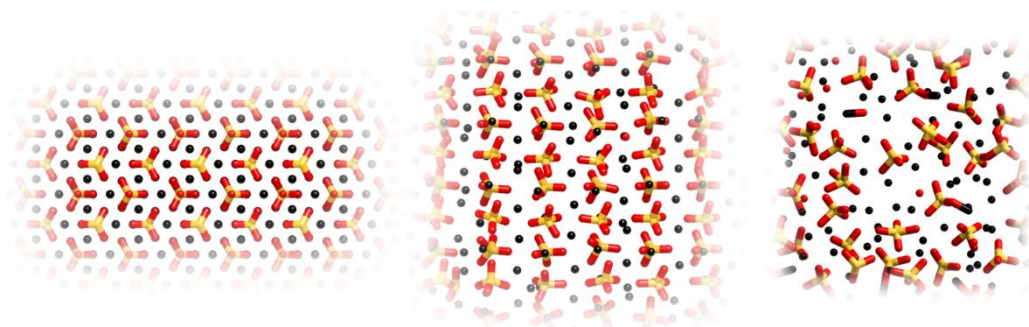


Figure 5.8 Left: periodic structure of perfectly crystalline forsterite. Centre: structure for a non-crystalline olivinic material, preserving a partial long-range order (Si and Mg atoms are disposed in “column and rows”, but silicate tetrahedra are partially distorted and rotated). Right: structure for a non-crystalline bulk material with a forsterite stoichiometry with no local and periodic order (highly distorted and partially polymerised SiO_4 tetrahedra, with some formation of MgO units). Colour code: same as **Figure 5.2**.

In the left panel of **Figure 5.9**, we graphically report the RMSD-Si data for all the PBE/OIBS-optimized NPs (data for the 418 formula-units NPs are omitted for a clearer representation. See **Table 5.1** for the values). The RMSD-Si values for BC particles are low even for the smallest considered NP sizes. For A NPs, the RMSD-Si values are several times larger and spread over a wider range. These data show that BC NPs preserve a high degree of periodic crystalline order, while the relatively lower crystallinity of the A NPs is clear.

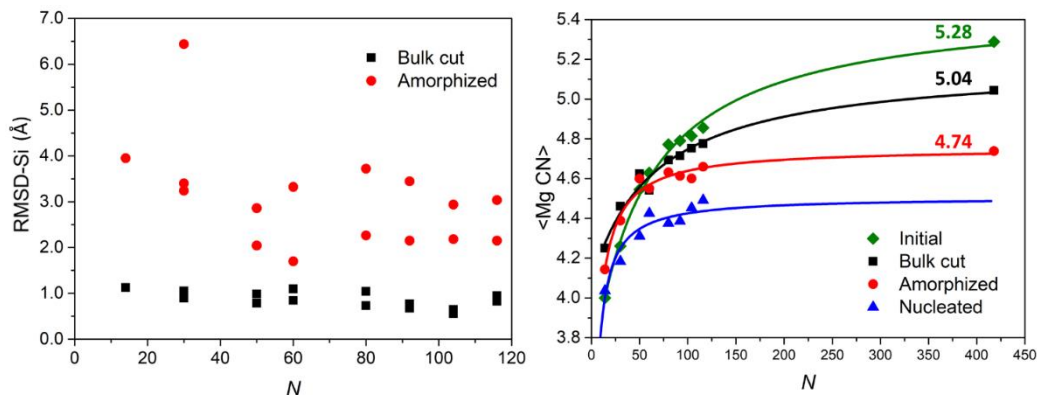


Figure 5.9 Left panel: root-mean-square-displacements of the silicon atoms (RMSD-Si) in Å with respect to the initial cuts of **Figure 5.3** as a function of the size of the particles, N (data for the 418 formula-units NPs are not shown. See **Table 5.1** for the numerical values). Right panel: average Mg coordination numbers, $\langle \text{Mg CN} \rangle$, as a function of the size of the particles (N). See **Table 5.1** for the numerical values. Numbers close to each line correspond to the largest 418 formula-units NPs. Lines are added as a guide to the eye.

Finally, we note that the RMSD-Si value for the 30a Å NP after a 2400 K MD run is almost double that of the corresponding NP after a 1800 K MD run (3.24 Å vs 6.44 Å, **Table 5.1**), with the latter value being the highest among all PBE/OIBS optimized particles. This indicates that the use of higher temperatures could produce an even more amorphized NPs. However, as we will show in next Section, this large difference in the RMSD-Si value does not produce significant differences in the simulated IR spectra.

In the right panel of **Figure 5.9**, we graphically show the $\langle \text{Mg CN} \rangle$ values as a function of the number of formula-units N for our three sets of NPs, plotting the average when we have more than one NP for a given N . In this figure, the $\langle \text{Mg CN} \rangle$ values of the initial NPs (**Figure 5.3**) are also incorporated in order to compare the values with respect to the perfect crystalline structure for every NP size (see **Table 5.1** for values). From **Figure 5.9**, it can be seen that the initial unrelaxed cut NPs have the largest $\langle \text{Mg CN} \rangle$ values of all considered NPs, corresponding to the fact that, by construction, they are structurally most like the

bulk crystal. However, even for this family of NPs, the largest initial cut NP has a $\langle \text{Mg CN} \rangle$ value of 5.28 which is still significantly different from the bulk crystal limiting value of 6 due to the lower coordination of Mg cations near the NP surface. From the other three families of NPs, as expected, BC NPs have $\langle \text{Mg CN} \rangle$ values which are the closest to those of the initial cut NPs. Here the largest BC has a lower $\langle \text{Mg CN} \rangle$ value of 5.04 indicating that initial cut NPs preferentially relax to lower energy structures with slightly lower crystallinities. The lowering of $\langle \text{Mg CN} \rangle$ values going from the perfect initial cut NPs to relaxed BC NP structures points to the fact that even the most crystalline material at the nanoscale cannot be described as completely crystalline. Visual inspection of the NPs suggests that the BC NPs should be considered as being core-shell structures (*i.e.*, with highly crystalline cores and slightly disordered near surface shells). For the largest A NP, the $\langle \text{Mg CN} \rangle$ value is equal to 4.74, while for a hypothetical 418 N NPs it can be predicted from the trends of the existing data to be even smaller (~ 4.60). These lower $\langle \text{Mg CN} \rangle$ values correspond to a higher degree of local structural disorder and thus even lower crystallinities. These data strengthen our above analysis concerning the structural (and energetic) distinguishability of BC, A and N NPs.

The $\langle \text{Mg CN} \rangle$ and RMSD-Si values are averages over the whole structure of a NP and thus do not spatially differentiate regions of more or less local structural change within a NP. Changes in both O-Si-O angle and Si-O bond distances are typical ways in which local structural relaxation can take place. Although separated in IR spectra, relaxations of these structural features combine to distort the SiO₄ tetrahedra in NPs. From our discussion above, we should expect that in a relaxed BC NP, the relaxation of SiO₄ tetrahedral should be mainly close to the surface, whereas for an amorphous NP we should expect all SiO₄ tetrahedral to be fairly equally distorted. In **Figure 5.10**, we show two cuts through the relaxed 116 BC NP (left) and a cut through the 116 A NP (right) showing only the Si

atoms and where the degree of local SiO_4 tetrahedral disorder (*i.e.* of the surrounding four oxygen atoms which are not shown) is related to the colour of the Si atom in question. We take the tetrahedral arrangement of oxygen atoms around the Si atoms in forsterite as our benchmark for the highest tetrahedrality. We measure the degree of distortion of each SiO_4 centre by taking the RMSD of the atom positions with those of rotationally aligned SiO_4 centre from the forsterite crystal. In **Figure 5.10**, we give the lightest colour to Si atoms with associated SiO_4 centres having structures very close to those in forsterite and progressively darker shading to more distorted tetrahedrons. For the amorphized 116 formula-units NP (right, **Figure 5.10**) the darker shading of all Si atoms shows that all SiO_4 centres have significantly distorted structures. However, for the BC (left, **Figure 5.10**) it is clear that significant tetrahedral distortion only occurs at the surface of the NP (*i.e.* due to surface relaxation).

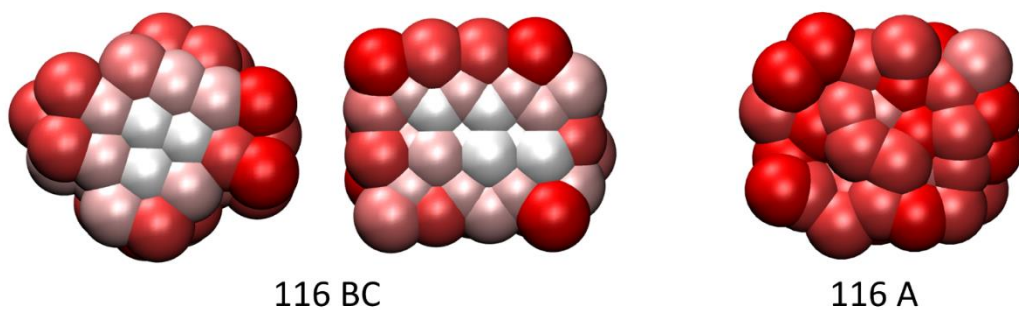


Figure 5.10 Cuts through 116 NPs showing only Si atoms with the degree of local tetrahedral distortion of the associated SiO_4 centres indicated by shading (lighter: less distortion; darker: more distortion). Left: two perpendicular cuts through the 116 BC NP. Right: a single cut through the 116 A NP.

In summary, from our average measures (*i.e.* $\langle \text{Mg CN} \rangle$ and RMSD-Si values) we find that BC NPs preserve a higher degree of periodic crystallinity than A NPs, while BC, A and N NPs all show some degree of local structural distortion which increases with the level of amorphization. We note that our BC NP structures correspond to the most crystalline possible morphologies for their size (*i.e.*

relaxed crystal cuts), even though our structural measures show that they do not possess the full structural order of the perfect, infinite crystal. In principle, average local structural measures such as our $\langle \text{Mg CN} \rangle$ values could be measured and/or observed from X-ray absorption spectra. Interestingly, preliminary estimates of the proportion of crystalline dust in the ISM based on such X-ray observations have placed tentative upper limits which are significantly in excess of those derived from IR observations.³⁵ From our spatially resolved maps of tetrahedral distortion of individual SiO_4 centres, we can further confirm that, although amorphized NPs are distorted fairly homogeneously throughout their structure, the main contribution to local structural disorder in BC NPs is through surface relaxation.

5.5 Full IR spectra

Besides structural identification, it is important to establish whether our OI NPs can be characterized by IR spectroscopy, as this corresponds to the main astronomical observable for silicate dust grains. Consequently, we employed frequency calculations to obtain the full IR spectra of all optimized NPs.

The PBE/OIBs full IR harmonic spectra with CRYSTAL were simulated only for a few NPs, *i.e.*, all the 14 and 30 formula-units NPs and the 50 BC NP. For all NPs, we also simulated the full IR spectra with the GULP code at the Walker FF level (**Figure 5.2**, panel **B**). In all cases the line shapes of the IR spectral peaks were obtained from sums of Gaussian functions centred at the computed IR frequencies with heights adjusted to the corresponding absolute IR intensities. The full width at half maximum (FWHM) for the Gaussian functions was set equal to 10 cm^{-1} . This choice is fully justified in our published work, and it corresponds to a temperature of about 100 K, close to the typical temperatures of the ISM.¹ In **Figure 5.11**, **A-E** panels, we report the full IR spectra for some selected particles in the $8\text{-}26 \mu\text{m}$ ($1250\text{-}385 \text{ cm}^{-1}$) region. The reliability of the IR spectra from both CRYSTAL and GULP calculations is confirmed through a

comparison with experimental data for both amorphous and crystalline Ol (Figure 5.1).

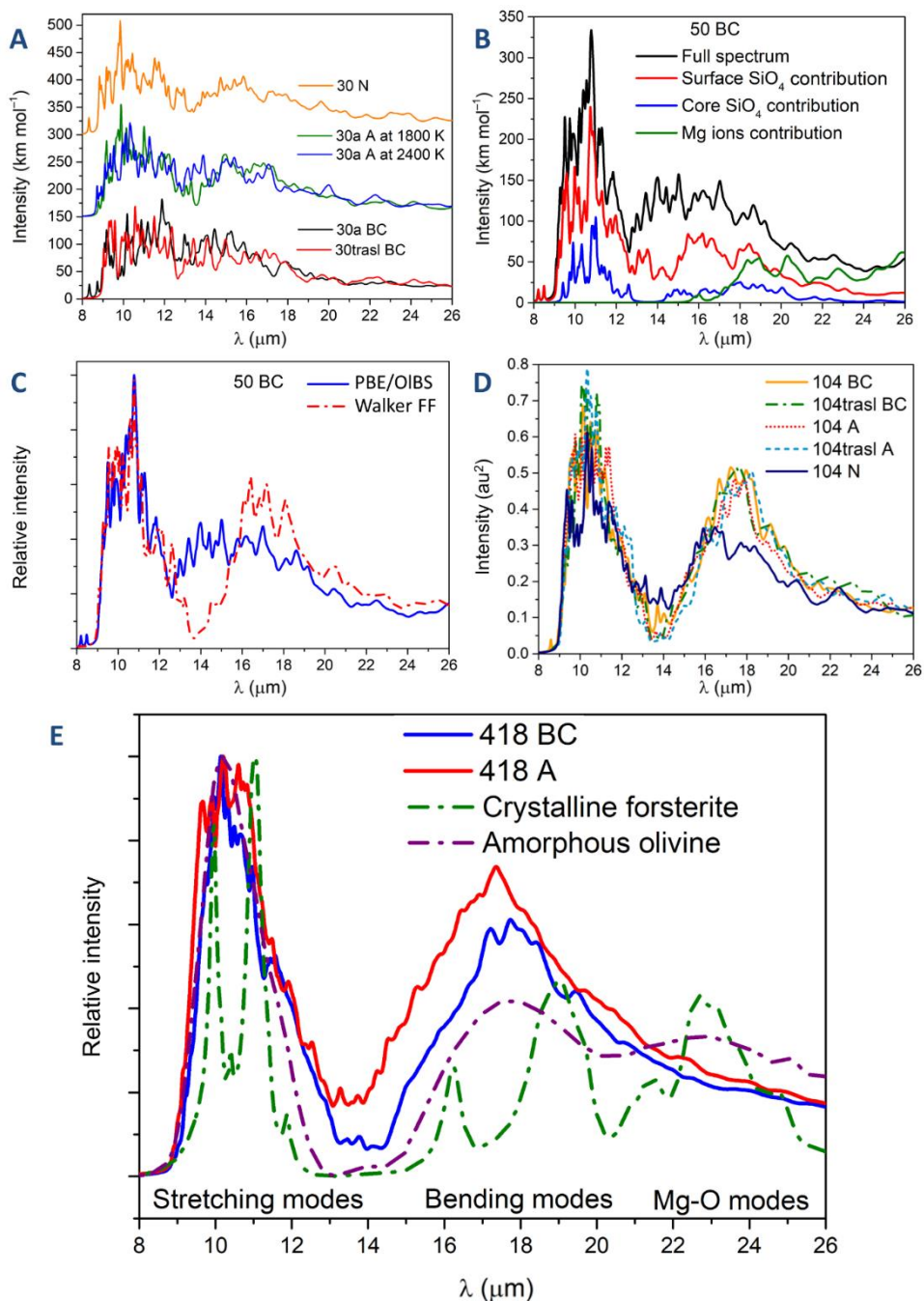


Figure 5.11 A-E: Simulated IR spectra for some selected NPs: **A:** some 30 formula-units NPs calculated with DFT (spectra for A and N NPs are vertically transposed). **B:** the 50

BC NP IR spectrum calculated with DFT. Contributions from subsets of atoms are also reported. **C**: the 50 BC NP IR spectrum as calculated using DFT and the Walker FF. **D**: all 104 NPs IR spectra calculated with the Walker FF. **E**: 418 units BC and A NPs IR spectra calculated using the Walker FF. The spectra for experimentally-synthesized crystalline forsterite and amorphous olivine are also reported for comparison.²¹ These experimental spectra have been reproduced with the authors' permission.

Figure 5.11A reports the IR spectra of a wide selection of 30 formula unit NPs including examples of BC (both translated and non-translated), A (amorphized at 1800 K and 2400 K) and N families. At such a small NP size, and using 10 cm^{-1} as FWHM, clearly we do not have only two distinct peaks typical of amorphous silicates.^{2,3,36,37} Indeed, many individual small narrow peaks extending over a wide range of wavelengths can be easily distinguished. However, even though the individual peaks of the spectra for each NPs differ in their position, the overall profile of all spectra is quite similar. In particular, the IR spectral profiles of these NPs are broadly characterized by two distinct regions, namely the Si-O stretching between 8 to 12 μm and the O-Si-O bending between 13 to 18 μm . Silicate NPs at these sizes tend to show sharp spectral features due to the limited number of atoms, irrespectively of the amorphous/crystalline nature of the specific NP in question. Calculated IR spectra of even smaller olivine and pyroxene silicate nanoclusters have been also reported showing a similar behaviour.³⁸ The comparison of all the spectra in **Figure 5.11A** suggests that small crystalline and amorphous silicate NPs with an olivinic $\text{Mg}_2\text{Si}_2\text{O}_4$ composition are indistinguishable by IR spectroscopy irrespectively of their origin. Generally, the large number of distinct peaks can be attributed to the effect of the high surface to core ratio of these NPs and the subsequent effect that surface relaxation exerts on the core of the NP. This is well underlined by **Figure 5.11B** which shows the contribution to the IR spectrum of the 50 BC NP with respect to different chemical species (*i.e.*, “surface shell” and “core” silicates and Mg cations). Surface shell SiO_4 units contribute to the whole spectrum, while Mg ions in this region involve

modes from $\lambda > 17 \mu\text{m}$ ($\sim 590 \text{ cm}^{-1}$). The contributions from bulk SiO_4 units are also present throughout the 8-20 μm ($\sim 1250\text{-}500 \text{ cm}^{-1}$) range, but to a minor extent.

As IR calculations using DFT are extremely expensive for NPs larger than 50 formula-units, the IR spectra of larger NPs were analysed by means of FF calculations. The IR spectra of these NPs were calculated using the Walker FF, which provides a reasonable account of the IR peak positions of silicate NPs (see **Figure 5.1**). **Figure 5.11C** shows a comparison between the IR spectrum of the 50 BC NP as calculated using the Walker FF and DFT at a PBE/OlBS level. The IR spectrum from a CM-based FF calculation can only provide an approximation to the more accurate QM-based DFT-calculated spectrum, however, the overall FF description of the IR spectrum appears to still be fairly well captured. In particular, the spectrum of the 50 formula-units NP in both cases is comprised of a wide range of features with two main regions: the Si-O stretching region around 10 μm and the O-Si-O bending region. While the FF calculation reproduces the 10 μm features very well, intensity at the O-Si-O region (*i.e.* $\sim 13\text{-}16 \mu\text{m}$) are less well captured and which seems to be shifted towards longer wavelengths with respect to the DFT-calculated IR spectrum. This behaviour mirrors what shown in the comparison of the Walker FF calculated spectrum of forsterite with corresponding DFT-calculated spectrum and that from experiment (see **Figure 5.1**), and is thus perhaps a systematic feature of IR spectra calculated using the Walker FF. Nevertheless, the qualitative broad and double-peaked IR spectrum is well reproduced in both calculations, which in both cases clearly do not provide evidence for a highly crystalline NP.

Figure 5.11D shows the full IR spectra for all the 104 formula unit NPs calculated using the Walker FF as illustrative examples. As for the 50 BC NP in **Figure 5.11B**, the characteristic broad double peaked silicate profile is reproduced for all BC, A and N NPs. In particular, the spectra from the two BC and the two A NPs

are almost identical, with very similar absolute intensities for the two main peaks. As the sizes are increased, the O-Si-O bending region appears to be less sharp and more featureless and becomes more similar to the typical features observed in the spectra of ISM silicates. This similarity is even more clear for the spectra of the largest 418 formula-units NPs, depicted in **Figure 5.11E**, shown together with two experimental IR spectra for crystalline forsterite and amorphous olivine.²¹ At this size, which corresponds to a NP diameter of ~4.6 nm, the BC NP IR spectrum is still dominated by the two broad silicate peaks and thus, like the A NP, spectroscopically non-crystalline.

The N NPs show slight changes from the BC and A particles. The first noticeable change corresponds to the decreases of the intensities of both peaks. In addition, the O-Si-O peak is arguably shifted towards lower values. This effect is found in the spectra of all the N NPs and is probably the result of the formation of silicate polymerization and MgO segregation. The displacement of the O-Si-O band has previously been linked to the progressive change of silicate structure along the mineral series olivine-pyroxene-silica.^{10,11,39}

We finally note that the width of the Si-O stretching peak in our larger NPs ranges from 1.7 to 2.0 μm which is in line with typical ISM 9.7 μm peak widths.⁴⁰ Although consistent with observation, our calculations only deal with a very small selection of NP structures, sizes and compositions and the possible significance of this match should not be overstated.

Resuming, the simulated NP spectra for all our larger NPs closely resemble those assumed to arise from amorphous cosmic silicates. Thus, contrary to the spectroscopic distinguishability of large crystalline and amorphous dust grains, Mg-rich olivinic nanograins (at least in the size range considered herein) cannot be classified as being in an amorphous or crystalline state only from their IR spectra, despite the fact that they can be explicitly and measurably shown to be structurally and energetically distinguishable.

5.6 Concluding remarks

In this Chapter we provided a comprehensive study of the energetic, structural and IR spectroscopic properties of crystalline and non-crystalline Mg-rich olivine (Mg_2SiO_4) NPs possessing 10s to 1000s of atoms (from ~ 1 to ~ 5 nm in diameter). Bulk cut (BC) crystalline-like NPs were modelled using the top-down Wulff construction, while two kinds of non-crystalline NPs were studied: thermally annealed (amorphized, A) NPs based on the Wulff constructed cuts, and nucleated (N) particles grown by monomeric addition. While the amorphized and bulk cut NPs share some structural features similar to bulk crystalline forsterite (*e.g.* isolated SiO_4 units), the nucleated NPs show the presence of pyroxene-like chains and small MgO regions, and thus can be seen as partial solid mixtures. In terms of energetics, BC NPs are metastable with respect to annealed amorphous NPs, while nucleated NPs are higher in energy than both other NP types. In the bulk phase, however, crystalline forsterite is the most energetically stable phase. From the size-dependent energetic trends of the annealed and crystalline NPs, we tentatively estimate that the energetic stability cross-over size between these two NP families will occur for a NP size of ~ 12 nm diameter.

We have analysed the structures of our NPs in detail in order to evaluate the effects of amorphization by comparing three measures of crystallinity to assess local and periodic order. The displacements of silicon atoms were used to characterize the periodic order and demonstrated that the amorphous NPs are easily structurally differentiated as more disordered with respect to the crystalline BC NPs. From the analysis of the “average Mg coordination number” $\langle \text{Mg CN} \rangle$, our local order descriptor, we show that the BC NPs have lower than bulk values due to surface effects, which cause a lowering of the Mg coordination. However, the A and N NPs show even lower $\langle \text{Mg CN} \rangle$ values due to their more disordered structures. Examining the spatially resolved local structural distortion of tetrahedral SiO_4 units in BC and A NPs we also confirm that: *i*) A-type NPs show

a homogenous distribution of disorder throughout the whole NP, and *ii*) BC NPs show only significant local structural distortion at their surfaces.

The IR spectra of the smallest NPs are composed of a large collection of distinct signals. As the NP size increases the IR spectra of all NP families show broader peaks in the characteristic ~ 10 and ~ 18 μm regions, in accordance with typical astronomical silicate IR spectra. Surprisingly, both thermally annealed structurally amorphous NPs and NPs relaxed from bulk crystalline cuts show similar double-peaked broad spectra. Indeed, from the calculated IR spectra, our larger BC and A NPs would be clearly judged as spectroscopically amorphous. This result implies that that it would be very difficult to accurately estimate the degree of crystallinity of nanosilicate grains in the ~ 1 - 5 nm diameter regime using IR spectroscopy alone. In contrast, the IR spectra from nucleated NPs arising from gas phase monomeric addition show some features that make them distinguishable from the A and BC NPs.

Further work is necessary to provide a more accurate estimate of the cross-over NP size for the amorphous-crystalline transition. Moreover, the IR spectra of maximally crystalline nanograins (*i.e.* BC NPs) having diameters of ~ 4.5 nm cannot be distinguished from the corresponding spectra of amorphous nanograins (*i.e.* A NPs). This surprising result may cast some doubts on the currently established upper limits of the fraction of crystalline silicate dust in the ISM based on observed IR spectra. If a large population of crystalline nanograins exists in the ISM, a traditional analysis would lead to their observed IR spectra being interpreted as showing the presence of amorphous grains. Generally, the existence of many highly crystalline nanograins could be hidden in IR spectra that are usually taken to indicate only amorphous silicates. Our results may provide support for preliminary results from X-ray absorption observations^{35,41} which indicate a relatively large fraction of crystalline silicate dust in the ISM as compared to estimates based on analyses of IR spectra.⁴²

Bibliography

- (1) Zamirri, L.; Macià Escatllar, A.; Marinoso Guiu, J.; Ugliengo, P.; Bromley, S. T. What Can Infrared Spectra Tell Us about the Crystallinity of Nanosized Interstellar Silicate Dust Grains? *ACS Earth Sp. Chem.* **2019**, *3*, 2323–2338.
- (2) Henning, T. Cosmic Silicates. *Annu. Rev. Astron. Astrophys.* **2010**, *48*, 21–46.
- (3) Henning, T. Cosmic Silicates - A Review. In *Solid State Astrochemistry*; Pirronello, V., Krelowski, J., Manicò, G., Eds.; Proceedings of the NATO Advanced Study Institute on Solid State Astrochemistry, 2000; pp 85–103.
- (4) Malfait, K.; Waelkens, C.; Waters, L. B. F. M.; Vandenbussche, B.; Huygen, E.; de Graauw, M. S. The Spectrum of the Young Star HD 100546 Observed with the Infrared Space Observatory. *Astron. Astrophys.* **1998**, *332*, L25–L28.
- (5) Hanner, M. S. The Silicate Material in Comets. *Space Sci. Rev.* **1999**, *90*, 99–108.
- (6) Waters, L. B. F. M.; Molster, F. J.; de Jong, T.; Beintema, D. A.; Waelkens, C.; Boogert, A. C. A.; Boxhoorn, D. R.; de Graauw, T.; Drapatz, S.; Feuchtgruber, H.; *et al.* Mineralogy of Oxygen-Rich Dust Shells. *Astron. Astrophys.* **1996**, *315*, L361–L364.
- (7) Molster, F. J.; Kemper, C. Crystalline Silicates. *Space Sci. Rev.* **2005**, *119*, 3–28.
- (8) Jäger, C.; Molster, F. J.; Dorschner, J.; Henning, T.; Mutschke, H.; Waters, L. B. F. M. Steps toward Interstellar Silicate Mineralogy. IV. The Crystalline Revolution. *Astron. Astrophys.* **1998**, *339*, 904–916.
- (9) Molster, F. J.; Waters, L. B. F. M.; Tielens, A. G. G. M. Crystalline Silicate Dust around Evolved Stars II. The Crystalline Silicate Complexes. *Astron. Astrophys.* **2002**, *240*, 222–240.
- (10) Jäger, C.; Dorschner, J.; Mutschke, H.; Posch, T.; Henning, T. Steps toward

- Interstellar Silicate Mineralogy VII. Spectral Properties and Crystallization Behaviour of Magnesium Silicates Produced by the Sol-Gel Method. *Astron. Astrophys.* **2003**, *408*, 193–204.
- (11) Speck, A. K.; Whittington, A. G.; Hofmeister, A. M. Disordered Silicates in Space: A Study of Laboratory Spectra of “Amorphous” Silicates. *Astrophys. J.* **2011**, *740*, 17pp.
- (12) Hallenbeck, S. L.; Nuth III, J. A.; Nelson, R. N. Evolving Optical Properties of Annealing Silicate Grains: From Amorphous Condensate to Crystalline Mineral. *Astrophys. J.* **2000**, *535*, 247–255.
- (13) Thompson, S. P.; Parker, J. E.; Tang, C. C. The 10 μm Band in Amorphous MgSiO_3 : The Influence of Medium-Range Structure, Defects and Thermal Processing. *Astron. Astrophys. Astrophys.* **2012**, *545*, A60.
- (14) Demyk, K.; D’Hendecourt, L.; Leroux, H.; Jones, A. P.; Borg, J. IR Spectroscopic Study of Olivine, Enstatite and Diopside Irradiated with Low Energy H^+ and He^+ Ions. *Astron. Astrophys.* **2004**, *420*, 233–243.
- (15) Chiar, J. E.; Tielens, A. G. G. M. Pixie Dust: The Silicate Features in the Diffuse Interstellar Medium. *Astrophys. J.* **2006**, *637*, 774–785.
- (16) Fogerty, S.; Forrest, W.; Watson, D. M.; Sargent, B. A.; Koch, I. Silicate Composition of the Interstellar Medium. *Astrophys. J.* **2016**, *830*, 71 (11 pp).
- (17) Li, A.; Draine, B. T. On Ultrasmall Silicate Grains in the Diffuse Interstellar Medium. *Astrophys. J.* **2001**, *550*, L213–L217.
- (18) Kogut, A.; Banday, a. J.; Bennett, C. L.; Gorski, K.; Hinshaw, G.; Smoot, G. F.; Wright, E. L. Microwave Emission at High Galactic Latitudes. *Astrophys. J.* **1996**, *464*, L5–L9.
- (19) Draine, B. T.; Lazarian, A. Diffuse Galactic Emission from Spinning Dust Grains. *Astrophys. J.* **1998**, *494*, L19–L22.
- (20) Draine, B. T.; Lazarian, A. Electric Dipole Radiation from Spinning Dust Grains. *Astrophys. J.* **1998**, *508*, 157–179.

- (21) Yamamoto, D.; Tachibana, S. Water Vapor Pressure Dependence of Crystallization Kinetics of Amorphous Forsterite. *ACS Earth Sp. Chem.* **2018**, *2*, 778–786.
- (22) Lamiel-Garcia, O.; Cuko, A.; Calatayud, M.; Illas, F.; Bromley, S. T. Predicting Size-Dependent Emergence of Crystallinity in Nanomaterials: Titania Nanoclusters versus Nanocrystals. *Nanoscale* **2017**, *9*, 1049–1058.
- (23) Puigdollers, A. R.; Illas, F.; Pacchioni, G. Structure and Properties of Zirconia Nanoparticles from Density Functional Theory Calculations. *J. Phys. Chem. C* **2016**, *120*, 4392–4402.
- (24) Bostrom, D. Single-Crystal X-Ray Diffraction Studies of Synthetic Ni–Mg Olivine Solid Solution. *Am. Mineral.* **1987**, *72*, 965–972.
- (25) Momma, K.; Izumi, F. VESTA 3 for Three-Dimensional Visualization of Crystal, Volumetric and Morphology Data. *J. Appl. Crystallogr.* **2011**, *44*, 1272–1276.
- (26) Bruno, M.; Massaro, F. R.; Prencipe, M.; Demichelis, R.; De La Pierre, M.; Nestola, F. Ab Initio Calculations of the Main Crystal Surfaces of Forsterite (Mg₂SiO₄): A Preliminary Study to Understand the Nature of Geochemical Processes at the Olivine Interface. *J. Phys. Chem. C* **2014**, *118*, 2498–2506.
- (27) Zamirri, L.; Corno, M.; Rimola, A.; Ugliengo, P. Forsterite Surfaces as Models of Interstellar Core Dust Grains: Computational Study of Carbon Monoxide Adsorption. *ACS Earth Sp. Chem.* **2017**, *1*, 384–398.
- (28) Plimpton, S. Fast Parallel Algorithms for Short-Range Molecular Dynamics. *J. Comput. Phys.* **1995**, *117*, 1–19.
- (29) Johnston, R. L. *Atomic and Molecular Clusters*; CRC Press, Taylor & Francis Group, 2002.
- (30) Viñes, F.; Lamiel-Garcia, O.; Illas, F.; Bromley, S. T. Size Dependent Structural and Polymorphic Transitions in ZnO: From Nanocluster to Bulk. *Nanoscale* **2017**, *9*, 10067–10074.

- (31) Suh, K. W. Crystalline Silicates in the Envelopes and Discs around Oxygen-Rich Asymptotic Giant Branch Stars. *Mon. Not. R. Astron. Soc.* **2002**, *332*, 513–528.
- (32) Gail, H.-P.; Sedlmayr, E. Mineral Formation in Stellar Winds. I. Condensation Sequence of Silicate and Iron Grains in Stationary Oxygen Rich Outflows. *Astron. Astrophys.* **1999**, *347*, 594–616.
- (33) Molster, F. J.; Yamamura, I.; Waters, L. B. F. M.; Nyman, L.-A.; Kaufl, H.-U.; de Jong, T.; Loup, C. IRAS 09425–6040: A Carbon Star Surrounded by Highly Crystalline Silicate Dust. *Astron. Astrophys.* **2001**, *366*, 923–929.
- (34) Gail, H. P.; Sedlmayr, E. Inorganic Dust Formation in Astrophysical Environments. *Faraday Discuss.* **1998**, *109*, 303–319.
- (35) Zeegers, S. T.; Costantini, E.; de Vries, C. P.; Tielens, A. G. G. M.; Chihara, H.; de Groot, F.; Mutschke, H.; Waters, L. B. F. M.; Zeidler, S. Absorption and Scattering by Interstellar Dust in the Silicon K-Edge of GX5-1. *Astron. Astrophys.* **2017**, *599*, A117 (11 pp).
- (36) Meeus, G.; Waters, L. B. F. M.; Bouwman, J.; van den Ancker, M. E.; Waelkens, C.; Malfait, K. ISO Spectroscopy of Circumstellar Dust in 14 Herbig Ae/Be Systems: Towards an Understanding of Dust Processing. *Astron. Astrophys.* **2001**, *365*, 476–490.
- (37) Draine, B. T. Interstellar Dust Grains. *Annu. Rev. Astron. Astrophys.* **2003**, *41*, 241–289.
- (38) Macià, A.; Lazauskas, T.; Woodley, S.; Bromley, S. T. Structure and Properties of Nanosilicates with Olivine ($\text{Mg}_2\text{Si}_2\text{O}_4$)_N and Pyroxene (MgSiO_3)_N Compositions. *ACS Earth Sp. Chem.* **2019**.
- (39) Ossenkopf, V.; Henning, T.; Mathis, J. S. Constraints on Cosmic Silicates. *Astron. Astrophys.* **1992**, *261*, 567–578.
- (40) Shao, Z.; Jiang, B. W.; Li, A.; Gao, J.; Lv, Z.; Yao, J. Probing the 9.7 μm Interstellar Silicate Extinction Profile through the Spitzer/IRS

- Spectroscopy of OB Stars. *Mon. Not. R. Astron. Soc.* **2018**, *478*, 3467–3477.
- (41) Zeegers, S. . T.; Costantini, E.; Rogantini, D.; de Vries, C. P.; Mutschke, H.; Mohr, P.; de Groot, F.; Tielens, A. G. G. M. Dust Absorption and Scattering in the Silicon K-Edge. *Astron. Astrophys.* **2019**, *627*, A16 (18 pages).
- (42) Kemper, F.; Vriend, W. J.; Tielens, A. G. G. M. The Absence of Crystalline Silicates in the Diffuse Interstellar Medium. *Astrophys. J.* **2004**, *609*, 826–837.

6 Appendix

6.1 CO on forsterite surfaces

In Chapter 5, we discussed about crystalline-like, olivine particles with a forsterite (Fo) stoichiometry, the BC NPs. These NPs reflect the shape of the Fo Wulff polyhedron, *i.e.* the aspect of a perfect macroscopic crystal. To generate such shapes, the Miller indices (hkl) and the surface energy E_S of each surface must be known. As described in Section 4.3, the easiest way to simulate a surface, at least with a Gaussian BS-based code like CRYSTAL, is by cutting a slab model (where PBC are applied to two dimensions) from a bulk model. Consequently, slab models do show two ends which are exposed to void (see **Figure 4.3A** as an illustrative example) and an infinitely repeating unit surface characterized by a given area A . The surface energy is then defined as:

$$E_S = \frac{E_{(hkl)} - mE_{bulk}}{2A} \quad 6.1$$

i.e. as the difference between the energy of the slab model with indices (hkl) ($E_{(hkl)}$) and that of the bulk (E_{bulk}), normalized to the unit area (A). The m and 2 factors account for the relative stoichiometry of the slab and bulk models and for the two ends of the slab model, respectively.

In a recent work, we dealt with the shape of the most stable Fo crystalline surfaces, as characterized by carbon monoxide (CO) adsorption on selected exposed Mg^{2+} ion sites.¹ Some of the data of that work have been used to define the starting structures of the BC NPs in Chapter 5. Therefore, in this Appendix, we report some of the most important results of such a work.

6.1.1 Fo bulk structural properties

Forsterite (Mg_2SiO_4), the Mg end-member of the olivines isomorphous solid solution (Mg,Fe) $_2SiO_4$, belongs to $Pbnm$ space group. Its bulk structure is

composed of a distorted hexagonally close-packed array of oxygen with 1/8 of the tetrahedral sites occupied by Si^{4+} (SiO_4 units) and 1/2 of the octahedral sites occupied by divalent cations (Mg^{2+}) usually denoted as M1 and M2 (MgO_6 units). Of the two octahedral sites, the M1 site, which is more distorted and compact than M2 one, forms edge-sharing chains parallel to the c axis. The adsorption surface sites for all the seven slab models are either Mg^{2+} cations or oxygen atoms belonging to external SiO_4 groups. We labelled each Mg^{2+} site in alphabetic order following its z -coordinate value, from the most (highest z -coordinate) to the least (lowest z -coordinated) exposed to void (see **Figure 6.1**).

6.1.2 Computational details

In this brief Section, we report only the most important Computational aspects. For further information, please refer to the original work.¹

All calculations have been conducted with the CRYSTAL code within the DFT framework at B3LYP level,²⁻⁴ with the addition of the Grimme's D2 correction for dispersive forces⁵ as modified by Civalleri *et al.* (D2*).⁶ The BS we adopted for the Fo atoms has been borrowed from a former work by Demichelis *et al.* where the authors developed a specific BS which gave excellent results in the description of Fo bulk properties ("FoBS").⁷ To describe CO atoms, we adopted Ahlrichs TZV BS with the addition of some polarization functions (as in Chapter 3).⁸ All geometry optimizations have been performed with CRYSTAL default values. For the calculation of the CO stretching frequencies, we adopted the same strategy as in Chapter 3.

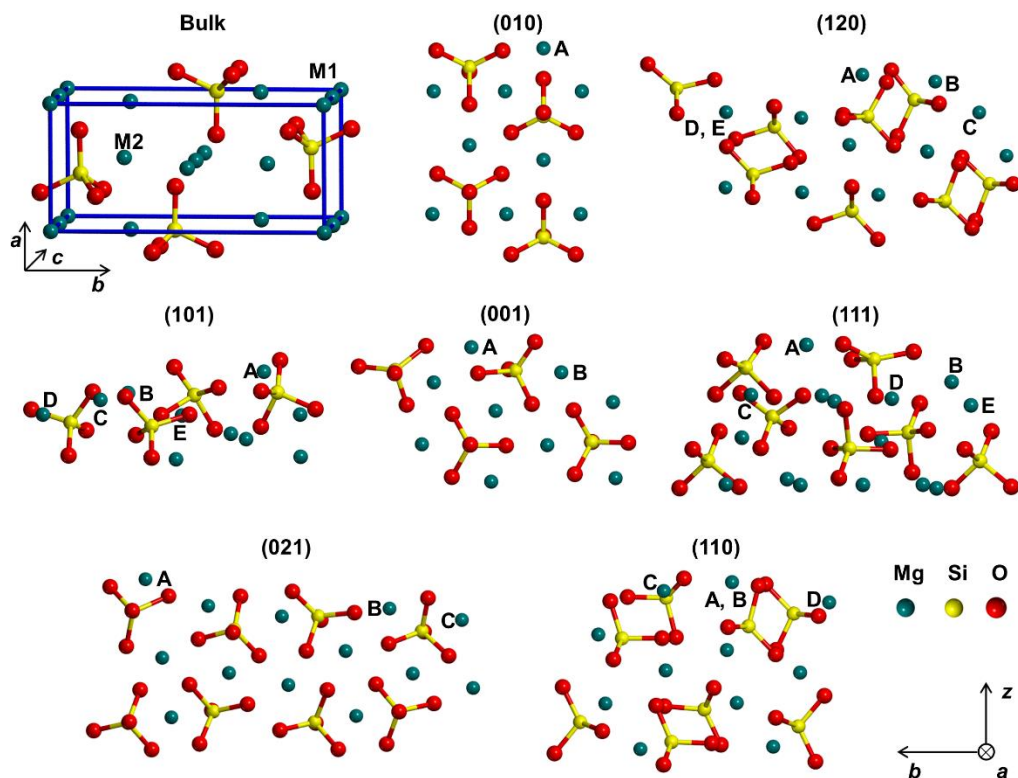


Figure 6.1 Forsterite bulk (top-left corner, unit cell borders in blue) and side views of the seven slab models, as a result of the B3LYP-D2*/FoBS optimization. M1 and M2 indicate the Mg octahedral sites. The figure only shows few atomic layers for sake of clarity. Mg cations available for adsorption are labelled in alphabetic order according to their z -coordinated. For the (120) and (110) surfaces, Mg D/E and Mg A/B are indicated as “D, E” and “A, B”, respectively, as they are eclipsed in this representation.

6.1.3 Slab properties

The slab models we used for all calculations have been borrowed by a former work by Bruno *et al.*⁹ dealing with the characterization of the seven most stable Fo surfaces at B3LYP only level. All the seven slabs are electrically neutral, as they stoichiometrically correspond to a Fo bulk tetramer (*i.e.* the m factor in Equation 6.1 is equal to 4). Generally speaking, Fo crystalline surfaces are not flat, as some of them naturally show “steps” and “corners” due to the peculiar ionic/covalent nature of Fo (**Figure 6.1**). This is really important for the CO adsorption because it means that Fo surfaces present a large variety of adsorption

Appendix

sites (see, for example, the (120) and the (111) slabs). Moreover, as we have already outlined in Chapter 5, silicate units are characterized by high mobilities. in particular in the not flat surfaces, which produce a partial amorphization.

The seven slabs have been reoptimized at B3LYP-D2*/FoBS level and the results compared with those obtained by Bruno *et al.*⁹ (**Table 6.1**).

Table 6.1 Structural and energetic features for the seven slab models. A is the surface area (in Å²) from the B3LYP-D2*/FoBS optimization, E_S (in J m⁻²) is the surface energy from Equation 6.1 with $m = 4$ (values free from the dispersion correction in parentheses) and MRI is the “morphological relevance index” (see text for details). % Δ are the percentage variations of our surface energies free from dispersion contribution with respect to Bruno’s values.

(hkl)	A	E_S			MRI	
		This work	Bruno [§]	% Δ	This work	Bruno [§]
(010)	28.98	1.44 (1.23)	1.22	0.8	23.8	21.7
(120)	83.71	1.68 (1.37)	1.36	0.7	29.7	37.0
(101)	79.41	1.96 (1.62)	1.78	-9.0	20.7	12.2
(001)	48.76	1.98 (1.72)	1.78	-3.4	19.8	15.8
(111)	82.70	2.19 (1.83)	1.84	-0.5	2.5	8.2
(021)	75.55	2.24 (1.91)	1.90	0.5	3.5	5.1
(110)	67.53	2.46 (2.17)	2.18	-0.5	0.0	0.0

§: Ref. 9.

From the computed surface energies, we were able to evaluate the “morphological relevance index (MRI)”, *i.e.* the ratio, expressed as percentage, between the unit area of a single surface and the total area of the crystal and, through the Wulff theorem,¹⁰ the equilibrium shape of the crystal at 0 K (**Figure 6.2**). Computed data are in good accordance with the work by Bruno *et al.*,⁹ even if some strong discrepancies can be outlined (as in the (101) and (111) cases). Nevertheless, the overall descriptions are very similar to one another. It is worth mentioning that the initial NPs in Chapter 5 (**Figure 5.3**) have been generated by maintaining the ratios among MRI values in the 6th column of **Table 6.1**.

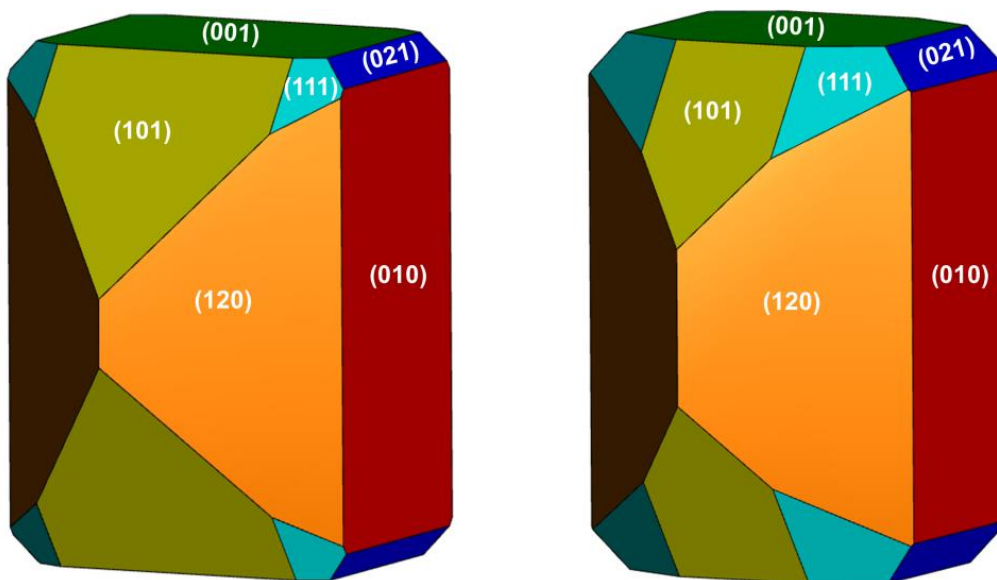


Figure 6.2 Comparison between the equilibrium shape at 0 K of crystalline forsterite from the Wulff's construction,¹⁰ by using surface energy values from our (inclusive of D2* dispersion, left) and from Bruno's work⁹ (right). We adopted an RGB colour scale to highlight the surface stability order, from the most (red) to the least (blue) stable one.

Apart from their morphological complexity, Fo surfaces are also characterized by very complicated electrostatic features. For the purpose of adsorption, electrostatic potential maps (ESPMs) probably represent of the most useful tool. Briefly, ESPMs are obtained from a 3D-grid of points surrounding a given atomistic model. At these points, thanks to the information stored in the wave function, the electron density and the electrostatic potential (ESP) can be evaluated by two integral expressions (see, for details, the CRYSTAL17 User's manual¹¹). Data are then plotted together and an RGB colour scale is adopted to represent negative (red), neutral (green) and positive (blue) ESP regions for a given value of the electron density. The result of this procedure applied to the CO case and to two distinct surfaces (as illustrative examples) are reported in **Figure 6.3**.

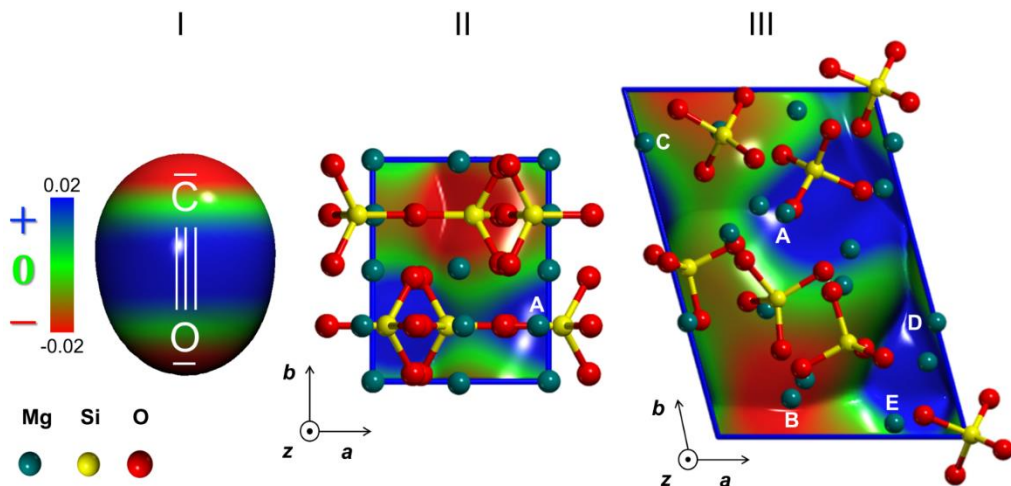


Figure 6.3 B3LYP-D2* ESPMs superimposed to the ground state electron densities (blue = positive, green = neutral and red = negative ESP values). **I**: quadrupolar nature of carbon monoxide molecule. **II**: unit cell top view of the (010) surface superimposed on the ESPM. **III**: unit cell top view of the (111) surface superimposed on the ESP map: Mg sites are labeled in alphabetic order from the most (A) to the least exposed (E) to void. The electron density value is set equal to 10^{-6} au.

6.1.4 CO adsorption

We simulated the CO adsorption by placing one or two CO molecules onto the exposed Mg ions. We started by adsorbing CO molecules at about 2.2 \AA from the exposed Mg ions at both the upper/lower surfaces. For all the surfaces, we first considered the lowest CO coverage, by adsorbing a single CO molecule on each Mg available ion, to probe them separately. We then considered the highest CO coverage by adsorbing the CO molecule on all available exposed Mg ions at the same time. For the (120), (101), (001) and (111) surfaces we also tested intermediate coverages.

For all the optimized structures, we computed the energetics of adsorption *per* adsorbed CO molecule. The BSSE-corrected interaction energies fall into a quite wide range (from -68 to -23 kJ mol^{-1} *per* adsorbed CO), indicating that CO is only physisorbed to the Fo surfaces. In all cases, we found a fundamental role of dispersive forces and of BSSE in determining the final energetics and,

consequently, the geometry of adsorption. All details can be found in the original work.¹

When dealing with the adsorbed CO molecule, a key quantity is its stretching frequency shift value with respect to the free CO one ($\Delta\bar{\nu}$). Positive, or hypsochromic, shifts are referred as “blue-shifts”, while negative, or bathochromic, ones as “red-shift”. Blue-shifts imply a CO bond shortening with a corresponding increase in the bond force constant and vibrational frequency. The reverse happens for red-shifted cases.¹² The relevance of the CO vibrational shift is to probe the electric field and the chemical features of the adsorbing surface sites. For example, on transition metal ionic systems with d^0 orbitals the $\bar{\nu}(\text{CO})$ is red-shifted, due to donation of the CO sigma anti-bond orbital in the empty d orbitals.^{12–15} On non-transition metal ionic systems, or when the metal ion is in the d^{10} configuration, the $\bar{\nu}(\text{CO})$ is blue-shifted, being dominated by electrostatic effects (dipole-charge interaction).^{12,16,17} For Ca(II), Na(I), Zn(II), Ag(I) and Cu(I) exchanged zeolites, Bolis and coworkers reported the existence of a linear correlation between experimental $\Delta\bar{\nu}$ and the values of desorption enthalpies in the CO zero coverage limit.^{18,19} They showed that any deviation from the linear behavior reveals the incoming effect due to increasing charge transfer and back-donation towards CO. Despite the highly ionic nature of the forsterite surfaces, we did not observe such a correlation (data not showed). Furthermore, for some cases we computed red-shifted values. These cases represent a small percentage of the total (7 cases out of a total of 37, see **Figure 6.4II**). The missing expected linear correlation between energetic and spectroscopic features reveals a more complex interaction for the present case with respect to the systems considered by Bolis *et al.*,^{18,19} in which the surrounding of the adsorbing cation was much more regular than in forsterite surfaces. The complexity of the surface sites in the present case and the important role of dispersion interaction deviate from the simpler ion/dipole model for the

systems accounted for by the Bolis *et al.*^{18,19} Nevertheless, we found a very good linear correlation between shifts and C–O distances (d_{CO}), as predicted by the Blyholder model¹² (**Figure 6.4I**). This linear relation is useful for quickly evaluating the CO vibrational shift without performing an expensive frequency calculation, by only using its C–O bond length.

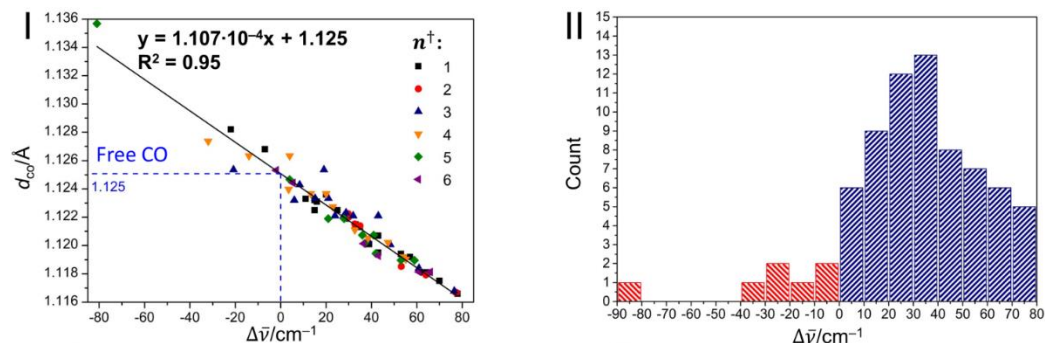


Figure 6.4 I: linear correlation between CO bond lengths (d_{CO}) and the shift values ($\Delta\bar{\nu}$). Data are grouped by the number of CO molecule *per* unit cell (n^\dagger) in each model. **II:** histogram distribution of $\Delta\bar{\nu}$ values.

To the best of our knowledge, while bathochromic shifts have been reported for CO adsorbed in cation-exchanged zeolites,^{19,20} no experimental evidence of that has ever been reported for CO adsorbed on extended ionic surfaces in the CO low coverage regime.

We rationalized the presence of red-shifted cases by invoking the role of some specific features present at the Fo surfaces which can influence the electrostatic of adsorption. This aspect has been extensively revised in a subsequent work dealing again with the CO adsorption of Fo surfaces and centred at this specific topic. We will briefly talk about this aspect in the next Section.

6.1.4.1 Red-shifts and quadrupolar interactions

In a recent work, we deeply investigated the role of quadrupolar forces in determining the vibrational shift of CO adsorbed on selected Fo surfaces.²¹ Specifically, starting from the B3LYP-D2*-optimized geometries of two

redshifted cases of the previous work (which, from now on, we will label as Zamirri2017¹), where only on CO *per* unit cell was adsorbed on the (110) and (101) Fo surfaces, we run farther optimizations (and frequency calculations) at different levels of theory. The two test cases are labelled as “(110) 1C” and “(101) 1B”. Some of the most relevant data are resumed in **Table 6.2**. For all other data, please refer to the original work.²¹

Table 6.2 Resume of some data for the “(110) 1C” and (101) 1B” CO adsorption cases of Fo. $\Delta\bar{\nu}$ is the vibrational shift (in cm^{-1}), while $d_{\text{C-O}}$ and $d_{\text{CM-O}^-}$ represent the C–O bond length and the distance between the CO centre of mass (CM) and the closest, negative O atom (O^-) of the Fo surface (both in Å). Data from the Zamirri2017 work in italics.²¹

Code	Functional-dispersion	$\Delta\bar{\nu}$	$d_{\text{C-O}}$	$d_{\text{CM-O}^-}$
(110) 1C				
<i>CRYSTAL</i>	<i>B3LYP-D2*</i>	–7	<i>1.1268</i>	<i>2.6522</i>
CRYSTAL	B3LYP-D2*	+3	1.1253	2.8010
CRYSTAL	B3LYP-D2**	+12	1.1244	2.9233
CRYSTAL	B3LYP-D3	–2	1.1261	2.7403
CRYSTAL	B3LYP	+15	1.1238	3.0318
CRYSTAL	PBE-D2	–59	1.1449	2.5385
CRYSTAL	PBE	–39	1.1422	2.5904
VASP	PBE-D2	–25	1.1468	2.6303
VASP	PBE	+13	1.1419	3.0998
(101) 1B				
<i>CRYSTAL</i>	<i>B3LYP-D2*</i>	–21	<i>1.1283</i>	<i>2.5731</i>
CRYSTAL	B3LYP-D2*	–26	1.1289	2.5609
CRYSTAL	B3LYP-D2**	–26	1.1288	2.5627
CRYSTAL	B3LYP-D3	–38	1.1305	2.5018
CRYSTAL	B3LYP	+28	1.1221	2.9541
CRYSTAL	PBE-D2	–90	1.1499	2.3840
CRYSTAL	PBE	–97	1.1508	2.3681
VASP	PBE-D2	–71	1.1533	2.4225
VASP	PBE	–76	1.1541	2.4026

For both test cases, we run two kinds of calculations, namely with localized BSs (CRYSTAL code, with the same BS as in Zamirri2017) and with BSSE-free plane wave BSs (VASP code). B3LYP-D2** is a revised version of Civalleri’s D2* where we arbitrarily set the dispersion coefficient of Mg ions equal to zero, in line with a previous work.²² We also tested the D3 version of Grimme’s correction (Section 2.3.2) at B3LYP level, as well as the pure D2 at PBE level. Finally, pure B3LYP and PBE calculations have been also tested. We performed plane wave calculations at PBE-D2 and PBE levels only. The B3LYP-D2* optimized geometries for the two test cases are reported in **Figure 6.5**.

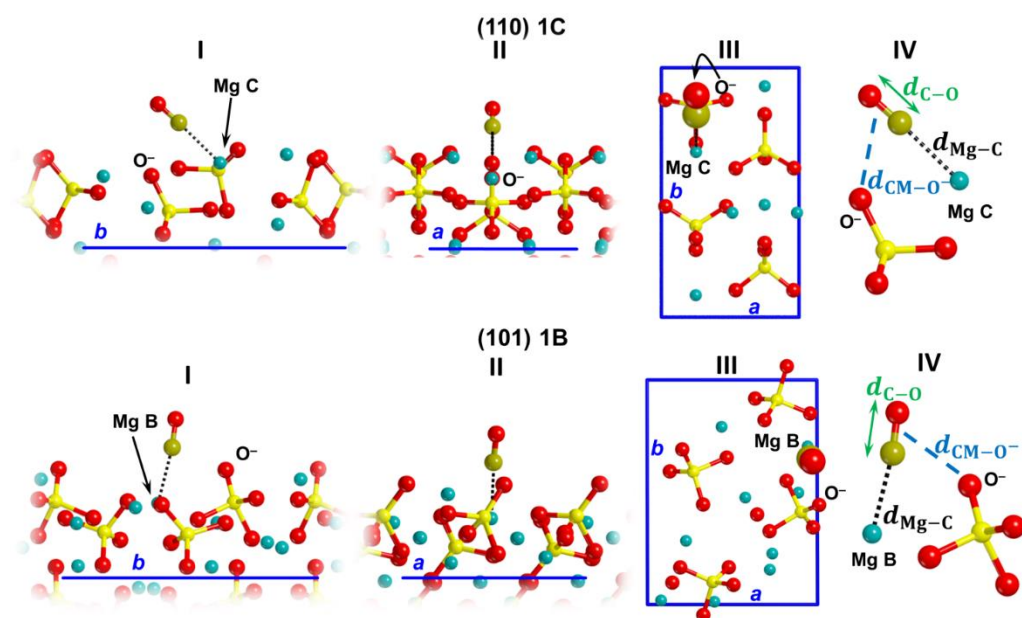


Figure 6.5 Final optimized geometries for the “(110) 1C” (top) and “(101) 1B” (bottom) cases computed at B3LYP-D2* level. The structural features for all other cases are analogous. **I** and **II**: details of the side views along a and b lattice vectors, respectively. **III**: top views (C and O atoms of the CO molecules as van der Waals spheres). **IV**: Zoomed views of the local atomic environments surrounding the CO molecule; the two distances reported in **Table 6.2** are also highlighted.

As a first comment, the final value of the vibrational shift strongly depends on the adopted level of theory. Secondly, in all red-shifted cases, the $CM-O^-$ distance is lower than 2.75 \AA , while for blueshifted cases it is always higher. Moreover, the

presence of red-shifts at PBE (-D2) level with the BSSE-free VASP code confirms that these red-shifts do not derive from computational artefacts (as BSSE is), but rather should be considered as the result of a true interaction. Nevertheless, as highlighted in **Figure 6.6**, the CM-O^- distance well linearly correlates with the negative values of the vibrational shift, while for positive values these linear correlations are lost, confirming our initial hypothesis that such a strange behaviour is the result of the quadrupolar interaction of the CO molecule (blue positive bend in **Figure 6.3**) with the negatively charged O atoms of the Fo surfaces. When such a distance is greater than a specific threshold (whose value depends on the specific case), these quadrupolar interaction is so small that is overcome by other forces, and the CO vibrational shift becomes positive.

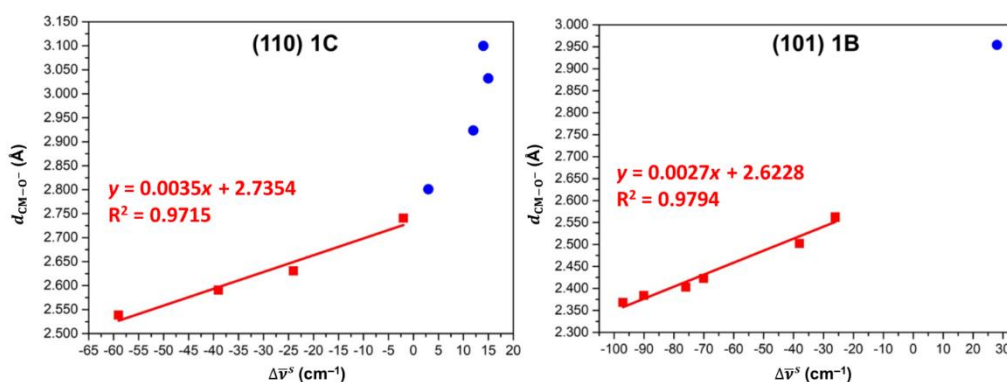


Figure 6.6 Distances between the CO centre of mass and the O^- atoms ($d_{\text{CM-O}^-}$) vs $\Delta\bar{\nu}^s$ for the “(110) 1C” (left) and “(101) 1B” cases. Only negative shifts (red squares) correlate with $d_{\text{CM-O}^-}$ values.

Bibliography

- (1) Zamirri, L.; Corno, M.; Rimola, A.; Ugliengo, P. Forsterite Surfaces as Models of Interstellar Core Dust Grains: Computational Study of Carbon Monoxide Adsorption. *ACS Earth Sp. Chem.* **2017**, *1*, 384–398.
- (2) Becke, A. D. A New Mixing of Hartree-Fock and Local-Density-Functional Theories. *J. Chem. Phys.* **1993**, *98*, 1372–1377.
- (3) Becke, A. D. Density-Functional Exchange-Energy Approximation with Correct Asymptotic Behavior. *Phys. Rev. A* **1988**, *38*, 3098–3100.
- (4) Lee, C.; Yang, W.; Parr, R. G. Development of the Colle-Salvetti Correlation-Energy Formula into a Functional of the Electron Density. *Phys. Rev. B* **1988**, *37*, 785–789.
- (5) Grimme, S. Semiempirical GGA-Type Density Functional Constructed with a Long-Range Dispersion Correction. *J. Comput. Chem.* **2006**, *27*, 1787–1799.
- (6) Civalleri, B.; Zicovich-Wilson, C. M.; Valenzano, L.; Ugliengo, P. B3LYP Augmented with an Empirical Dispersion Term (B3LYP-D*) as Applied to Molecular Crystals. *CrystEngComm* **2008**, *10*, 405–410.
- (7) Demichelis, R.; Civalleri, B.; Ferrabone, M.; Dovesi, R. On the Performance of Eleven DFT Functionals in the Description of the Vibrational Properties of Aluminosilicates. *Int. J. Quantum Chem.* **2010**, *110*, 406–415.
- (8) Schäfer, A.; Horn, H.; Ahlrichs, R. Fully Optimized Contracted Gaussian-Basis Sets for Atoms Li to Kr. *J. Chem. Phys.* **1992**, *97*, 2571–2577.
- (9) Bruno, M.; Massaro, F. R.; Prencipe, M.; Demichelis, R.; De La Pierre, M.; Nestola, F. Ab Initio Calculations of the Main Crystal Surfaces of Forsterite (Mg₂SiO₄): A Preliminary Study to Understand the Nature of Geochemical Processes at the Olivine Interface. *J. Phys. Chem. C* **2014**, *118*, 2498–2506.
- (10) Wulff, G. Zur Frage Der Geschwindigkeit Des Wachstums Und Der


- Auflosung Der Krystallflächen. *Zeitschrift für Kryst. und Mineral.* **1901**, 34, 449–530.
- (11) Dovesi, R.; Saunders, V. R.; Roetti, C.; Orlando, R.; Pascale, F.; Civalleri, B.; Doll, K.; Harrison, N. M.; Bush, I. J.; D’Arco, P.; *et al.* CRYSTAL17. User’s Manual. 2018.
- (12) Blyholder, G. Molecular Orbital View of Chemisorbed Carbon Monoxide. *J. Phys. Chem.* **1964**, 68, 2772–2777.
- (13) Bistoni, G.; Rampino, S.; Scafuri, N.; Ciancaleoni, G.; Zuccaccia, D.; Belpassi, L.; Tarantelli, F. How π Back-Donation Quantitatively Controls the CO Stretching Response in Classical and Non-Classical Metal Carbonyl Complexes. *Chem. Sci.* **2016**, 7, 1174–1184.
- (14) Tiana, D.; Francisco, E.; Blanco, M. A.; Macchi, P.; Sironi, A.; Martín Pendás, A. Bonding in Classical and Nonclassical Transition Metal Carbonyls: The Interacting Quantum Atoms Perspective. *J. Chem. Theory Comput.* **2010**, 6, 1064–1074.
- (15) Pilme, J.; Silvi, B.; Alikhanim, M. E. Structure and Stability of M–CO, M = First-Transition-Row Metal: An Application of Density Functional Theory and Topological Approaches. *J. Phys. Chem. A* **2003**, 107, 4506–4514.
- (16) Goldman, A. S.; Krogh-Jespersen, K. Why Do Cationic Carbon Monoxide Complexes Have High C-O Stretching Force Constants and Short C-O Bonds? Electrostatic Effects, not σ -Bonding. *J. Am. Chem. Soc.* **1996**, 118, 12159–12166.
- (17) Lupinetti, A. J.; Fau, S.; Frenking, G.; Strauss, S. H. Theoretical Analysis of the Bonding between CO and Positively Charged Atoms. *J. Phys. Chem. A* **1997**, 101, 9551–9559.
- (18) Bolis, V.; Barbaglia, A.; Bordiga, S.; Lamberti, C.; Zecchina, A. Heterogeneous Nonclassical Carbonyls Stabilized in Cu (I) - and Ag (I) - ZSM-5 Zeolites: Thermodynamic and Spectroscopic Features. *J. Phys.*

- Chem. B* **2004**, *108*, 9970–9983.
- (19) Bolis, V.; Fubini, B.; Garrone, E.; Giamello, E.; Morterra, C. A Comparison Between the Lewis Acidity of Non-D Metal Cations in Y-Zeolites and on Ionic Surfaces. *Stud. Surf. Sci. Catal.* **1989**, *48*, 159–166.
- (20) Ugliengo, P.; Garrone, E.; Ferrari, A. M.; Zecchina, A. Quantum Chemical Calculations and Experimental Evidence for O-Bonding of Carbon Monoxide to Alkali Metal Cations in Zeolites. *J. Phys. Chem. B* **1999**, *103*, 4839–4846.
- (21) Zamirri, L.; Pantaleone, S.; Ugliengo, P. Carbon Monoxide Adsorption at Forsterite Surfaces as Models of Interstellar Dust Grains: An Unexpected Bathochromic (Red) Shift of the CO Stretching Frequency. *J. Chem. Phys.* **2019**, *150*, 064702 (9 pp).
- (22) Tosoni, S.; Sauer, J. Accurate Quantum Chemical Energies for the Interaction of Hydrocarbons with Oxide Surfaces: CH₄/MgO(001). *Phys. Chem. Chem. Phys.* **2010**, *12*, 14330–14340.

6 List of published works

In this brief Chapter, we report the full list of all articles that are already published in chronological order.

- 1) L. Zamirri, M. Corno, A. Rimola, P. Ugliengo. “Forsterite Surfaces as Models of Interstellar Dust Grains: Computational Study of Carbon Monoxide Adsorption”. *ACS Earth and Space Chemistry*, **2017**, 1, 384–398.



Article
<http://pubs.acs.org/journal/aescqj>

Forsterite Surfaces as Models of Interstellar Core Dust Grains: Computational Study of Carbon Monoxide Adsorption

Lorenzo Zamirri,[†] Marta Corno,^{*,†,§} Albert Rimola,[‡] and Piero Ugliengo^{*,†}

[†]Dipartimento di Chimica and NIS, Nanostructured Interfaces and Surfaces, Centre, Università degli Studi di Torino, via P. Giuria 7, 10125, Torino, Italy
[‡]Departament de Química, Universitat Autònoma de Barcelona, 08193 Bellaterra, Spain

- 2) L. Zamirri, S. Casassa, A. Rimola, M. Segado-Centellas, C. Ceccarelli, P. Ugliengo. “IR spectral fingerprint of carbon monoxide in interstellar water–ice models”. *Monthly Notices of the Royal Astronomical Society*, **2018**, 480, 1427–1444.

Monthly Notices
of the
ROYAL ASTRONOMICAL SOCIETY

MNRAS **480**, 1427–1444 (2018)
Advance Access publication 2018 July 19



doi:10.1093/mnras/sty1927

IR spectral fingerprint of carbon monoxide in interstellar water–ice models

Lorenzo Zamirri,^{1,2} Silvia Casassa,^{1,2*} Albert Rimola,³ Mireia Segado-Centellas,⁴ Cecilia Ceccarelli,^{5,6} and Piero Ugliengo^{1,2}



¹Dipartimento di Chimica, Università degli Studi di Torino, via P. Giuria 7, I-10125, Torino, Italy
²Nanostructured Interfaces and Surfaces (NIS) Centre, Università degli Studi di Torino, via P. Giuria 7, I-10125, Torino, Italy
³Departament de Química, Universitat Autònoma de Barcelona, E-08193, Bellaterra, Spain
⁴Institut Català d'Investigació Química (ICIQ), Avinguda Països Catalans 16, E-43007, Tarragona, Spain
⁵Institut de Planétologie et d'Astrophysique de Grenoble (IPAG), rue de la Piscine, F-38041, Grenoble, France
⁶INAF-Osservatorio Astrofisico di Arcetri, largo E. Fermi 5, I-50125, Firenze, Italy

- 3) M. Signorile, C. Salvini, L. Zamirri, F. Bonino, G. Martra, M. Sodupe, P. Ugliengo. “Formamide Adsorption at the Amorphous Silica Surface: A Combined Experimental and Computational Approach”. *Life*, **2018**, 8, 42 (13 pp).



Article

Formamide Adsorption at the Amorphous Silica Surface: A Combined Experimental and Computational Approach

Matteo Signorile ¹, Clara Salvini ¹, Lorenzo Zamirri ¹, Francesca Bonino ¹, Gianmario Martra ¹, Mariona Sodupe ² and Piero Ugliengo ^{1,*}

¹ Dipartimento di Chimica and NIS, Università di Torino, Via P. Giuria 7 — 10125 Torino and Via G. Quarelo 15/A — 10135 Torino, Italy; matteo.signorile@unito.it (M.S.); clara.salvini@edu.unito.it (C.S.); lorenzo.zamirri@unito.it (L.Z.); francesca.bonino@unito.it (F.B.); gianmario.martra@unito.it (G.M.)

² Departament de Química, Universitat Autònoma de Barcelona, 08193 Bellaterra, Catalonia, Spain; mariona.sodupe@uab.cat

* Correspondence: piero.ugliengo@unito.it; Tel.: +39-011-670-4596

- 4) L. Zamirri, S. Pantaleone, P. Ugliengo. “Carbon monoxide adsorption at forsterite surfaces as models of interstellar dust grains: An unexpected bathochromic (red) shift of the CO stretching frequency”. *The Journal of Chemical Physics*, **2019**, 150, 064702 (9 pp).




The Journal of Chemical Physics




ARTICLE

scitation.org/journal/jcp

Carbon monoxide adsorption at forsterite surfaces as models of interstellar dust grains: An unexpected bathochromic (red) shift of the CO stretching frequency

Cite as: *J. Chem. Phys.* **150**, 064702 (2019); doi: [10.1063/1.5075632](https://doi.org/10.1063/1.5075632)
Submitted: 23 October 2018 • Accepted: 21 January 2019 •
Published Online: 12 February 2019


  

Lorenzo Zamirri,^{1,2}  Stefano Pantaleone,³  and Piero Ugliengo^{1,2a)} 

AFFILIATIONS

¹Dipartimento di Chimica, Università degli Studi di Torino, Via P. Giuria 7, I-10125 Torino, Italy
²Nanostructured Interfaces and Surfaces (NIS) Centre, Università degli Studi di Torino, Via P. Giuria 7, I-10125 Torino, Italy
³Departament de Química, Universitat Autònoma de Barcelona, E-08193 Bellaterra, Spain

- 5) L. Zamirri, P. Ugliengo, C. Ceccarelli, A. Rimola. “Quantum Mechanical Investigations on the Formation of Complex Organic Molecules on Interstellar Ice Mantles. Review and Perspectives”. *ACS Earth and Space Chemistry*, **2019**, 3, 1499–1523.



Review

Cite This: *ACS Earth Space Chem.* 2019, 3, 1499–1523 <http://pubs.acs.org/journal/aescq>

Quantum Mechanical Investigations on the Formation of Complex Organic Molecules on Interstellar Ice Mantles. Review and Perspectives

Lorenzo Zamirri,^{†,‡,Ⓧ} Piero Ugliengo,^{†,‡,Ⓧ} Cecilia Ceccarelli,[§] and Albert Rimola^{*,||,Ⓧ}

[†]Dipartimento di Chimica, Università degli Studi di Torino, via P. Giuria 7, 10125 Torino, Italy
[‡]Nanostructured Interfaces and Surfaces (NIS) Centre, Università degli Studi di Torino, via P. Giuria 7, 10125 Torino, Italy
[§]Université Grenoble Alpes, CNRS, Institut de Planétologie et d’Astrophysique de Grenoble (IPAG), rue de la Piscine 414, 38000 Grenoble, France
^{||}Departament de Química, Universitat Autònoma de Barcelona, 08193 Bellaterra, Catalonia, Spain

- 6) L. Zamirri, P. Ugliengo, C. Ceccarelli, A. Rimola. “What Can Infrared Spectra Tell Us about the Crystallinity of Nanosized Interstellar Silicate Dust Grains?”. *ACS Earth and Space Chemistry*, **2019**, 3, 2323–2338.



Article

Cite This: *ACS Earth Space Chem.* XXXX, XXX, XXX–XXX <http://pubs.acs.org/journal/aescq>

What Can Infrared Spectra Tell Us about the Crystallinity of Nanosized Interstellar Silicate Dust Grains?

Lorenzo Zamirri,^{†,||,Ⓧ} Antoni Macià Escatllar,^{‡,||} Joan Mariñoso Guiu,[‡] Piero Ugliengo,^{*,†,Ⓧ} and Stefan T. Bromley^{*,‡,§,Ⓧ}

[†]Dipartimento di Chimica and Nanostructured Interfaces and Surfaces (NIS) Centre, Università degli Studi di Torino, via P. Giuria 7, IT-10125 Torino, Italy
[‡]Departament de Ciència de Materials i Química Física and Institut de Química Teòrica i Computacional (IQTCUB), Universitat de Barcelona, C/Martí i Franquès 1, ES-08028 Barcelona, Spain
[§]Institució Catalana de Recerca i Estudis Avançats (ICREA), ES-08010 Barcelona, Spain

List of acronyms and abbreviations

The following list does not include chemical formula for molecular, radical and ionic species.

Acronym/ abbreviation	Meaning
(i)COM	(interstellar) Complex organic molecule
AGB	Asymptotic giant branch (stars)
AIB	Aromatic interstellar band
AIMD	<i>Ab initio</i> molecular dynamics
AME	Anomalous microwave emission
AO	Atomic orbital
ASW	Amorphous solid water
au	Atomic units
B3LYP	Becke-3 (parameters)-Lee-Yang-Parr (functional)
BE	Binding energy
BF	Bloch function
BFGS	Broyden-Fletcher-Goldfarb-Shanno
BS	Basis set
BSSE	Basis set superposition error
cc	Correlation-consistent
CC	Coupled cluster
CI	Configuration interaction
CM	Classical mechanics
CMBR	Cosmic microwave background radiation
CNO	Carbon-nitrogen-oxygen (cycle)
CO	Crystalline orbital
CP	Counterpoise
CR	Cosmic ray
CSS	Circumstellar shell
DC	Dark cloud
DFT	Density functional theory
EM	Electromagnetic
EMS	Electromagnetic spectrum
ESP	Electrostatic potential
ESPM	Electrostatic potential map
FF	Force field
Fo	Forsterite
GGA	Generalized gradient approximation
GMC	Giant molecular cloud
GTO	Gaussian-type orbital

List of acronyms and abbreviations

GULP	General utility lattice program
HAC	Hydrogenated amorphous carbon
HF	Hartree-Fock
HPC	High-performance computing
IR	Infrared
ISM	Interstellar medium
ISP	Interstellar particle
KS-MO	Kohn-Sham molecular orbital
LAMMPS	Large-scale atomic/molecular massively parallel simulator
LBV	Luminous blue variable (star)
LCAO	Linear combination of atomic orbitals
LDA	Local density approximation
LMC	Large Magellanic cloud
MC	Molecular cloud
MD	Molecular dynamics
ML	Monolayer
MM	Molecular mechanics
MO	Molecular orbital
MP n	n^{th} order Møller-Plesset (method)
MRI	Morphological relevance index
MRN	Mathis-Rumpl-Nordsieck (model)
NP	Nanoparticle
OI	Olivine
PAH	Polycyclic aromatic hydrocarbon
PBC	Periodic boundary conditions
PBE	Perdew-Burke-Ernzerhof (functional)
PDR	Photodissociation region
PES	Potential energy surface
PN	Planetary nebula
QM	Quantum mechanics
RGB	Red-green-blue
RH	Roothan-Hall
RSG	Red super giant (star)
SC	Supercell
SCA	Spherical cluster approximation
SCF	Self-consistent field
SI	Supporting information
SMC	Small Magellanic cloud
SN	Supernova/supernovae
SP	Single point
STO	Slater-type orbital
TPD	Thermal programmed desorption
UV	Ultraviolet

List of acronyms and abbreviations

VASP	Vienna <i>ab-initio</i> simulation package
VMD	Visual molecular dynamics
WR	Wolf-Rayet (star)

List of figures

Figure	Brief description	Page
1.1	Black body spectrum for CMBR.....	7
1.2	Einstein, Fridman, Hubble, Lemaître, Wilson and Penzias...	8
1.3	Average BE <i>per</i> hadron <i>vs</i> atomic mass number.....	11
1.4	The stellar lifecycle.....	15
1.5	ISM components.....	20
1.6	Examples of ISM nebulae.....	21
1.7	Examples of extinction curves.....	28
1.8	IR absorption spectrum around YSO AFGL 7009 S.....	36
2.1	Examples of first hydrogen-like orbitals.....	57
2.2	The electron density surrounding two bound nuclei.....	61
2.3	The Jacob's ladder of DFT functionals.....	66
3.1	IR spectra for the CO/H ₂ O interface.....	101
3.2	Pure CO systems: gas <i>vs</i> solid phase.....	105
3.3	Single CO adsorption on P-ice surfaces.....	107
3.4	Multiple CO adsorption on P-ice surfaces.....	109
3.5	CO entrapped in different water cages.....	112
3.6	CO expelled from partial water cages.....	113
3.7	MD IR spectra for a CO/H ₂ O mixed ice.....	115
3.8	Structural features of CO/H ₂ O mixed ice.....	116
3.9	Overall simulated spectra for all CO/H ₂ O interactions.....	118
4.1	PES and coordinate reaction.....	136
4.2	Half-life time <i>vs</i> Gibbs free energy barrier.....	137
4.3	Different ways to simulate a water ice surface.....	141
4.4	Formation of methanol from methyl cation plus water.....	143
4.5	Formation of COOH· from OH· + CO.....	148
4.6	The proton-relay mechanism illustrated.....	149
4.7	Gibbs free energy profile for aminoacetonitrile formation...	150
4.8	Different initial water clusters for formaldehyde amination...	152
4.9	The Strecker synthesis of glycine.....	154
4.10	Two syntheses of glycine form methanimine.....	156
5.1	IR spectra for crystalline forsterite and amorphous olivine...	183
5.2	Resume of all calculations in Chapter 5.....	186
5.3	Initial structures of forsterite nanoparticles.....	188
5.4	DFT-optimized BC nanoparticles.....	189
5.5	DFT-optimized A nanoparticles.....	190
5.6	DFT-optimized N nanoparticles.....	191
5.7	Energetic stability of olivine nanoparticles.....	195
5.8	Different phases of olivinic material.....	199
5.9	Structural descriptors for olivine nanoparticles.....	200

5.10	Local SiO ₄ distortion.....	202
5.11	Simulated IR spectra for some nanoparticles.....	204
6.1	Forsterite bulk and slabs.....	217
6.2	Wulff's construction for forsterite.....	219
6.3	Electrostatic potential maps for CO and forsterite.....	220
6.4	CO adsorption on forsterite: some data.....	222
6.5	CO adsorption on forsterite: red-shifted cases.....	224
6.6	Some correlations fore red-shifted cases.....	225

List of schemes

Scheme	Brief description	Page
1.1	The CNO cycle.....	13
4.1	Hydrogenation of carbon monoxide.....	145
4.2	Hydrogenation of hydrogen cyanide.....	146
4.3	Amination and hydration of formaldehyde.....	151
4.4	Hydantoin formation from NH ₂ CH ₂ CN + CO ₂	157

List of tables

Table	Brief description	Page
1.1	The history of the Universe.....	9
1.2	Stages of thermonuclear generation in stars.....	14
1.3	ISM components and their properties.....	20
1.4	Species detected in diffuse clouds.....	22
1.5	Identified molecules in the ISM.....	25
1.6	Sources of information about dust grains.....	30
1.7	Sources of different type of interstellar particles.....	33
1.8	Relative abundances of solid phase species.....	35
3.1	Resume of some CO/H ₂ O signals assignments.....	101
3.2	Gas and solid phase CO: experiments <i>vs</i> simulation.....	105
3.3	All data for the CO/H ₂ O ice interactions.....	119
5.1	Energetic and structural features for olivine particles.....	193
6.1	Structural and energetic features of forsterite surfaces.....	218
6.2	CO red-shifted cases: some data.....	223

Acknowledgements

First, and most of all, I wish to thank Professor Piero Ugliengo for his incredible efforts in supporting the realization of this work. Without his fundamental assistance, indeed, most of the scientific results of this Thesis might not have come to light.

I wish also to thank the entire Department of Chemistry of the University of Turin, and in particular the Chemical Physics and Computational Chemistry groups.

Special thanks go to the people that helped me in improving my scientific activity and shared with me most of the efforts: Professors Bartolomeo Civalleri, Silvia Casassa, Cecilia Ceccarelli, Mariona Sodupe, Gianmario Martra, Mario Chiesa, and Stefan Bromley; Doctors Albert Rimola, Alessandro Erba, and Francesca Bonino; my friends and colleagues Dr. Michele Cutini, Dr. Marco Fabbiani, Dr. Stefano Pantaleone, Dr. Simone Salustro, Dr. Matteo Signorile, Andrea Martini, Clara Salvini, Stefano Ferrero, Antoni Macià, Irene Bechis, Massimo Bocus, Lorenzo Donà, Loredana Daga, Guillermo Solano, Rosangela Santalucia, Guillermo Escolano and Ilia Pankin.

A big thank goes, finally, to my friend Federico Gastaldi for the beautiful cover picture and, particularly, to my family and parents who supported me during this long journey.

Astronomy and astrophysics probably represent two of the oldest fields of research for humans. For centuries, the only investigation instrument we possessed was our eye, but then the first telescopes were invented and utilized to reveal the secrets of our Universe. Since that early stages of modern science, astrophysics has dramatically changed, but the original spirit still persists. From modern astronomical observations, we now know that the Space is far away from being “void”, but rather it is characterized by a surprisingly vivid chemistry. Consequently, in the past century a new discipline, dealing with the composition of interstellar matter, arose: astrochemistry. In quite recent years, this new branch of astrophysics has gained the attention of the computational chemistry community, since computer simulations represent a powerful and complementary tool for the astrochemical research. In this Thesis, we extensively show some examples of the application of computational methods to a specific but fundamental astrochemical topic, the modelling of the solid phase of interstellar matter.

